

NASA/TM-2002-211780



Experimental Test Results of Energy Efficient Transport (EET) High-Lift Airfoil in Langley Low-Turbulence Pressure Tunnel

Harry L. Morgan, Jr.
Langley Research Center, Hampton, Virginia

December 2002

The NASA STI Program Office . . . in Profile

Since its founding, NASA has been dedicated to the advancement of aeronautics and space science. The NASA Scientific and Technical Information (STI) Program Office plays a key part in helping NASA maintain this important role.

The NASA STI Program Office is operated by Langley Research Center, the lead center for NASA's scientific and technical information. The NASA STI Program Office provides access to the NASA STI Database, the largest collection of aeronautical and space science STI in the world. The Program Office is also NASA's institutional mechanism for disseminating the results of its research and development activities. These results are published by NASA in the NASA STI Report Series, which includes the following report types:

- **TECHNICAL PUBLICATION.** Reports of completed research or a major significant phase of research that present the results of NASA programs and include extensive data or theoretical analysis. Includes compilations of significant scientific and technical data and information deemed to be of continuing reference value. NASA counterpart of peer-reviewed formal professional papers, but having less stringent limitations on manuscript length and extent of graphic presentations.
- **TECHNICAL MEMORANDUM.** Scientific and technical findings that are preliminary or of specialized interest, e.g., quick release reports, working papers, and bibliographies that contain minimal annotation. Does not contain extensive analysis.
- **CONTRACTOR REPORT.** Scientific and technical findings by NASA-sponsored contractors and grantees.

- **CONFERENCE PUBLICATION.** Collected papers from scientific and technical conferences, symposia, seminars, or other meetings sponsored or co-sponsored by NASA.
- **SPECIAL PUBLICATION.** Scientific, technical, or historical information from NASA programs, projects, and missions, often concerned with subjects having substantial public interest.

TECHNICAL TRANSLATION. English-language translations of foreign scientific and technical material pertinent to NASA's mission.

Specialized services that complement the STI Program Office's diverse offerings include creating custom thesauri, building customized databases, organizing and publishing research results . . . even providing videos.

For more information about the NASA STI Program Office, see the following:

- Access the NASA STI Program Home Page at <http://www.sti.nasa.gov>
- Email your question via the Internet to help@sti.nasa.gov
- Fax your question to the NASA STI Help Desk at (301) 621-0134
- Telephone the NASA STI Help Desk at (301) 621-0390
- Write to:
NASA STI Help Desk
NASA Center for AeroSpace Information
7121 Standard Drive
Hanover, MD 21076-1320

NASA/TM-2002-211780



Experimental Test Results of Energy Efficient Transport (EET) High-Lift Airfoil in Langley Low-Turbulence Pressure Tunnel

Harry L. Morgan, Jr.
Langley Research Center, Hampton, Virginia

National Aeronautics and
Space Administration

Langley Research Center
Hampton, Virginia 23681-2199

December 2002

Available from:

NASA Center for AeroSpace Information (CASI)
7121 Standard Drive
Hanover, MD 21076-1320
(301) 621-0390

National Technical Information Service (NTIS)
5285 Port Royal Road
Springfield, VA 22161-2171
(703) 605-6000

This report is also available in electronic form at URL <http://techreports.larc.nasa.gov/ltrs/>.
A CD-ROM supplement to this report is available from the NASA Center for AeroSpace Information.

Summary

An experimental study has been conducted in the Langley Low-Turbulence Pressure Tunnel to determine the effects of Reynolds number and Mach number on the two-dimensional aerodynamic performance of the Langley Energy Efficient Transport (EET) High-Lift Airfoil. This high-lift airfoil is a supercritical-type airfoil with a thickness-to-chord ratio of 0.12 and is equipped with a leading-edge slat and a double-slotted trailing-edge flap. The two-element trailing-edge flap consisted of a large-chord vane and small-chord aft flap. All the elements were supported by a set of brackets that held each element at fixed deflection, gap, and overlap. The leading-edge slat brackets consisted of a set of four brackets with deflections of -30° , -40° , -50° , and -60° . The trailing-edge flap brackets were designed for equal deflections between the main and vane elements and between the vane and aft-flap elements and consisted of a set of four brackets with deflections of 7.5° , 15° , 22.5° , and 30° . These sets of slat and flap brackets resulted in 16 different configurations each with accurately defined and highly repeatable lofted geometries. The model was equipped with a densely defined row of chordwise surface pressure taps along the model midspan and two coarsely defined chordwise rows 2.5 in. from each sidewall. The aerodynamic forces and moment were measured by a yoke-type three-component, strain-gauge balance and model support system that had an angle-of-attack range of -8° to 26° . All 16 configurations were tested at a free-stream Mach number of 0.20 and, for a few selected configurations, through a Mach number range of 0.10 to 0.35. In addition, all of the configurations were tested through a Reynolds number range of 2.5×10^6 to 18×10^6 . For a few selected configurations, the drag was measured with a downstream mounted wake traversing system that held a rake consisting of three equally spaced, five-hole pressure probes. During the testing, the spanwise two-dimensionality of the flow over the model was controlled by energizing the tunnel sidewall boundary layer to delay or prevent separation with a set of four tangential blowing slots located at specific locations on each model endplate.

The test results demonstrate the tremendous effect of Reynolds number and Mach number on the aerodynamic performance of this supercritical-type high-lift airfoil. Analysis of the test data revealed several inconsistencies in the trends observed showing the effects of an increase in Reynolds number and Mach number on the maximum lift performance of the high-lift airfoil. The endplate blowing system developed was able to adequately control the separation of the sidewall boundary layer; thereby, spanwise uniformity of the flow around the model during the test was maintained. The model geometry, surface pressures, balance-measured forces and moment, and wake data obtained are very well defined for all 16 configurations tested; therefore, these data are well suited for the validation and calibration of computer codes that predict high-lift system performance and flow field characteristics.

Introduction

During the early 1970s through the late 1980s the National Aeronautics and Space Administration was actively involved in an aeronautical research effort to improve the energy efficiency of modern wide-body jet transport aircraft. The Aircraft Energy Efficiency (ACEE) project was formulated to encourage industry participation and to coordinate the industry and NASA research efforts. One element of the ACEE project was the Energy Efficient Transport (EET) program, which was concerned primarily with the development of advanced aerodynamics and active-controls technology for application to derivative or next-generation transport aircraft. A part of the EET program was the development, by NASA Langley Research Center personnel, of advanced supercritical wings with greater section thickness-to-chord ratios, higher aspect ratios, higher cruise lift coefficients, and lower sweepback than the conventional wings of current transports. These supercritical wings were tested extensively in the Langley wind tunnels to determine their high-speed cruise performance characteristics. Because of their high cruise lift coefficients and high aspect ratios, these wings could be smaller and more fuel efficient than wings used

currently provided high-lift flaps systems could be designed to ensure that takeoff and landing requirements could be met.

As part of the EET Program, a high-lift flap system was designed for a representative supercritical wing and tested on both a two-dimensional airfoil model and on two different scaled three-dimensional wing models. One high-lift wing model with a span of 7.5 ft was tested at high Reynolds number, high-pressure conditions in the Ames 12-Foot Pressure Tunnel. The other model with a span of 12 ft was tested at low Reynolds number, atmospheric conditions in the Langley 14- by 22-Foot Subsonic Tunnel. The 7.5-ft span model was also tested in the Langley 14- by 22-Foot Subsonic Tunnel to obtain support system interference and wall corrections for the Ames tests. Both models had an aspect ratio of 12, a quarter-chord sweep of 27° , and the wing and body shape of the NASA supercritical SCW-2a high-speed transonic model tested in the Langley 8-Foot Transonic Pressure Tunnel and reported in references 1 and 2. Both high-lift models were tested extensively from the late 1970s to the mid 1980s and the data are reported in references 3 through 9. A photograph of the 12-ft span model mounted in the Langley 14- by 22-Foot Subsonic Tunnel is shown in figure 1.

The high-lift flap for these models consisted of a part-span double-slotted trailing-edge flap and a full-span leading-edge slat. The trailing-edge flap consisted of a large-chord vane and small-chord aft flap combination, as opposed to the more conventionally used small-chord vane and large-chord aft flap combinations. Vane-flap combinations similar to the combination used on these models had also been under development by several aircraft manufacturers and had achieved maximum two-dimensional lift coefficients approaching those of more complex triple-slotted flap combinations. Each model was also equipped with inboard high-speed ailerons, outboard low-speed ailerons, two wing-mounted flow-through nacelles, landing gear, movable horizontal tails, and interchangeable wingtips that provided for aspect ratios of both 10 and 12. Each model was instrumented with a six-component strain-gauge balance to measure aerodynamic forces and moments and with chordwise pressure taps at three spanwise stations to determine representative wing and flap loads.

The cruise wing for these three-dimensional high-lift models had a break station at the 38.3-percent semispan location as shown in figure 2. The airfoil t/c at this location is 0.12 and was close to the average t/c of the wing, which has a root t/c of 0.144 and a tip t/c of 0.10. The high-lift flap system for the wing was designed first by defining the element shapes at the break station and then extending those shapes to the inboard and outboard wing location through linear extrapolation. A constant-chord model of the high-lift airfoil at the wing break station was built and tested in the Langley Low-Turbulence Pressure Tunnel (LTPT). The results from the test of that model are presented in this report. These data cover a range of Reynolds numbers from 2.5×10^6 to 18×10^6 and Mach numbers from 0.10 to 0.35. The data consist of chordwise surface static pressures on each element and tunnel centerline floor and ceiling pressures from the tunnel pressure scanning system, section lift and pitching-moment data from the tunnel balance system, and selective drag data from the tunnel wake rake survey system.

Symbols

A_f	balance measured axial force, lb
AR	aspect ratio of EET High-Lift Wing Model
b	model span, 36.0 in.
C_p	local surface static pressure coefficient
c	airfoil reference chord, 21.654 in.

c_d	section drag coefficient
c'_d	wake point drag coefficient
c_l	section lift coefficient
c_m	section pitching-moment coefficient
d_{wt}	distance from model weight center to endplate center of rotation, in.
H_{tr}	sidewall blowing-box thrust distance from center of turntable (positive up), in.
h	tunnel height, 90.0 in.
h_t	wake probe height, in.
M_∞	free-stream Mach number
\dot{m}	blowing-box mass flow, slugs/min
N_f	balance measured normal force, lb
P_m	balance measured pitching moment, in-lb
q_∞	free-stream dynamic pressure, lb/in ²
R_n	Reynolds number based on reference chord
T_{bx}	sidewall blowing-box thrust, lb
t/c	airfoil thickness-to-chord ratio, 0.12
W_t	model weight, lb
x	distance along chord of model, in.
y	distance perpendicular to chord of model, in.
z	distance along span of model, in.
α	angle of attack (positive nose up), deg
Δ	deflection angle between longest chords of adjacent elements, deg
δ	slat, vane, or flap deflection (positive for trailing edge down), deg
ϵ_s	solid blockage correction factor
ϵ_w	wake blockage correction factor

η	nondimensional spanwise position, z/b
λ	body shape correction factor
σ	wall correction factor
Φ	sidewall blowing-box thrust angle, deg
ϕ	deflection of element longest chord, deg

Subscripts:

bx	blowing box
c	corrected
f	flap
le (L.E.)	leading edge
lg	longest chord
max	maximum
ps	wake static pressure
pt	wake total pressure
s	slat
te (T.E.)	trailing edge
u	uncorrected
v	vane

Wind Tunnel and Test Apparatus

Wind Tunnel

The EET High-Lift Airfoil test was conducted in the Langley Low-Turbulence Pressure Tunnel (LTPT). The LTPT is a single-return, closed-throat wind tunnel that can be operated at tunnel total pressures from near vacuum to 10 atmospheres (ref. 10). A sketch of the tunnel circuit arrangement is shown in figure 3. The tunnel test section is 3 ft wide, 7.5 ft high, and 7.5 ft long, which when combined with a 17.6-to-1 contraction ratio makes the LTPT ideally suited for low-turbulence, two-dimensional airfoil testing. The Reynolds number capability of the tunnel for a typical high-lift airfoil test is shown in figure 4. The tunnel can achieve a maximum Reynolds number of 15×10^6 per foot at a Mach number of 0.24. The maximum empty-tunnel speed at a total pressure of 1 atmosphere is a Mach number of 0.47 with a corresponding Reynolds number of 3×10^6 per foot. The tunnel total temperature is controlled through a set of internal heat exchange coils located upstream of the screens in the contraction section of the tunnel. During the warmer months of operation, cooling water is pumped through the heat exchanger and circulated through the cooling tower located in the inner courtyard. During the colder months of operation, the circulation water is heated by a stream injection system.

Model-Support and Force-Balance System

During the early 1970s a new model-support and force-balance system capable of handling both single-element and multielement airfoils was installed in the LTPT to provide the capability for two-dimensional high Reynolds number testing. A sketch of this model-support and force-balance system is shown in figure 5. An airfoil model is mounted between two endplates that are connected to the inner drums. These inner drums are held in place by an outer drum and yoke arm support system. The yoke arm support system is mounted to the force balance, which is connected to the tunnel through a balance platform. The attitude of the model is controlled by a motor-driven, externally mounted pitch mechanism that rotates the bearing-mounted inner drums. A multipath labyrinth seal is used to minimize air leakage from the test section into the outer tunnel plenum.

The force balance is a three-component strain-gauge balance of the external virtual-image type. The maximum balance loads are 18 000 lb in lift, 550 lb in drag, and 12 000 ft-lb in pitching moment. The balance is temperature compensated and calibrated to account for first- and second-order interactions, and it has a general accuracy of ± 0.5 percent of design loads.

Sidewall Boundary-Layer Control System

To ensure spanwise uniformity of the flow field when testing high-lift airfoils near the maximum lift condition, some form of tunnel sidewall boundary-layer control (BLC) was needed. The large adverse pressure gradients induced on the tunnel sidewalls by a high-lift airfoil near maximum lift can cause the sidewall boundary layer to separate with a corresponding loss of spanwise uniformity of the flow on the airfoil surface and a resulting premature loss of lift. Because a source of high-pressure air was available for the LTPT, tangential blowing was selected as the means of providing sidewall BLC during the tests of this high-lift airfoil. Four blowing boxes with tangential blowing slots were mounted on the model endplates on both sides of the tunnel and were positioned around the airfoil within the confines of the endplates. High-pressure air was supplied to each box through a flexible hose connected to the blowing-box control cart with remote-controlled valves for each box. A cross-sectional sketch of a typical blowing box is presented in figure 6. The blowing boxes were designed to provide uniform tangential flow at the slot exit. High-pressure air flows into an inner manifold distribution chamber and is then distributed through slots to an outer manifold chamber. An adjustable slot lip and the box itself form the exit slot. For this test, the width of the slot exit for all the boxes was set at 0.060 in. and the box supply air pressures were adjusted to achieve the maximum mass-flow rate through the boxes. The chordwise

location and slot lengths for each of the four boxes are presented in figure 7.

The tangential flow of air from the blowing boxes on the endplates produced a thrusting force and skin-friction force in the upstream direction that was considered a tare load on the force-balance system. During the initial part of the test, wind-off tare runs were performed at different tunnel total pressures with the box mass flows set at maximum. These data were curve fit and a set of tare values derived that were subtracted from the measured wind-on data.

Remote-Controlled Wake Survey Apparatus

A limited amount of airfoil drag data was computed during this investigation with the momentum method applied to the measured downstream wake properties. The momentum deficient in the wake was measured with a pressure probe that was traversed through the wake by a remotely controlled traverse system. Detailed descriptions of the mechanism, the calibration of the probe head, and the drag equations used are given in reference 10. A sketch of the wake traverse apparatus is presented in figure 8. The vertical support strut attaches the wake rake assembly to the tunnel sting-support arc sector and houses the traverse system. The wake traverse system provides vertical motion of the pressure rake within a total range of 47 in. The vertical drive mechanism consists of a vertically mounted direct-current stepper motor that drives a ball screw, which, in turn, drives the exterior traverse arm. An optical shaft encoder tracks the vertical position with a position accuracy of 0.0005 in. The probe head is attached to the pitch arm, which is supported by the exterior traverse. Extension arms can be placed between the exterior traverse and the pitch arm to provide the capability to position the probes at streamwise locations of 22 in., 33 in., and 44 in. downstream from the turntable center of rotation.

During this investigation, the probes were positioned at the 44-in. location. A sketch of the pitch arm, probe head, and pressure probes is shown in figure 9. The probe head can be pitched about its pitch arm attachment point within a $\pm 45^\circ$ range. This motion is driven by a pitch link mechanism that is controlled by a globe gear motor. The probe head also has a variable roll orientation capability. The probe head tip rotates relative to a fixed inner cylinder that can be locked into several roll angle positions. These fixed roll positions are 0° , 7.6° , 30° , 48.6° , and 90° as indicated on the cross-sectional drawings of the probe head in figure 9. This particular set of roll angles provides the capability to take spanwise measurements at 0, 0.5, 1, 2, 3, 4, 6, and 8 in. from the centerline. The roll axis of the probe head is located at the midspan location (18 in.) of the tunnel test section. During this investigation, the roll orientation was set at 90° , which placed probe 1 at the model midspan, probe 2 at 4 in. off the midspan, and probe 3 at 8 in. off the midspan. A photograph of the probe head rotated to the 0° position is shown in figure 10.

High-Lift Airfoil Model

The high-lift airfoil tested during this investigation has been designated as the Langley EET High-Lift Airfoil. The cruise airfoil with all elements nested has the same coordinates as those of the wing section at the break station of the NASA supercritical SCW-2a wing described in references 1 and 2. This high-lift airfoil has a thickness-to-chord ratio of 0.12 and a chord of 21.654 in. Normally airfoils built for testing in the LTPT have a chord of 24 in.; however, after the high-lift flap system was designed and deflections of the elements set, it was found that a slightly reduced chord would ensure that all the deflected elements would fit within the contours of the endplates. This was important because the tunnel walls start to diverge just downstream of the aft edge of the wall endplates; therefore, any aft element surfaces that extended beyond the endplate would produce a gap between the element edge and the wall that would require the addition of filler material. The EET High-Lift Airfoil had a span of 36 in. It was designed to operate at the maximum tunnel operating conditions of 10 atmospheres at a Mach number of 0.2. The airfoil had an area of 5.414 ft^2 , and at the maximum tunnel dynamic pressure of 576 lb/ft^2 and with an anticipated maximum lift coefficient of 4.5, the resultant lift force would be approximately 14000

lb, which is near the maximum balance limit. This very high load required that the model be constructed of high-strength stainless steel. Because of this high-strength material, the model was considered to be rigid and not have appreciable deflections under load. The model was built with removable leading- and trailing-edge sections to provide the capability of modifying either the number of elements or the contours of an element; thereby, the costs of future fabrication would be minimized.

The EET High-Lift Airfoil has a leading-edge slat and a double-slotted trailing-edge flap. The double-slotted flap is a large-vane and small-aft-flap combination as compared to the typical small-vane and large-aft-flap combination on most conventional wide-body transports. A typical supercritical airfoil has a much flatter upper surface contour than the typical NACA airfoils that form the basic wing section of many contemporary transport configurations. This flattened upper surface resulted in an increase in the aft loading on the airfoil and pushed the shock location farther aft.; thereby, the high-speed cruise performance of the airfoil was improved. This increased aft loading required thicker trailing edges and higher camber near the trailing edge to reduce the leading-edge suction peaks at the low-speed takeoff and landing conditions. Typically, these supercritical airfoils have a trailing-edge stall pattern at low speeds; this means that as the angle of attack is increased, the upper surface boundary layer will continually separate as it moves forward from the trailing edge. With this type of stall pattern, the farther downstream the aft slot is the better the chance of energizing the flap confluent boundary layers and delaying separation to higher angles of attack; thereby, the maximum lift potential of the high-lift system is increased. An additional advantage of the large-vane and small-aft-flap combination is that with higher loads on the vane than on the aft-flap the nose-down pitching moments will be reduced; thereby, the horizontal tail area required to trim the aircraft is reduced with a corresponding reduction in cruise drag. Another feature of the supercritical airfoil is that the flattened loading results in higher lift coefficients at the same angle of attack compared with conventional airfoils and, therefore, requires a smaller wing area to meet the lift requirements. This smaller area results in an increase in wing aspect ratio with a corresponding reduction in induced drag. However, this reduction in wing area also requires greater high-lift system performance than those for conventional wings.

The contours of the EET High-Lift Airfoil are shown in figure 11 and the tabulated coordinates are listed in tables 1 through 4. The leading-edge slat has a chord of 15.5 percent of the baseline airfoil chord. The trailing-edge vane has a chord of 21.5 percent of the baseline chord and the flap has a 12-percent chord. The nested chord of the vane and flap is 30 percent of the baseline chord. The main element leading edge starts at 3.8 percent of the chord and ends at 90 percent of the chord. Each of the four elements were instrumented with densely spaced chordwise pressure taps along the midspan location and coarsely spaced chordwise pressure taps at spanwise stations 2.5 in. from each sidewall. These rows near the sidewalls were included as a means of checking the spanwise two-dimensionality of the flow at the high angle of attack near the maximum lift conditions on the model. The pressure tap locations for each element are shown in figures 12 through 15 and the corresponding tabulated coordinates are listed in tables 5 through 8. Each pressure tap has a five-character designation. The first character represents the element: S for slat, M for main, V for vane, and F for flap. The next three characters are the tap number and the fifth character is the spanwise location: E for the row 2.5 in. from east wall (left-hand wall facing the model), C for the midspan location, and W for the row 2.5 in. from the west wall (right-hand wall facing the model). The slat was instrumented with 13 upper surface and 11 lower surface pressure taps, the main with 32 upper surface and 20 lower surface pressure taps, the vane with 14 upper surface and 11 lower surface pressure taps, and the flap with 13 upper surface and 5 lower surface pressure taps. This resulted in 72 upper and 47 lower surface pressure taps which, when added together, results in a total of 119 pressure taps along the midspan. The pressure taps were distributed on each element using the curvature distribution method utilized in the theoretical analysis computer code entitled the "Multi-Component Airfoil Code" (MCARF) as reported in reference 11. This method distributes the points with closer spacing in areas of higher surface curvature.

For this investigation, the deflections of the slat, vane, and flap were set equal to values representative of both takeoff and landing conditions. These deflections included four slat-to-main deflections of -30° , -40° , -50° , and -60° , and four main-to-vane and vane-to-flap deflections of 7.5° , 15° , 22.5° , and 30° . The vane and flap were always deflected with the same deflections, resulting in four coupled deflections of 15° , 30° , 45° , and 60° . The four different leading-edge slat and four different trailing-edge flap deflections resulted in 16 different test configurations. A sketch illustrating the definition of each element deflection, gap, and overlap is presented in figure 16. The deflections and overlaps are defined relative to the longest chords of the particular elements. The longest chord is defined as the distance from the trailing-edge bisector of the element to the forward-most leading-edge coordinate in the nose region of the element. The overlap is defined as the distance from the lower surface trailing-edge coordinate for the forward element along the longest chord to a point at which a perpendicular dropped from the chord intersects the forward-most coordinate on the leading edge of the aft element. The gap is defined as the shortest distance from the lower surface trailing-edge coordinate of the forward element to the upper surface of the aft element. The gaps and overlap positions for each of the four slat and vane-flap deflections were determined by performing lift optimization studies using the MCARF computer code of reference 11. The resultant gaps, overlaps, and lofting pivot point data and lofting equations are presented in table 9. The lofted coordinates of the slat, vane, and flap at each of the four deflections are tabulated in tables 10, 11, and 12, respectively.

Photographs of the EET High-Lift Airfoil mounted in the LTPT are presented in figures 17 and 18. Figure 17 shows a view of the upper surface of the model looking upstream at the trailing-edge vane and flap elements of the model. Three of the sidewall blowing boxes can be seen in this view. Figure 18 shows a view of the lower surface of the model looking downstream. The slat and flap brackets are visible as well as the lower surface sidewall blowing box. The slat brackets and flap brackets are located at spanwise locations of 4.0 in. and 13.3 in. from the each sidewall. Each bracket has the same width dimension of 0.625 in. and are rectangular in cross-sectional shape with rounded corners. A 0.31-inch-wide slot was cut along each bracket to hold the surface pressure tubing routed from the element over to the main element and through the model support tangs to pressure measuring scanivalves located in the tunnel plenum. The shape and major dimensions of a typical slat and a typical vane-flap bracket are shown in figures 19 and 20, respectively.

High-Lift Test Procedures and Corrections

In general, multielement high-lift airfoils produce very high velocities around the leading-edge elements at high angles of attack. These high velocities induce rather large pressure gradients on the wind tunnel sidewalls that can cause the sidewall boundary layer to separate which results in a loss of spanwise two-dimensionality of the flow on the model and a corresponding reduction in the maximum attainable lift. To control this sidewall separation some type of energy addition or removal can be employed. For this investigation, energy addition was used in the form of injecting high-pressure air tangentially from blowing boxes located at four specific locations on each endplate. These four blowing boxes were located at critical chordwise locations ahead of the maximum pressure locations on the slat and vane and downstream of the maximum pressure location on the upper and lower surface of the main element as shown in figure 7. Each blowing box had a remote-controlled pressure regulator that allowed individual adjustment to account for asymmetries in the slot openings between corresponding boxes on opposite endplates.

During the initial calibration phase of the test, the mass flow through each box was adjusted independently and the spanwise two-dimensionality checked by a real time comparison of the chordwise pressure distributions at the model centerline and at locations 2.5 in. from each sidewall. Ideally, the box mass flows should be adjusted at each test angle of attack; however, this was not possible because of the

excessive amount of test time required to do so. An alternate approach was to set the model angle of attack at the predicted angle for maximum lift and to then adjust the box mass flows to ensure spanwise two-dimensionality of the flow and to leave the mass flows set at those values at all other lower angles of attack. This procedure resulted in a slight excess of blowing mass flow at the sidewalls at the lower angles; however, the test results showed that this excess mass flow had little or no effect on the two-dimensionality of the flow.

Sidewall Blowing Tares

The injection of high-pressure air by the blowing boxes on the endplates produced an additional thrust component that was included in the resultant balance output readings. The components of this thrust were subtracted from the resultant balance readings to get a true indication of the lift, drag, and pitching moment. These tare corrections were defined as follows:

$$\text{Normal force increment:} \quad \Delta N_f = T_{bx} \sin(\Phi + \alpha) \quad (1)$$

$$\text{Axial force increment:} \quad \Delta A_f = -T_{bx} \cos(\Phi + \alpha) \quad (2)$$

$$\text{Pitching-moment increment:} \quad \Delta P_m = -T_{bx} H_{tr} + W_t d_{wt} (1 - \cos \alpha) \quad (3)$$

where T_{bx} is the total thrust produced by the blowing boxes, Φ is the angle of the thrust vector with the model positioned at an angle of attack of 0° , α is the angle of attack, H_{tr} is the perpendicular distance from the center of endplate rotation to the total thrust vector, W_t is the model weight, and d_{wt} is the distance from the model center of weight to the endplate center of rotation. At various intervals during the test, tare data were taken with various levels of blowing-box mass flows. These data were plotted and the various parameters in the correction equations were curve fit as a function of total blowing-box mass flow.

The first parameter curve fit was T_{bx} which is the resultant of the balance normal and axial forces, $T_{bx} = \sqrt{N_f^2 + A_f^2}$, measured during the tare run and is presented in figure 21. The best curve fit to these data was a second-order curve with the following coefficients:

$$T_{bx} = 24.6 \dot{m} - 0.592 \dot{m}^2 \quad (4)$$

The next parameter that was curve fit was the thrust vector angle Φ . Either the normal or axial force tare data could be used to fit this parameter. The axial force data were used because the lower load range of the balance axial force ensured more accurate tare readings. From equation (2),

$\Phi = \cos^{-1}(-\Delta A_f / T_{bx}) - \alpha$, which is plotted in figure 22 as a function of the blowing-box mass flow.

The best fit to these data is a first-order curve with the coefficients:

$$\Phi = 29.2 + 0.4 \dot{m} \quad (5)$$

The next parameter to determine was the model weight center distance d_{wt} . From equation (3) with $T_{bx} = 0$ because $\dot{m} = 0$, $P_m = W_t d_{wt} (1 - \cos \alpha)$. A tare run was performed with no blowing-box mass flow and the pitching-moment data are plotted in figure 23 as a function of $1 - \cos \alpha$. The model was weighed prior to installation in the tunnel and was found to weigh 730 lb. A linear curve fit of the data in figure 23 yields a slope of 10462, which divided by the model weight yields a d_{wt} of 14.33 in.

The last parameter to curve fit was the perpendicular distance to the thrust center H_{tr} . From equation (3), $H_{tr} = \left[\frac{W_t d_{wt} (1 - \cos \alpha) - P_m}{\sqrt{N_f^2 + A_f^2}} \right]$, which is plotted in figure 24 as a function of blowing-box mass flow. The best fit to these data was a linear curve with the coefficient

$$H_{tr} = 0.213\dot{m} \quad (6)$$

The experimental data used in the tare curve fit (figs. 21 through 24) show a relatively large amount of scatter, which was expected based on the very high load limit for the balance. Many measurements were within the quoted balance accuracy of 0.5-percent of full-scale loads. Measured and computed tare loads using the above curve fit equations are presented in figures 25, 26, and 27 for normal force, axial force, and pitching moment, respectively. As shown in these figures, most of the data fell within a ± 10 percent band, which was believed to be about as accurate as possible with this balance and model combination.

Wake Integrations

Drag measurements were made by using a downstream wake rake with three evenly spaced five-hole pressure probes with hemispherical heads. Each probe head has one forward-facing center tap and four side-mounted taps placed 90° apart. A complete description of these probes and the procedure used to calibrate them are presented in reference 10. During the traverse of the downstream wake, each probe measured the local total C_{pt} and static C_{ps} profiles. The local drag coefficient was computed by using the well-known Jones method described in reference 12. This method is based on the assumptions that the total pressure remains constant along every streamline in the wake (flow proceeds with no energy loss from one location to the next along the steam tube), and that Bernoulli's equation can be applied along the steam tube. Based on these assumptions, the point drag is defined as

$$c'_d = 2 \sqrt{C_{pt} - C_{ps}} \left(1 - \sqrt{C_{pt}} \right) \quad (7)$$

In addition, the total drag is defined as

$$c_d = \int c'_d d(h_t / c) \quad (8)$$

A plot of the three drag profiles obtained during a typical traverse is presented in figure 28. As shown in this figure, each profile starts and ends at a value of c'_d slightly above zero. This shift is the result of an increase in the local flow due to the blockage effects of the rather thick wakes behind high-lift airfoils in tunnels with solid floors and ceilings. The computer program that is used to integrate the drag profiles estimates the offset values and subtracts them from the final computed values. The final integrated drag value for each profile is listed above each profile in the plot and the offset value is shown as a vertical dotted line.

Data Corrections

A detailed description of corrections applied to data taken on two-dimensional models tested in solid-wall tunnels is presented in chapter 6 of reference 13. These corrections are classified as solid and wake blockage and the corrections are due to the lateral constraint of the solid walls on the flow around the model. The following equations are derived in chapter 6 of reference 13 for the corrections to the measured force and moment coefficients and free-stream conditions:

Lift coefficient:

$$c_{L,c} = c_{L,u}(1 - \sigma - 2\varepsilon) \quad (9)$$

where $\varepsilon = \varepsilon_s + \varepsilon_w$

Drag coefficient:

$$c_{d,c} = c_{d,u}(1 - 3\varepsilon_s - 2\varepsilon_w) \quad (10)$$

Pitching-moment coefficient:

$$c_{m,c} = c_{m,u}(1 - 2\varepsilon) + \frac{\sigma c_{L,u}}{4} \quad (11)$$

Angle of attack:

$$\alpha_c = \alpha_u + \frac{90\sigma}{\pi^2}(c_{L,u} + 4c_{m,u}) \quad (12)$$

Mach number:

$$M_{\infty,c} = M_{\infty,u}(1 + \varepsilon) \quad (13)$$

Free-stream dynamic pressure:

$$q_{\infty,c} = q_{\infty,u}(1 + 2\varepsilon) \quad (14)$$

Reynolds number:

$$R_{n,c} = R_{n,u}(1 + \varepsilon) \quad (15)$$

For the EET High-Lift Airfoil with a chord (c) of 21.6536 in., maximum thickness ($t = 0.12c$) of 2.5984 in., and a tunnel height (h) of 90 in., the following parameters can be derived:

Body shape factor:

$$\lambda = 0.41 \left(\frac{c}{t} - 0.9 \right) + 1 = 4.04767 \quad (16)$$

Wall correction factor:

$$\sigma = \frac{\pi^2}{48} \left(\frac{c}{h} \right)^2 = 0.0119024 \quad (17)$$

Solid blockage factor:

$$\varepsilon_s = 0.822\lambda \left(\frac{t}{h} \right)^2 = 0.0027734 \quad (18)$$

Wake blockage factor:

$$\varepsilon_w = \frac{1}{4} \left(\frac{c}{h} \right) c_{d,u} = 0.0601489c_{d,u} \quad (19)$$

For each angle of attack, the forces and moments were measured with the tunnel balance system and, for most angles of attack, calculated from an integration of the measured surface pressure distributions. Integrated wake measured drag coefficients were taken for only a selected few angles of attack. Therefore, the only consistent set of data was the balance-measured forces and moment, which were used as the uncorrected values in the free-stream correction equations (9), (10), (11), (12), and (19).

Presentation of Test Results

The test of the EET High-Lift Airfoil was divided into three major areas of study: (1) the effect of Reynolds number on aerodynamic performance, (2) the effect of Mach number on aerodynamic performance, and (3) the effect of sidewall blowing on the spanwise two-dimensionality of the flow field around the airfoil. The model had a leading-edge slat with 4 different deflections and a trailing-edge vane-flap combination with 4 different deflections for a total of 16 configurations. Unless otherwise stated, the Mach number for all the figures listed in this section of the report was 0.20. The following table lists the 16 configurations tested to determine the effect of Reynolds number on aerodynamic performance and their corresponding test run number and report figure number containing the plotted lift and pitching-moment coefficients:

δ_s , deg	δ_v and δ_f , deg	Run at $R_n/10^6$ of –					Figure
		2.5	4.3	6	12	18	
–30	7.5	70		71	72	73	29
–40	7.5	66		67	68	69	30
–50	7.5	62		63	64	65	31
–60	7.5	58		59	60	61	32
–30	15	74		75	76	77	33
–40	15	78		79	80	81	34
–50	15	83	89	91	96	98	35
–60	15	99		100	102	103	36
–30	22.5	28		29	32	34	37
–40	22.5	20		23	25	27	38
–40	22.5	114		115	116	117	39
–50	22.5	4		6	9	11	40
–50	22.5	112		106	107	109	41
–50	22.5			105			
–60	22.5	13		15	17	18	42
–60	22.5	118		119	120	121	43
–30	30	37		39	41	42	44
–40	30	43	44	45	46	47	45
–40	30	48					
–50	30	49	50	51	52	53	46
–60	30	54		55	56	57	47

The following table lists the two configurations tested to show the effect of Mach number on aerodynamic performance and their corresponding test run number and report figure number containing the plotted lift and pitching-moment coefficients:

δ_s , deg	δ_v and δ_r , deg	$R_n/10^6$	Run at M_∞ of –								Figure
			0.10	0.15	0.20	0.25	0.28	0.287	0.30	0.35	
-50	15	1.3	82								48
-50	15	2.5			83						48
-50	15	3.0				84					48
-50	15	3.7							85		48
-50	15	4.3								86	48
-50	15	6.0	95	92	91	90			88	87	49
-50	15	12.0		97	96	94		93			50
-30	22.5	12.0		33	32	31	30				51

The following table lists the four configurations tested to show the effect of sidewall blowing on the spanwise two-dimensionality of the flow around the high-lift airfoil and their corresponding test run number and report figure number containing the plotted lift and pitching-moment coefficients:

δ_s , deg	δ_v and δ_r , deg	$R_n/10^6$	Run for sidewall blowing on/off		Figure
			On	Off	
-60	15	6	100	101	52
-50	22.5	2.5	4	2	53
-50	22.5	2.5	112	104	54
-50	22.5	18.0	109	111	55
-60	22.5	2.5	13	14	56
-60	22.5	6.0	119	122 (box 1 off)	57
-60	22.5	6.0	119	125 (box 1,2,3 off)	57
-60	22.5	6.0	119	126	57
-30	30	2.5	37	36	58
-30	30	6.0	39	40	59

The data for each run listed in the previous three tables are also presented in tabular form in appendix A.

The following table lists the configurations tested where the downstream wake profiles were measured and integrated to obtain a drag coefficient and their corresponding test run number and plotted drag coefficient figure number:

δ_s , deg	δ_v and δ_f , deg	Run for $R_w/10^6$ of –					Figure
		2.5	4.3	6	12	18	
-30	7.5			71			60
-50	7.5				64		61
-40	15	78					62
-60	15	99					63
-30	22.5	28					64
-30	22.5				32		65
-40	22.5			115			66
-50	22.5	4					67
-50	22.5	112					68
-50	22.5			106			69
-50	22.5			6			70
-50	22.5				107		71
-50	22.5				9		72
-50	22.5					109	73
-60	22.5			15			74
-60	22.5				17		75
-60	22.5					18	76
-50	30	49					77
-50	30		50				78
-50	30				52		79
-60	30	54					80

The tabulated and plotted data for each of the three probes for the runs listed in this table are presented in appendix B. The plotted airfoil midspan-chordwise, airfoil spanwise, and tunnel floor and ceiling centerline pressure distributions for each point for all the runs presented in this report are presented in appendices C, D, and E, respectively.

The following table lists the configurations that are presented to show the agreement between the balance and C_p -integrated force and moment coefficients:

δ_s , deg	δ_v and δ_f , deg	$R_n/10^6$	Run	Figure
-30	7.5	12	72	81(a)
-40	7.5	12	68	81(b)
-50	7.5	12	64	81(c)*
-60	7.5	12	60	81(d)
-30	15	12	76	82(a)
-40	15	12	80	82(b)
-50	15	12	96	82(c)
-60	15	12	102	82(d)
-30	22.5	12	32	83(a)
-40	22.5	12	116	83(b)
-50	22.5	12	9	83(c)*
-60	22.5	12	120	83(d)
-30	22.5	2.5	112	84(a)*
-40	22.5	6	106	84(b)*
-50	22.5	12	107	84(c)*
-60	22.5	18	109	84(d)*
-30	30	12	41	85(a)
-40	30	12	46	85(b)
-50	30	12	52	85(c)*
-60	30	12	56	85(d)

An asterisk (*) in the table after a figure number indicates that the drag data obtained from the integration of the downstream wake probe measurements are also presented. The wake drag value presented at each angle of attack is an average of the three integrated values.

The most notable parameter used to evaluate the performance of a high-lift system is the maximum lift coefficient produced at various flight conditions. A set of summary maximum lift coefficient plots are presented and discussed in this report. The following table lists these summary figure numbers and their corresponding comparison parameters:

δ_s , deg	δ_v and δ_f , deg	$R_n/10^6$	M_∞	Figure
-30, -40, -50, -60	7.5	2.5 to 18	0.2	86
-30, -40, -50, -60	15	2.5 to 18	0.2	87
-30, -40, -50, -60	22.5	2.5 to 18	0.2	88
-40, -50, -60	30	2.5 to 18	0.2	89
-30, -40, -50, -60	22.5	2.5 to 18	0.2	90 repeat of 88
-50	15	Varies – tunnel total pressure of 1 atm	0.10 to 0.35	91
-50	15	6 and 12	0.10 to 0.35	92
-30	22.5	12	0.15 to 0.30	93
-30, -40, -50, -60	7.5, 15, 22.5, 30	2.5	0.2	94
-30, -40, -50, -60	7.5, 15, 22.5, 30	6.1	0.2	95
-30, -40, -50, -60	7.5, 15, 22.5, 30	12.2	0.2	96
-30, -40, -50, -60	7.5, 15, 22.5, 30	18.5	0.2	97

Discussion of Results

The overall purpose of this investigation was to obtain a set of data on a representative high-lift airfoil at high Reynolds numbers for use during the validation and calibration of computer codes to predict the performance of multielement airfoils. A secondary objective was to obtain two-dimensional data on an airfoil that was used as the basic section on a three-dimensional wing for future use during the development of methods to extend two-dimensional airfoil characteristics to three-dimensional wings. The high-lift airfoil chosen for this investigation was the EET High-Lift Airfoil, which was one of the earliest advanced supercritical airfoils and was of great interest by the airframe manufacturers for application to future transport design. During a typical high-lift airfoil test, one of the primary objectives of the test is to find the optimum positions of the elements based on maximum lift requirements; however, this was not the primary objective of this investigation. The optimization was performed using the existing computer code MCARF that employed a coupled potential flow and viscous boundary-layer method to predict the attached flow aerodynamic characteristics of multielement airfoils. Optimizing in this manner also allowed for the use of element support brackets with fixed rather than adjustable features, which ensured repeatability during the test and from one test to the next. The EET High-Lift Airfoil was designed with only 4 positions for the leading-edge slat and only 4 positions for the trailing-edge vane-flap combination, which resulted in 16 combinations of leading- and trailing-edge element positions. All 16 configurations were tested over a range of Reynolds numbers from 2.5×10^6 to 18×10^6 at a constant Mach number of 0.20. A smaller subset was tested over a Mach number range of 0.10 to 0.36 at various Reynolds numbers. In addition, a smaller subset was tested to determine the effects of various amounts of sidewall blowing on the performance of the high-lift airfoil.

Effect of Sidewall Blowing on Flow Two-Dimensionality

The first procedure performed prior to actual data acquisition was to determine the amount of sidewall blowing required to ensure spanwise two-dimensionality of the flow from the attached flow conditions at low angles of attack to the separated flow conditions at or near maximum lift. The sidewall blowing boxes were positioned on the endplates near the slat element and vane element peak pressure locations and at the 40-percent chord location on the upper and lower surface of main element. Because the position of the blowing boxes were fixed relative to the model, the only variable was the mass of the flow from each box which was a function of the slot gap, internal air pressure, and slot back pressure. The mass flows were computed real-time based on the measured box internal pressure and slot exit back pressure. The model was instrumented with a sparse row of chordwise pressure taps 2.5 in. from each sidewall. For each of the 16 combinations of element positions, the pressure measured on a sidewall surface tap near the slot exit for each blowing box was chosen as the reference slot back pressure. The two-dimensionality of the flow was checked by plotting the spanwise measured surface pressures and checking for uniformity through the angle-of-attack range.

Because both the slot and air pressure could be varied to each of the four boxes on each side, an enormous number of possible combinations existed to obtain varying amounts of mass flow. It was decided the simplest approach would be to set the box slot gap at the maximum position of 0.060 in. and to then adjust the high-pressure air until the spanwise two-dimensionality of the flow was restored. The model was set at an angle of attack near separation and the mass flow increased to improve the two-dimensionality. The angle of attack was then farther increased and the mass flow increased again to maintain two-dimensionality. This procedure was repeated until farther increases in mass flow did not improve the two-dimensionality. Ideally, less mass flow would be required at the lower angles of attack to keep the two-dimensionality uniform and, in fact, it is possible to over blow the sidewalls at lower angles causing a stronger than usual model-to-wall juncture vortex. Adjusting the blowing-box mass flows at each angle of attack would have greatly lengthened the required test time and was not a feasible

approach for this test. Therefore, it was decided to use the same mass flow settings through the angle-of-attack range. As the tunnel pressure was increased to obtain higher Reynolds number conditions, the blowing-box pressures were proportionally increased to maintain spanwise two-dimensionality. Performance data were then measured through the complete angle-of-attack range with and without sidewall blowing.

At various intervals during the test, the sidewall control was turned off and the run repeated to illustrate the tremendous effect of the control on the aerodynamic performance. The results for the first configuration with the blowing turned off are shown in figure 53. These results show an increase in the angle for maximum lift coefficient from 16° to 20° and a small increase in the lift coefficient at a given angle of attack from 0° to near maximum lift. At angles of attack above maximum lift, the decrease in lift was less abrupt with sidewall blowing. However, at negative angles of attack, the lift curves varied considerably, but these data are of little practical use and were not a factor in the determination of the correct amount of sidewall blowing. For a few selected configurations during the test, the sidewall blowing was turned off and the performance measured. These data are presented in figures 52 through 59, and all show the same basic effect of an increase in the angle of attack for maximum lift and a small-to-large increase in lift at a given angle of attack with no change in the slope of the lift curve. The change in pitching-moment coefficient shows a similar trend with sidewall blowing. The nose-down (negative) pitching-moment coefficient increases with sidewall blowing with little or no change in the slope of the curve.

After completion of the tests of the matrix of 16 configurations, several additional runs were made to determine the effects on the aerodynamic performance of turning off the air supply to not only all the blowing boxes but also to only part of the blowing boxes. These results are shown in figure 57, and they show that, as the boxes were turned off, the angle of attack for and magnitude of the maximum lift decreased. Surprisingly, turning off the most-forward box (box 1) just ahead of the slat had only a slight effect on performance. Turning off the most-forward box (box 1) and the box above (box 2) and below (box 3) the model near the midchord position accounted for about one half the loss in performance. This indicates that the rather large rear box (box 4) near the juncture of the main and the vane accounted for almost one half the benefits of sidewall blowing.

Comparisons Between Balance and C_p -Integrated Force and Moments

Comparisons of the balance and C_p -integrated force and moment coefficients for each of the 16 configurations tested are presented in figure 81 through 85. The averaged value of the wake-probe-measured drag coefficient is also plotted for comparison with the balance and C_p -integrated values for the runs where data were available. A complete polar of wake drag data was not taken during all runs because the length of time required to complete a survey was rather long. The data presented in these figures show excellent agreement between the balance and C_p -integrated lift coefficient and good agreement for the drag and pitching-moment coefficients.

The lift coefficient is primarily a function of the forces generated normal to the chord of the model; therefore, it was expected that the agreement between the balance and C_p -integrated values would be very good. The blowing-box thrust forces normal to the model chord were generally small compared with the model-produced force. For instance, at a maximum lift coefficient of 4.0 and at the maximum test condition of a Reynolds number of 18×10^6 the lift force is approximately 10000 lb and the normal thrust tare from the blowing boxes is 230 lb (fig. 25), which is 2.3 percent of the total.

The drag coefficient is primarily a function of the forces generated parallel to the chord of the model and is generally 5 to 6 percent of the lift-generated forces. Therefore, small errors in the estimation of the axial tare forces can result in large errors in the resultant balance drag force. In a

similar manner, the computation of the axial force from the measured surface pressure distributions often produces poor values; therefore, it is rarely used. This poor computation is because the computed axial force is the difference between the very few numbers of rather large pressure values forward of the maximum pressure location and the much greater number of smaller pressure values aft of the maximum pressure location. A good computation of the axial force requires a very large number of pressure taps in the forward nose region of the airfoil where it is often not feasible unless the taps can be staggered spanwise. For most of the cases presented, the agreement between the balance and wake-measured drag coefficients is very good. The wake-measured drag is not completely representative of the true two-dimensional value because the slat and vane-flap support brackets produce vortices that create nonuniformity in the downstream flow. The three-probe wake data for the limited number of configurations and angles of attack measured are presented in figures 60 through 80 and show a rather large variation in drag coefficient. Averaging the integrated values of the three spanwise measured wake profiles tends to improve the result, but many more profiles at different spanwise stations would be needed to improve the accuracy of the drag value.

The pitching-moment coefficient is a function of both the axial and normal forces on the model. The agreement between the balance measured and C_p -integrated values are generally very good for most of the comparisons presented. For each case presented, the general trend of the two curves is the same with the balance data indicating slightly more nose-down (negative) moment. This difference is probably due to the inaccuracy of the pitching-moment tare value as illustrated in figure 27. As stated in the section "High-Lift Test Procedures and Corrections" of this report, the pretest calibrations indicated that the model weight center was 14.33 in. ahead of the center of the turntable (fig. 23). This distance was estimated based on pitching-moment data that were only in a range of 0 to 100 ft-lb, which is about 0.8 percent of the balance maximum and very near the balance accuracy limits of ± 0.5 percent. The true moment center is probably much closer to the turntable center, which would produce a smaller tare value and improve the agreement between the balance and C_p -integrated values.

Effect of Reynolds Number on Aerodynamic Performance

The effect of a variation in Reynolds number on the aerodynamic performance of each of the 16 configurations at a Mach number of 0.2 is shown in figures 29 through 47. The configurations are grouped as four sets of vane-flap settings of 7.5° , 15° , 22.5° , and 30° with each having four slat deflections of -30° , -40° , -50° , and -60° . The 22.5° vane-flap configuration also has repeat sets of runs at slat deflections of -40° , -50° , and -60° . The corresponding plots of the maximum lift as a function of Reynolds number for each of the four basic vane-flap configurations are presented in figures 86 through 89. The maximum lift plots for the repeat runs for the 22.5° vane-flap configuration are presented in figure 90. The data presented in figures 29 through 47 are for lift and pitching-moment coefficients measured with the tunnel balance system. As previously discussed, the balance and C_p -integrated drag data are not very reliable and the wake probe data are too limited; therefore, the effect of Reynolds number on drag is not included in this discussion.

Increasing the Reynolds number should cause the boundary layers on each element of a high-lift system to become thinner and the performance to approach the optimum potential flow values. The increase in performance would translate into an increase in the lift curve slope, an increase in the angle of attack for and value of the maximum lift, and an increase in the nose down pitching moment at a given angle of attack. However, as shown in figures 29 through 47, the only significant effect of Reynolds number on performance occurred between 2.5×10^6 and 6×10^6 . The slope of the lift curve increased noticeably between these two Reynolds numbers for all 16 configurations tested and the differences in the slopes were greater for the higher vane-flap deflections. In addition, an increase in Reynolds number generally caused a slight increase of 1° to 3° in the angle of attack at which the maximum lift or stall

occurred. The change in the pitching-moment coefficient was also the greatest between these two Reynolds numbers. As shown in figures 86 through 90, an increase in Reynolds number greater than 6×10^6 produced very small changes in maximum lift performance. In addition, the change in pitching moment was very small above 6×10^6 Reynolds number. Below 6×10^6 , the shift in pitching moment was unpredictable because in some cases, it was a nose-down shift and, in other cases, it was a nose-up shift.

Effect of Mach Number on Aerodynamic Performance

During testing in nonpressurized wind tunnel facilities, an increase in Reynolds number can only be accomplished by increasing the free-stream Mach number. The increase in free-stream Mach number causes a corresponding increase in the local Mach numbers on the surface of each element. In general, the leading-edge element has the highest local Mach numbers with the flow, in some cases, becoming supersonic, which causes premature transition of the boundary layer from laminar to turbulent. This premature transition can cause a further thickening of the boundary layers on the downstream elements, which are more susceptible to possible separation, and loss of maximum lift. The effects of this type of Mach number variation are shown in figure 48 for the 15° vane-flap deflection with the slat set at -50° . These results show the expected loss of lift and decrease in stall angle of attack with an increase Mach number, but they also show an unexpected large positive shift in lift and pitching moment between Mach numbers of 0.103 and 0.205.

The LTPT facility is a pressurized tunnel; therefore, the Mach number can be varied and the Reynolds number held at a constant value, which produces results that are more realistic. The same configuration, whose data are presented in figure 48, was tested through the Mach number range at both 6×10^6 and 12×10^6 Reynolds number and the results are presented in figure 49 and 50, respectively. These data also show the expected decrease in stall angle of attack and slight positive increase in lift and nose-down pitching moment with increased Mach number. As shown in figure 51, the same trend was observed for a configuration with a higher vane-flap deflection of 22.5° and a slat deflection of -30° .

The effects of Mach number on the maximum lift performance of the EET High-Lift Airfoil are presented in figures 91, 92, and 93. For the configuration with a slat deflection of -50° and a vane-flap deflection of 15° , the effect of Mach number obtained by varying only the tunnel speed with tunnel pressure at atmospheric conditions is presented in figure 91, showing a maximum lift value of 3.6 occurred at a Mach number of 0.25. However, by varying the tunnel pressure to maintain a constant Reynolds number during the run as shown in figure 92, the same configuration has a maximum lift of 3.98 at a Mach number of 0.15. As shown in figure 93 for a higher vane-flap deflection of 22.5° and lower slat deflection of -30° and at a constant Reynolds number of 12×10^6 , the maximum lift value is 4.22 at a Mach number of 0.20. These results illustrate the difficulty of predicting the effects of Mach number on high-lift system performance and the importance of testing high-lift systems in pressurized facilities that allow for the proper simulation of Reynolds number and Mach number.

Effect of Slat and Vane-Flap Deflection on Maximum Lift Performance

The effects of slat and vane-flap deflection on the maximum lift performance of the EET High-Lift Airfoil are presented in figures 94, 95, 96, and 97 for Reynolds numbers of 2.5×10^6 , 6×10^6 , 12×10^6 , and 18×10^6 , respectively. As shown in these figures, the maximum lift condition at each Reynolds number occurred at a slat deflection of -40° and a vane and flap deflection of 27° which is approximately midway between the tested deflections of 22.5° and 30° . At each Reynolds number and for a fixed vane-flap deflection, the maximum lift generally increased from a slat deflection of -30° to -40° and decreased from -40° to -60° . Each of the slat deflections follow a consistent pattern with vane-flap

deflection except the curves for the -50° slat deflection which show a larger than expected increase in maximum lift value at the lower vane-flap deflections below 22.5° . These results, once again, illustrate the importance of testing high-lift systems at the proper Reynolds and Mach numbers conditions.

Concluding Remarks

The experimental test of the EET High-Lift Airfoil demonstrated the tremendous effects of Reynolds number and Mach number on high-lift system aerodynamic performance. The greatest increase in performance occurred at the lower Reynolds numbers between 2.5×10^6 and 6×10^6 followed by a very small increase from 6×10^6 to 18×10^6 . The maximum lift performance obtained was 4.22 and occurred at a Reynolds number of 18×10^6 with the slat deflected to -40° and the vane-flap combination deflected to 22.5° . Increasing the Mach number above 0.2 resulted in the expected rapid reduction in maximum lift due to the effects of compressibility on the boundary-layer transition on the slat element. The sidewall blowing-box system was able to control the boundary-layer separation on the model endplates; thereby, spanwise uniformity of the flow up to the angle of attack for maximum lift was maintained. The agreement between the balance-measured and C_p -integrated lift and pitching-moment coefficients was very good. The drag data obtained from the wake rake system showed considerable variations due to the vortices generated by the slat and vane-flap support brackets. For all 16 configurations tested, the quality and quantity of surface pressure data are excellent and are well documented for the complete angle-of-attack, Mach number, and Reynolds number ranges.

Appendix A

Aerodynamic Performance Data

This appendix contains only a sample of the tabulated listings of the aerodynamic performance data taken during LTPT Test 342 of the EET High-Lift Airfoil. The complete data set consists of 51 pages of tabulated data and is available on the CD-ROM supplement L-18221 in the directory APPENDX as file AppendixA.doc (Microsoft Word Document). The computer-generated tabulated headings are defined as follows:

POINT	point number
ALPHAC	corrected angle of attack, deg
QINFC	corrected free-stream dynamic pressure, lb/in ²
MINFC	corrected free-stream Mach number
RN/10**6	corrected Reynolds number based of reference chord, 10 ⁶
MDOT	sidewall blowing-box mass flow, \dot{m} , slugs/min
CLBU	uncorrected lift coefficient from balance
CLBC	corrected lift coefficient from balance
CLPC	corrected lift coefficient from C_p -integration
CMBU	uncorrected pitching-moment coefficient from balance
CMBC	corrected pitching-moment coefficient from balance
CMPC	corrected pitching-moment coefficient from C_p -integration
CDBU	uncorrected drag coefficient from balance
CDBC	corrected drag coefficient from balance
CDPC	corrected drag coefficient from C_p -integration
CDWK1	uncorrected drag coefficient from integration of c'_d measured with wake probe 1
CDWK2	uncorrected drag coefficient from integration of c'_d measured with wake probe 2
CDWK3	uncorrected drag coefficient from integration of c'_d measured with wake probe 3

Tabulated data for a specific run x are available in electronic form on the CD-ROM supplement L-18221 in directory F&Mdata as the files RUN x .txt (Text format) and RUN x .doc (Microsoft Word Document format).

LTPT TEST 342 -- EET HIGH-LIFT MODEL -- RUN 2

SLAT DEFLECTION = -50.0 DEG. VANE AND FLAP DEFLECTION = 22.5 DEG.

POINT	ALPHAC	QINFC	MINFC	RN/10**6	MDOT	CLBU	CLBC	CLPC	CMBU	CMBC	CMPC	CDBU	CDBC	CDPC	CDWK1	CDWK2	CDWK3
19	-8.089	0.424	0.204	2.590	0.000	-0.2453	-0.2349	-0.1883	-0.0520	-0.0511	-0.0455	0.2086	0.2016	0.1540			
20	-4.002	0.423	0.204	2.594	0.000	0.0364	0.0350	0.0000	-0.0131	-0.0127	0.0000	0.1811	0.1757	0.0000			
21	-0.036	0.420	0.203	2.585	0.000	2.5095	2.4282	2.4056	-0.6879	-0.6663	-0.6794	0.1244	0.1215	0.0631	0.0465	0.0375	0.0505
22	4.041	0.424	0.204	2.598	0.000	3.0117	2.9074	0.0000	-0.6576	-0.6337	0.0000	0.1429	0.1392	0.0000			
23	8.124	0.417	0.202	2.577	0.000	3.3626	3.2411	3.2410	-0.5789	-0.5549	-0.5641	0.1553	0.1511	0.0934			
24	10.149	0.429	0.205	2.611	0.513	3.4759	3.3297	0.0000	-0.5263	-0.5001	0.0000	0.2047	0.1979	0.0000	0.0531	0.0440	0.0367
25	12.183	0.424	0.204	2.597	0.553	3.6123	3.4559	3.5034	-0.4814	-0.4555	-0.4705	0.2147	0.2073	0.1191			
26	14.265	0.429	0.205	2.610	0.628	3.7815	3.6068	3.6771	-0.4262	-0.4003	-0.4136	0.2390	0.2301	0.1245			
27	15.286	0.426	0.204	2.599	0.642	3.8316	3.6492	3.7165	-0.3913	-0.3659	-0.3898	0.2508	0.2411	0.1354			
28	16.258	0.425	0.204	2.597	0.667	3.8758	3.6938	3.7622	-0.3976	-0.3722	-0.3631	0.2454	0.2361	0.1404			
29	17.294	0.433	0.206	2.617	0.641	3.5012	3.2800	3.3981	-0.4744	-0.4397	-0.4344	0.3801	0.3595	0.3306			
30	18.506	0.440	0.207	2.634	0.640	3.4442	3.1625	3.2771	-0.3864	-0.3492	-0.4349	0.5348	0.4960	0.3867			
31	20.282	0.434	0.206	2.614	0.645	3.4248	3.1412	0.0000	-0.4363	-0.3952	0.0000	0.5434	0.5034	0.0000			

LTPT TEST 342 -- EET HIGH-LIFT MODEL -- RUN 4

SLAT DEFLECTION = -50.0 DEG. VANE AND FLAP DEFLECTION = 22.5 DEG.

POINT	ALPHAC	QINFC	MINFC	RN/10**6	MDOT	CLBU	CLBC	CLPC	CMBU	CMBC	CMPC	CDBU	CDBC	CDPC	CDWK1	CDWK2	CDWK3
51	-8.092	0.431	0.203	2.669	4.489	-0.3096	-0.2960	0.0000	-0.1334	-0.1300	0.0000	0.2223	0.2145	0.0000			
52	-4.044	0.421	0.201	2.635	4.443	2.1813	2.1270	0.0000	-0.8534	-0.8359	0.0000	0.0619	0.0609	0.0000			
54	-0.157	0.426	0.202	2.635	4.407	2.6463	2.5842	2.6620	-0.8608	-0.8430	-0.7054	0.0501	0.0494	0.0191	0.0615	0.0445	0.0642
55	3.962	0.427	0.202	2.635	4.469	3.2018	3.1282	0.0000	-0.8417	-0.8228	0.0000	0.0460	0.0454	0.0000			
56	8.103	0.424	0.202	2.627	4.763	3.4724	3.3785	0.0000	-0.6991	-0.6782	0.0000	0.0798	0.0784	0.0000			
57	10.177	0.428	0.203	2.630	4.807	3.6495	3.5482	0.0000	-0.6669	-0.6455	0.0000	0.0857	0.0841	0.0000	0.1081	0.0859	0.1016
58	12.149	0.426	0.202	2.621	4.842	3.7952	3.6838	0.0000	-0.6051	-0.5833	0.0000	0.0990	0.0970	0.0000			
59	14.220	0.427	0.202	2.621	4.854	3.8908	3.7639	0.0000	-0.5359	-0.5133	0.0000	0.1260	0.1231	0.0000			
61	15.104	0.426	0.202	2.608	4.871	3.9125	3.7832	3.8941	-0.5302	-0.5073	-0.3770	0.1297	0.1266	0.0768	0.1585	0.1097	0.1212
63	16.198	0.426	0.202	2.606	4.890	3.9306	3.7939	3.9125	-0.5029	-0.4797	-0.3500	0.1441	0.1404	0.0929			
64	17.183	0.432	0.204	2.622	4.906	3.9426	3.7898	3.9134	-0.4713	-0.4469	-0.3444	0.1771	0.1719	0.1341			
65	18.180	0.428	0.203	2.605	4.876	3.9133	3.7491	3.9201	-0.4705	-0.4447	-0.3346	0.2038	0.1971	0.1641			
66	20.228	0.421	0.201	2.582	4.907	3.8990	3.6946	3.8995	-0.4726	-0.4418	-0.3439	0.2907	0.2781	0.2609			
67	20.674	0.441	0.206	2.634	4.939	3.8862	3.6709	3.8892	-0.5253	-0.4909	-0.3767	0.3155	0.3009	0.3291			
68	10.100	0.424	0.203	2.556	0.000	3.4938	3.3833	3.4137	-0.5966	-0.5745	-0.5234	0.1177	0.1151	0.1054	0.1162	0.1005	0.1121

LTPT TEST 342 -- EET HIGH-LIFT MODEL -- RUN 6

SLAT DEFLECTION = -50.0 DEG. VANE AND FLAP DEFLECTION = 22.5 DEG.

POINT	ALPHAC	QINFC	MINFC	RN/10**6	MDOT	CLBU	CLBC	CLPC	CMBU	CMBC	CMPC	CDBU	CDBC	CDPC	CDWK1	CDWK2	CDWK3
92	-8.120	1.027	0.204	6.046	8.720	1.4385	1.4000	1.4510	-0.7522	-0.7367	-0.6650	0.0772	0.0758	0.0264			
93	-4.129	1.027	0.203	6.068	8.790	2.1453	2.0912	2.1315	-0.8103	-0.7932	-0.7344	0.0645	0.0635	0.0216			
94	0.144	1.046	0.204	6.140	8.776	2.6868	2.6187	2.6553	-0.7773	-0.7588	-0.6975	0.0658	0.0648	0.0206			
95	4.014	1.054	0.204	6.167	8.886	3.1520	3.0715	3.1005	-0.7329	-0.7136	-0.6462	0.0671	0.0660	0.0259			
96	8.102	1.037	0.203	6.117	9.516	3.5400	3.4438	3.4775	-0.6509	-0.6304	-0.5699	0.0809	0.0794	0.0445			
97	10.090	1.053	0.204	6.156	9.687	3.7040	3.6009	3.6409	-0.6043	-0.5837	-0.5237	0.0863	0.0847	0.0495			
98	12.165	1.051	0.204	6.151	9.730	3.8267	3.7138	3.7900	-0.5543	-0.5332	-0.4738	0.1003	0.0982	0.0648			
99	14.283	1.044	0.204	6.109	9.751	3.9806	3.8558	3.9332	-0.5054	-0.4837	-0.4203	0.1156	0.1131	0.0848			
100	15.199	1.032	0.204	6.050	9.802	4.0190	3.8899	3.9682	-0.4780	-0.4564	-0.3976	0.1220	0.1192	0.0956			
101	16.290	1.031	0.204	6.043	9.711	4.0397	3.9041	3.9742	-0.4576	-0.4356	-0.3706	0.1341	0.1308	0.1099			
102	17.152	1.039	0.205	6.069	9.750	4.0543	3.9104	4.0030	-0.4335	-0.4112	-0.3499	0.1502	0.1462	0.1184			
103	18.248	1.038	0.204	6.073	9.870	4.0784	3.9219	4.0458	-0.4027	-0.3799	-0.3307	0.1740	0.1689	0.1521			
104	19.256	1.037	0.204	6.068	9.859	4.0702	3.9087	4.0552	-0.4051	-0.3817	-0.3172	0.1848	0.1792	0.1725			
105	20.254	1.044	0.205	6.093	9.786	4.0496	3.8720	4.0583	-0.3802	-0.3560	-0.3178	0.2195	0.2119	0.2302			
106	22.292	1.071	0.207	6.185	9.906	4.0328	3.8209	4.0270	-0.3587	-0.3322	-0.2980	0.2918	0.2791	0.2988			
107	24.306	1.059	0.206	6.144	9.880	3.9960	3.7475	3.9763	-0.3631	-0.3329	-0.2912	0.3720	0.3523	0.3650			
108	10.081	1.037	0.204	6.082	9.593	3.7001	3.5979	3.6346	-0.5994	-0.5790	-0.5233	0.0846	0.0830	0.0493	0.1022	0.0825	0.1019

LTPT TEST 342 -- EET HIGH-LIFT MODEL -- RUN 9

SLAT DEFLECTION = -50.0 DEG. VANE AND FLAP DEFLECTION = 22.5 DEG.

POINT	ALPHAC	QINFC	MINFC	RN/10**6	MDOT	CLBU	CLBC	CLPC	CMBU	CMBC	CMPC	CDBU	CDBC	CDPC	CDWK1	CDWK2	CDWK3
156	-8.183	2.028	0.202	12.124	15.058	1.3319	1.2980	0.0000	-0.7312	-0.7173	0.0000	0.0668	0.0657	0.0000			
157	-4.165	2.011	0.202	12.049	15.055	2.1453	2.0965	0.0000	-0.8234	-0.8080	0.0000	0.0443	0.0437	0.0000			
158	-0.045	1.992	0.201	11.946	15.322	2.6838	2.6236	2.6320	-0.7973	-0.7810	-0.6994	0.0413	0.0407	0.0221			
159	4.020	2.010	0.201	12.000	15.632	3.1613	3.0884	3.0885	-0.7441	-0.7264	-0.6424	0.0468	0.0462	0.0248			
161	8.115	2.018	0.201	12.023	16.102	3.5831	3.4966	3.4970	-0.6763	-0.6574	-0.5730	0.0557	0.0548	0.0422			
162	10.128	2.015	0.201	12.003	16.261	3.7348	3.6414	3.6571	-0.6388	-0.6193	-0.5297	0.0628	0.0618	0.0528			
163	12.186	2.023	0.201	12.014	16.387	3.8942	3.7903	3.7971	-0.5908	-0.5704	-0.4818	0.0766	0.0753	0.0674			
164	14.244	2.039	0.202	12.061	16.460	4.0087	3.8938	3.9061	-0.5333	-0.5124	-0.4289	0.0932	0.0914	0.0860			
165	16.233	2.067	0.204	12.134	16.679	4.1022	3.9745	4.0041	-0.4886	-0.4670	-0.3839	0.1136	0.1111	0.1116			
167	17.438	2.054	0.203	12.087	16.704	4.1412	4.0068	4.0477	-0.4635	-0.4416	-0.3563	0.1248	0.1219	0.1296			
168	18.249	2.075	0.203	12.179	16.622	4.1260	3.9810	4.0524	-0.4357	-0.4133	-0.3430	0.1470	0.1432	0.1493			
169	19.267	2.114	0.204	12.345	16.771	4.0913	3.9304	4.0203	-0.4303	-0.4063	-0.3375	0.1817	0.1762	0.1962			
170	20.308	2.103	0.205	12.280	16.712	4.0515	3.8688	3.9917	-0.4176	-0.3917	-0.3379	0.2297	0.2215	0.2489			
171	10.242	2.083	0.204	12.240	16.314	3.7429	3.6487	3.6653	-0.6310	-0.6115	-0.5278	0.0643	0.0632	0.0555			
172	10.244	2.057	0.201	11.973	16.179	3.7456	3.6509	3.6574	-0.6270	-0.6075	-0.5270	0.0651	0.0640	0.0559	0.1003	0.0818	0.0985

Appendix B

Drag Data From Wake Traverser

This appendix contains only a sample of the plotted and tabulated drag profiles obtained from the three five-hole pressure probes on the wake traverser. The complete data set consists of 116 pages of plotted and tabulated material and is available on the CD-ROM supplement L-18221 in the directory APPENDX as file AppendixB.doc (Microsoft Word Document). All data were taken at a free-stream Mach number of 0.20. The following table lists the configurations tested and the corresponding run and point numbers and figure and table numbers for the plotted and tabulated data:

δ_s , deg	δ_v and δ_f , deg	Run	Point	$R_n/10^6$	α , deg	Profile Plot Figure Bx and Table xB	Drag Data Figure
-30	7.5	71	1155	6	0	1	60
-30	7.5	71	1157	6	6	2	60
-30	7.5	71	1160	6	12	3	60
-30	7.5	71	1163	6	18	4	60
-50	7.5	64	1028	12	0	5	61
-50	7.5	64	1030	12	4	6	61
-50	7.5	64	1032	12	8	7	61
-40	15	78	1292	2.5	12	8	62
-60	15	99	1629	2.5	10	9	63
-30	22.5	28	481	2.5	12	10	64
-30	22.5	32	532	12	0	11	65
-30	22.5	32	534	12	4	12	65
-40	22.5	115	1861	6	0	13	66
-40	22.5	115	1862	6	4	14	66
-40	22.5	115	1864	6	8	15	66
-40	22.5	115	1866	6	12	16	66
-40	22.5	115	1868	6	16	17	66
-40	22.5	115	1870	6	20	18	66
-50	22.5	4	54	2.6	0	19	67
-50	22.5	4	57	2.6	10	20	67
-50	22.5	4	68*	2.6	10	21	67
-50	22.5	4	61	2.6	15	22	67
-50	22.5	112	1817	2.5	0	23	68
-50	22.5	112	1818	2.5	4	24	68
-50	22.5	112	1820	2.5	8	25	68
-50	22.5	112	1822	2.5	12	26	68
-50	22.5	112	1824	2.5	16	27	68
-50	22.5	112	1826	2.5	20	28	68
-50	22.5	106	1730	6	0	29	69
-50	22.5	106	1731	6	4	30	69
-50	22.5	106	1733	6	8	31	69
-50	22.5	106	1735	6	12	32	69

The asterisk (*) beside the point number 68 indicates that the sidewall blowing was turned off.

δ_s , deg	δ_v and δ_f , deg	Run	Point	$R_n/10^6$	α , deg	Profile Plot Figure Bx and Table xB	Drag Data Figure
-50	22.5	106	1737	6	16	33	69
-50	22.5	6	108	6	10	34	70
-50	22.5	107	1748	12	0	35	71
-50	22.5	107	1749	12	4	36	71
-50	22.5	107	1751	12	8	37	71
-50	22.5	107	1753	12	12	38	71
-50	22.5	107	1755	12	16	39	71
-50	22.5	107	1757	12	20	40	71
-50	22.5	9	172	12	10	41	72
-50	22.5	109	1778	18	0	42	73
-50	22.5	109	1779	18	4	43	73
-50	22.5	109	1781	18	8	44	73
-50	22.5	109	1783	18	12	45	73
-50	22.5	109	1785	18	16	46	73
-50	22.5	109	1787	18	20	47	73
-60	22.5	15	259	6	0	48	74
-60	22.5	15	261	6	8	49	74
-60	22.5	15	263	6	12	50	74
-60	22.5	17	313	12	12	51	75
-60	22.5	18	337	18	12	52	76
-50	30	49	780	2.5	0	53	77
-50	30	49	781	2.5	4	54	77
-50	30	49	785	2.5	12	55	77
-50	30	50	787	2.5	16	56	77
-50	30	50	795	4.3	0	57	78
-50	30	50	796	4.3	4	58	78
-50	30	50	797	4.3	8	59	78
-50	30	50	800	4.3	12	60	78
-50	30	50	802	4.3	16	61	78
-50	30	52	825	12	0	62	79
-50	30	52	826	12	4	63	79
-50	30	52	827	12	8	64	79
-50	30	52	830	12	12	65	79
-50	30	52	832	12	16	66	79
-50	30	54	868	2.5	10	67	80

Tabulated data for a specific table are available in electronic form on CD-ROM supplement L-18221 in the directory WakeData as TABLExB.TXT (text format) where x is the table-figure number. The corresponding plotted data are also available on the CD-ROM in the directory WakeData as FIGBx.PS (PostScript format), as Bx.PDF (Adobe Acrobat Reader format), and as Bx.PNG (Portable Network Graphics format). Figures and tables are numbered in such a fashion to correspond directly to a given run number.

Plotted Wake Drag Profiles

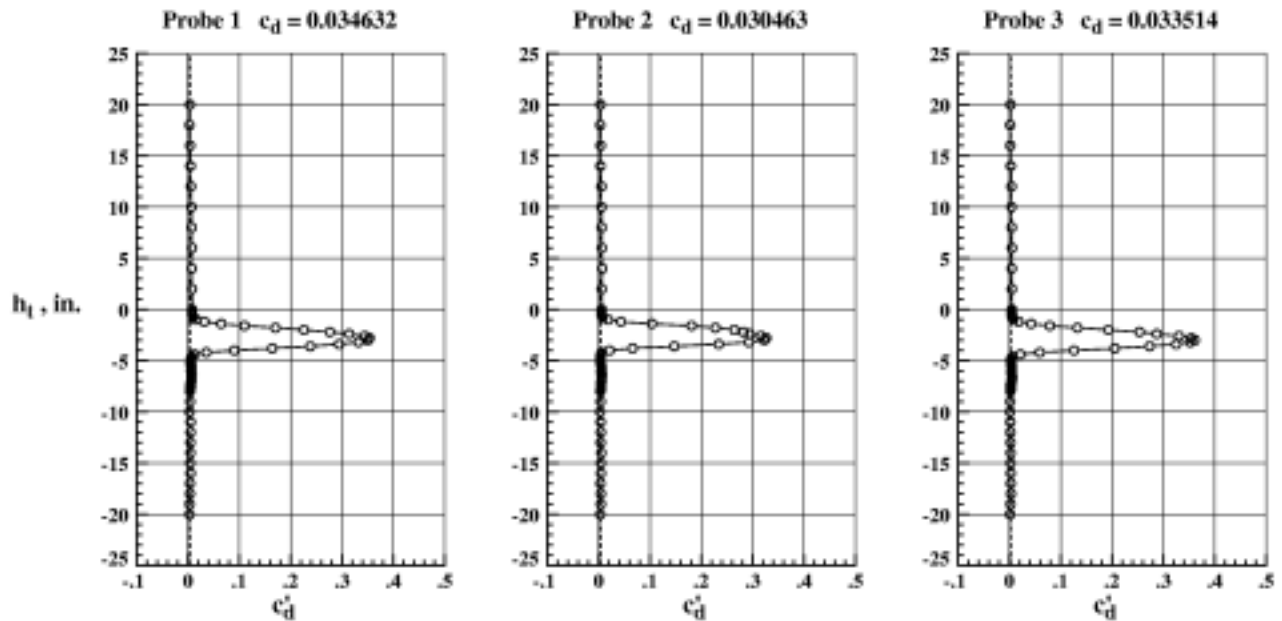


Figure B1. Wake drag profiles for EET High-Lift Airfoil with $\delta_s = -30.0^\circ$, $\delta_v = 7.5^\circ$, and $\delta_f = 7.5^\circ$.
(Run 71, Point 1155, $\alpha = -0.034^\circ$, $M_\infty = 0.201$, $R_n = 6.024 \times 10^6$)

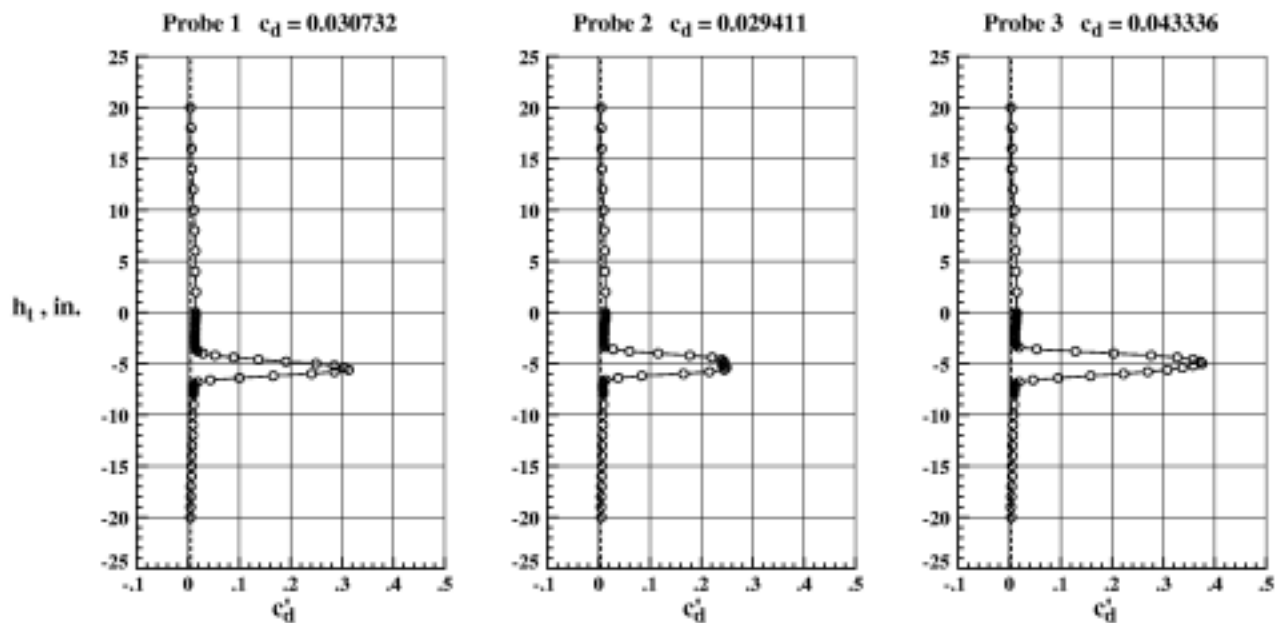


Figure B2. Wake drag profiles for EET High-Lift Airfoil with $\delta_s = -30.0^\circ$, $\delta_v = 7.5^\circ$, and $\delta_f = 7.5^\circ$.
(Run 71, Point 1157, $\alpha = 6.078^\circ$, $M_\infty = 0.201$, $R_n = 6.006 \times 10^6$)

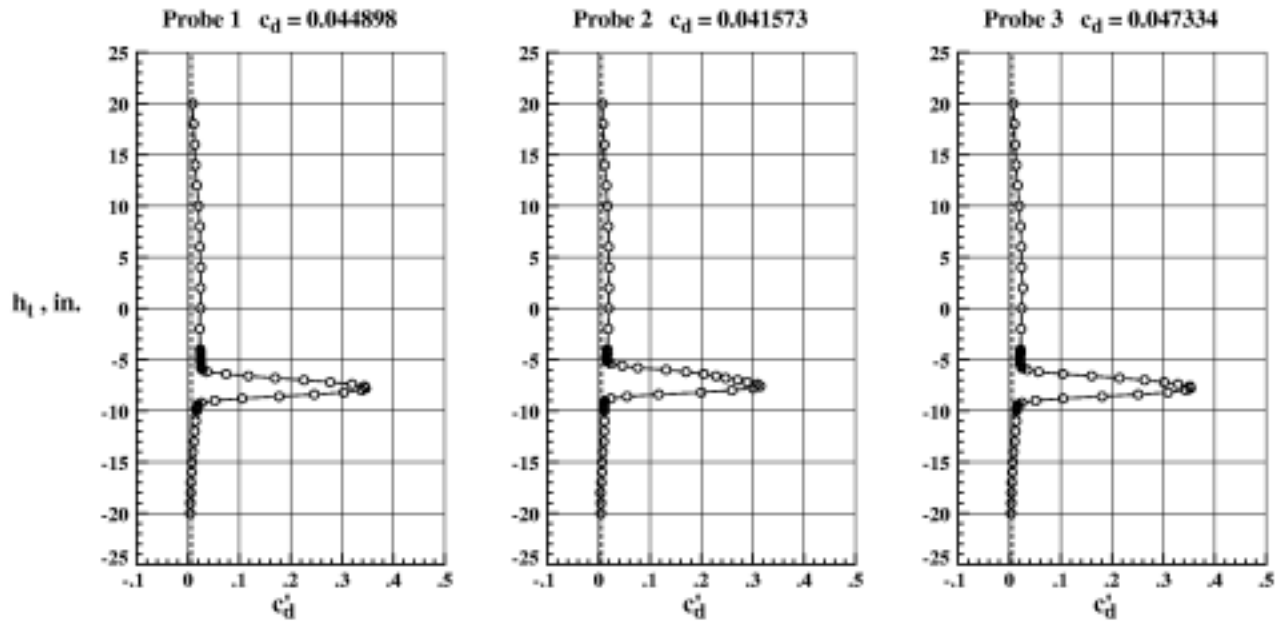


Figure B3. Wake drag profiles for EET High-Lift Airfoil with $\delta_s = -30.0^\circ$, $\delta_v = 7.5^\circ$, and $\delta_f = 7.5^\circ$.
 (Run 71, Point 1160, $\alpha = 12.193^\circ$, $M_\infty = 0.202$, $R_n = 6.082 \times 10^6$)

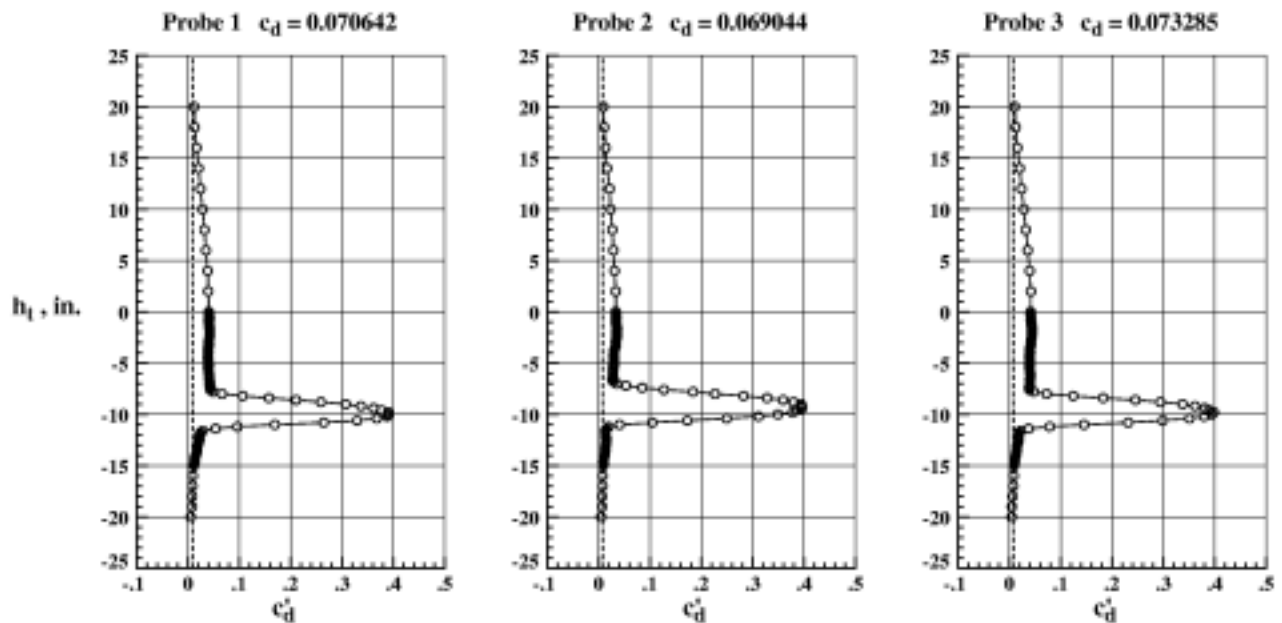


Figure B4. Wake drag profiles for EET High-Lift Airfoil with $\delta_s = -30.0^\circ$, $\delta_v = 7.5^\circ$, and $\delta_f = 7.5^\circ$.
 (Run 71, Point 1163, $\alpha = 18.309^\circ$, $M_\infty = 0.201$, $R_n = 6.047 \times 10^6$)

Tabulated Wake Drag Profile Data

The computer generated variable names listed on each table containing the tabulated wake drag data are defined as follows:

1. Cdp1off, Cdp2off, and Cdp3off – Offset value of c'_d for probe 1, 2, and 3, respectively
2. Cd1, Cd2, and Cd3 – Integrated wake drag coefficient c_d for probes 1, 2, and 3, respectively
3. Ht – Vertical position of probes relative to the tunnel centerline, in.
4. Cdp1, Cdp2, and Cdp3 – value of c'_d at the Ht position in the wake for probe 1, 2, and 3, respectively

The angle of attack, Mach number, and Reynolds number listed have been corrected for wind tunnel wall effects, but the drag increments and integrated values presented have not been corrected. Tabulated data for a specific table are available in electronic form on CD-ROM supplement L-18221 in the directory WakeData as TABLEx.B.TXT (text format) where x is the table-figure number. The corresponding plotted data are also available on the CD-ROM in the directory WakeData as FIGBx.PS (PostScript format), as Bx.PDF (Adobe Acrobat Reader format), and as Bx.PNG (Portable Network Graphics format). Figures and tables are numbered in such a fashion to correspond directly to a given run number.

Table Number 1B
 Run Number 71 Point Number 1155
 Angle of Attack = -0.034 deg.
 Mach Number = 0.201
 Reynolds Number (millions) = 6.024
 Slat Deflection = -30.0 deg.
 Vane Deflection = 7.5 deg.
 Flap Deflection = 7.5 deg.
 Cdploff = 0.003314 Cdp2off = 0.003490
 Cdp3off = 0.001905
 Cd1 = 0.034632 Cd2 = 0.030463
 Cd3 = 0.033514

Ht	Cdp1	Cdp2	Cdp3
-9.0	0.00423	0.00390	0.00178
-10.0	0.00323	0.00287	0.00143
-11.0	0.00498	0.00391	0.00187
-12.0	0.00492	0.00414	0.00215
-13.0	0.00472	0.00391	0.00252
-14.0	0.00469	0.00490	0.00257
-15.0	0.00423	0.00413	0.00255
-16.0	0.00477	0.00417	0.00273
-17.0	0.00399	0.00363	0.00270
-18.0	0.00400	0.00415	0.00321
-19.0	0.00325	0.00415	0.00233
-20.0	0.00299	0.00311	0.00135

Ht	Cdp1	Cdp2	Cdp3
20.0	0.00389	0.00363	0.00236
18.0	0.00313	0.00307	0.00158
16.0	0.00420	0.00391	0.00202
14.0	0.00476	0.00365	0.00270
12.0	0.00554	0.00525	0.00396
10.0	0.00660	0.00523	0.00402
8.0	0.00682	0.00573	0.00427
6.0	0.00761	0.00597	0.00485
4.0	0.00726	0.00668	0.00429
2.0	0.00747	0.00587	0.00456
0.0	0.00775	0.00557	0.00482
-0.2	0.00799	0.00550	0.00473
-0.4	0.00769	0.00567	0.00478
-0.6	0.00850	0.00585	0.00518
-0.8	0.00953	0.00773	0.00520
-1.0	0.01564	0.01864	0.00780
-1.2	0.03189	0.04349	0.01839
-1.4	0.06477	0.10361	0.04241
-1.6	0.10998	0.18101	0.07876
-1.8	0.17064	0.22756	0.13261
-2.0	0.22623	0.26440	0.19308
-2.2	0.27628	0.28209	0.25356
-2.4	0.31392	0.29454	0.28737
-2.6	0.34470	0.31600	0.33060
-2.8	0.35363	0.32626	0.35450
-3.0	0.35074	0.32255	0.36143
-3.2	0.33225	0.29263	0.35241
-3.4	0.29430	0.23392	0.32493
-3.6	0.23823	0.14730	0.27334
-3.8	0.16419	0.06619	0.20537
-4.0	0.09028	0.02129	0.12597
-4.2	0.03583	0.00579	0.05920
-4.4	0.01281	0.00436	0.02125
-4.6	0.00712	0.00335	0.00598
-4.8	0.00556	0.00365	0.00340
-5.0	0.00525	0.00313	0.00278
-5.2	0.00506	0.00371	0.00307
-5.4	0.00659	0.00448	0.00431
-5.6	0.00603	0.00523	0.00399
-5.8	0.00654	0.00574	0.00450
-6.0	0.00603	0.00497	0.00397
-6.2	0.00680	0.00525	0.00396
-6.4	0.00705	0.00626	0.00470
-6.6	0.00656	0.00577	0.00546
-6.8	0.00676	0.00572	0.00487
-7.0	0.00629	0.00549	0.00461
-7.2	0.00546	0.00417	0.00379
-7.4	0.00500	0.00445	0.00224
-7.6	0.00506	0.00449	0.00269
-7.8	0.00452	0.00420	0.00294
-8.0	0.00402	0.00343	0.00198

Table Number 2B

Run Number 71 Point Number 1157

Angle of Attack = 6.078 deg.

Mach Number = 0.201

Reynolds Number (millions) = 6.006

Slat Deflection = -30.0 deg.

Vane Deflection = 7.5 deg.

Flap Deflection = 7.5 deg.

Cdploff = 0.005140 Cdp2off = 0.004686

Cdp3off = 0.003679

Cd1 = 0.030732 Cd2 = 0.029411

Cd3 = 0.043336

Ht	Cdp1	Cdp2	Cdp3
-9.0	0.01022	0.00865	0.00866
-10.0	0.00865	0.00735	0.00776
-11.0	0.00905	0.00779	0.00711
-12.0	0.00912	0.00710	0.00679
-13.0	0.00783	0.00654	0.00573
-14.0	0.00710	0.00653	0.00598
-15.0	0.00677	0.00620	0.00504
-16.0	0.00657	0.00574	0.00526
-17.0	0.00555	0.00521	0.00432
-18.0	0.00554	0.00472	0.00400
-19.0	0.00509	0.00449	0.00329

Ht	Cdp1	Cdp2	Cdp3
20.0	0.00474	0.00451	0.00328
18.0	0.00591	0.00479	0.00420
16.0	0.00664	0.00531	0.00470
14.0	0.00746	0.00610	0.00435
12.0	0.00974	0.00752	0.00703
10.0	0.01120	0.00990	0.00986
8.0	0.01278	0.01065	0.01096
6.0	0.01408	0.01197	0.01218
4.0	0.01412	0.01256	0.01313
2.0	0.01553	0.01322	0.01449
0.0	0.01464	0.01234	0.01398
-0.2	0.01480	0.01328	0.01411
-0.4	0.01489	0.01309	0.01336
-0.6	0.01446	0.01265	0.01316
-0.8	0.01472	0.01270	0.01314
-1.0	0.01393	0.01140	0.01288
-1.2	0.01292	0.01062	0.01209
-1.4	0.01352	0.01068	0.01154
-1.6	0.01372	0.01090	0.01169
-1.8	0.01292	0.01009	0.01142
-2.0	0.01326	0.01119	0.01103
-2.2	0.01269	0.01037	0.01106
-2.4	0.01273	0.00989	0.01113
-2.6	0.01270	0.01037	0.01096
-2.8	0.01352	0.01039	0.01136
-3.0	0.01218	0.00979	0.01054
-3.2	0.01324	0.01050	0.01196
-3.4	0.01287	0.01229	0.01876
-3.6	0.01609	0.02833	0.05343
-3.8	0.01937	0.06034	0.12883
-4.0	0.02919	0.11613	0.20333
-4.2	0.05273	0.17751	0.27629
-4.4	0.08895	0.22104	0.32691
-4.6	0.13736	0.23955	0.35782
-4.8	0.19098	0.24386	0.37211
-5.0	0.24951	0.24413	0.37554
-5.2	0.28486	0.24129	0.35855
-5.4	0.30487	0.24861	0.33692
-5.6	0.31298	0.24449	0.30832
-5.8	0.28532	0.21577	0.26962
-6.0	0.24074	0.16531	0.22238
-6.2	0.16600	0.08393	0.15826
-6.4	0.10015	0.03809	0.09553
-6.6	0.04338	0.01356	0.04619
-6.8	0.01918	0.00873	0.01916
-7.0	0.01146	0.00807	0.01068
-7.2	0.01106	0.00768	0.01027
-7.4	0.01075	0.00793	0.00972
-7.6	0.01098	0.00843	0.00978
-7.8	0.01087	0.00885	0.00896
-8.0	0.01038	0.00836	0.00896

Appendix C

Chordwise Pressure Distributions

This appendix contains only a sample of the plotted chordwise pressure distributions taken during the test of the EET High-Lift Airfoil. The complete data set consists of 209 pages of plotted data and is available on the CD-ROM supplement L-18221 in the directory APPENDX as file AppendixC.doc (Microsoft Word Document). Several plotted forms of the data for a specific run x (numbers 2 – 126) and part y (letters a – e) are also available on the CD-ROM in the directory CP_CW as FIGC xy .PS (PostScript), C xy .PDF (Adobe Acrobat Reader), and C xy .PNG (Portable Network Graphics). The corresponding tabulated form of the data is contained in directory CPDATA as Tbx.DOC (Microsoft Word) and C px .TXT (text). Figures and tables are numbered in such a fashion to correspond directly to a given run number.

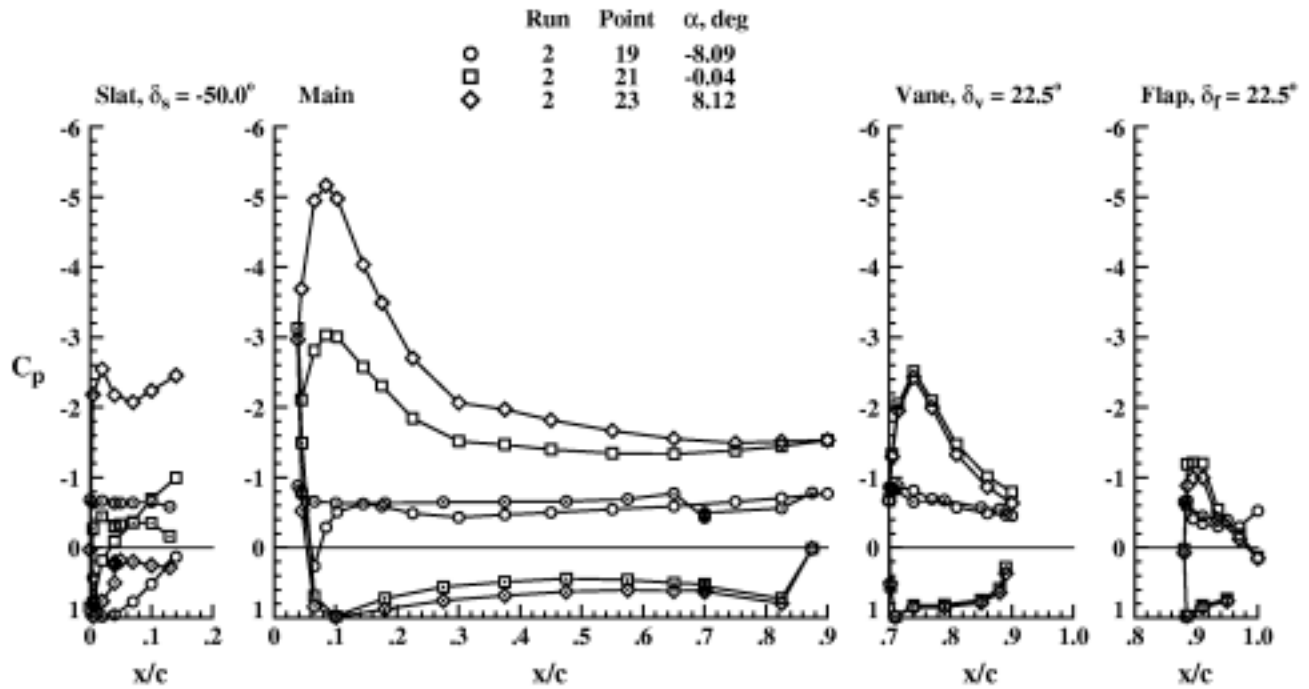


Figure C2a. Chordwise pressures on EET High-Lift Airfoil at $M_\infty = 0.203$ and $R_n = 2.584 \times 10^6$.

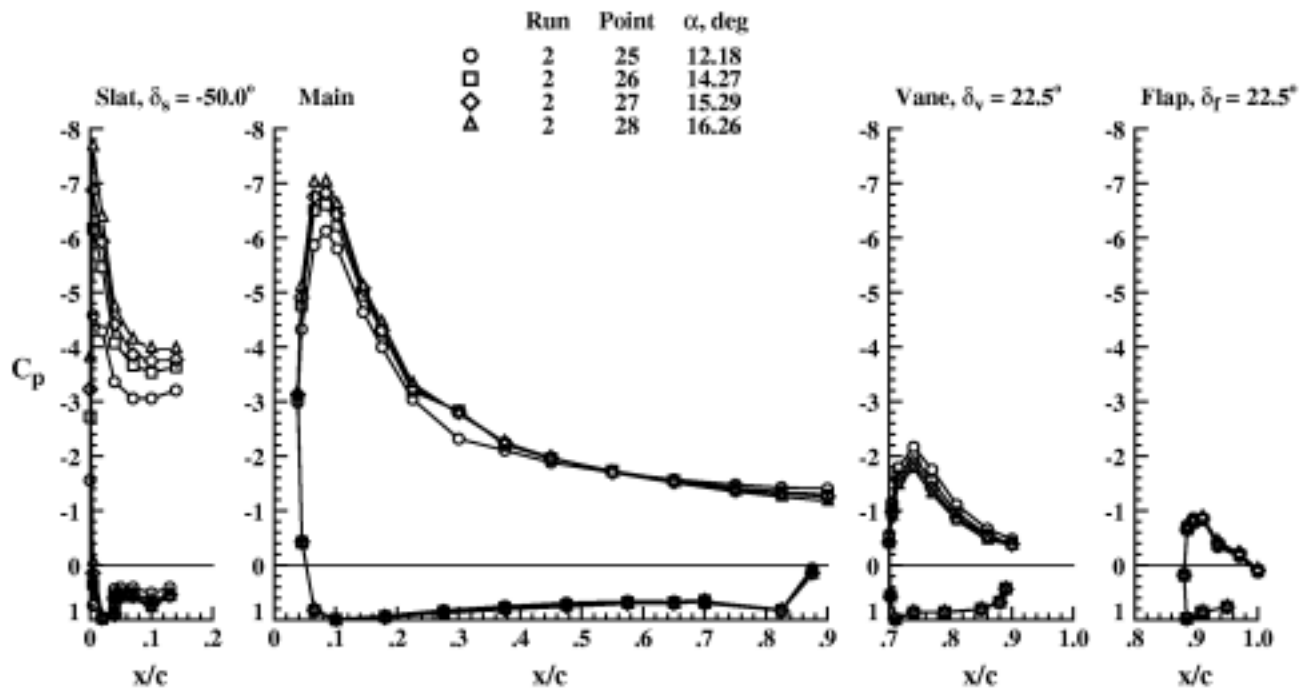


Figure C2b. Chordwise pressures on EET High-Lift Airfoil at $M_\infty = 0.204$ and $R_n = 2.601 \times 10^6$.

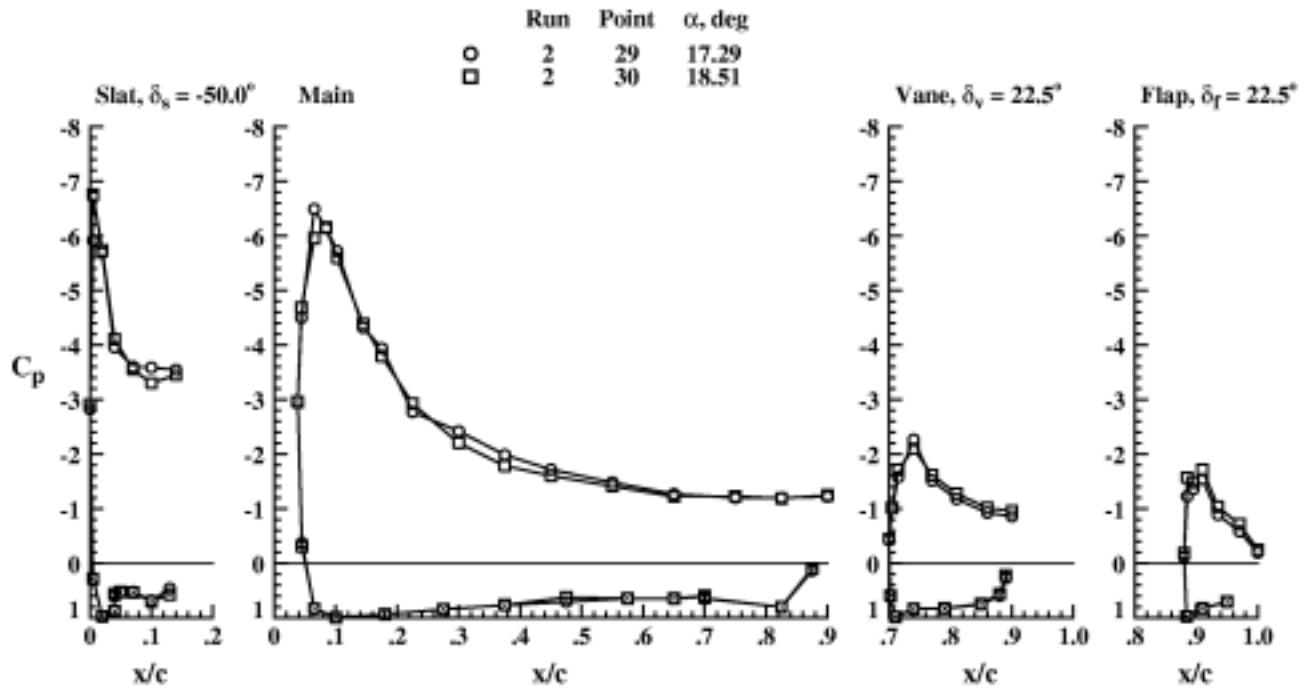


Figure C2c. Chordwise pressures on EET High-Lift Airfoil at $M_\infty = 0.207$ and $R_n = 2.625 \times 10^6$.

Appendix D

Spanwise Pressure Distributions

This appendix contains only a sample of the plotted spanwise pressure distributions taken for during the test of the EET High-Lift Airfoil. The complete data set consists of 209 pages of plotted data and is available on the CD-ROM supplement L-18221 in the directory APPENDX as file AppendixD.doc (Microsoft Word Document). Several plotted forms of the data for a specific run x (numbers 2 – 126) and part y (letters a – e) are also available on the CD-ROM in the directory CP_SW as FIGD xy .PS (PostScript), D xy .PDF (Adobe Acrobat Reader), and D xy .PNG (Portable Network Graphics). The corresponding tabulated form of the data is contained in directory CPDATA as Tbx.DOC (Microsoft Word) and Cpx.TXT (text). Figures and tables are numbered in such a fashion to correspond directly to a given run number.

	Run	Point	α , deg
○	2	19	-8.09
□	2	21	-0.04
◇	2	23	8.12

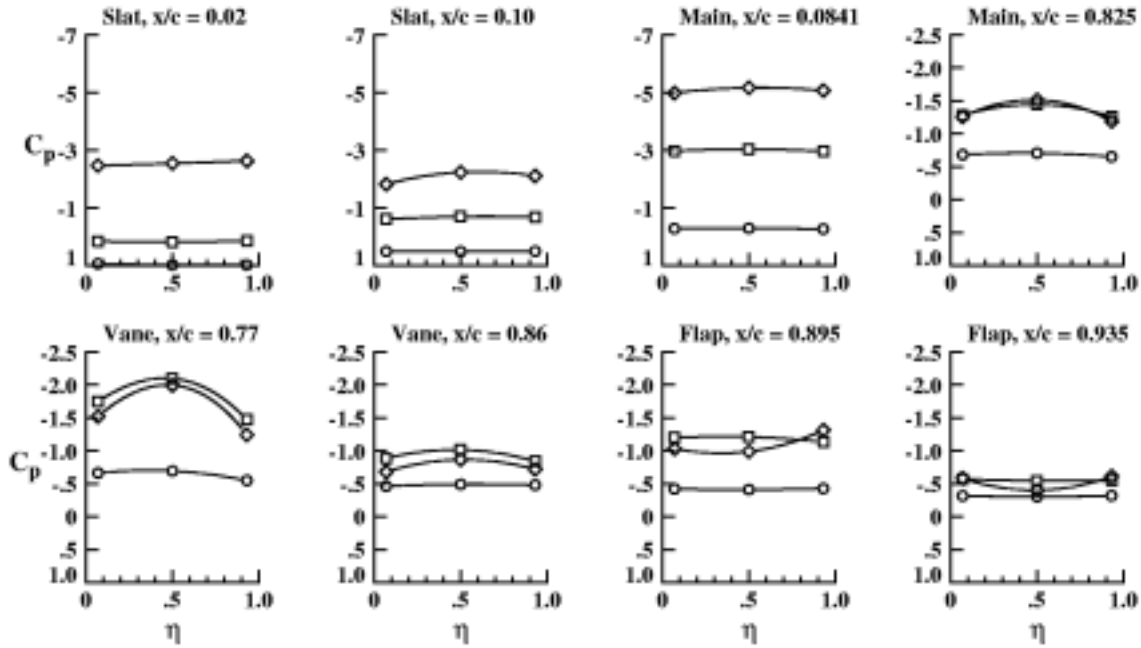


Figure D2a. Spanwise pressures on EET High-Lift Airfoil with $\delta_s = -50.0^\circ$, $\delta_v = 22.5^\circ$, and $\delta_f = 22.5^\circ$ at $M_\infty = 0.203$ and $R_n = 2.584 \times 10^6$.

	Run	Point	α , deg
○	2	25	12.18
□	2	26	14.27
◇	2	27	15.29
△	2	28	16.26

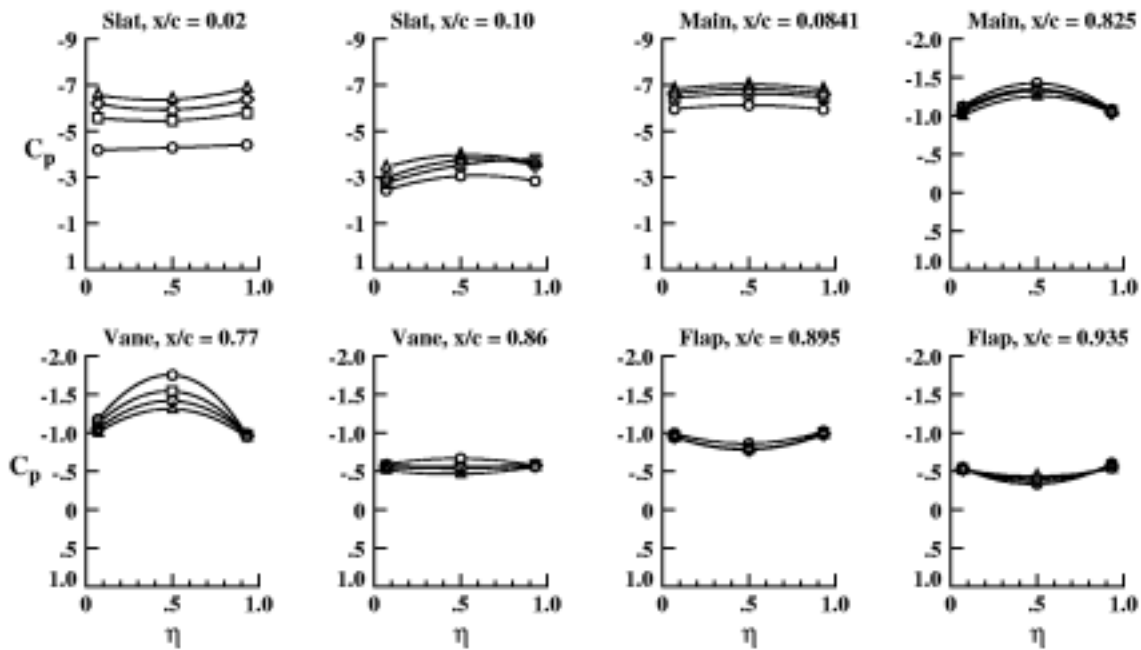


Figure D2b. Spanwise pressures on EET High-Lift Airfoil with $\delta_s = -50.0^\circ$, $\delta_v = 22.5^\circ$, and $\delta_f = 22.5^\circ$ at $M_\infty = 0.204$ and $R_n = 2.601 \times 10^6$.

	Run	Point	α , deg
○	2	29	17.29
□	2	30	18.51

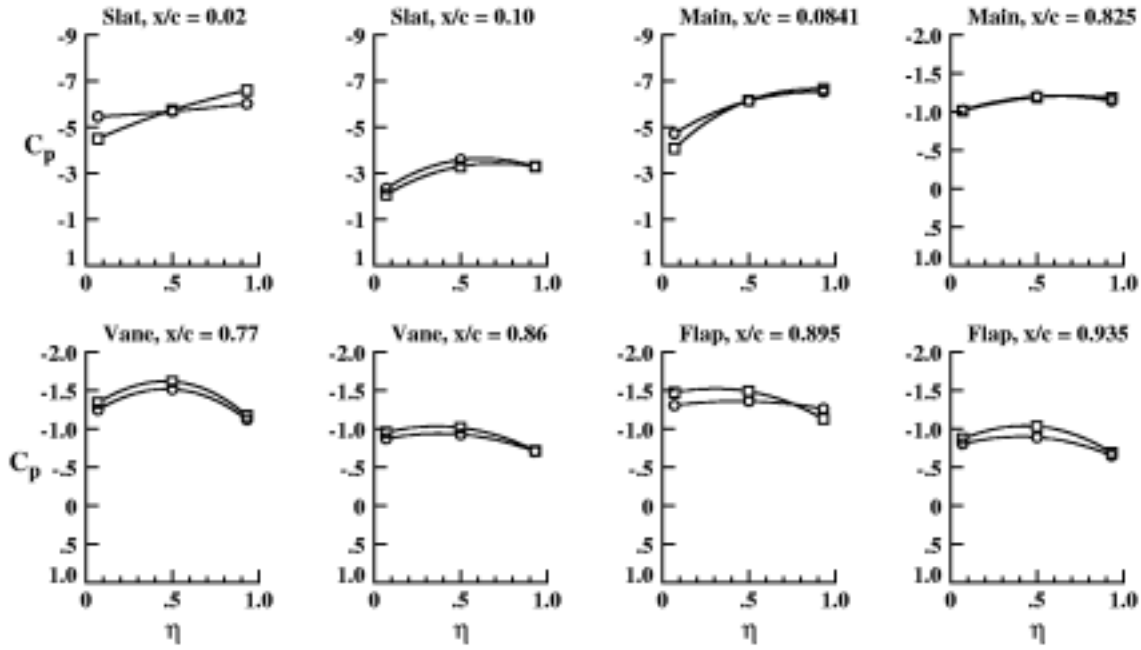


Figure D2c. Spanwise pressures on EET High-Lift Airfoil with $\delta_s = -50.0^\circ$, $\delta_v = 22.5^\circ$, and $\delta_f = 22.5^\circ$ at $M_\infty = 0.207$ and $R_n = 2.625 \times 10^6$.

Appendix E

Tunnel Floor and Ceiling Pressure Distributions

This appendix contains only a sample of the plotted tunnel floor and ceiling pressure distributions taken during the test of the EET High-Lift Airfoil. The complete data set consists of 99 pages of plotted data and is available on the CD-ROM supplement L-18221 in the directory APPENDX as file AppendixE.doc (Microsoft Word Document). Several plotted forms of the data for a specific run x (numbers 2 – 126) and part y (letters a – e) are also available on the CD-ROM in the directory CP_FC as FIGE xy .PS (PostScript), E xy .PDF (Adobe Acrobat Reader), and E xy .PNG (Portable Network Graphics). The corresponding tabulated form of the data is contained in directory CPDATA as Tbx.DOC (Microsoft Word) and Cpx.TXT (text).). Not all configurations tested have corresponding floor and ceiling pressures due to a mechanical problem that developed with the scanivalve driver motor about midway through the test. Of the 105 data runs reported in this paper, floor and ceiling pressures were obtained on only 51 runs. Figures and tables are numbered in such a fashion to correspond directly to a given run number.

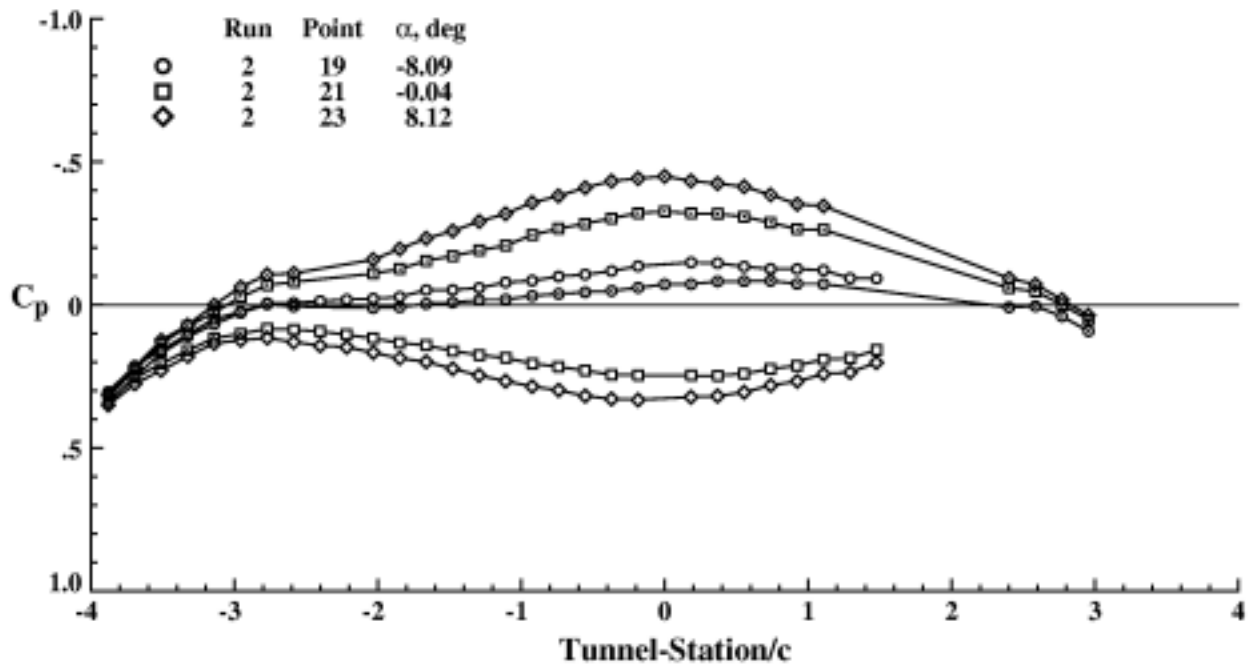


Figure E2a. Floor and ceiling pressures for EET High-Lift Airfoil with $\delta_s = -50.0^\circ$, $\delta_v = 22.5^\circ$, and $\delta_f = 22.5^\circ$ at $M_\infty = 0.203$ and $R_n = 2.584 \times 10^6$.

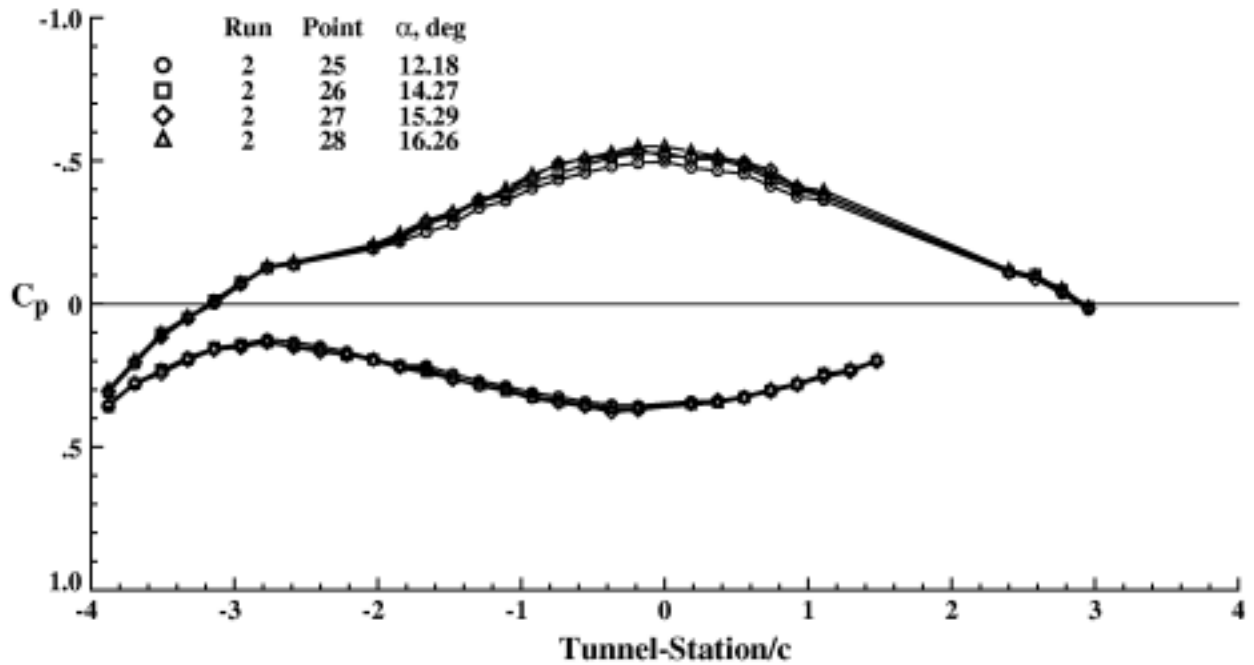


Figure E2b. Floor and ceiling pressures for EET High-Lift Airfoil with $\delta_s = -50.0^\circ$, $\delta_v = 22.5^\circ$, and $\delta_f = 22.5^\circ$ at $M_\infty = 0.204$ and $R_n = 2.601 \times 10^6$.

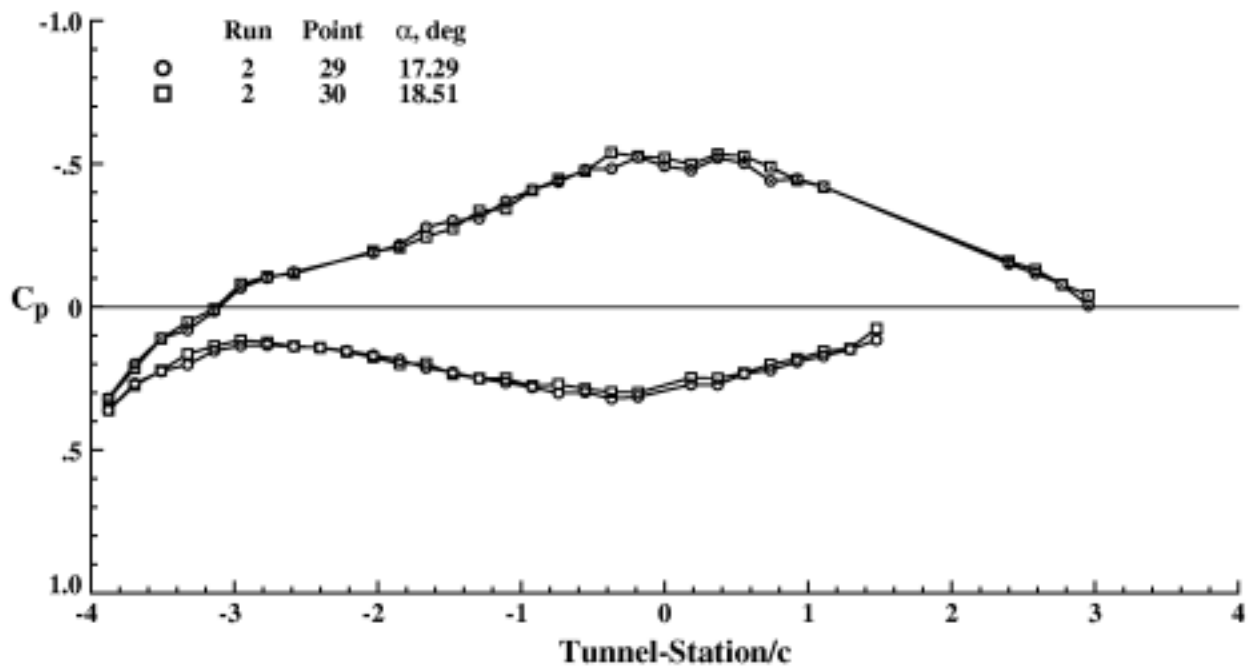


Figure E2c. Floor and ceiling pressures for EET High-Lift Airfoil with $\delta_s = -50.0^\circ$, $\delta_v = 22.5^\circ$, and $\delta_f = 22.5^\circ$ at $M_\infty = 0.207$ and $R_n = 2.625 \times 10^6$.

References

1. Bartlett, Dennis W.: *Wind-Tunnel Investigation of Several High Aspect-Ratio Supercritical Wing Configurations on a Wide-Body-Type Fuselage*. NASA TM X-71996, 1977.
2. Bartlett, Dennis W.; and Patterson, James C., Jr.: *NASA Supercritical-Wing Technology*. NASA TM-78731, 1978.
3. Morgan, Harry L., Jr.; and Paulson, John W., Jr.: *Low-Speed Aerodynamic Performance of a High-Aspect-Ratio Supercritical-Wing Transport Model Equipped With Full-Span Slat and Part-Span Double-Slotted Flaps*. NASA TP-1580, 1979.
4. Morgan, Harry L., Jr.: *Model Geometry Description and Pressure Distribution Data From Tests of EET High-Lift Research Model Equipped With Full-Span Slat and Part-Span Flaps*. NASA TM-80048, 1979.
5. Morgan, Harry L., Jr.: *Low-Speed Aerodynamic Performance of an Aspect-Ratio-10 Supercritical-Wing Transport Model Equipped With a Full-Span Slat and Part-Span and Full-Span Double-Slotted Flaps*. NASA TP-1805, 1981.
6. Morgan, Harry L., Jr.; and Kjelgaard, Scott O.: *Langley High-Lift Research on a High-Aspect-Ratio Supercritical Wing Configuration*. *Advanced Aerodynamics – Selected NASA Research*. NASA CP-2208, 1981, pp. 55–77.
7. Morgan, Harry L., Jr.: *Pressure Distribution Data From Tests of 2.29-Meter (7.5-Ft.) Span EET High-Lift Research Model in Langley 4- by 7-Meter Tunnel*. NASA TM-83111, 1982.
8. Morgan, Harry L., Jr.; and Kjelgaard, Scott O.: *Pressure Distribution Data From Tests of 2.29 m (7.5 ft) Span EET High-Lift Transport Aircraft Model in the Ames 12-Foot Pressure Tunnel*. NASA TM-4517, 1983.
9. Morgan, Harry L., Jr.; and Kjelgaard, Scott O.: *Low-Speed Tests of a High-Aspect-Ratio, Supercritical-Wing Transport Model Equipped With a High-Lift Flap System in the Langley 4- by 7-Meter and Ames 12-Foot Pressure Tunnels*. NASA TP-2097, 1983.
10. Friedman, Inger P.: *Calibration and Application of a New Wake Rake System for Drag Measurement of High Lift Airfoil Models*. M.S. Thesis, George Washington Univ., Mar. 1991.
11. Stevens, W. A.; Goradia, S. H.; and Braden, J. A.: *Mathematical Model for Two-Dimensional Multi-Component Airfoils in Viscous Flow*. NASA CR-1843, 1971.
12. Schlichting, Hermann: *Boundary-Layer Theory*. Sixth Edition, McGraw-Hill Book Co., 1968, pp. 711–714.
13. Pope, Alan; and Harper, John J.: *Low-Speed Wind Tunnel Testing*. John Wiley & Sons, Inc., 1966, pp. 300–377.

Table 1. Slat Element Surface Coordinates of EET High-Lift Airfoil

Upper Surface		Lower Surface	
x/c	y/c	x/c	y/c
0.0000	0.0000	0.0000	0.0000
0.0005	0.0047	0.0005	-0.0047
0.0008	0.0059	0.0008	-0.0059
0.0010	0.0065	0.0010	-0.0065
0.0025	0.0101	0.0025	-0.0101
0.0035	0.0119	0.0035	-0.0119
0.0050	0.0141	0.0050	-0.0140
0.0075	0.0168	0.0075	-0.0167
0.0100	0.0190	0.0100	-0.0189
0.0150	0.0224	0.0150	-0.0223
0.0200	0.0251	0.0200	-0.0249
0.0250	0.0274	0.0250	-0.0270
0.0300	0.0293	0.0300	-0.0289
0.0350	0.0310	0.0350	-0.0306
0.0400	0.0325	0.0400	-0.0321
0.0450	0.0339	0.0450	-0.0334
0.0500	0.0352	0.0467	-0.0339
0.0600	0.0374	0.0480	-0.0342
0.0700	0.0394	0.0480	-0.0338
0.0800	0.0412	0.0450	-0.0325
0.0900	0.0428	0.0435	-0.0315
0.1000	0.0443	0.0420	-0.0303
0.1100	0.0457	0.0410	-0.0292
0.1200	0.0469	0.0400	-0.0277
0.1300	0.0480	0.0395	-0.0268
0.1400	0.0491	0.0390	-0.0256
0.1500	0.0501	0.0385	-0.0240
0.1550	0.0506	0.0383	-0.0230
		0.0381	-0.0216
		0.0380	-0.0198
		0.0384	-0.0160
		0.0390	-0.0133
		0.0400	-0.0104
		0.0402	-0.0099
		0.0420	-0.0060
		0.0440	-0.0024
		0.0470	0.0017
		0.0500	0.0053
		0.0550	0.0104
		0.0600	0.0148
		0.0650	0.0185
		0.0700	0.0218
		0.0750	0.0249
		0.0800	0.0276
		0.0900	0.0323
		0.1000	0.0364
		0.1100	0.0398
		0.1200	0.0426
		0.1300	0.0451
		0.1400	0.0472
		0.1500	0.0490
		0.1550	0.0499

Table 2. Main Element Surface Coordinates of EET High-Lift Airfoil

Upper Surface		Lower Surface	
x/c	y/c	x/c	y/c
0.0380	-0.0198	0.0380	-0.0198
0.0384	-0.0160	0.0381	-0.0216
0.0390	-0.0133	0.0383	-0.0230
0.0402	-0.0099	0.0385	-0.0240
0.0420	-0.0060	0.0390	-0.0256
0.0440	-0.0024	0.0395	-0.0268
0.0470	0.0017	0.0400	-0.0277
0.0500	0.0053	0.0410	-0.0292
0.0550	0.0104	0.0420	-0.0303
0.0600	0.0148	0.0435	-0.0315
0.0650	0.0185	0.0450	-0.0325
0.0700	0.0218	0.0460	-0.0330
0.0750	0.0249	0.0470	-0.0334
0.0800	0.0276	0.0480	-0.0338
0.0841	0.0296	0.0500	-0.0345
0.0900	0.0323	0.0600	-0.0371
0.1000	0.0364	0.0700	-0.0391
0.1022	0.0372	0.0800	-0.0408
0.1100	0.0398	0.0900	-0.0424
0.1200	0.0426	0.1000	-0.0439
0.1400	0.0472	0.1100	-0.0453
0.1445	0.0480	0.1200	-0.0466
0.1500	0.0490	0.1400	-0.0489
0.1550	0.0499	0.1500	-0.0499
0.1600	0.0506	0.1600	-0.0509
0.1750	0.0522	0.1800	-0.0527
0.1800	0.0527	0.2000	-0.0541
0.2000	0.0542	0.2250	-0.0558
0.2250	0.0557	0.2500	-0.0572
0.2500	0.0571	0.2750	-0.0582
0.2750	0.0581	0.3000	-0.0590
0.3000	0.0588	0.3250	-0.0596
0.3250	0.0594	0.3500	-0.0599
0.3500	0.0598	0.4000	-0.0597
0.4000	0.0600	0.4500	-0.0585
0.4500	0.0595	0.5000	-0.0558
0.5000	0.0582	0.5500	-0.0513
0.5500	0.0563	0.6000	-0.0446
0.6000	0.0536	0.6500	-0.0364
0.6500	0.0502	0.7000	-0.0272
0.7000	0.0459	0.7060	-0.0261
0.7250	0.0434	0.7060	-0.0257
0.7500	0.0405	0.6750	-0.0257
0.7750	0.0374	0.6750	0.0000
0.8000	0.0339	0.6750	0.0270
0.8250	0.0301	0.7000	0.0270
0.8500	0.0258	0.7850	0.0270
0.8750	0.0212	0.8000	0.0254
0.9000	0.0160	0.8250	0.0228
		0.8500	0.0202
		0.8750	0.0175
		0.9000	0.0149

Table 3. Vane Element Surface Coordinates of EET High-Lift Airfoil

Upper Surface		Lower Surface	
x/c	y/c	x/c	y/c
0.7000	-0.0190	0.7000	-0.0190
0.7001	-0.0171	0.7001	-0.0205
0.7005	-0.0153	0.7005	-0.0218
0.7010	-0.0138	0.7010	-0.0228
0.7020	-0.0117	0.7020	-0.0239
0.7030	-0.0099	0.7030	-0.0247
0.7040	-0.0084	0.7040	-0.0252
0.7050	-0.0070	0.7050	-0.0255
0.7060	-0.0058	0.7060	-0.0257
0.7070	-0.0047	0.7070	-0.0258
0.7080	-0.0036	0.7080	-0.0257
0.7100	-0.0017	0.7100	-0.0253
0.7150	0.0021	0.7150	-0.0244
0.7200	0.0052	0.7200	-0.0234
0.7250	0.0077	0.7250	-0.0225
0.7300	0.0098	0.7300	-0.0215
0.7350	0.0117	0.7350	-0.0205
0.7400	0.0131	0.7400	-0.0196
0.7500	0.0155	0.7500	-0.0177
0.7600	0.0172	0.7600	-0.0158
0.7700	0.0184	0.7700	-0.0140
0.7800	0.0191	0.7800	-0.0122
0.7900	0.0196	0.7900	-0.0106
0.8000	0.0198	0.8000	-0.0090
0.8100	0.0199	0.8100	-0.0076
0.8200	0.0198	0.8200	-0.0062
0.8300	0.0196	0.8300	-0.0049
0.8400	0.0192	0.8400	-0.0038
0.8500	0.0189	0.8500	-0.0028
0.8600	0.0181	0.8600	-0.0021
0.8700	0.0175	0.8700	-0.0016
0.8800	0.0168	0.8800	-0.0012
0.8900	0.0159	0.8830	-0.0011
0.9000	0.0149	0.8830	-0.0008
0.9050	0.0144	0.8820	-0.0004
0.9100	0.0137	0.8810	0.0002
0.9150	0.0127	0.8805	0.0007
		0.8802	0.0014
		0.8801	0.0019
		0.8800	0.0030
		0.8801	0.0036
		0.8805	0.0049
		0.8810	0.0058
		0.8820	0.0070
		0.8840	0.0087
		0.8850	0.0093
		0.8870	0.0102
		0.8900	0.0112
		0.9000	0.0127
		0.9050	0.0130
		0.9100	0.0128
		0.9150	0.0122

Table 4. Flap Element Surface Coordinates of EET High-Lift Airfoil

Upper Surface		Lower Surface	
x/c	y/c	x/c	y/c
0.8800	0.0030	0.8800	0.0030
0.8801	0.0036	0.8801	0.0019
0.8802	0.0041	0.8802	0.0014
0.8805	0.0049	0.8805	0.0007
0.8810	0.0058	0.8810	0.0002
0.8820	0.0070	0.8820	-0.0004
0.8830	0.0079	0.8830	-0.0008
0.8840	0.0087	0.8840	-0.0010
0.8850	0.0093	0.8850	-0.0010
0.8870	0.0102	0.8870	-0.0010
0.8900	0.0112	0.8900	-0.0009
0.8950	0.0122	0.8950	-0.0009
0.9000	0.0127	0.9000	-0.0010
0.9050	0.0130	0.9050	-0.0011
0.9100	0.0128	0.9100	-0.0013
0.9150	0.0122	0.9150	-0.0015
0.9200	0.0114	0.9200	-0.0018
0.9250	0.0105	0.9250	-0.0022
0.9300	0.0093	0.9300	-0.0026
0.9350	0.0081	0.9350	-0.0031
0.9400	0.0069	0.9400	-0.0037
0.9450	0.0057	0.9450	-0.0043
0.9500	0.0044	0.9500	-0.0051
0.9600	0.0018	0.9600	-0.0067
0.9700	-0.0009	0.9700	-0.0087
0.9800	-0.0037	0.9800	-0.0110
0.9900	-0.0068	0.9900	-0.0135
1.0000	-0.0101	1.0000	-0.0164

Table 5. Pressure Tap Locations of Slat Element of EET High-Lift Airfoil

Upper Surface			Lower Surface		
Tap Identifier	x/c	y/c	Tap Identifier	x/c	y/c
S100W, S200C, S300E	0.0000	0.0000	S207C	0.0050	-0.0140
S201C	0.0050	0.0141	S103W, S208C, S303E	0.0200	-0.0249
S101W, S202C, S301E	0.0200	0.0251	S209C	0.0400	-0.0321
S203C	0.0400	0.0325	S210C	0.0380	-0.0198
S204C	0.0700	0.0394	S211C	0.0400	-0.0104
S102W, S205C, S302E	0.1000	0.0443	S212C	0.0500	0.0053
S206C	0.1400	0.0491	S213C	0.0700	0.0218
			S214C	0.1000	0.0364
			S215C	0.1300	0.0451

Note: Last letter of Tap Identifier equals E for taps near east wall, C for centerline taps, and W for taps near west wall.

Table 6. Pressure Tap Locations of Main Element of EET High-Lift Airfoil

Upper Surface			Lower Surface		
Tap Identifier	x/c	y/c	Tap Identifier	x/c	y/c
M104W, M216C, M304E	0.0380	-0.0198	M222C	0.0450	-0.0325
M217C	0.0440	-0.0024	M223C	0.0650	-0.0381
M105W, M218C, M305E	0.0650	0.0185	M107W, M224C, M307E	0.1000	-0.0439
M103W, M200C, M303E	0.0841	0.0296	M242C	0.1800	-0.0527
M108W, M201C, M308E	0.1022	0.0372	M113W, M243C, M313E	0.2750	-0.0582
M106W, M219C, M306E	0.1445	0.0480	M244C	0.3750	-0.0599
M220C	0.1750	0.0522	M245C	0.4750	-0.0574
M221C	0.2250	0.0557	M127W, M278C, M327E	0.5750	-0.0482
M112W, M239C, M312E	0.3000	0.0588	M279C	0.6500	-0.0364
M240C	0.3750	0.0600	M280C	0.7000	-0.0272
M241C	0.4500	0.0595	M281C	0.6750	0.0000
M125W, M273C, M325E	0.5500	0.0563	M282C	0.7000	0.0270
M274C	0.6500	0.0502	M284C	0.8250	0.0228
M275C	0.7500	0.0405	M285C	0.8750	0.0175
M126W, M276C, M326E	0.8250	0.0301			
M277C	0.9000	0.0160			

Note: Last letter of Tap Identifier equals E for taps near east wall, C for centerline taps, and W for taps near west wall.

Table 7. Pressure Tap Locations of Vane Element of EET High-Lift Airfoil

Upper Surface			Lower Surface		
Tap Identifier	x/c	y/c	Tap Identifier	x/c	y/c
V273C	0.7000	-0.0190	V287C	0.7020	-0.0239
V132W, V274C, V332E	0.7050	-0.0070	V135W, V286C, V335E	0.7100	-0.0253
V275C	0.7150	0.0021	V285C	0.7400	-0.0196
V276C	0.7400	0.0131	V136W, V284C, V336E	0.7900	-0.0106
V133W, V277C, V333E	0.7700	0.0184	V283C	0.8500	-0.0028
V278C	0.8100	0.0199	V282C	0.8800	-0.0012
V134W, V279C, V334E	0.8600	0.0181	V281C	0.8900	0.0112
V280C	0.9000	0.0149			

Note: Last letter of Tap Identifier equals E for taps near east wall, C for centerline taps, and W for taps near west wall.

Table 8. Pressure Tap Locations of Flap Element of EET High-Lift Airfoil

Upper Surface			Lower Surface		
Tap ID	x/c	y/c	Tap ID	x/c	y/c
F288C	0.8800	0.0030	F139W, F294C, F339E	0.8840	-0.0010
F289C	0.8850	0.0093	F295C	0.9100	-0.0013
F137W, F290C, F337E	0.8950	0.0122	F296C	0.9500	-0.0051
F291C	0.9100	0.0128			
F138W, F292C, F338E	0.9350	0.0081			
F293C	0.9700	-0.0009			
F140W, F297C, F340E	1.0000	-0.0133			

Note: Last letter of Tap Identifier equals E for taps near east wall, C for centerline taps, and W for taps near west wall.

Table 9. Lofting Data for EET High-Lift Airfoil

Element	δ_x , deg	Gap/c	Overlap/c	Δ_x , deg	x_{pivot}/c	y_{pivot}/c	x_{nose}/c	y_{nose}/c
Slat (x=s)	-30	0.020	0.020	-12.1128	-0.10628	-0.06291	0.00	0.000
	-40	0.020	0.020	-22.1128	-0.09481	-0.09188	0.00	0.000
	-50	0.020	0.020	-32.1128	-0.07856	-0.11766	0.00	0.000
	-60	0.020	0.020	-42.1128	-0.05822	-0.13956	0.00	0.000
Vane (x=v)	7.5	0.015	0.045	13.8751	0.85693	-0.02183	0.70	-0.019
	15.0	0.015	0.040	21.3751	0.86174	-0.01618	0.70	-0.019
	22.5	0.020	0.030	28.8751	0.87236	-0.01678	0.70	-0.019
	30.0	0.020	0.030	36.3751	0.87260	-0.01335	0.70	-0.019
Flap (x=f)	7.5	0.010	0.010	4.9461	1.06156	-0.06097	0.88	0.003
	15.0	0.010	0.010	19.9461	1.06013	-0.07985	0.88	0.003
	22.5	0.010	0.010	34.9461	1.06136	-0.10437	0.88	0.003
	30.0	0.010	0.005	49.9461	1.05376	-0.12583	0.88	0.003
Longest Chord Data								
Element	x_{le}/c	y_{le}/c	x_{te}/c	y_{te}/c	ϕ_x , deg	c_{lg}/c		
Slat (x=s)	0.0010	-0.0065	0.1550	0.05025	20.2292	0.16412		
Main (x=m)	0.0380	-0.0198	0.9000	0.01546	2.3420	0.86272		
Vane (x=v)	0.7001	-0.0205	0.9150	0.01245	8.7171	0.21741		
Flap (x=f)	0.8800	0.0030	1.0000	-0.01325	-7.7119	0.12110		

<u>Lofting Equations</u>		(c = 21.654 in.)
$x_{loft} = x_{pivot} + (x_{input} - x_{nose}) \cos \Delta_x + (y_{input} - y_{nose}) \sin \Delta_x$		
$y_{loft} = y_{pivot} + (y_{input} - y_{nose}) \cos \Delta_x - (x_{input} - x_{nose}) \sin \Delta_x$		

$\Delta_s = \delta_s - \phi_m + \phi_s$	Subscripts: s = slat; m = main; v = vane; f = flap; le = leading edge; te = trailing edge; lg = longest chord	
$\Delta_v = \delta_v - \phi_m + \phi_v$		
$\Delta_f = \delta_f + \delta_v - \phi_m + \phi_f$		

Table 10. Lofted Slat Coordinates of EET High-Lift Airfoil

$\delta_s = -30^\circ$		$\delta_s = -40^\circ$		$\delta_s = -50^\circ$		$\delta_s = -60^\circ$	
x/c	y/c	x/c	y/c	x/c	y/c	x/c	y/c
0.03465	0.01909	0.02974	0.01334	0.02583	0.00759	0.02283	0.00192
0.02987	0.01755	0.02530	0.01100	0.02186	0.00451	0.01946	-0.00181
0.02030	0.01447	0.01641	0.00631	0.01392	-0.00165	0.01271	-0.00925
0.01075	0.01130	0.00756	0.00153	0.00603	-0.00790	0.00603	-0.01678
0.00121	0.00813	-0.00129	-0.00326	-0.00185	-0.01415	-0.00065	-0.02430
-0.00832	0.00485	-0.01010	-0.00813	-0.00968	-0.02048	-0.00727	-0.03189
-0.01780	0.00139	-0.01884	-0.01320	-0.01741	-0.02698	-0.01374	-0.03964
-0.02726	-0.00218	-0.02754	-0.01835	-0.02508	-0.03357	-0.02016	-0.04746
-0.03671	-0.00584	-0.03620	-0.02360	-0.03270	-0.04024	-0.02650	-0.05535
-0.04611	-0.00970	-0.04479	-0.02903	-0.04021	-0.04708	-0.03271	-0.06339
-0.05546	-0.01375	-0.05330	-0.03465	-0.04762	-0.05409	-0.03879	-0.07158
-0.06478	-0.01800	-0.06174	-0.04045	-0.05492	-0.06127	-0.04473	-0.07992
-0.06940	-0.02032	-0.06588	-0.04353	-0.05847	-0.06503	-0.04757	-0.08424
-0.07399	-0.02274	-0.06999	-0.04671	-0.06196	-0.06887	-0.05034	-0.08863
-0.07856	-0.02526	-0.07405	-0.04999	-0.06539	-0.07280	-0.05304	-0.09309
-0.08310	-0.02797	-0.07805	-0.05344	-0.06873	-0.07690	-0.05561	-0.09771
-0.08759	-0.03087	-0.08196	-0.05708	-0.07195	-0.08116	-0.05805	-0.10247
-0.09199	-0.03417	-0.08573	-0.06110	-0.07496	-0.08577	-0.06022	-0.10753
-0.09631	-0.03786	-0.08935	-0.06548	-0.07776	-0.09071	-0.06211	-0.11288
-0.10049	-0.04223	-0.09270	-0.07051	-0.08019	-0.09625	-0.06354	-0.11876
-0.10247	-0.04491	-0.09419	-0.07349	-0.08114	-0.09944	-0.06392	-0.12207
-0.10435	-0.04807	-0.09549	-0.07693	-0.08182	-0.10306	-0.06397	-0.12575
-0.10535	-0.05054	-0.09605	-0.07954	-0.08192	-0.10572	-0.06360	-0.12839
-0.10596	-0.05251	-0.09630	-0.08158	-0.08181	-0.10778	-0.06314	-0.13039
-0.10667	-0.05634	-0.09633	-0.08548	-0.08117	-0.11162	-0.06184	-0.13407
-0.10674	-0.05697	-0.09629	-0.08611	-0.08102	-0.11224	-0.06158	-0.13465
-0.10678	-0.05821	-0.09612	-0.08734	-0.08063	-0.11341	-0.06100	-0.13574
-0.10628	-0.06291	-0.09481	-0.09188	-0.07856	-0.11766	-0.05822	-0.13956
-0.10480	-0.06740	-0.09258	-0.09605	-0.07564	-0.12138	-0.05470	-0.14271
-0.10426	-0.06851	-0.09185	-0.09704	-0.07475	-0.12223	-0.05367	-0.14340
-0.10394	-0.06906	-0.09144	-0.09753	-0.07426	-0.12263	-0.05312	-0.14371
-0.10172	-0.07226	-0.08869	-0.10030	-0.07107	-0.12489	-0.04959	-0.14538
-0.10036	-0.07381	-0.08709	-0.10159	-0.06927	-0.12588	-0.04764	-0.14604
-0.09845	-0.07555	-0.08491	-0.10297	-0.06688	-0.12686	-0.04512	-0.14659
-0.09544	-0.07766	-0.08158	-0.10453	-0.06333	-0.12782	-0.04146	-0.14692
-0.09254	-0.07929	-0.07843	-0.10563	-0.06004	-0.12835	-0.03813	-0.14687
-0.08693	-0.08157	-0.07252	-0.10689	-0.05400	-0.12857	-0.03214	-0.14604
-0.08150	-0.08306	-0.06691	-0.10742	-0.04838	-0.12812	-0.02669	-0.14462
-0.07617	-0.08406	-0.06149	-0.10748	-0.04303	-0.12724	-0.02157	-0.14282
-0.07088	-0.08487	-0.05614	-0.10736	-0.03779	-0.12619	-0.01659	-0.14088
-0.06564	-0.08548	-0.05087	-0.10705	-0.03265	-0.12497	-0.01174	-0.13879
-0.06043	-0.08590	-0.04567	-0.10656	-0.02762	-0.12359	-0.00702	-0.13655
-0.05527	-0.08612	-0.04055	-0.10588	-0.02269	-0.12203	-0.00244	-0.13416
-0.05351	-0.08626	-0.03878	-0.10571	-0.02098	-0.12155	-0.00084	-0.13339
-0.05217	-0.08628	-0.03747	-0.10550	-0.01972	-0.12111	0.00032	-0.13274
-0.05226	-0.08589	-0.03762	-0.10513	-0.01994	-0.12077	0.00005	-0.13245
-0.05546	-0.08524	-0.04089	-0.10505	-0.02317	-0.12127	-0.00304	-0.13349
-0.05714	-0.08458	-0.04265	-0.10469	-0.02497	-0.12122	-0.00483	-0.13376
-0.05886	-0.08372	-0.04449	-0.10414	-0.02688	-0.12100	-0.00674	-0.13387
-0.06007	-0.08286	-0.04583	-0.10350	-0.02831	-0.12060	-0.00822	-0.13373

Table 10. Concluded

$\delta_s = -30^\circ$		$\delta_s = -40^\circ$		$\delta_s = -50^\circ$		$\delta_s = -60^\circ$	
x/c	y/c	x/c	y/c	x/c	y/c	x/c	y/c
-0.06136	-0.08160	-0.04733	-0.10249	-0.02995	-0.11986	-0.00997	-0.13328
-0.06204	-0.08082	-0.04813	-0.10184	-0.03086	-0.11936	-0.01095	-0.13295
-0.06278	-0.07976	-0.04904	-0.10092	-0.03192	-0.11861	-0.01212	-0.13240
-0.06360	-0.07830	-0.05011	-0.09962	-0.03319	-0.11752	-0.01357	-0.13155
-0.06401	-0.07736	-0.05067	-0.09877	-0.03389	-0.11678	-0.01438	-0.13094
-0.06450	-0.07603	-0.05138	-0.09755	-0.03481	-0.11570	-0.01547	-0.13003
-0.06497	-0.07430	-0.05215	-0.09592	-0.03585	-0.11423	-0.01675	-0.12877
-0.06538	-0.07050	-0.05321	-0.09225	-0.03753	-0.11080	-0.01900	-0.12568
-0.06536	-0.06773	-0.05367	-0.08952	-0.03846	-0.10819	-0.02037	-0.12327
-0.06499	-0.06468	-0.05384	-0.08646	-0.03915	-0.10521	-0.02157	-0.12045
-0.06490	-0.06415	-0.05384	-0.08592	-0.03925	-0.10468	-0.02176	-0.11995
-0.06396	-0.05996	-0.05364	-0.08163	-0.03980	-0.10042	-0.02304	-0.11585
-0.06276	-0.05602	-0.05314	-0.07754	-0.04002	-0.09630	-0.02397	-0.11183
-0.06068	-0.05139	-0.05191	-0.07261	-0.03965	-0.09124	-0.02449	-0.10678
-0.05851	-0.04724	-0.05048	-0.06815	-0.03903	-0.08659	-0.02468	-0.10210
-0.05469	-0.04120	-0.04777	-0.06154	-0.03750	-0.07961	-0.02439	-0.09496
-0.05072	-0.03585	-0.04479	-0.05558	-0.03561	-0.07323	-0.02364	-0.08835
-0.04661	-0.03118	-0.04156	-0.05027	-0.03334	-0.06744	-0.02241	-0.08225
-0.04241	-0.02691	-0.03817	-0.04533	-0.03086	-0.06198	-0.02091	-0.07645
-0.03817	-0.02283	-0.03470	-0.04058	-0.02827	-0.05670	-0.01928	-0.07079
-0.03385	-0.01914	-0.03108	-0.03620	-0.02547	-0.05176	-0.01738	-0.06544
-0.02506	-0.01244	-0.02359	-0.02808	-0.01950	-0.04246	-0.01312	-0.05525
-0.01614	-0.00634	-0.01587	-0.02051	-0.01321	-0.03367	-0.00845	-0.04550
-0.00708	-0.00091	-0.00788	-0.01360	-0.00655	-0.02547	-0.00331	-0.03627
0.00211	0.00392	0.00033	-0.00724	0.00043	-0.01779	0.00223	-0.02749
0.01136	0.00846	0.00865	-0.00116	0.00758	-0.01035	0.00797	-0.01893
0.02070	0.01262	0.01712	0.00455	0.01493	-0.00326	0.01398	-0.01066
0.03010	0.01647	0.02571	0.00998	0.02244	0.00358	0.02019	-0.00262
0.03480	0.01840	0.03000	0.01270	0.02620	0.00700	0.02330	0.00140

Table 11. Lofted Vane Coordinates of EET High-Lift Airfoil

$\delta_v = 7.5^\circ$		$\delta_v = 15^\circ$		$\delta_v = 22.5^\circ$		$\delta_v = 30^\circ$	
x/c	y/c	x/c	y/c	x/c	y/c	x/c	y/c
1.07326	-0.04261	1.07350	-0.06502	1.07594	-0.09285	1.06451	-0.11534
1.06864	-0.04044	1.06921	-0.06227	1.07204	-0.08955	1.06108	-0.11157
1.06396	-0.03856	1.06481	-0.05979	1.06800	-0.08653	1.05746	-0.10804
1.05922	-0.03688	1.06034	-0.05751	1.06387	-0.08368	1.05374	-0.10467
1.04976	-0.03351	1.05139	-0.05293	1.05559	-0.07797	1.04628	-0.09793
1.04026	-0.03024	1.04241	-0.04845	1.04727	-0.07235	1.03876	-0.09128
1.03072	-0.02716	1.03335	-0.04415	1.03885	-0.06691	1.03112	-0.08478
1.02116	-0.02418	1.02426	-0.03995	1.03038	-0.06156	1.02343	-0.07837
1.01164	-0.02101	1.01524	-0.03556	1.02201	-0.05603	1.01585	-0.07180
1.00201	-0.01832	1.00603	-0.03163	1.01340	-0.05094	1.00798	-0.06562
0.99239	-0.01553	0.99687	-0.02762	1.00484	-0.04576	1.00016	-0.05937
0.98273	-0.01294	0.98763	-0.02379	0.99618	-0.04075	0.99223	-0.05328
0.97305	-0.01044	0.97835	-0.02005	0.98747	-0.03584	0.98424	-0.04727
0.96332	-0.00814	0.96900	-0.01650	0.97866	-0.03109	0.97613	-0.04142
0.95356	-0.00594	0.95962	-0.01304	0.96981	-0.02644	0.96796	-0.03565
0.94373	-0.00403	0.95012	-0.00986	0.96081	-0.02205	0.95961	-0.03012
0.93386	-0.00231	0.94056	-0.00687	0.95172	-0.01783	0.95114	-0.02475
0.92386	-0.00107	0.93081	-0.00434	0.94238	-0.01405	0.94238	-0.01979
0.91374	-0.00033	0.92088	-0.00228	0.93280	-0.01071	0.93332	-0.01523
0.90346	-0.00026	0.91069	-0.00087	0.92289	-0.00799	0.92384	-0.01123
0.89827	-0.00042	0.90552	-0.00035	0.91783	-0.00680	0.91899	-0.00939
0.89296	-0.00106	0.90017	-0.00030	0.91254	-0.00605	0.91383	-0.00795
0.88760	-0.00190	0.89475	-0.00043	0.90715	-0.00547	0.90856	-0.00668
0.88215	-0.00313	0.88918	-0.00093	0.90156	-0.00525	0.90306	-0.00573
0.87655	-0.00494	0.88340	-0.00200	0.89568	-0.00555	0.89719	-0.00526
0.87079	-0.00743	0.87736	-0.00371	0.88947	-0.00646	0.89091	-0.00535
0.86839	-0.00880	0.87480	-0.00476	0.88680	-0.00716	0.88817	-0.00570
0.86716	-0.00963	0.87347	-0.00541	0.88540	-0.00764	0.88672	-0.00599
0.86592	-0.01045	0.87214	-0.00607	0.88399	-0.00812	0.88526	-0.00628
0.86466	-0.01138	0.87077	-0.00683	0.88253	-0.00869	0.88374	-0.00665
0.86336	-0.01250	0.86933	-0.00777	0.88098	-0.00943	0.88211	-0.00719
0.86202	-0.01371	0.86785	-0.00880	0.87938	-0.01026	0.88041	-0.00780
0.86062	-0.01522	0.86626	-0.01011	0.87764	-0.01135	0.87854	-0.00866
0.85915	-0.01702	0.86457	-0.01170	0.87575	-0.01271	0.87649	-0.00976
0.85830	-0.01836	0.86355	-0.01292	0.87458	-0.01378	0.87520	-0.01067
0.85748	-0.02001	0.86253	-0.01445	0.87337	-0.01516	0.87381	-0.01188
0.85693	-0.02183	0.86174	-0.01618	0.87236	-0.01678	0.87260	-0.01335
0.85667	-0.02331	0.86129	-0.01761	0.87172	-0.01814	0.87179	-0.01462
0.85674	-0.02467	0.86119	-0.01897	0.87145	-0.01947	0.87134	-0.01590
0.85699	-0.02576	0.86129	-0.02008	0.87140	-0.02059	0.87115	-0.01700
0.85770	-0.02707	0.86182	-0.02147	0.87175	-0.02204	0.87130	-0.01848
0.85848	-0.02808	0.86246	-0.02258	0.87223	-0.02322	0.87164	-0.01972
0.85933	-0.02881	0.86321	-0.02341	0.87287	-0.02414	0.87214	-0.02071
0.86023	-0.02934	0.86403	-0.02406	0.87360	-0.02489	0.87277	-0.02155
0.86115	-0.02977	0.86489	-0.02461	0.87438	-0.02554	0.87346	-0.02230
0.86210	-0.03011	0.86578	-0.02506	0.87521	-0.02611	0.87420	-0.02298
0.86309	-0.03025	0.86675	-0.02533	0.87613	-0.02651	0.87507	-0.02349
0.86513	-0.03034	0.86876	-0.02569	0.87807	-0.02713	0.87692	-0.02435
0.87020	-0.03067	0.87374	-0.02668	0.88289	-0.02875	0.88147	-0.02659
0.87529	-0.03090	0.87876	-0.02757	0.88775	-0.03029	0.88609	-0.02875

Table 11. Concluded

$\delta_v = 7.5^\circ$		$\delta_v = 15^\circ$		$\delta_v = 22.5^\circ$		$\delta_v = 30^\circ$	
x/c	y/c	x/c	y/c	x/c	y/c	x/c	y/c
0.88036	-0.03122	0.88374	-0.02855	0.89256	-0.03192	0.89065	-0.03099
0.88546	-0.03145	0.88877	-0.02944	0.89742	-0.03346	0.89527	-0.03315
0.89055	-0.03168	0.89379	-0.03033	0.90228	-0.03500	0.89989	-0.03532
0.89562	-0.03200	0.89877	-0.03132	0.90710	-0.03662	0.90445	-0.03756
0.90578	-0.03256	0.90877	-0.03319	0.91677	-0.03979	0.91363	-0.04196
0.91595	-0.03311	0.91878	-0.03507	0.92645	-0.04295	0.92281	-0.04636
0.92609	-0.03376	0.92875	-0.03704	0.93607	-0.04620	0.93193	-0.05084
0.93623	-0.03441	0.93872	-0.03901	0.94570	-0.04946	0.94104	-0.05532
0.94632	-0.03526	0.94861	-0.04116	0.95523	-0.05289	0.95005	-0.05996
0.95641	-0.03610	0.95851	-0.04332	0.96476	-0.05631	0.95905	-0.06461
0.96645	-0.03714	0.96833	-0.04566	0.97419	-0.05992	0.96793	-0.06941
0.97650	-0.03818	0.97815	-0.04800	0.98362	-0.06352	0.97681	-0.07421
0.98652	-0.03932	0.98794	-0.05043	0.99301	-0.06721	0.98563	-0.07910
0.99649	-0.04065	0.99765	-0.05305	1.00229	-0.07108	0.99434	-0.08414
1.00644	-0.04207	1.00733	-0.05577	1.01153	-0.07503	1.00298	-0.08927
1.01631	-0.04379	1.01689	-0.05876	1.02063	-0.07925	1.01145	-0.09463
1.02614	-0.04570	1.02639	-0.06194	1.02963	-0.08364	1.01980	-0.10016
1.03595	-0.04771	1.03585	-0.06521	1.03858	-0.08812	1.02808	-0.10577
1.03888	-0.04834	1.03868	-0.06621	1.04125	-0.08948	1.03056	-0.10747
1.03895	-0.04805	1.03879	-0.06593	1.04140	-0.08921	1.03074	-0.10723
1.03808	-0.04742	1.03800	-0.06519	1.04071	-0.08838	1.03017	-0.10631
1.03725	-0.04660	1.03729	-0.06427	1.04013	-0.08737	1.02972	-0.10524
1.03689	-0.04599	1.03700	-0.06362	1.03993	-0.08669	1.02961	-0.10454
1.03676	-0.04524	1.03698	-0.06286	1.04001	-0.08594	1.02979	-0.10380
1.03679	-0.04473	1.03707	-0.06236	1.04016	-0.08545	1.03000	-0.10333
1.03695	-0.04364	1.03738	-0.06130	1.04061	-0.08444	1.03057	-0.10239
1.03719	-0.04308	1.03769	-0.06078	1.04098	-0.08396	1.03101	-0.10197
1.03741	-0.04262	1.03796	-0.06035	1.04131	-0.08357	1.03139	-0.10162
1.03789	-0.04191	1.03854	-0.05971	1.04196	-0.08302	1.03210	-0.10116
1.03860	-0.04116	1.03933	-0.05906	1.04283	-0.08247	1.03304	-0.10073
1.03985	-0.04023	1.04070	-0.05830	1.04429	-0.08190	1.03456	-0.10035
1.04104	-0.03960	1.04196	-0.05783	1.04560	-0.08160	1.03590	-0.10022
1.04220	-0.03906	1.04318	-0.05745	1.04686	-0.08138	1.03718	-0.10017
1.04332	-0.03872	1.04433	-0.05725	1.04803	-0.08134	1.03834	-0.10028
1.04548	-0.03833	1.04652	-0.05714	1.05021	-0.08151	1.04048	-0.10074
1.04863	-0.03807	1.04968	-0.05731	1.05332	-0.08209	1.04349	-0.10172
1.05372	-0.03830	1.05470	-0.05820	1.05818	-0.08362	1.04811	-0.10388
1.05870	-0.03902	1.05954	-0.05955	1.06280	-0.08560	1.05243	-0.10644
1.06362	-0.03992	1.06430	-0.06110	1.06733	-0.08775	1.05663	-0.10916
1.06843	-0.04132	1.06889	-0.06311	1.07161	-0.09034	1.06054	-0.11229
1.07314	-0.04310	1.07332	-0.06549	1.07570	-0.09328	1.06421	-0.11574

Table 12. Lofted Flap Coordinates of EET High-Lift Airfoil

$\delta_f = 7.5^\circ$		$\delta_f = 15^\circ$		$\delta_f = 22.5^\circ$		$\delta_f = 30^\circ$	
x/c	y/c	x/c	y/c	x/c	y/c	x/c	y/c
1.17998	-0.08437	1.16846	-0.13310	1.16846	-0.13310	1.12095	-0.22611
1.17031	-0.08022	1.16019	-0.12659	1.16019	-0.12659	1.11704	-0.21633
1.16061	-0.07627	1.15185	-0.12026	1.15185	-0.12026	1.11298	-0.20669
1.15089	-0.07262	1.14340	-0.11422	1.14340	-0.11422	1.10869	-0.19723
1.14116	-0.06906	1.13492	-0.10827	1.13492	-0.10827	1.10432	-0.18784
1.13142	-0.06561	1.12641	-0.10241	1.12641	-0.10241	1.09988	-0.17851
1.12655	-0.06388	1.12215	-0.09949	1.12215	-0.09949	1.09765	-0.17385
1.12167	-0.06226	1.11786	-0.09665	1.11786	-0.09665	1.09536	-0.16925
1.11679	-0.06063	1.11357	-0.09382	1.11357	-0.09382	1.09306	-0.16465
1.11192	-0.05900	1.10928	-0.09098	1.10928	-0.09098	1.09076	-0.16005
1.10704	-0.05738	1.10499	-0.08815	1.10499	-0.08815	1.08846	-0.15545
1.10214	-0.05605	1.10060	-0.08560	1.10060	-0.08560	1.08593	-0.15104
1.09722	-0.05482	1.09617	-0.08314	1.09617	-0.08314	1.08332	-0.14670
1.09229	-0.05379	1.09167	-0.08087	1.09167	-0.08087	1.08057	-0.14249
1.08733	-0.05316	1.08704	-0.07898	1.08704	-0.07898	1.07750	-0.13853
1.08232	-0.05303	1.08224	-0.07755	1.08224	-0.07755	1.07405	-0.13490
1.07730	-0.05310	1.07737	-0.07632	1.07737	-0.07632	1.07045	-0.13139
1.07223	-0.05366	1.07233	-0.07555	1.07233	-0.07555	1.06647	-0.12821
1.06915	-0.05440	1.06917	-0.07547	1.06917	-0.07547	1.06378	-0.12655
1.06708	-0.05512	1.06698	-0.07563	1.06698	-0.07563	1.06180	-0.12560
1.06604	-0.05564	1.06583	-0.07586	1.06583	-0.07586	1.06070	-0.12522
1.06497	-0.05635	1.06462	-0.07627	1.06462	-0.07627	1.05944	-0.12497
1.06390	-0.05716	1.06337	-0.07677	1.06337	-0.07677	1.05811	-0.12479
1.06280	-0.05827	1.06203	-0.07756	1.06203	-0.07756	1.05655	-0.12479
1.06222	-0.05912	1.06125	-0.07823	1.06125	-0.07823	1.05554	-0.12499
1.06185	-0.05989	1.06069	-0.07888	1.06069	-0.07888	1.05473	-0.12528
1.06171	-0.06038	1.06043	-0.07932	1.06043	-0.07932	1.05428	-0.12552
1.06156	-0.06097	1.06013	-0.07985	1.06013	-0.07985	1.05376	-0.12583
1.06156	-0.06207	1.05985	-0.08092	1.05985	-0.08092	1.05298	-0.12661
1.06162	-0.06258	1.05977	-0.08142	1.05977	-0.08142	1.05266	-0.12701
1.06186	-0.06330	1.05982	-0.08218	1.05982	-0.08218	1.05232	-0.12769
1.06231	-0.06385	1.06011	-0.08282	1.06011	-0.08282	1.05226	-0.12840
1.06326	-0.06453	1.06085	-0.08373	1.06085	-0.08373	1.05244	-0.12955
1.06422	-0.06501	1.06165	-0.08445	1.06165	-0.08445	1.05278	-0.13057
1.06520	-0.06530	1.06253	-0.08497	1.06253	-0.08497	1.05327	-0.13147
1.06620	-0.06539	1.06347	-0.08532	1.06347	-0.08532	1.05392	-0.13223
1.06819	-0.06556	1.06535	-0.08600	1.06535	-0.08600	1.05520	-0.13376
1.07119	-0.06572	1.06820	-0.08693	1.06820	-0.08693	1.05721	-0.13599
1.07617	-0.06615	1.07290	-0.08863	1.07290	-0.08863	1.06043	-0.13982
1.08114	-0.06668	1.07757	-0.09043	1.07757	-0.09043	1.06357	-0.14371
1.08611	-0.06721	1.08223	-0.09223	1.08223	-0.09223	1.06671	-0.14760
1.09108	-0.06784	1.08686	-0.09413	1.08686	-0.09413	1.06977	-0.15156
1.09604	-0.06847	1.09150	-0.09602	1.09150	-0.09602	1.07284	-0.15552
1.10100	-0.06920	1.09609	-0.09801	1.09609	-0.09801	1.07583	-0.15954
1.10594	-0.07003	1.10066	-0.10009	1.10066	-0.10009	1.07874	-0.16362
1.11089	-0.07086	1.10522	-0.10217	1.10522	-0.10217	1.08165	-0.16771
1.11583	-0.07179	1.10975	-0.10435	1.10975	-0.10435	1.08448	-0.17185

Table 12. Concluded

$\delta_f = 7.5^\circ$		$\delta_f = 15^\circ$		$\delta_f = 22.5^\circ$		$\delta_f = 30^\circ$	
x/c	y/c	x/c	y/c	x/c	y/c	x/c	y/c
1.12076	-0.07282	1.11425	-0.10662	1.11425	-0.10662	1.08724	-0.17607
1.12569	-0.07385	1.11874	-0.10889	1.11874	-0.10889	1.09000	-0.18028
1.13060	-0.07508	1.12317	-0.11134	1.12317	-0.11134	1.09261	-0.18462
1.14043	-0.07753	1.13202	-0.11626	1.13202	-0.11626	1.09782	-0.19331
1.15022	-0.08039	1.14074	-0.12155	1.14074	-0.12155	1.10272	-0.20225
1.15998	-0.08354	1.14936	-0.12712	1.14936	-0.12712	1.10739	-0.21138
1.16973	-0.08689	1.15790	-0.13289	1.15790	-0.13289	1.11192	-0.22065
1.17944	-0.09064	1.16631	-0.13902	1.16631	-0.13902	1.11613	-0.23017



L-78-1654

Figure 1. EET High-Lift Wing Model mounted in Langley 14- by 22-Foot Subsonic Tunnel.

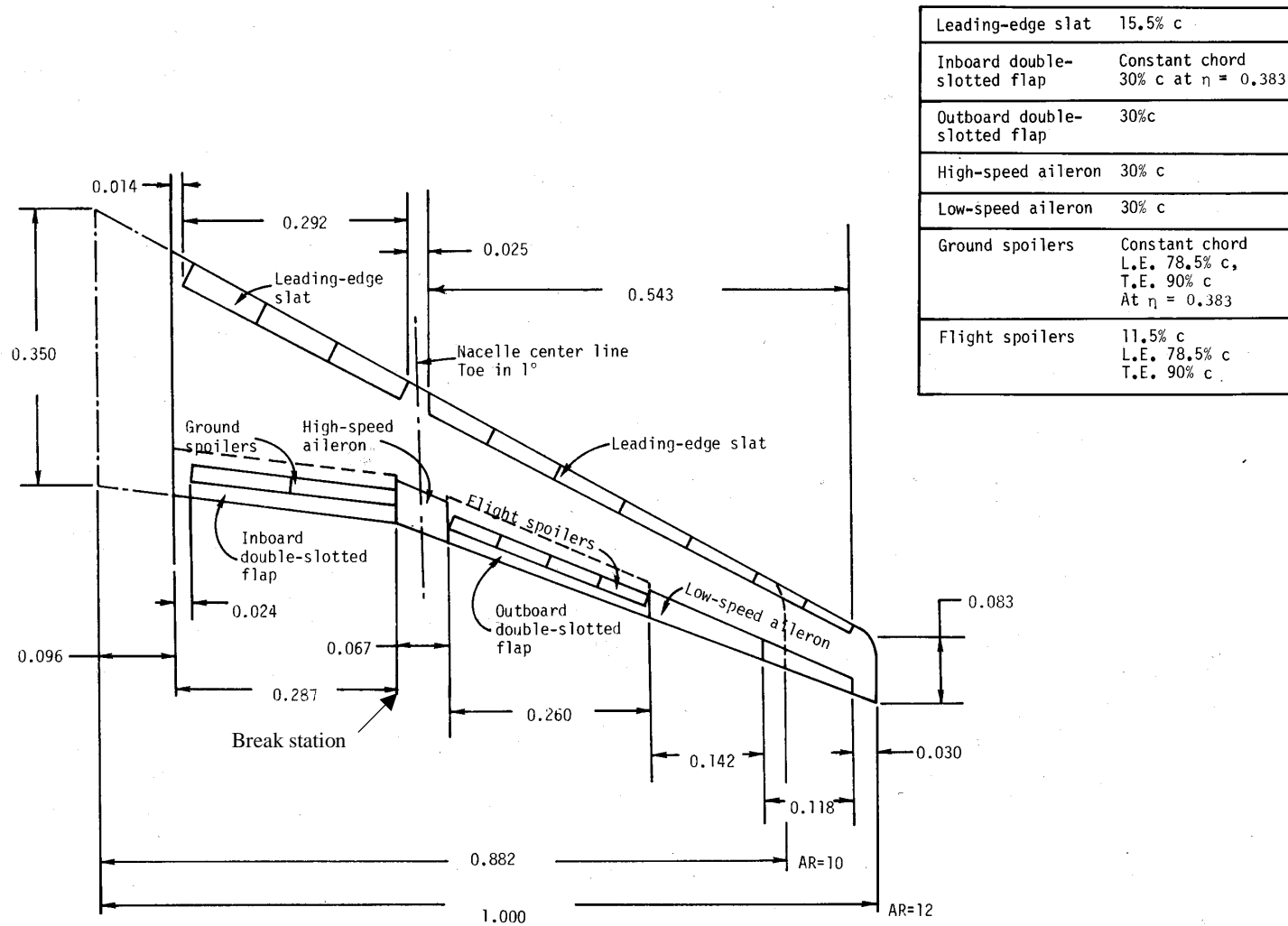


Figure 2. Planform details of EET High-Lift Wing Model.

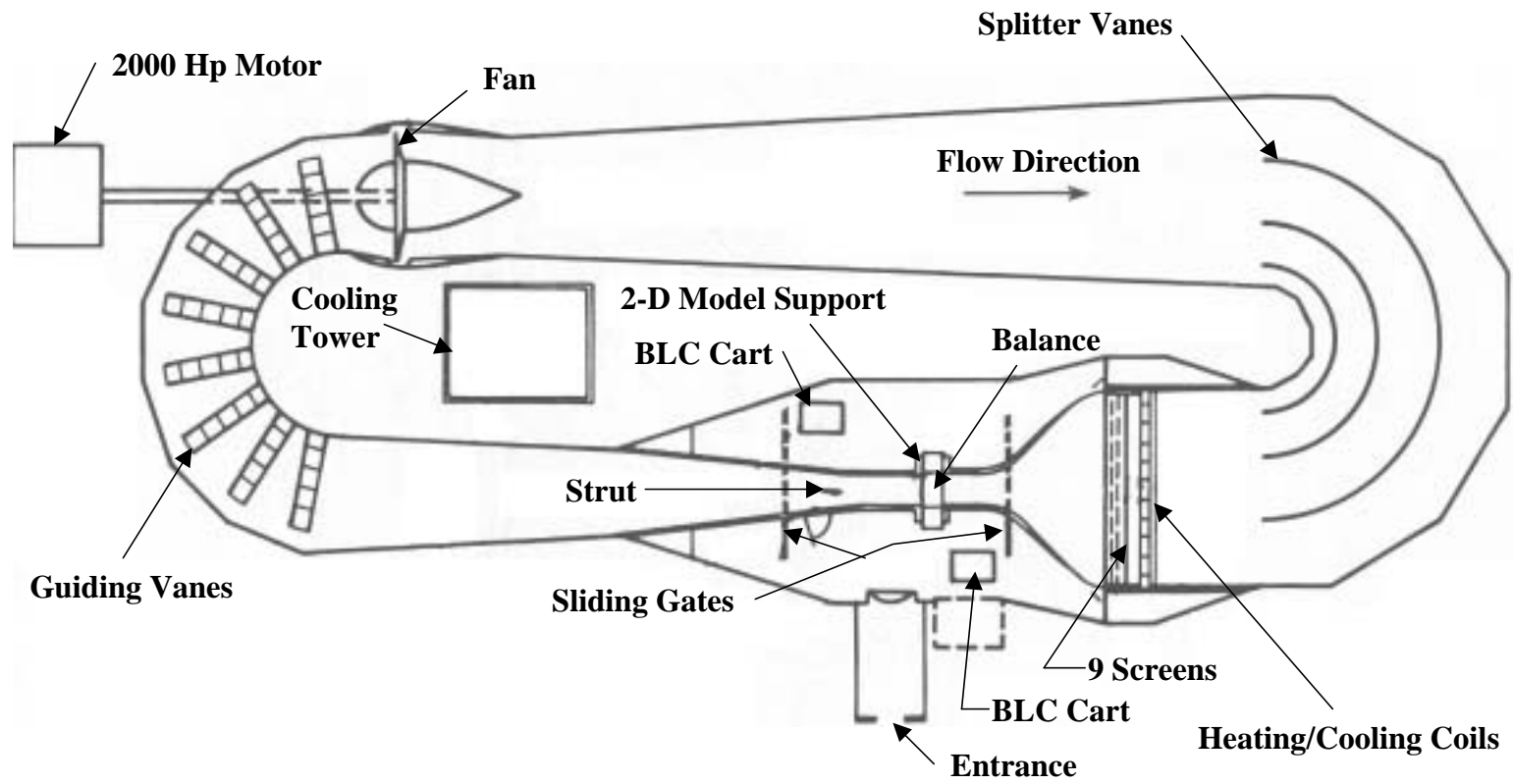


Figure 3. Schematic of Langley Low-Turbulence Pressure Tunnel.

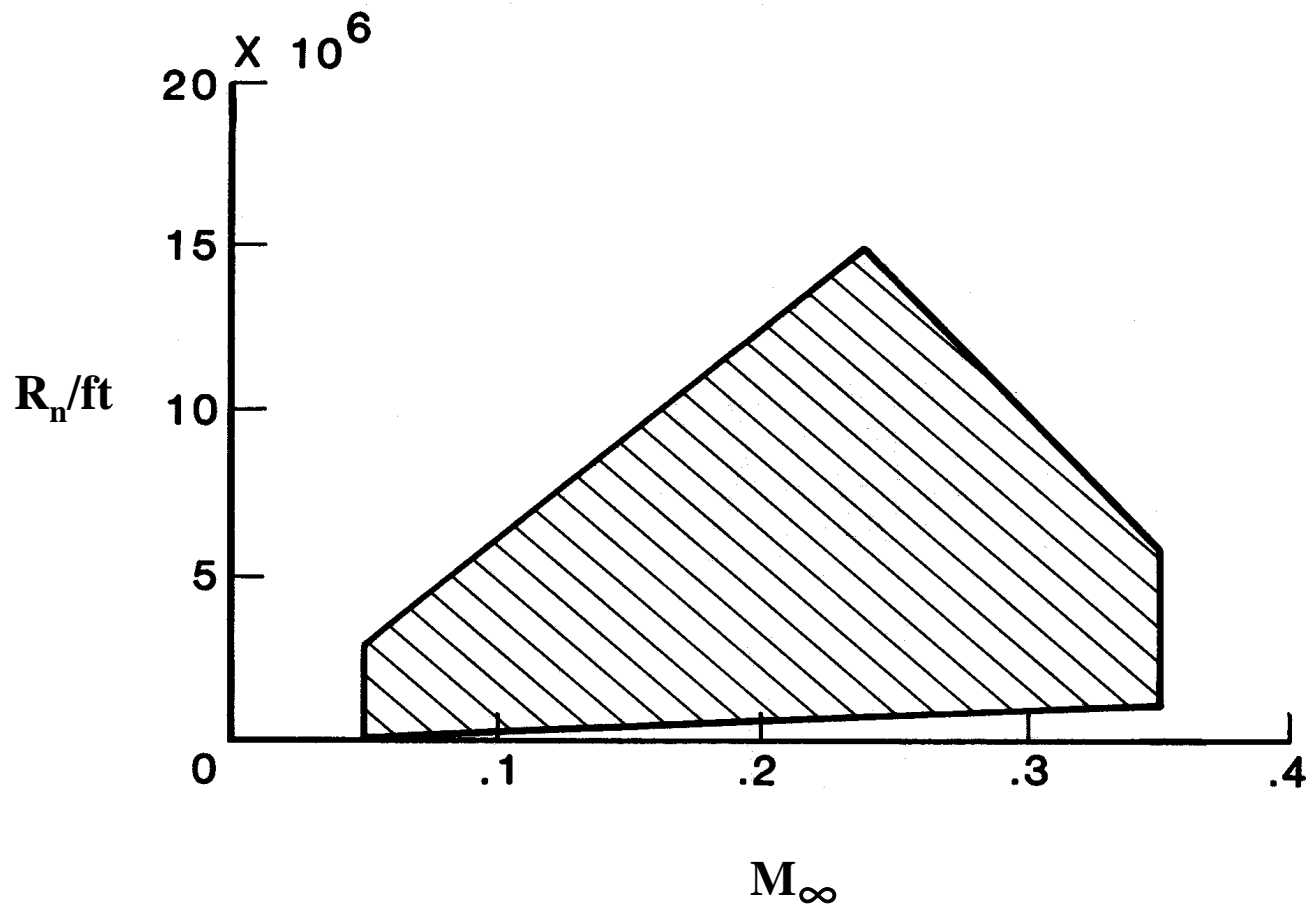


Figure 4. Reynolds number capability of Langley Low-Turbulence Pressure Tunnel.

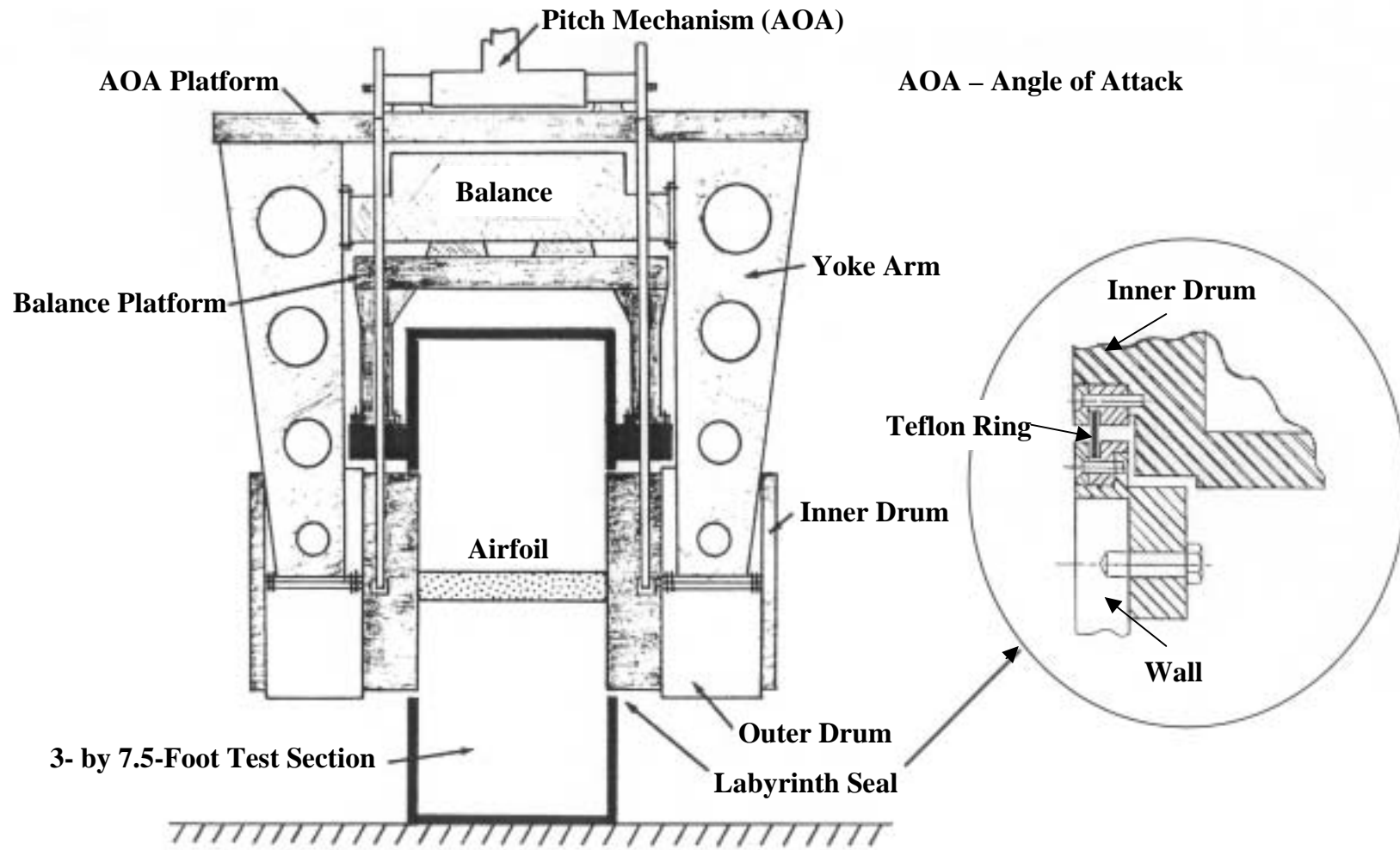


Figure 5. Model-support and force-balance systems for Langley Low-Turbulence Pressure Tunnel.

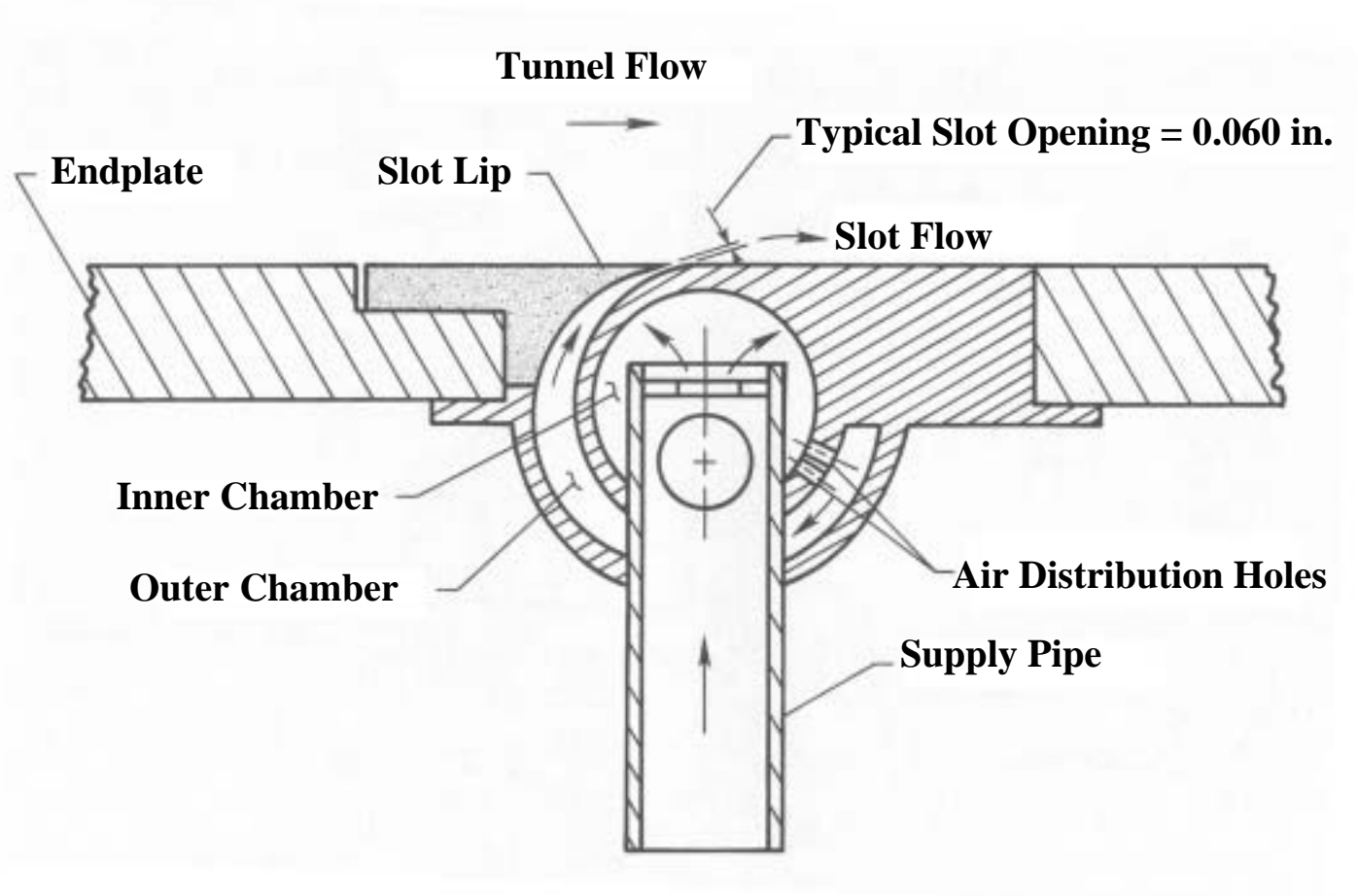


Figure 6. Sketch of cross section of typical blowing box.

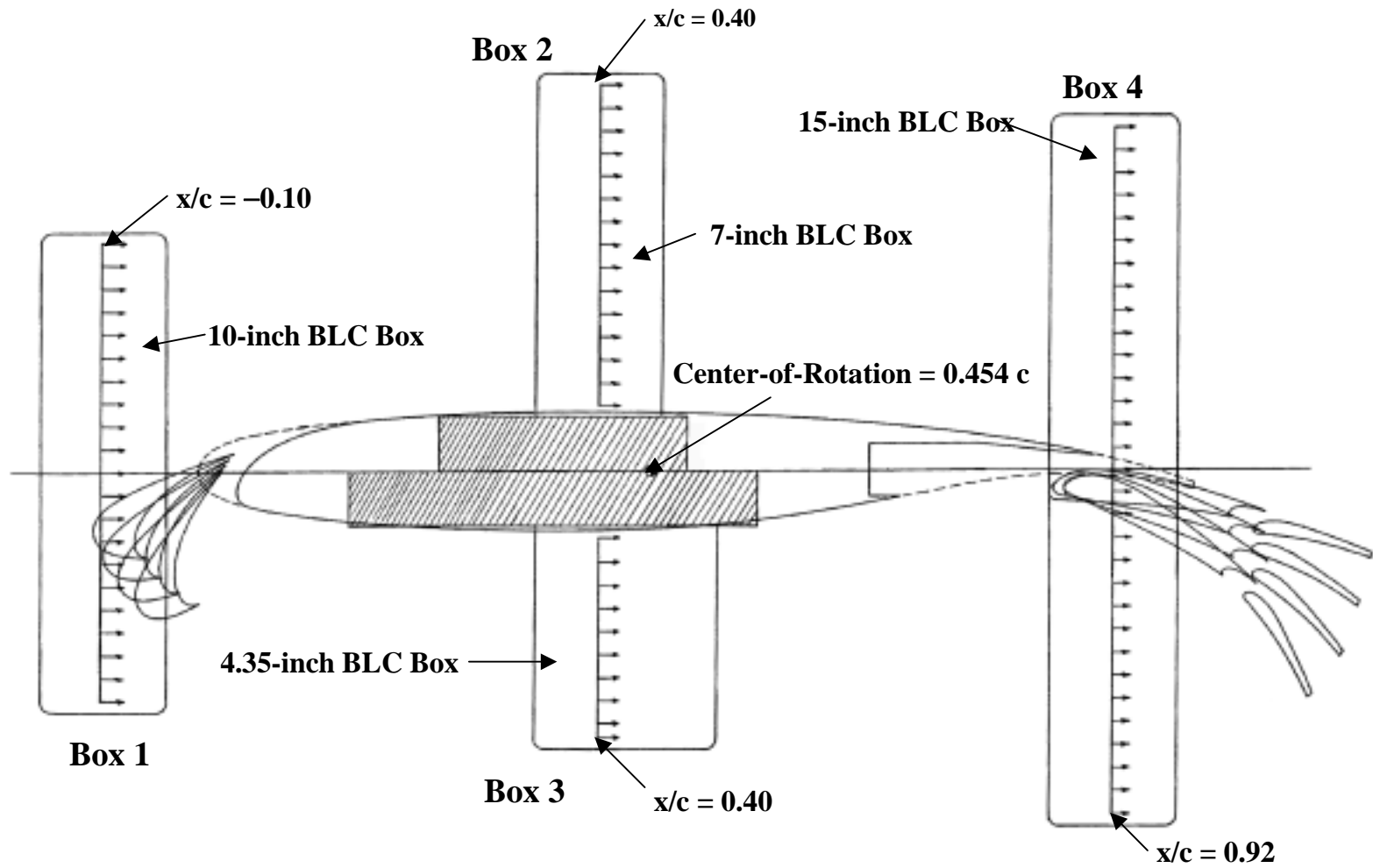


Figure 7. Location and height of Boundary Layer Control (BLC) blowing boxes for EET High-Lift Airfoil.

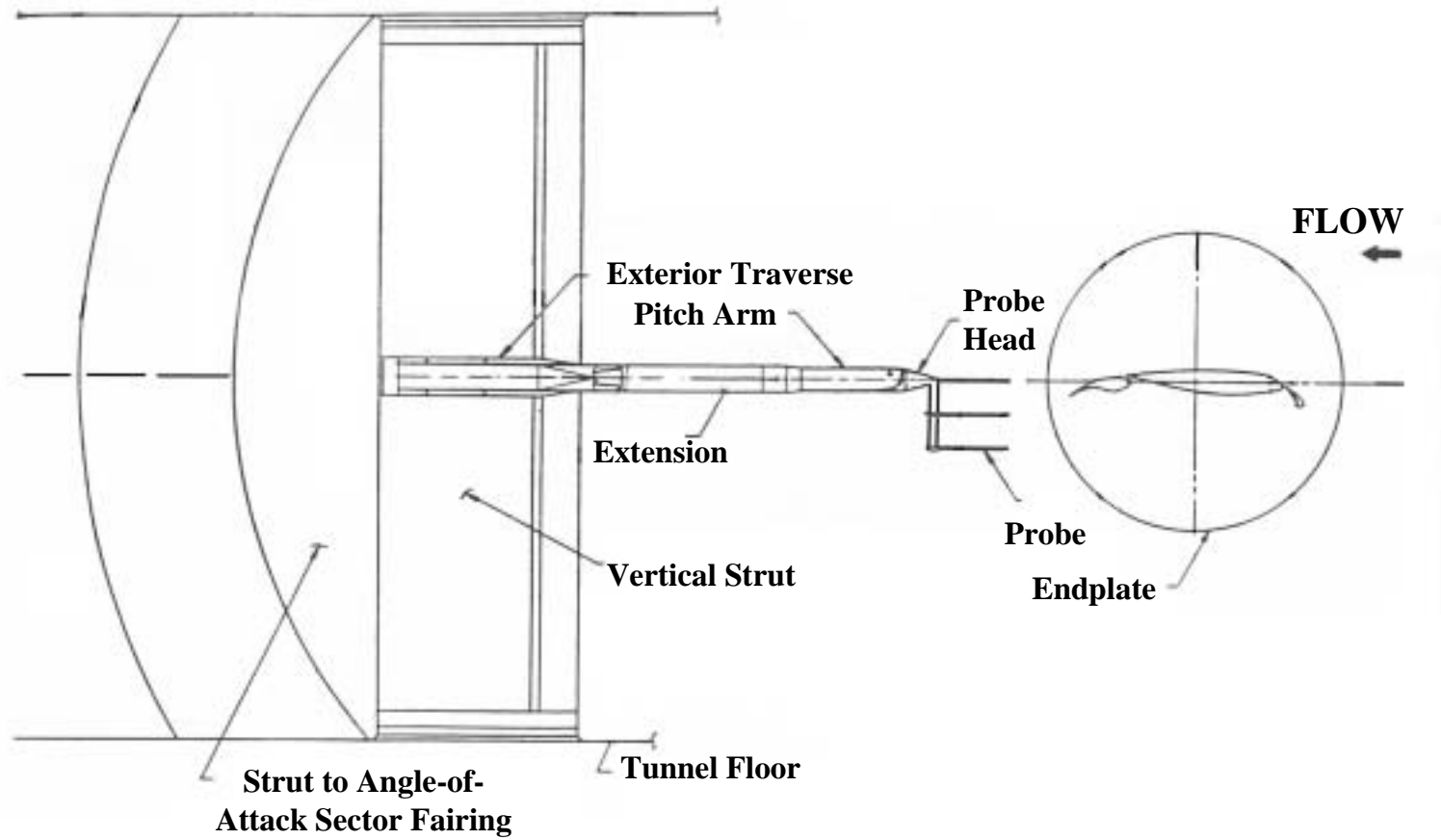
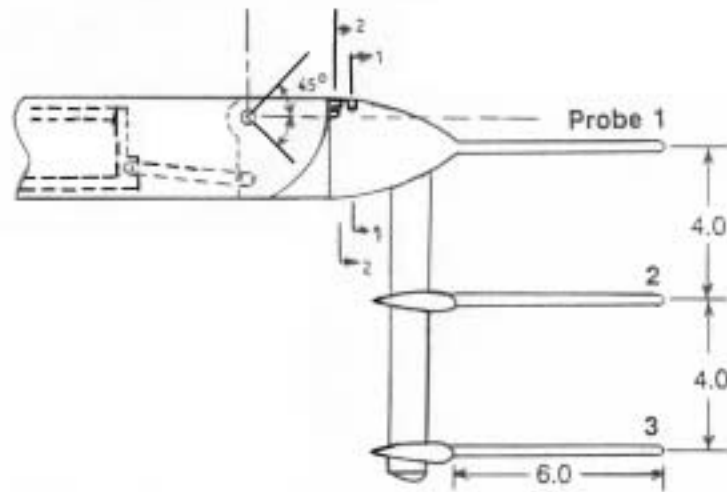
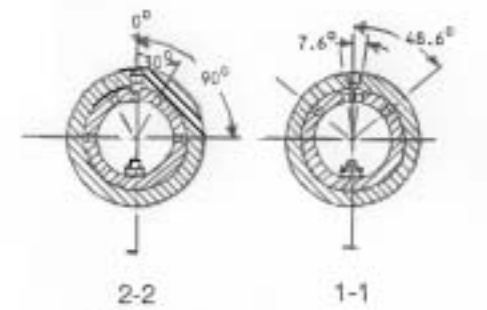


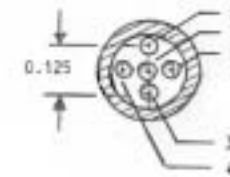
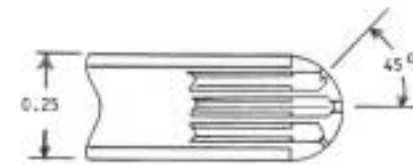
Figure 8. Wake rake assembly in Langley Low-Turbulence Pressure Tunnel.



Pitch Arm and Probe Head

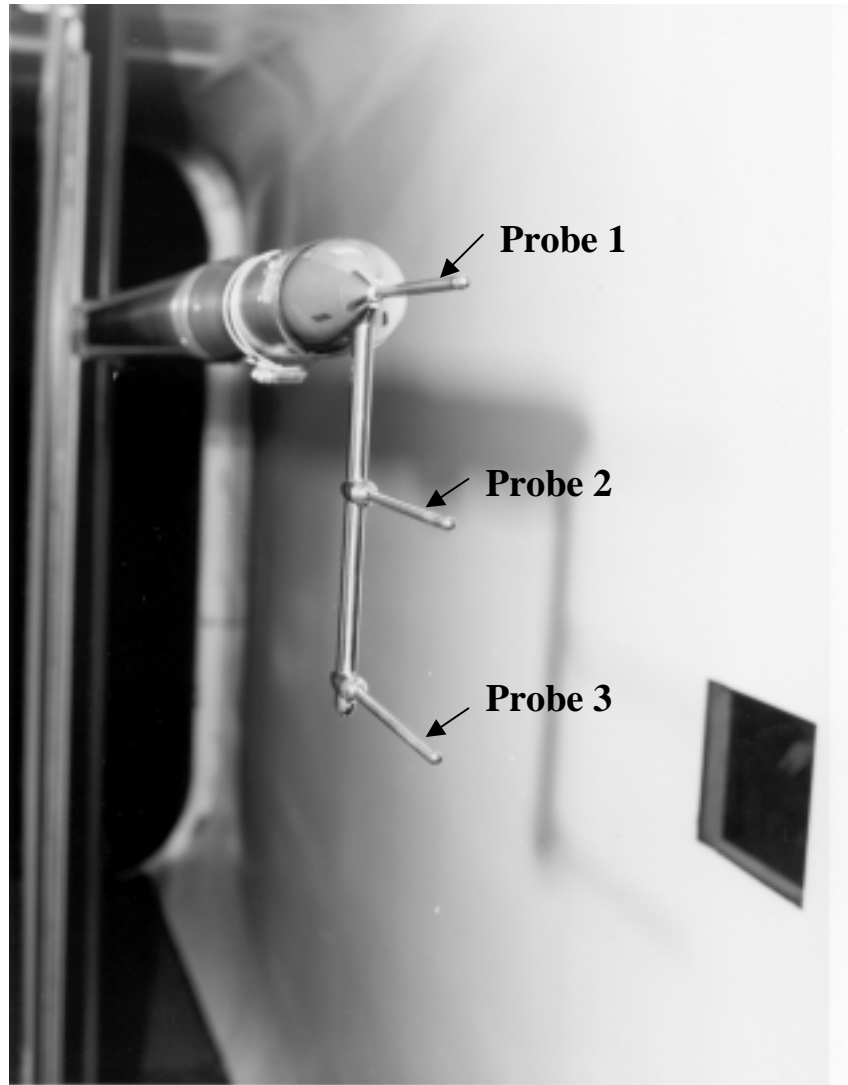


Probe Head Tip Cross Section



Layout of Probe Tip Orifices

Figure 9. Details of wake rake pitch arm, probe head, and probe tip.



L- 88-04535

Figure 10. Probe head and pressure probes of LTPT wake traverser.

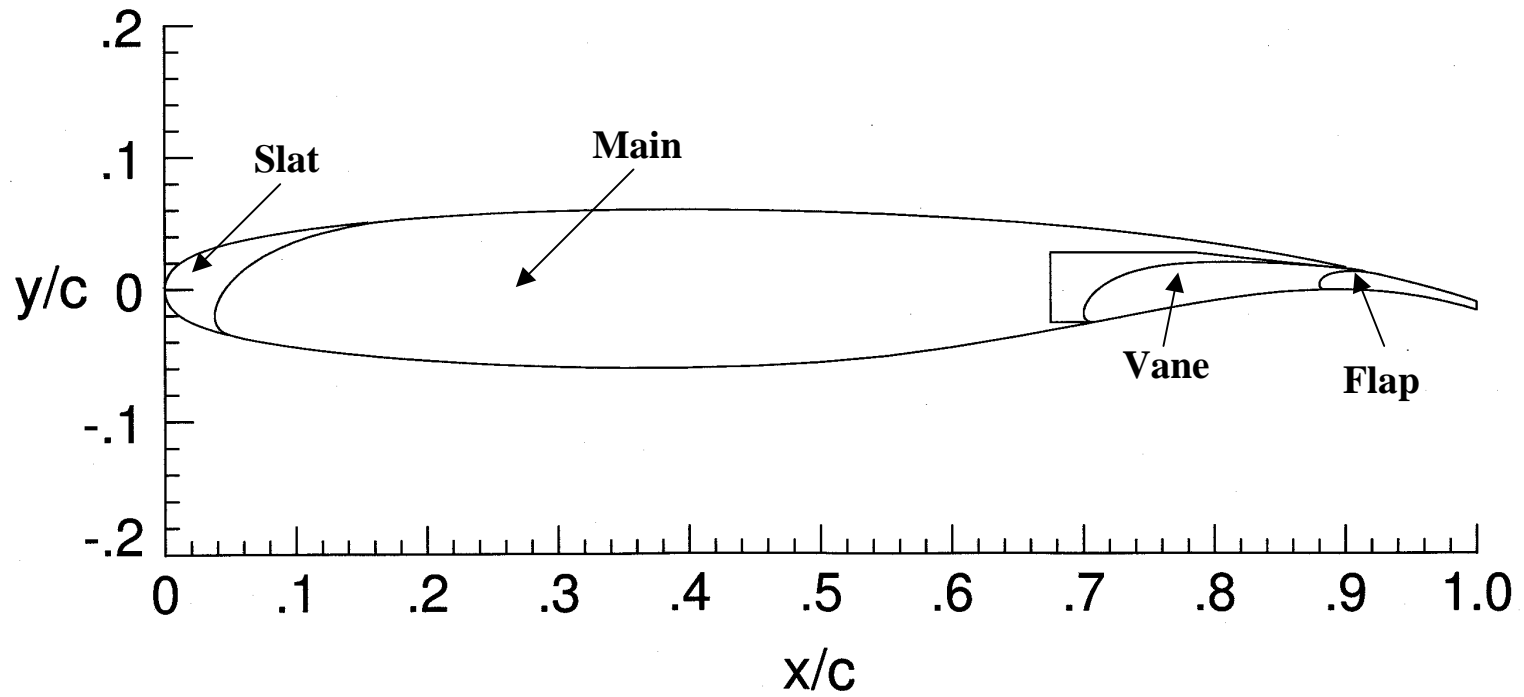


Figure 11. Contours and elements of Langley EET High-Lift Airfoil.

⊕ Pressure Tap Location

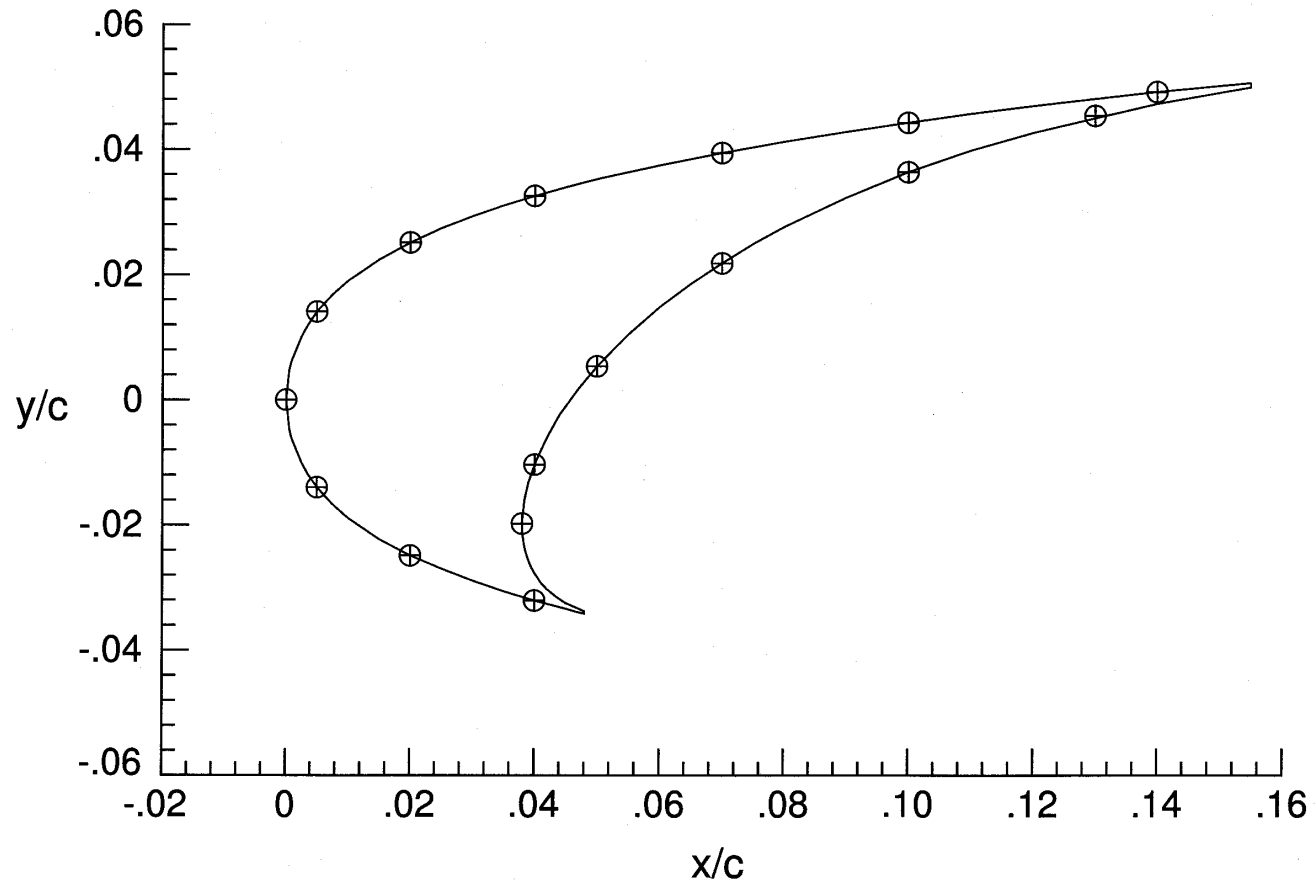


Figure 12. Contour and pressure tap locations of slat element of EET High-Lift Airfoil.

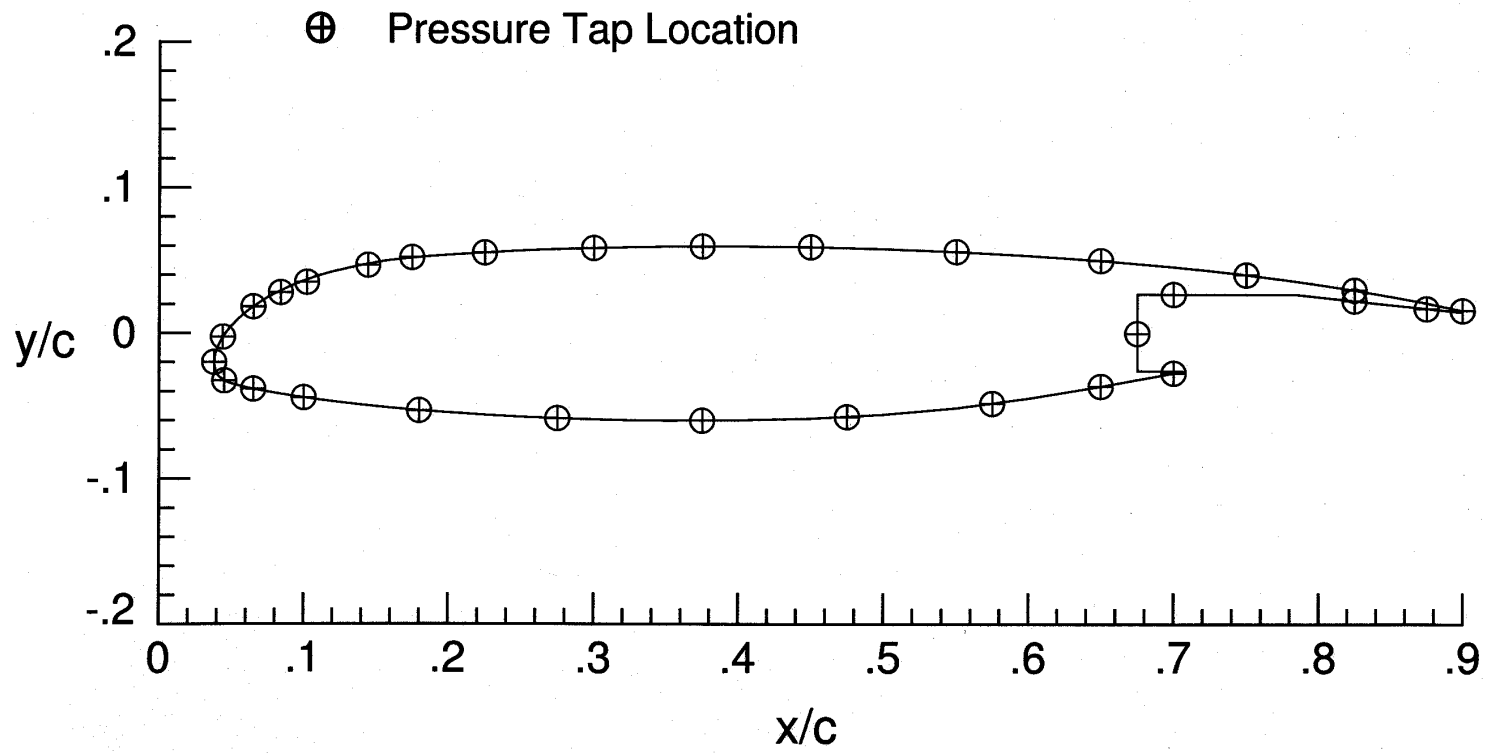


Figure 13. Contour and pressure tap locations of main element of EET High-Lift Airfoil.

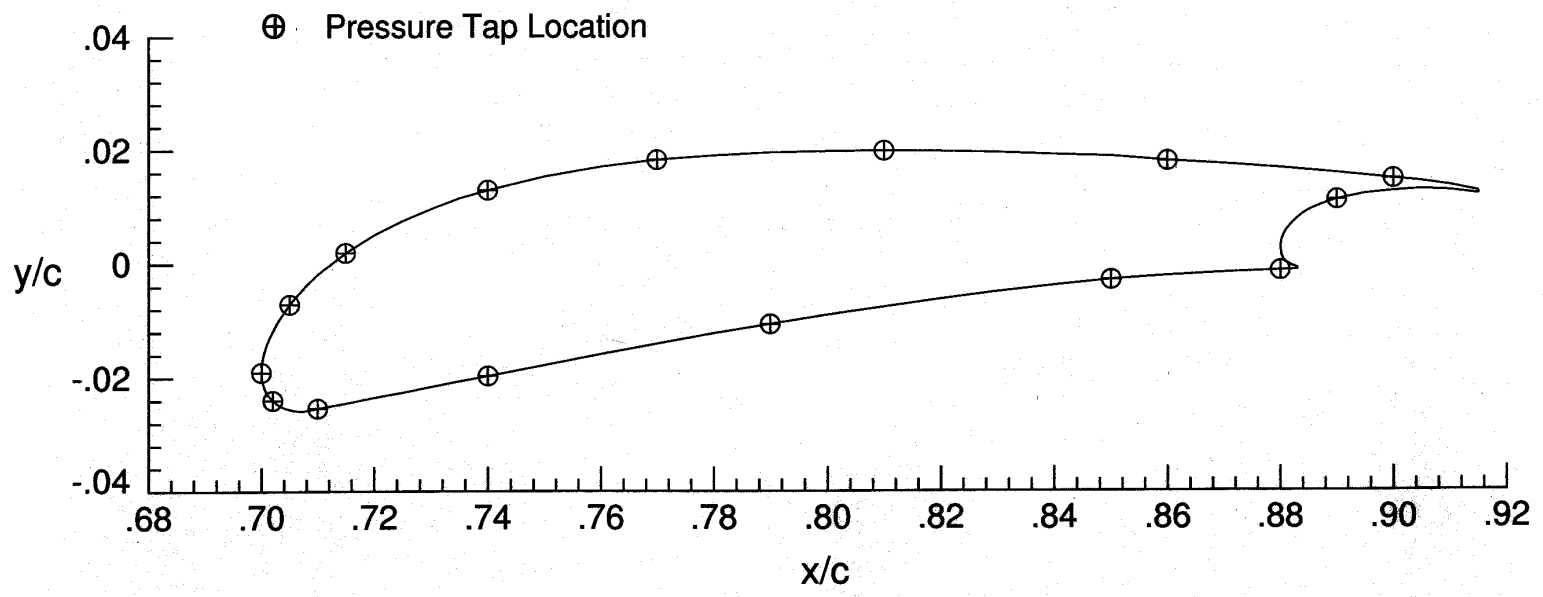


Figure 14. Contour and pressure tap locations of vane element of EET High-Lift Airfoil.

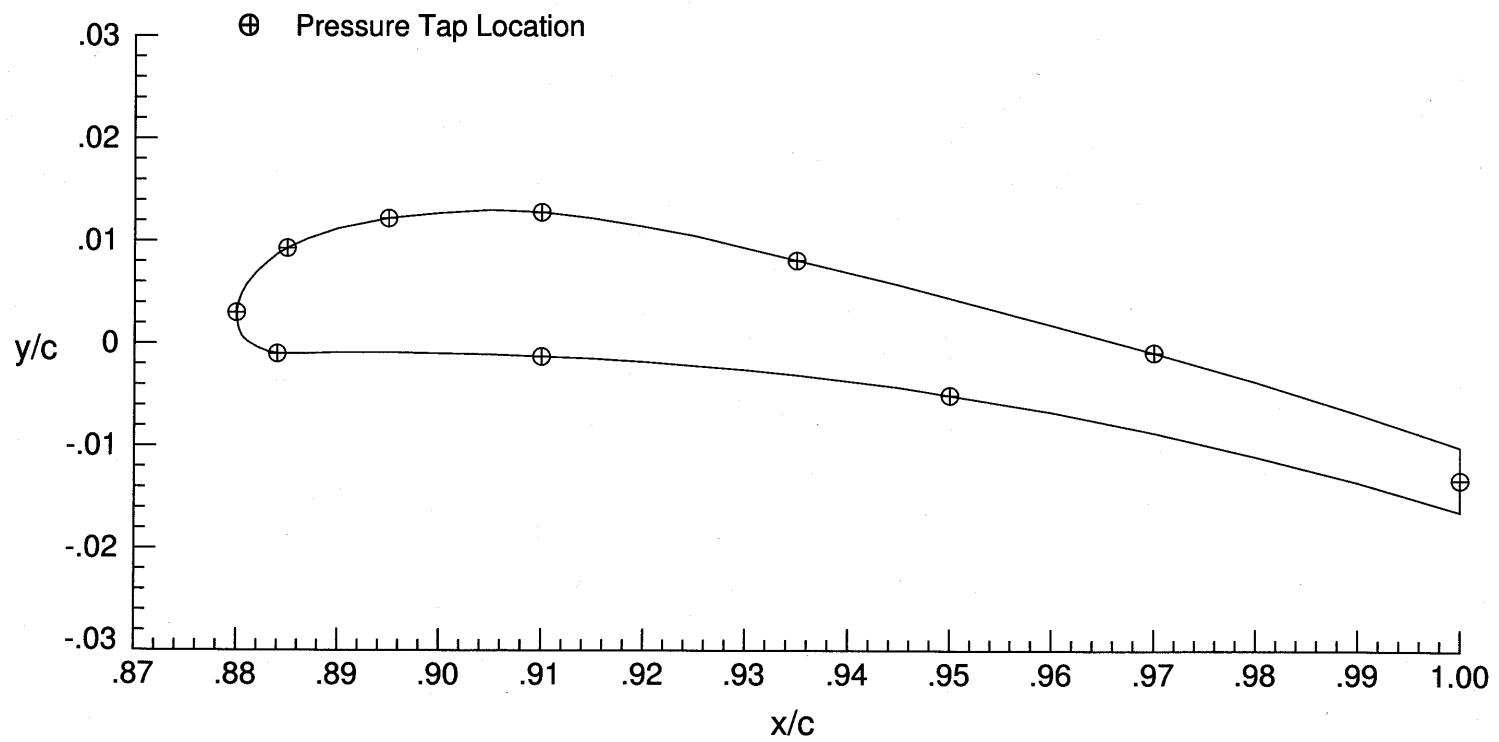


Figure 15. Contour and pressure tap locations of flap element of EET High-Lift Airfoil.

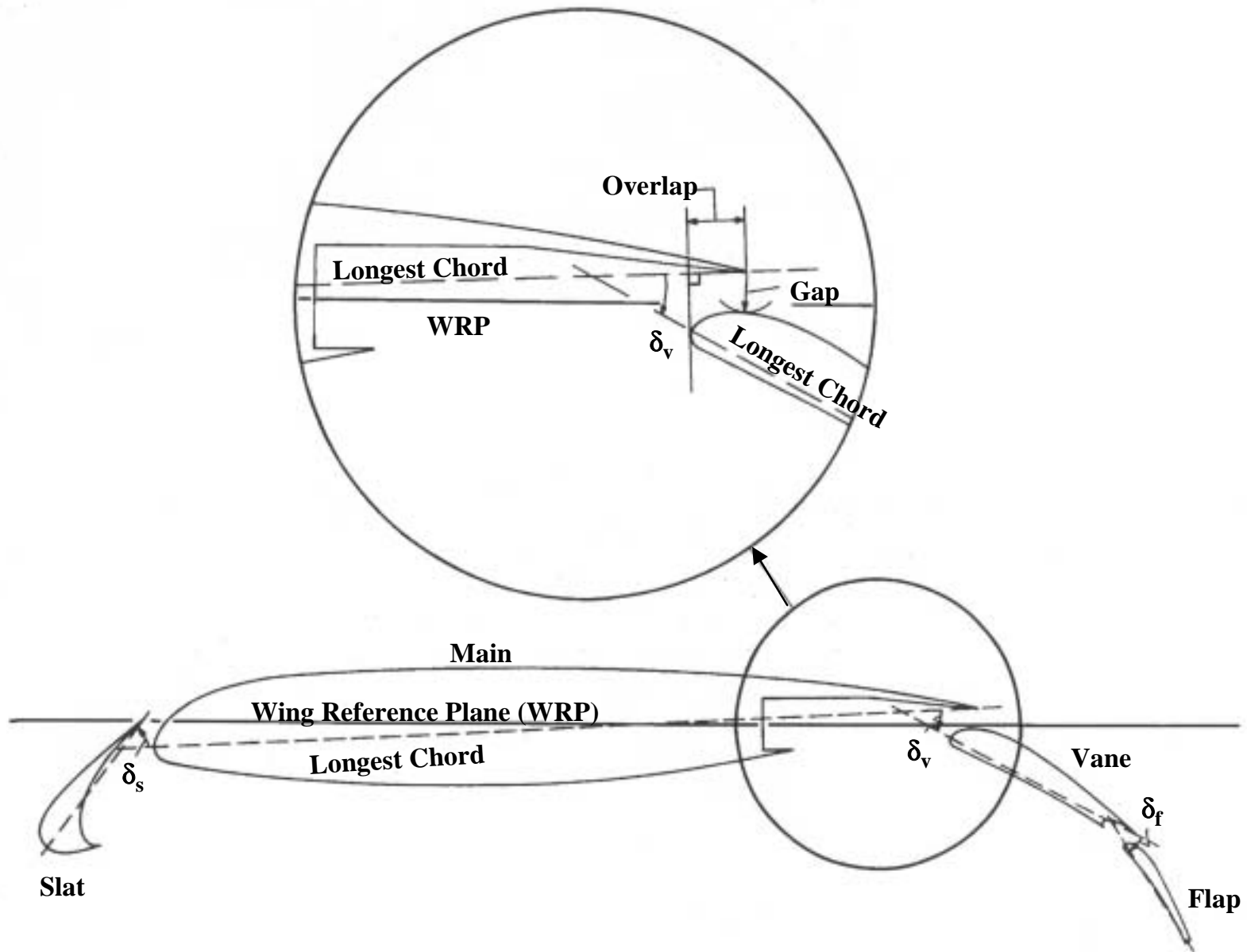
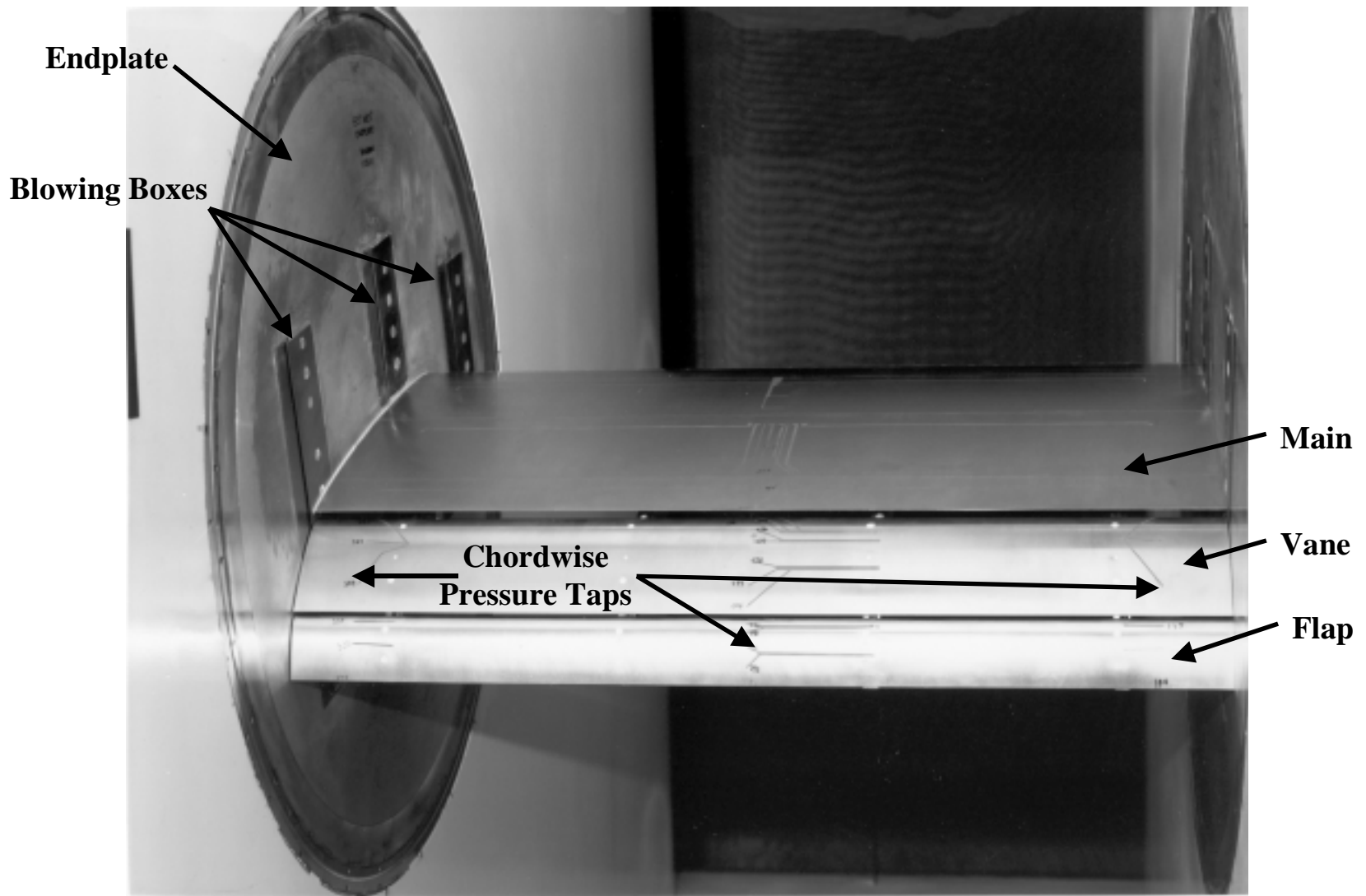


Figure 16. Definition of gap, overlap, and deflection for slat, vane, and flap of EET High-Lift Airfoil.



L-89-04362

Figure 17. Upstream view of EET High-Lift Airfoil mounted in Langley Low-Turbulence Pressure Tunnel.

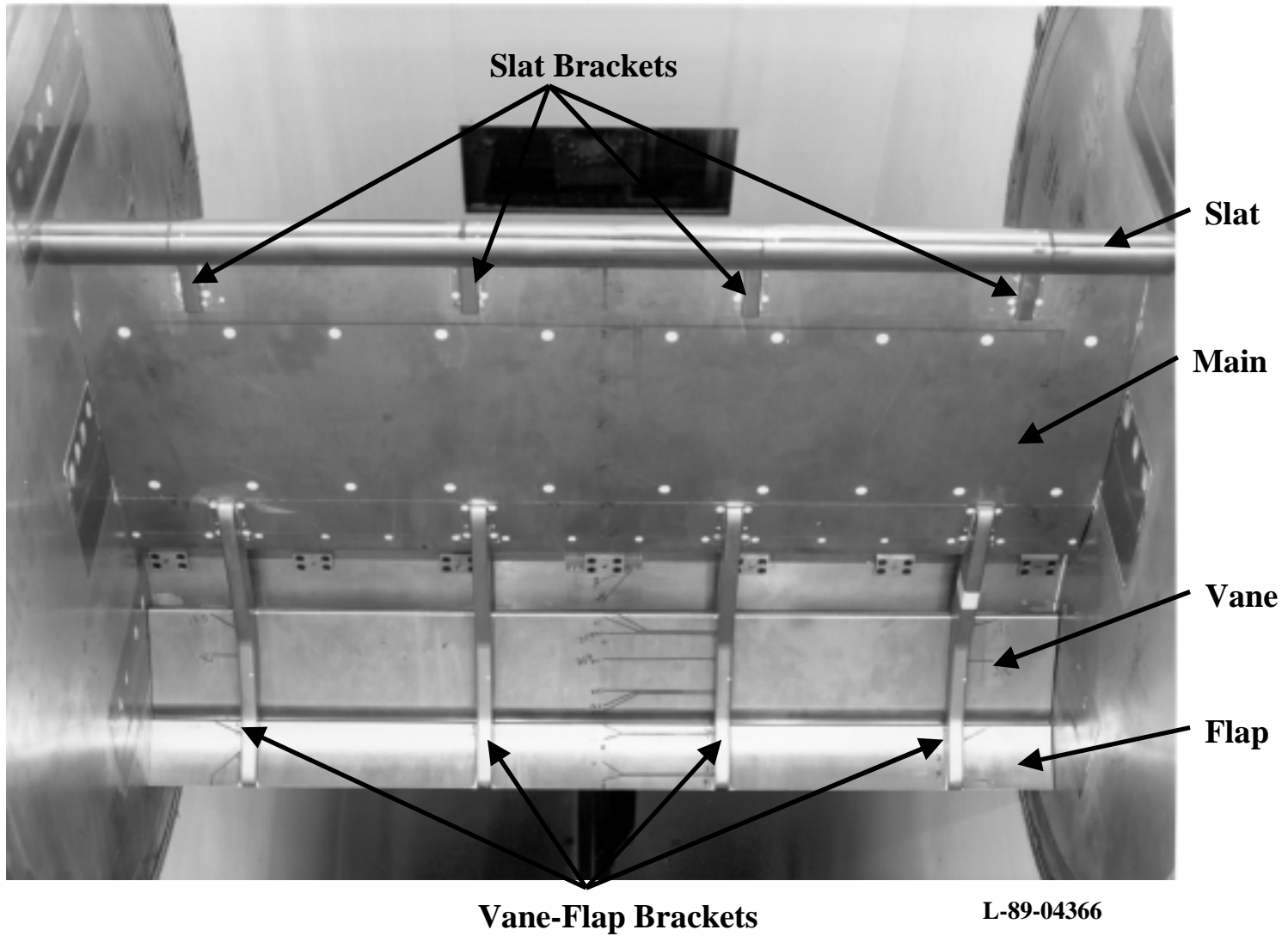
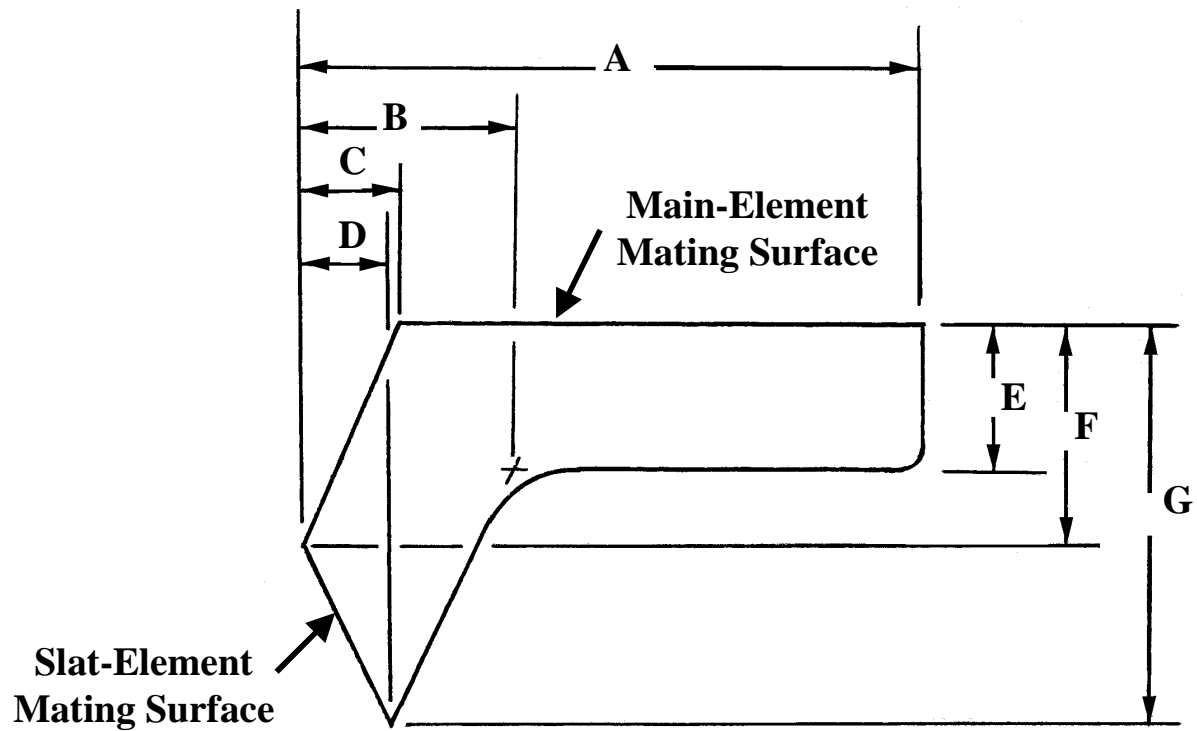


Figure 18. Lower surface view of EET High-Lift Airfoil showing bracket locations and sizes.



δ_s , deg.	A	B	C	D	E	F	G
-30	4.257	0.659	0.279	-0.121	0.850	0.215	1.408
-40	4.175	1.150	0.570	0.089	0.850	0.629	1.824
-50	3.975	1.302	0.722	0.295	0.850	1.000	2.163
-60	3.720	1.285	0.565	0.492	0.850	1.321	2.414

Note: A-G dimensions are inches.

Figure 19. Slat bracket geometry definitions.

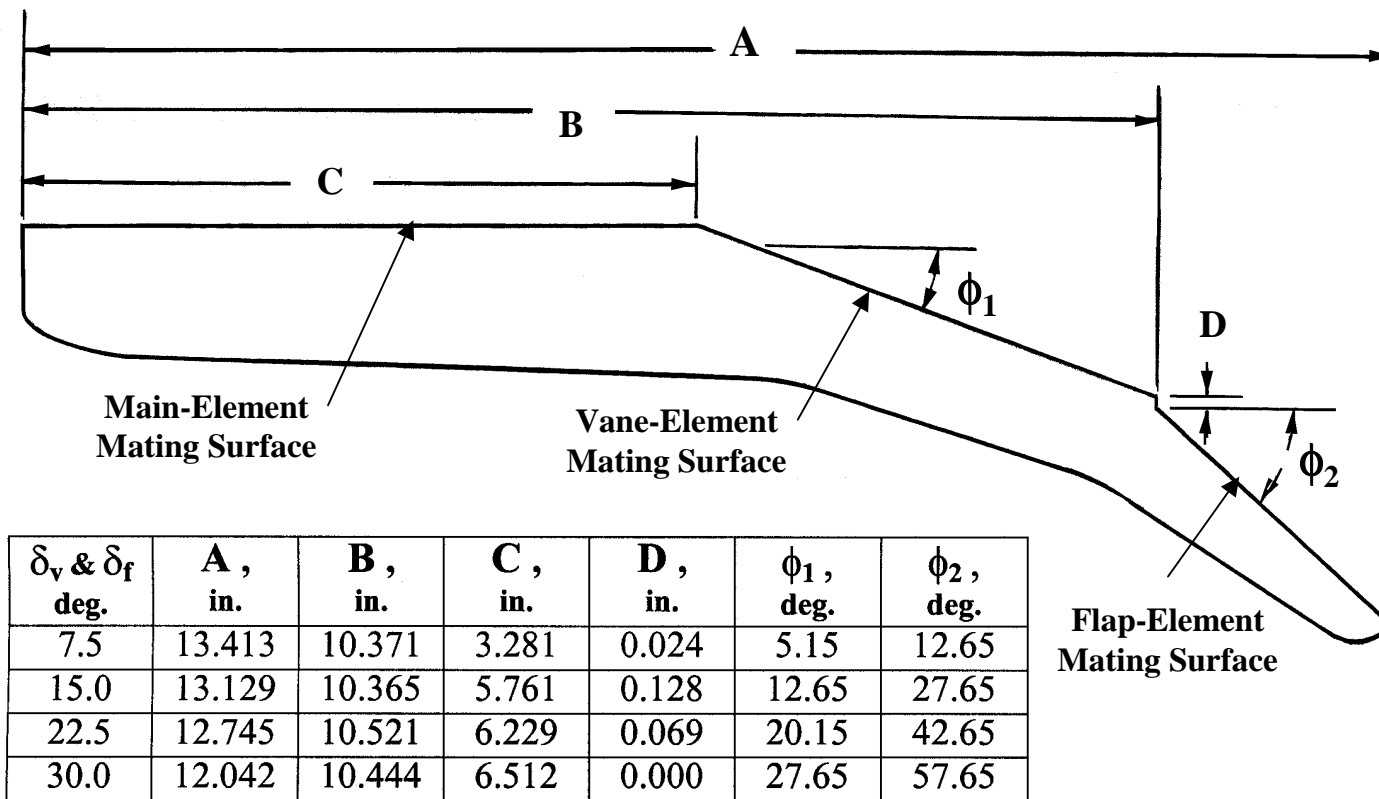


Figure 20. Vane-flap bracket geometry definition.

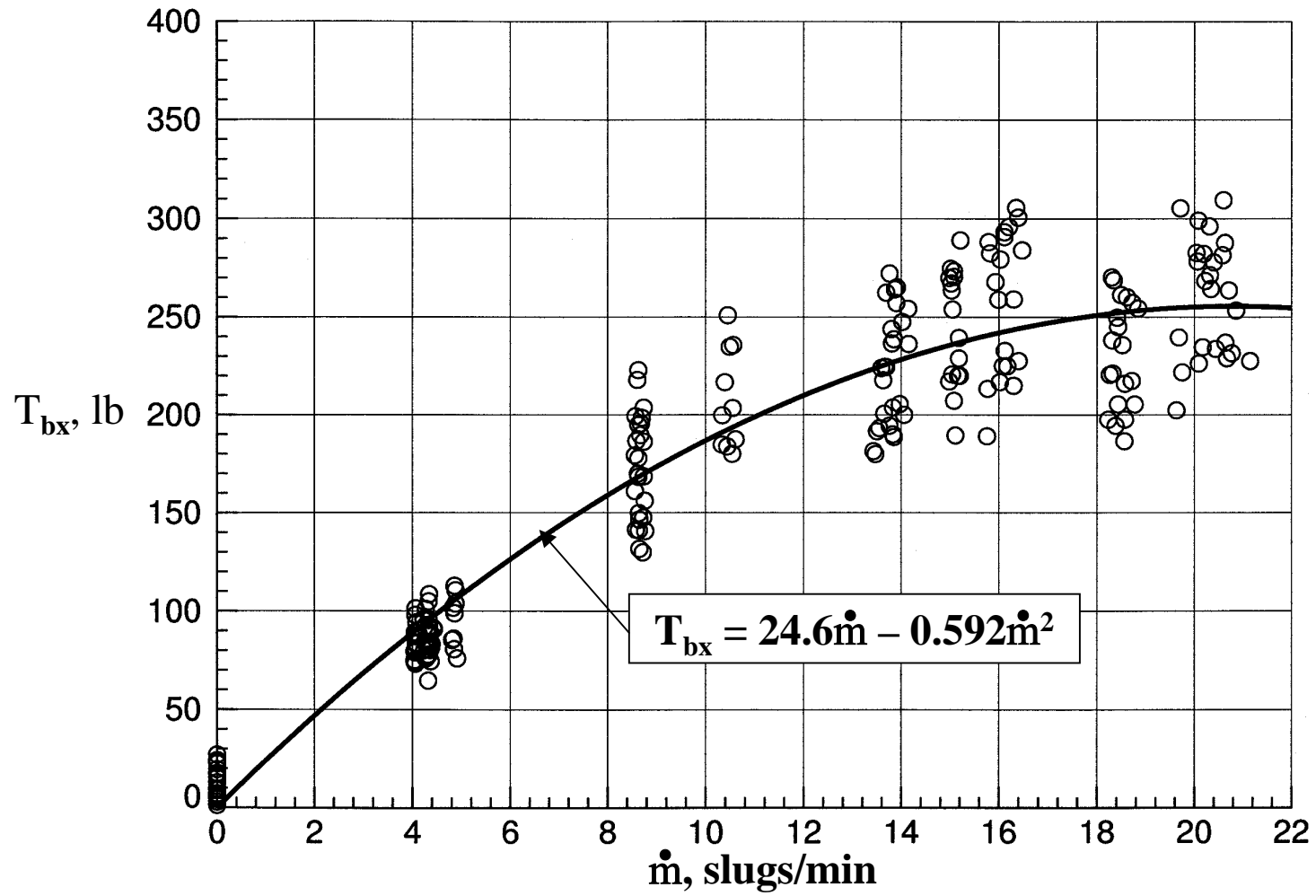


Figure 21. Blowing-box thrust calibration curve fit for EET High-Lift Airfoil test.

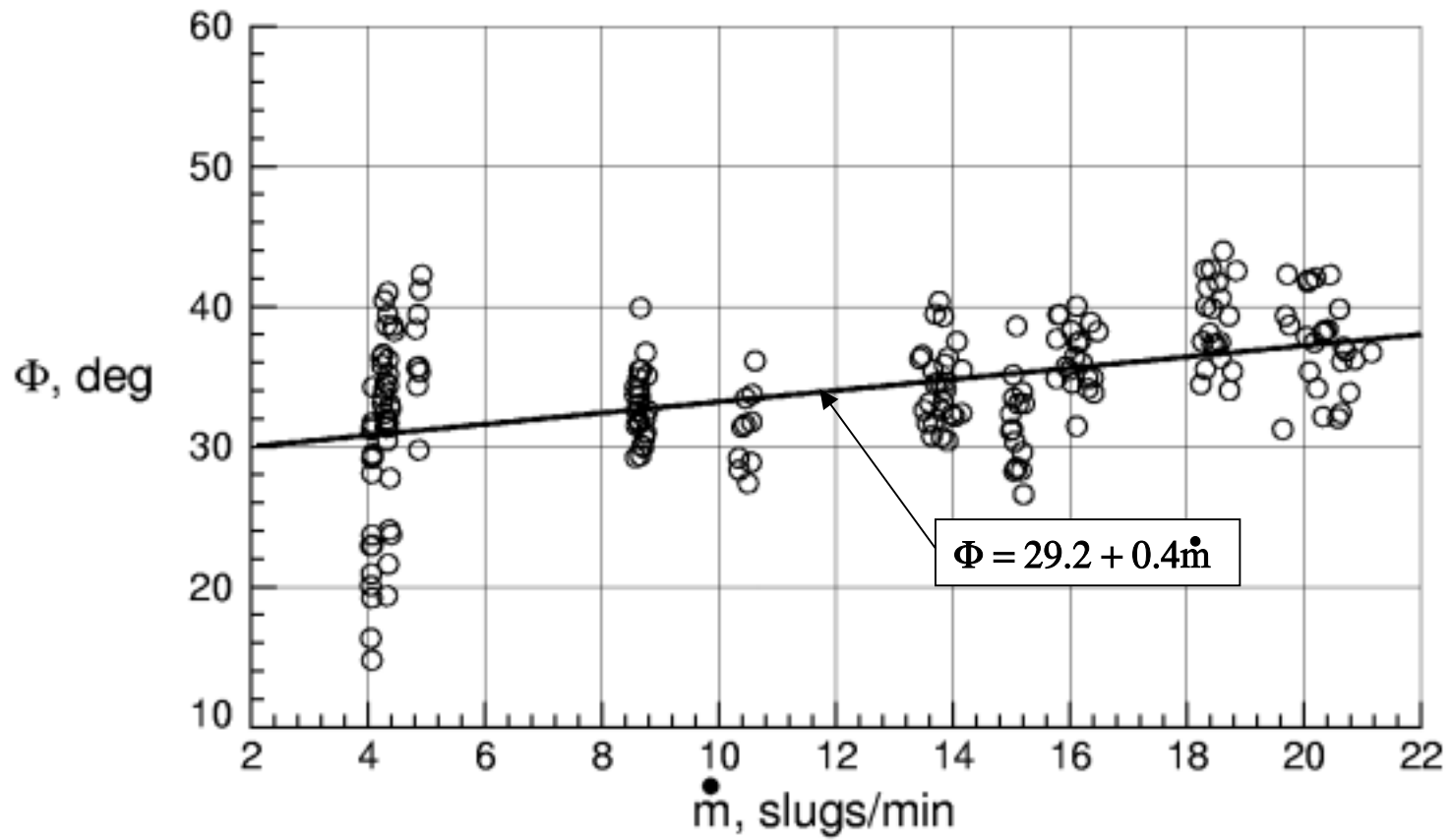


Figure 22. Blowing-box thrust angle calibration curve fit for EET High-Lift Airfoil test.

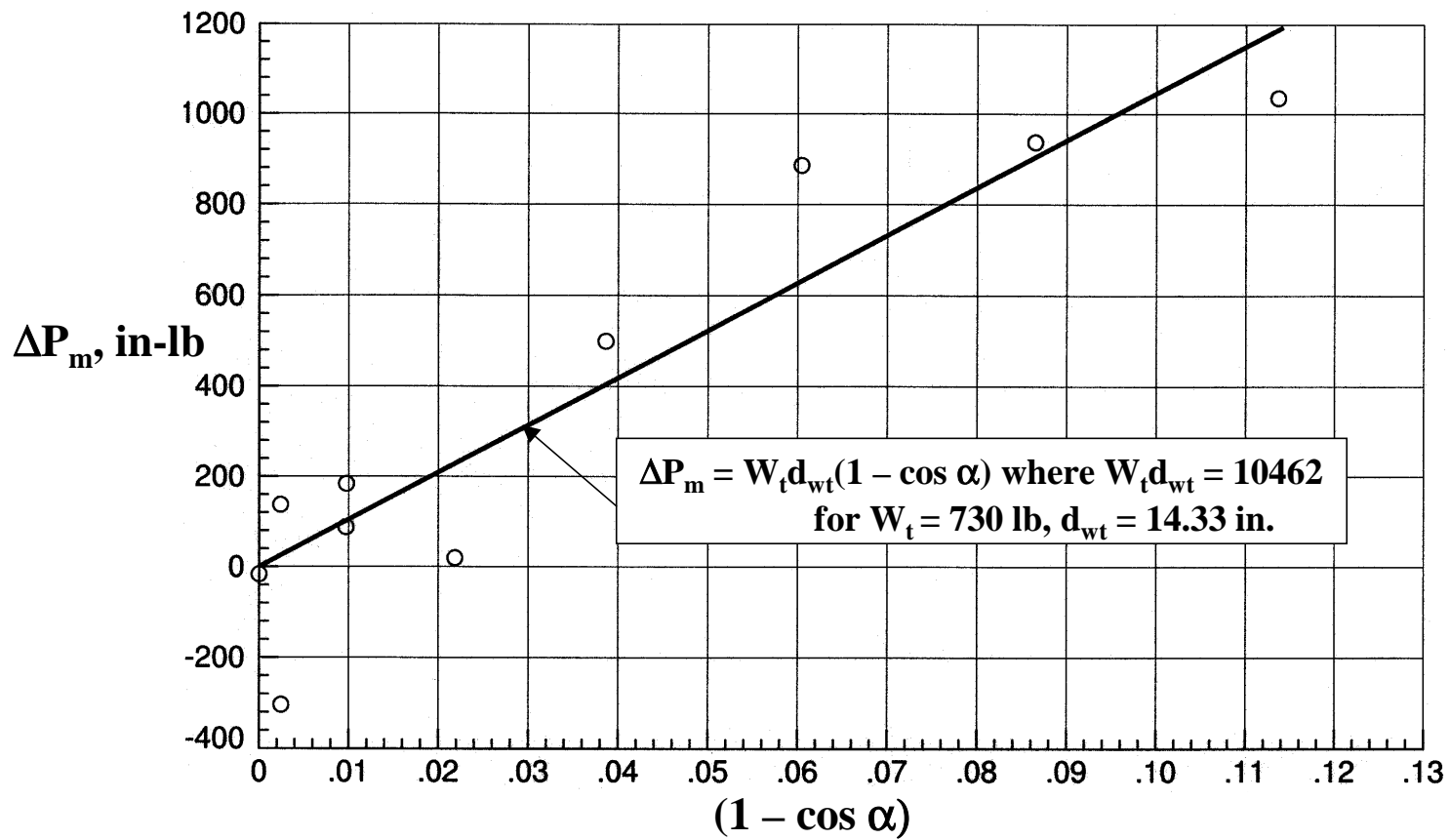


Figure 23. Model weight center calibration curve fit for EET High-Lift Airfoil test.

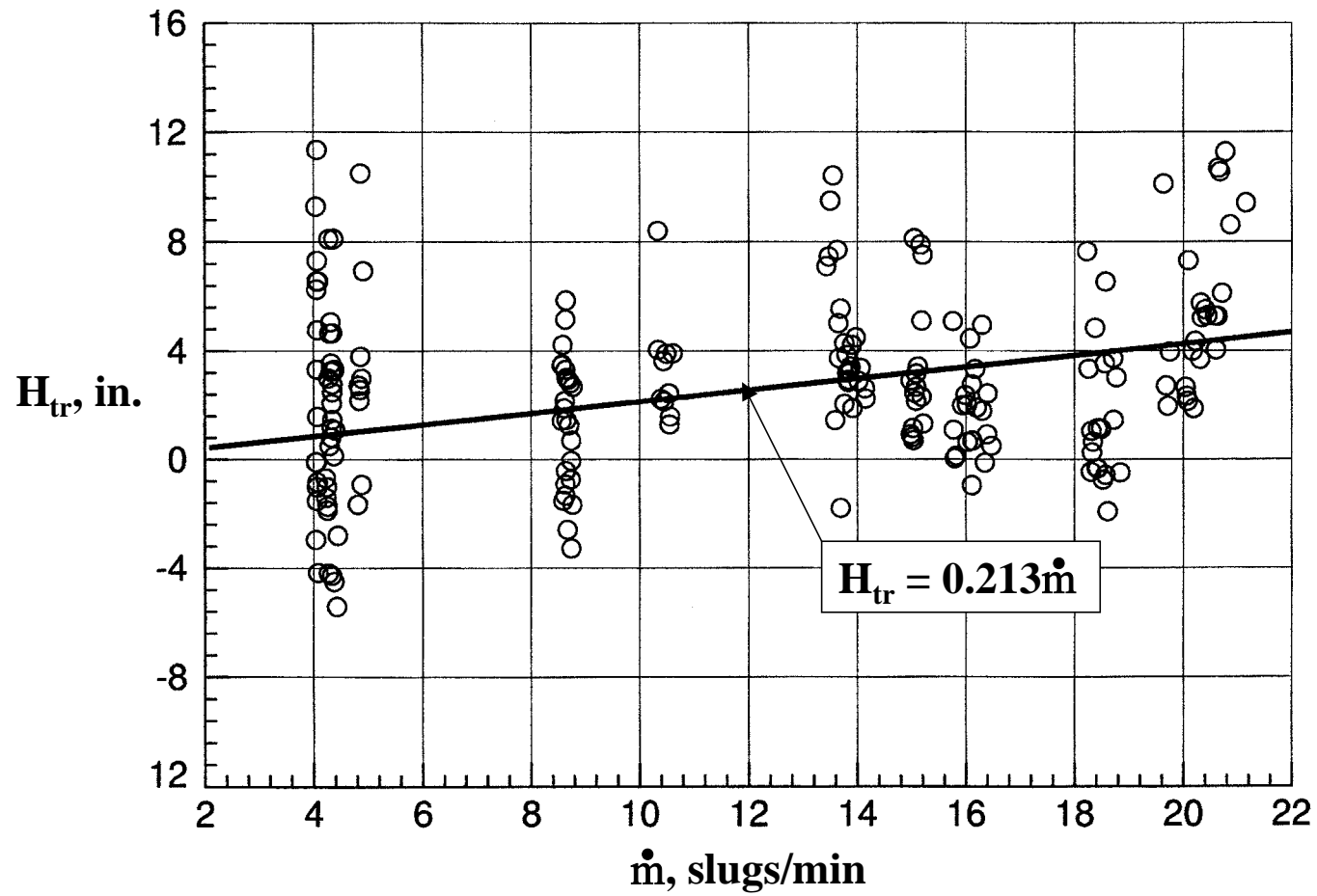


Figure 24. Blowing-box thrust distance calibration curve fit for EET High-Lift Airfoil test.

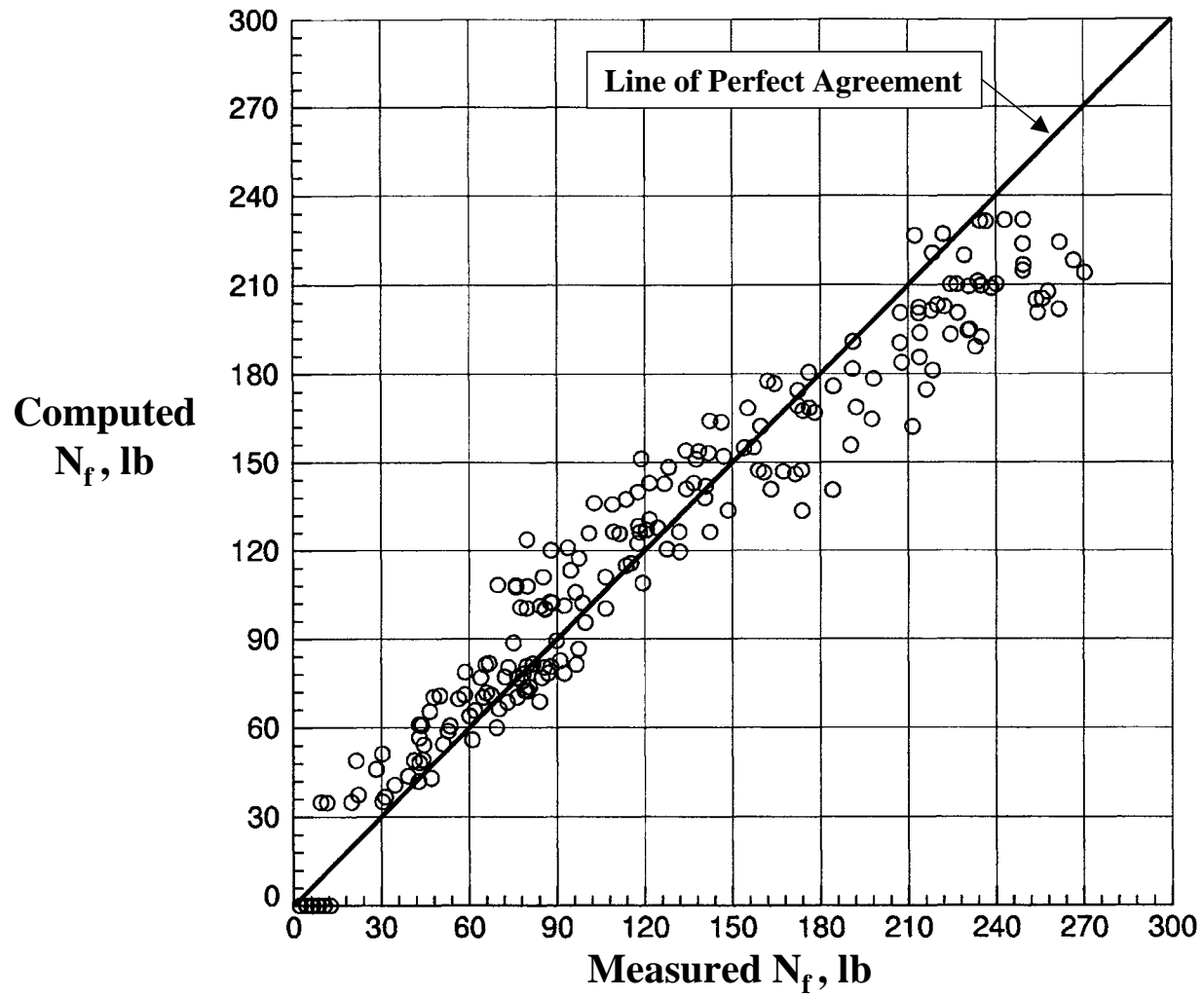


Figure 25. Measured and computed normal force tares.

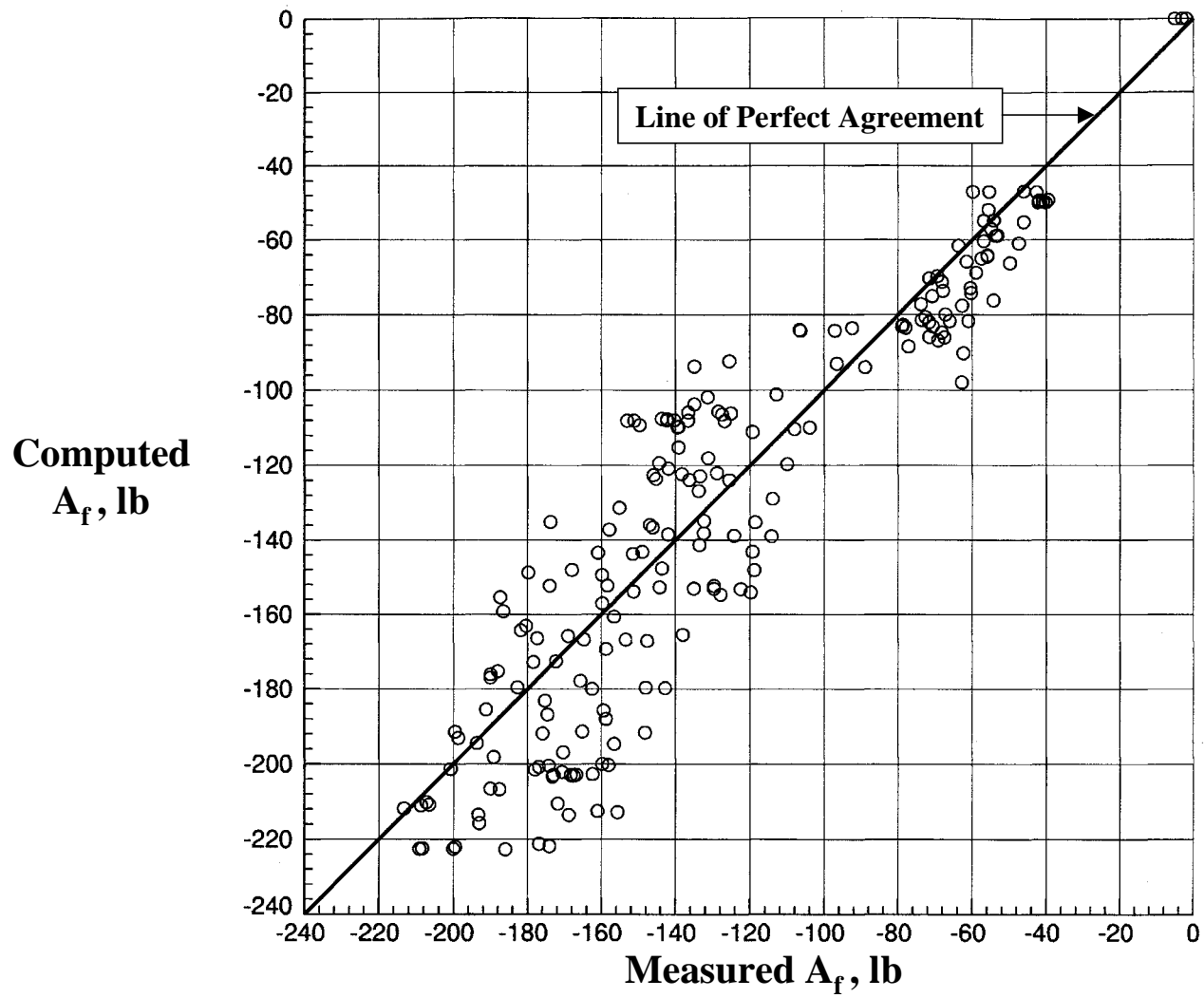


Figure 26. Measured and computed axial force tares.

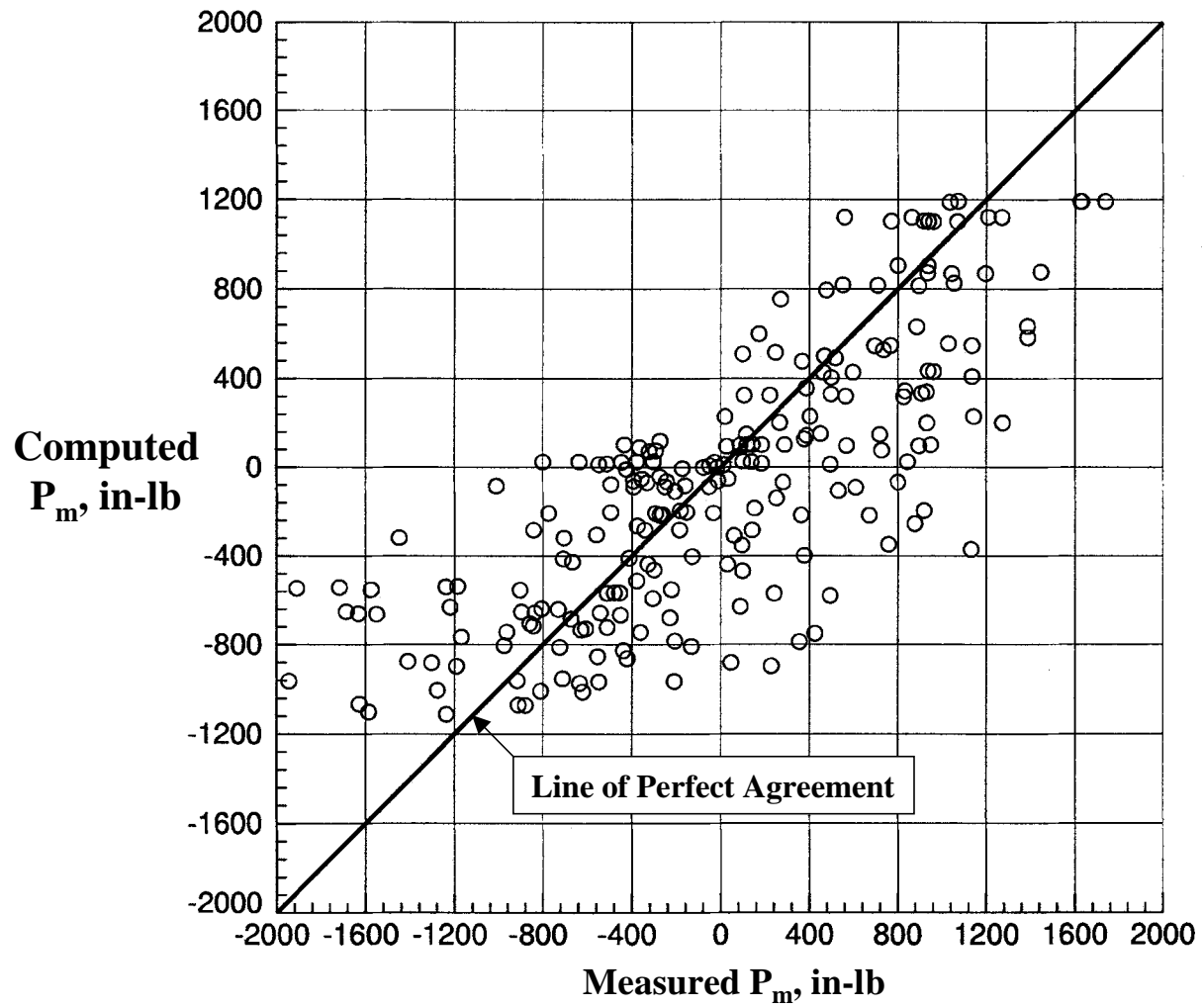


Figure 27. Measured and computed pitching-moment tares.

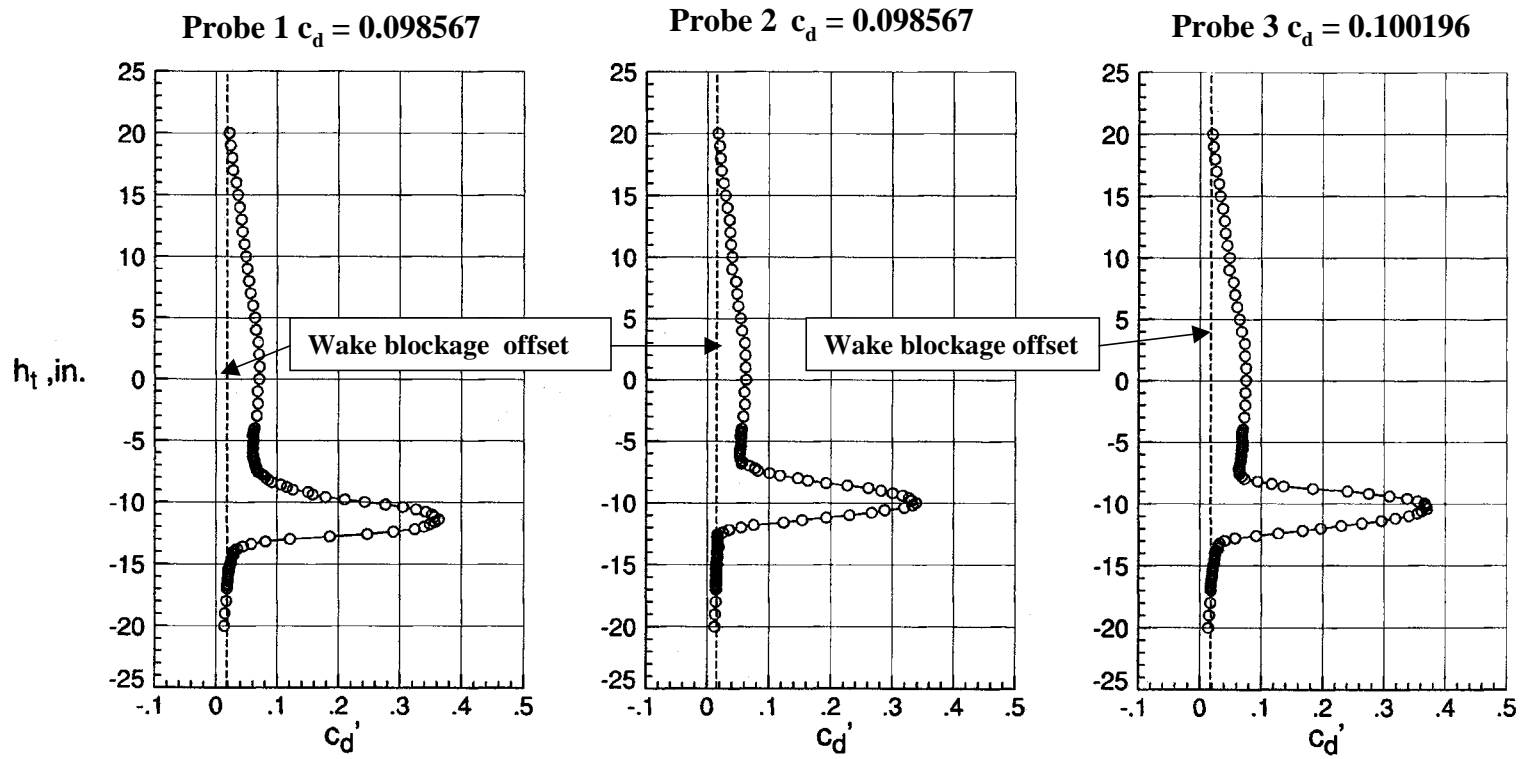


Figure 28. Sample drag profiles from wake probes.

	Run	$R_n / 10^6$
○	70	2.54
□	71	6.07
◇	72	12.04
△	73	18.12

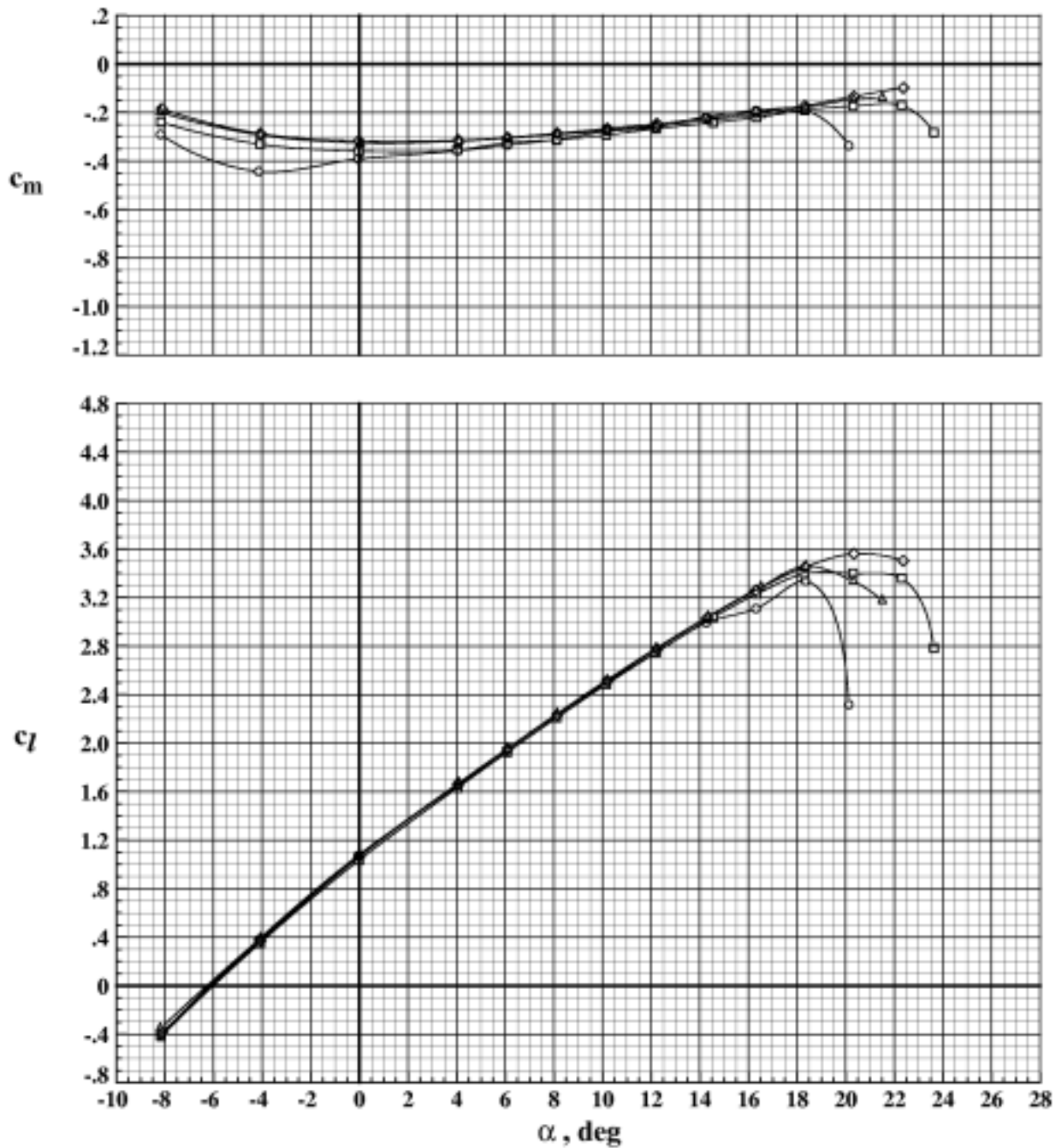


Figure 29. Effect of Reynolds number on aerodynamic performance of EET High-Lift Airfoil with $\delta_s = -30.0^\circ$, $\delta_v = 7.5^\circ$, and $\delta_f = 7.5^\circ$ at $M_\infty = 0.201$.

	Run	$R_n / 10^6$
○	66	2.56
□	67	6.06
◇	68	12.10
△	69	18.13

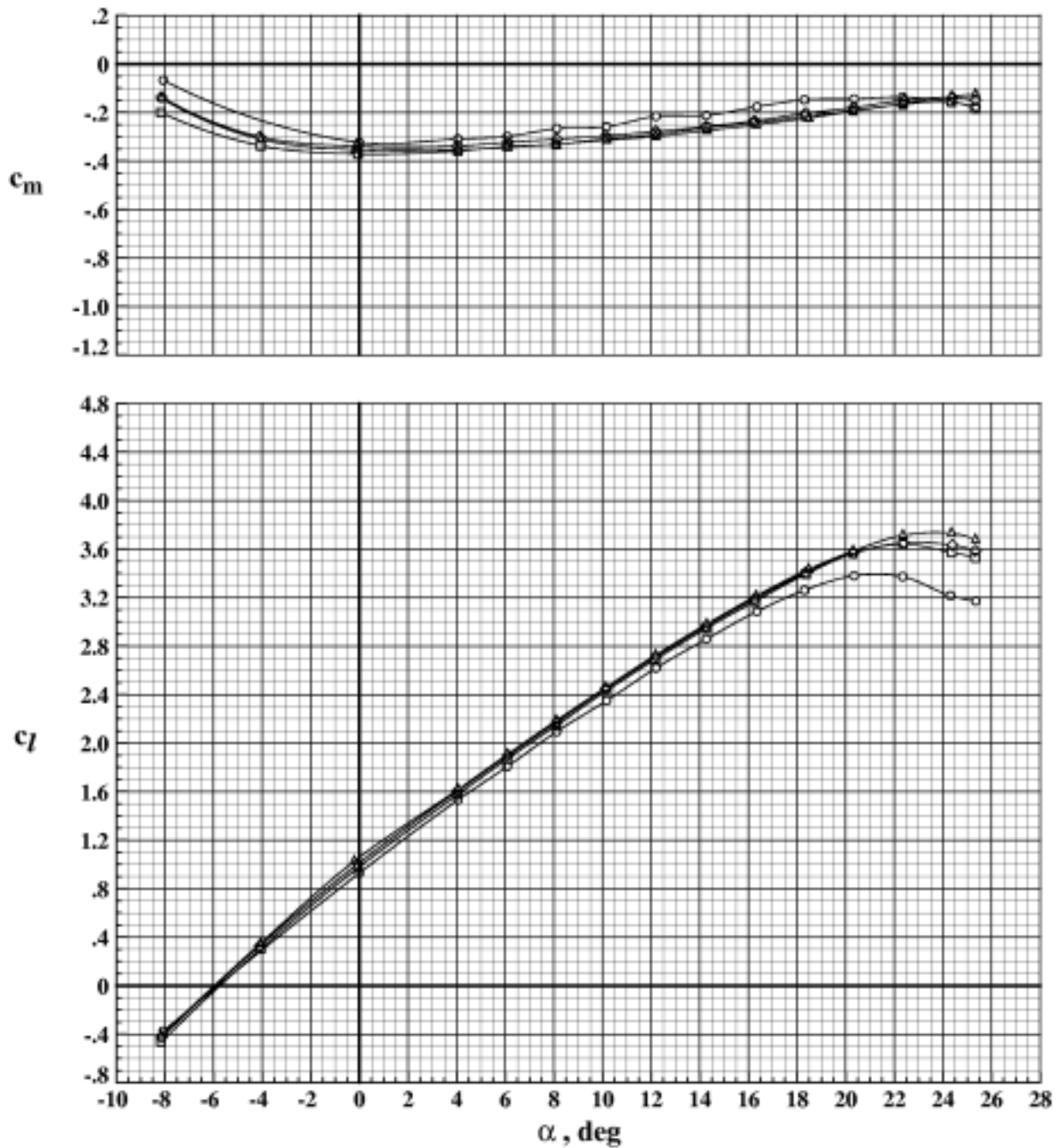


Figure 30. Effect of Reynolds number on aerodynamic performance of EET High-Lift Airfoil with $\delta_s = -40.0^\circ$, $\delta_v = 7.5^\circ$, and $\delta_f = 7.5^\circ$ at $M_\infty = 0.202$.

	Run	$R_n / 10^6$
○	62	2.53
□	63	6.06
◇	64	12.13
△	65	18.18

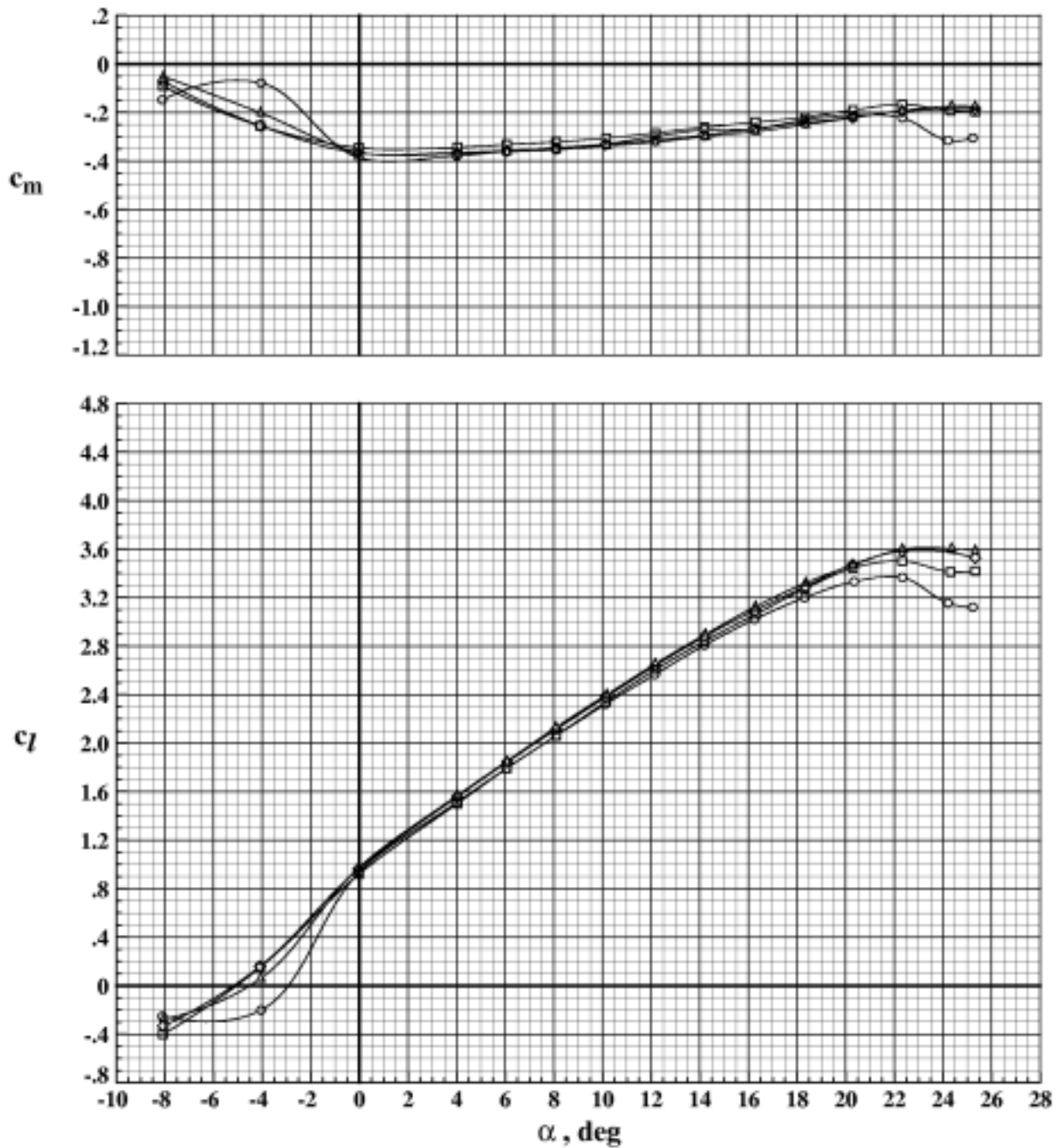


Figure 31. Effect of Reynolds number on aerodynamic performance of EET High-Lift Airfoil with $\delta_s = -50.0^\circ$, $\delta_v = 7.5^\circ$, and $\delta_f = 7.5^\circ$ at $M_\infty = 0.202$.

	Run	$R_n / 10^6$
○	58	2.50
□	59	6.08
◇	60	12.16
△	61	18.19

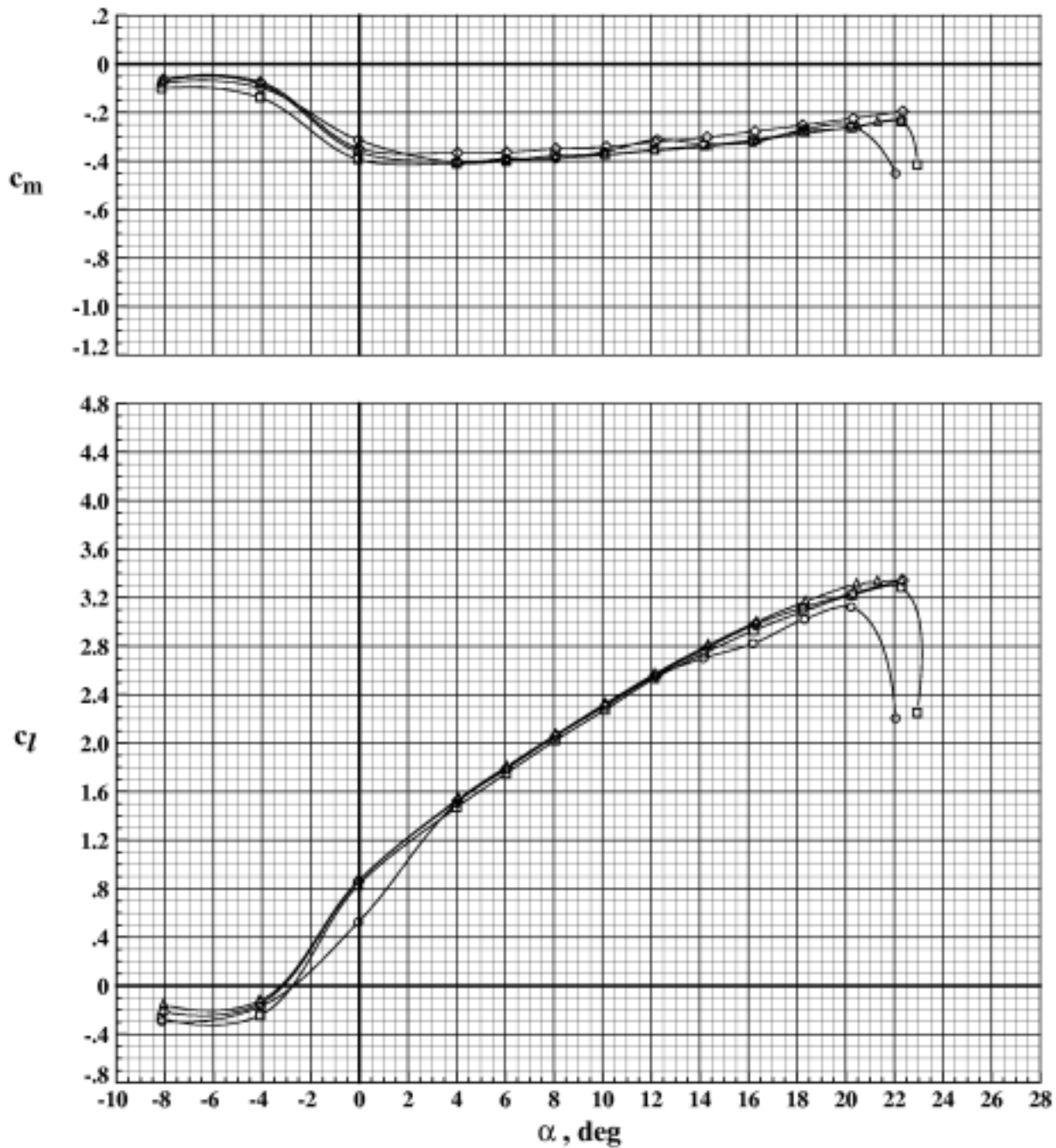


Figure 32. Effect of Reynolds number on aerodynamic performance of EET High-Lift Airfoil with $\delta_s = -60.0^\circ$, $\delta_v = 7.5^\circ$, and $\delta_f = 7.5^\circ$ at $M_\infty = 0.202$.

	Run	$R_n / 10^6$
○	74	2.53
□	75	6.04
◇	76	12.10
△	77	18.14

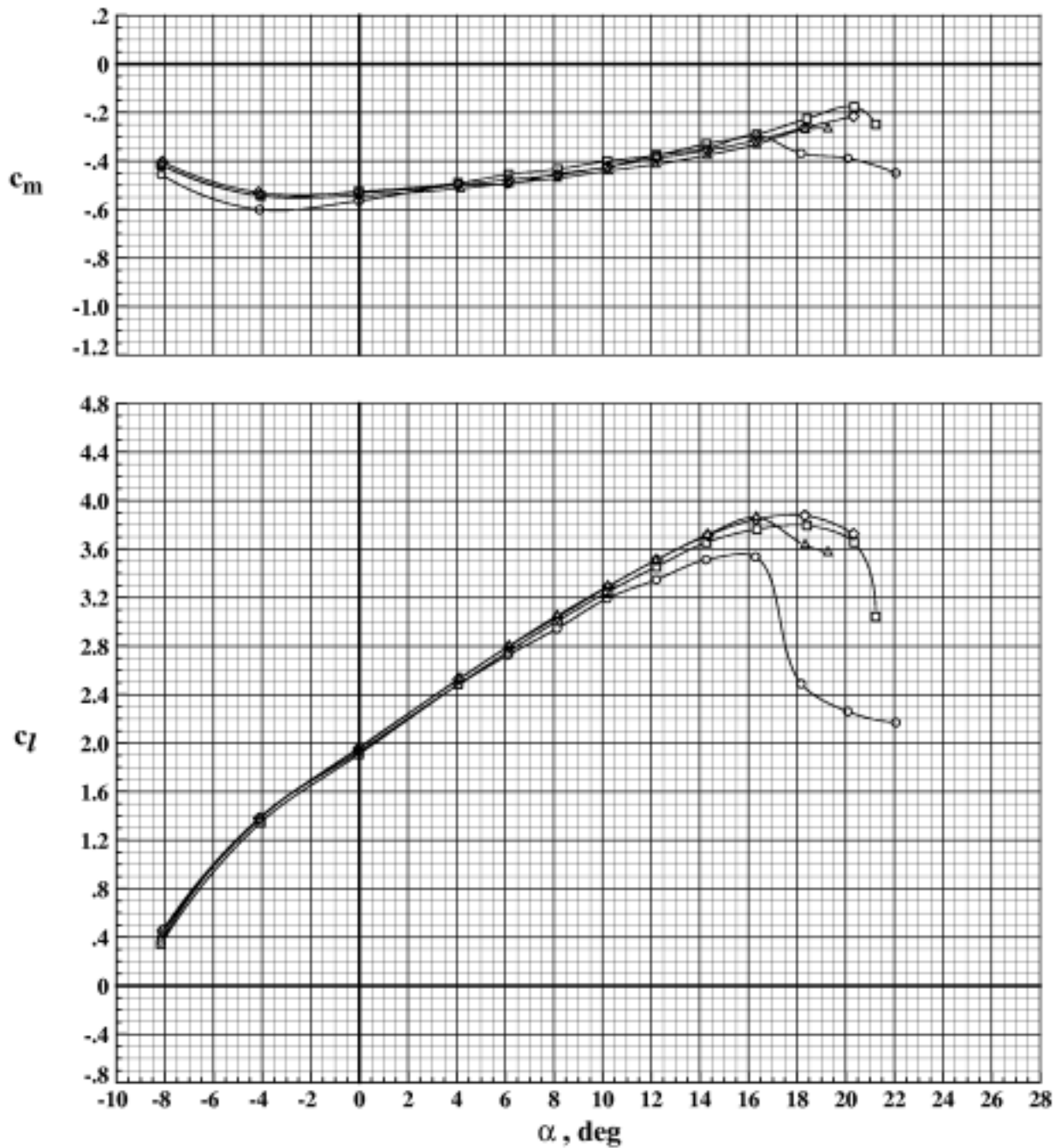


Figure 33. Effect of Reynolds number on aerodynamic performance of EET High-Lift Airfoil with $\delta_s = -30.0^\circ$, $\delta_v = 15.0^\circ$, and $\delta_T = 15.0^\circ$ at $M_\infty = 0.202$.

	Run	$R_n / 10^6$
○	78	2.54
□	79	6.05
◇	80	12.15
△	81	18.16

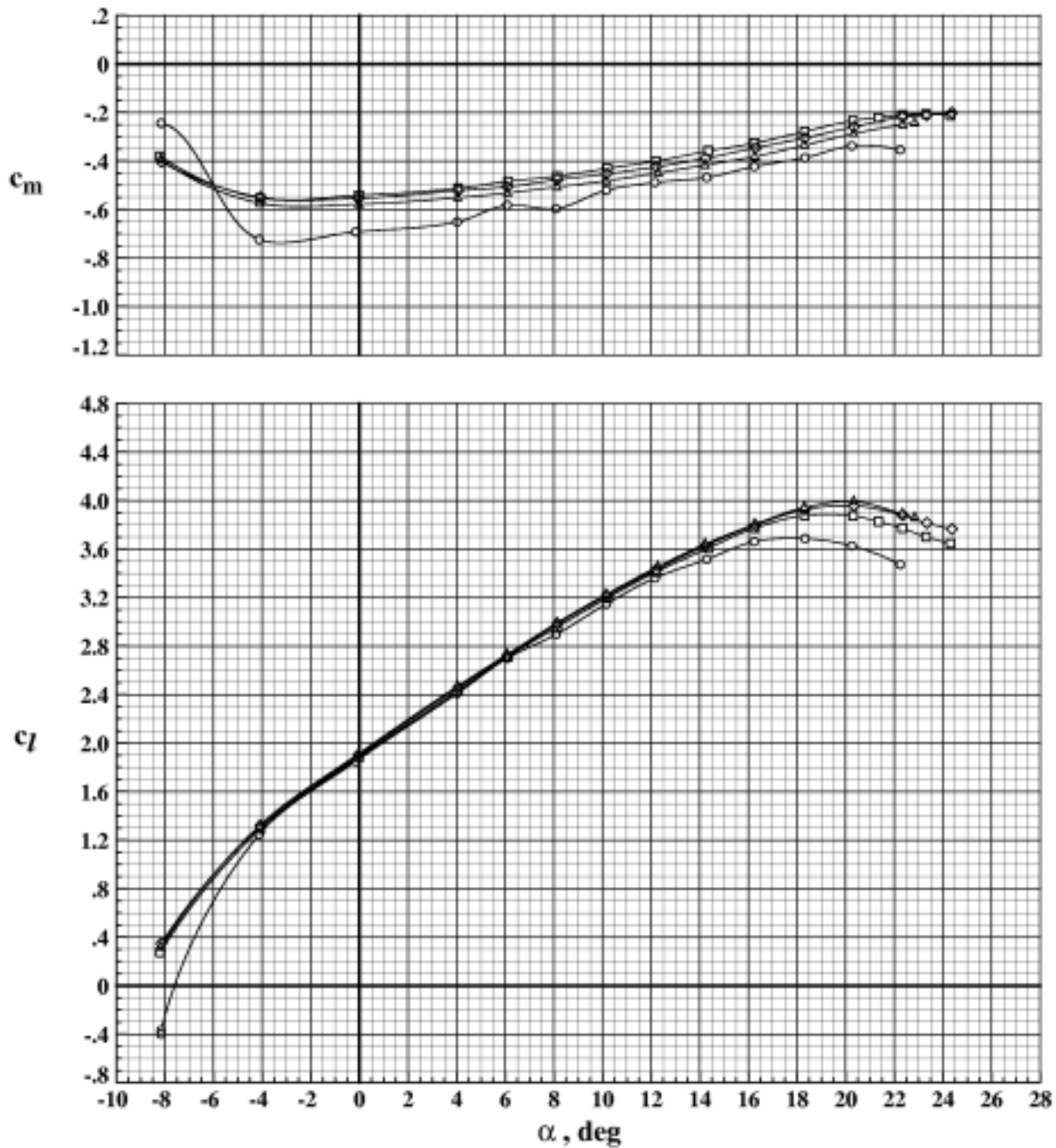


Figure 34. Effect of Reynolds number on aerodynamic performance of EET High-Lift Airfoil with $\delta_s = -40.0^\circ$, $\delta_v = 15.0^\circ$, and $\delta_f = 15.0^\circ$ at $M_\infty = 0.202$.

	Run	$R_n / 10^6$
○	83	2.51
□	89	4.24
◇	91	6.08
△	96	12.18
▽	98	18.17

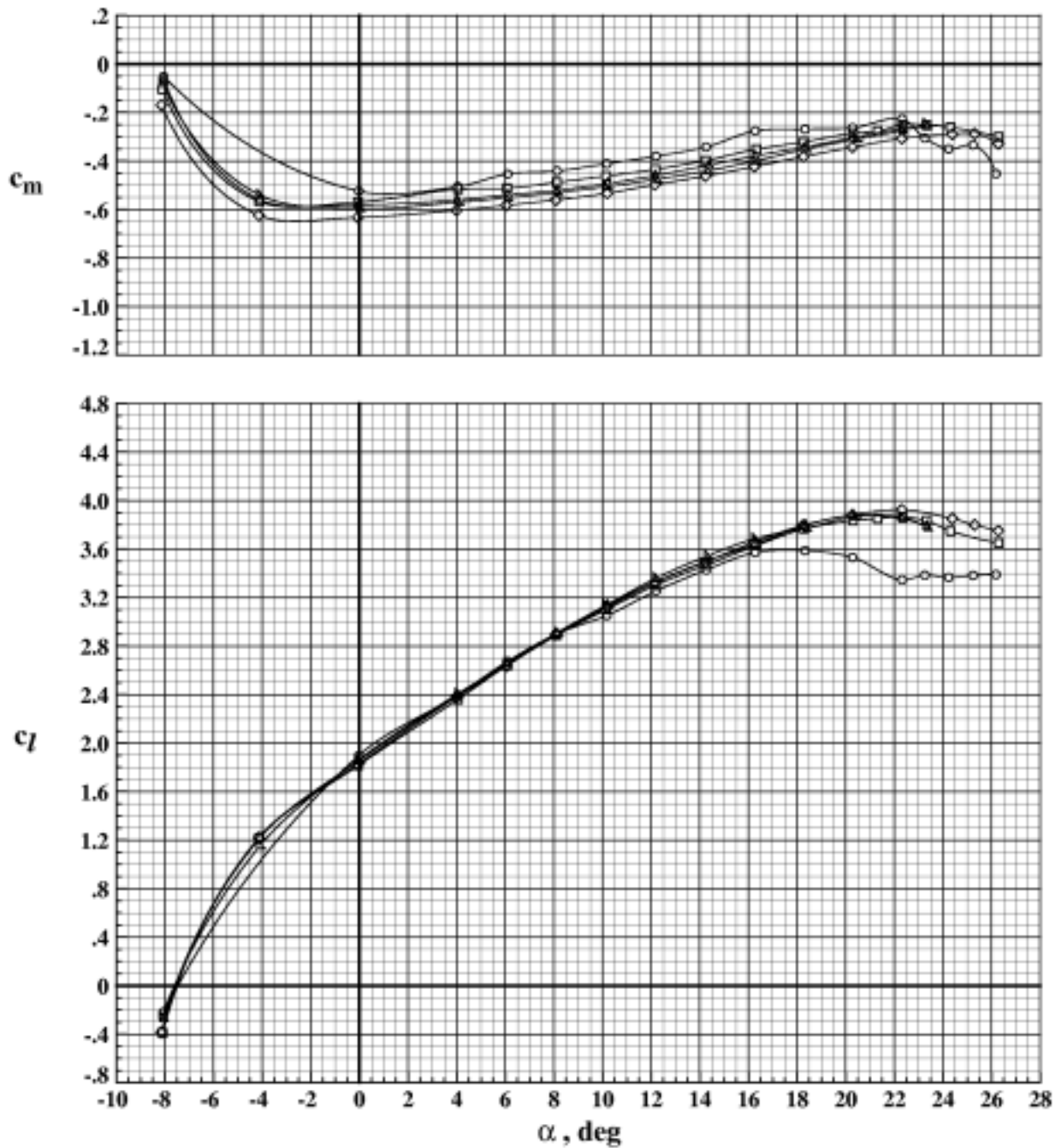


Figure 35. Effect of Reynolds number on aerodynamic performance of EET High-Lift Airfoil with $\delta_s = -50.0^\circ$, $\delta_v = 15.0^\circ$, and $\delta_f = 15.0^\circ$ at $M_\infty = 0.203$.

	Run	$R_n / 10^6$
○	99	2.52
□	100	6.20
◇	102	12.14
△	103	18.21

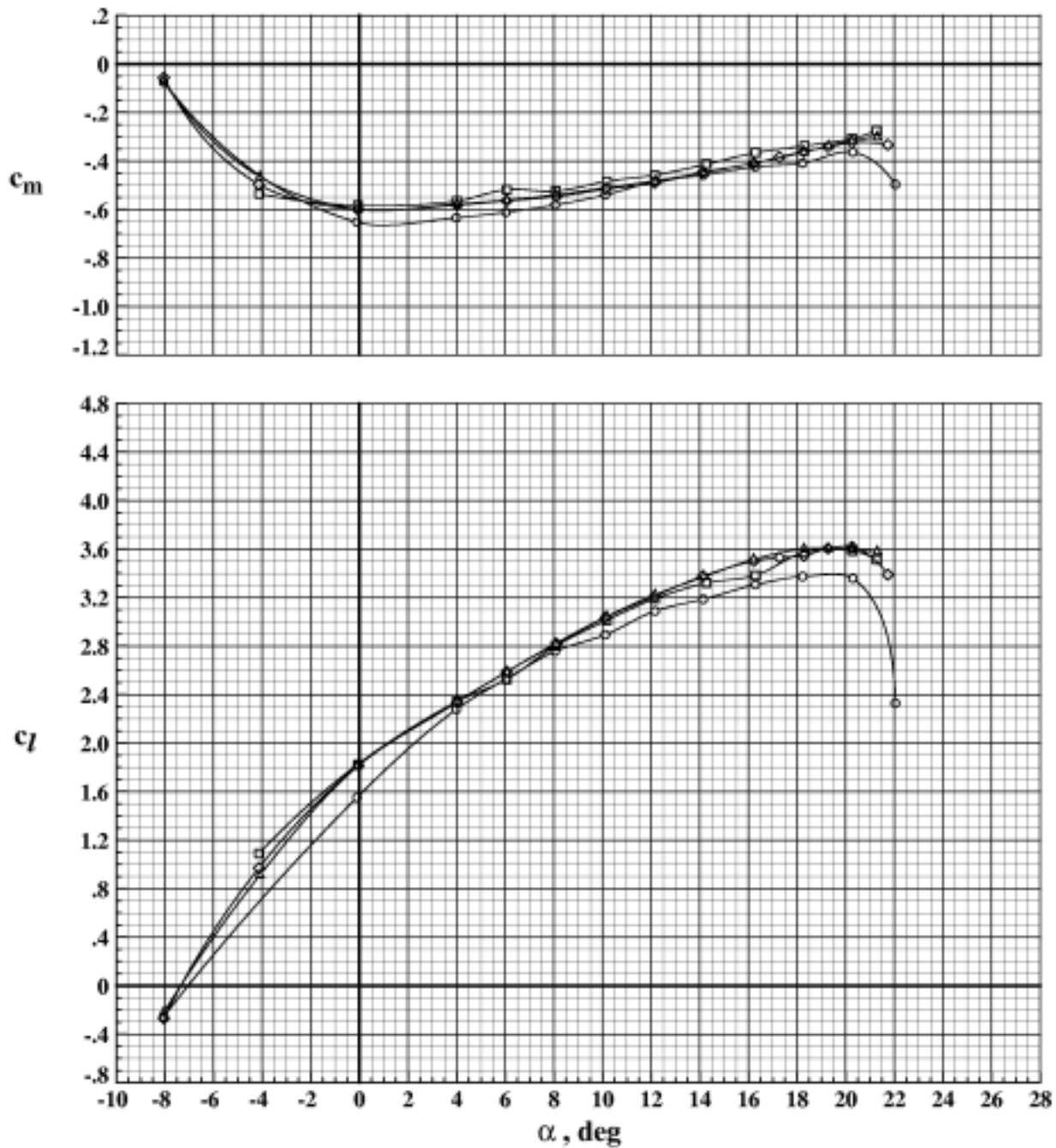


Figure 36. Effect of Reynolds number on aerodynamic performance of EET High-Lift Airfoil with $\delta_s = -60.0^\circ$, $\delta_v = 15.0^\circ$, and $\delta_f = 15.0^\circ$ at $M_\infty = 0.202$.

	Run	$R_n / 10^6$
○	28	2.52
□	29	6.09
◇	32	12.12
△	34	18.19

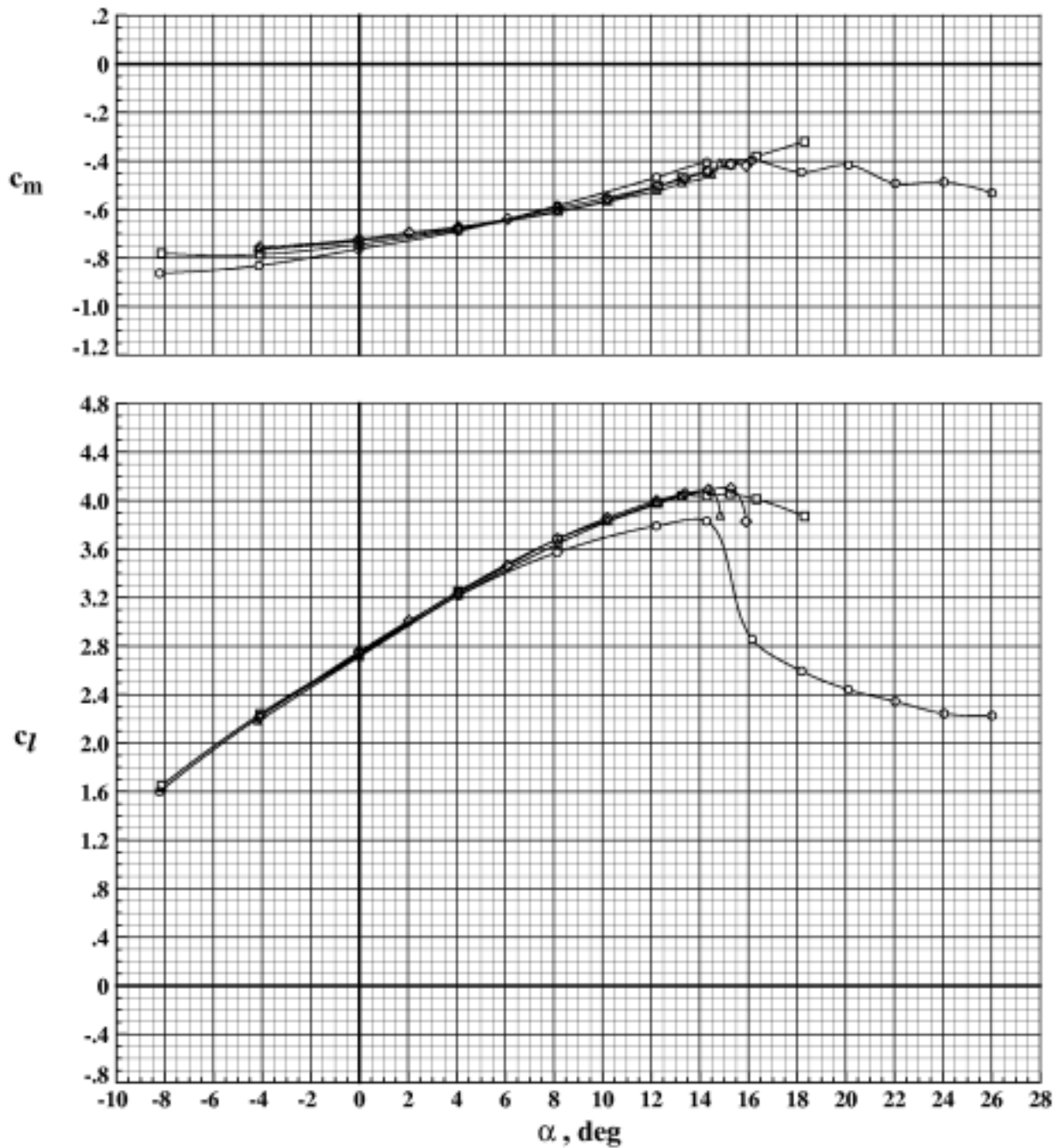


Figure 37. Effect of Reynolds number on aerodynamic performance of EET High-Lift Airfoil with $\delta_s = -30.0^\circ$, $\delta_v = 22.5^\circ$, and $\delta_f = 22.5^\circ$ at $M_\infty = 0.203$.

	Run	$R_n / 10^6$
○	20	2.51
□	23	6.08
◇	25	12.15
△	27	18.16

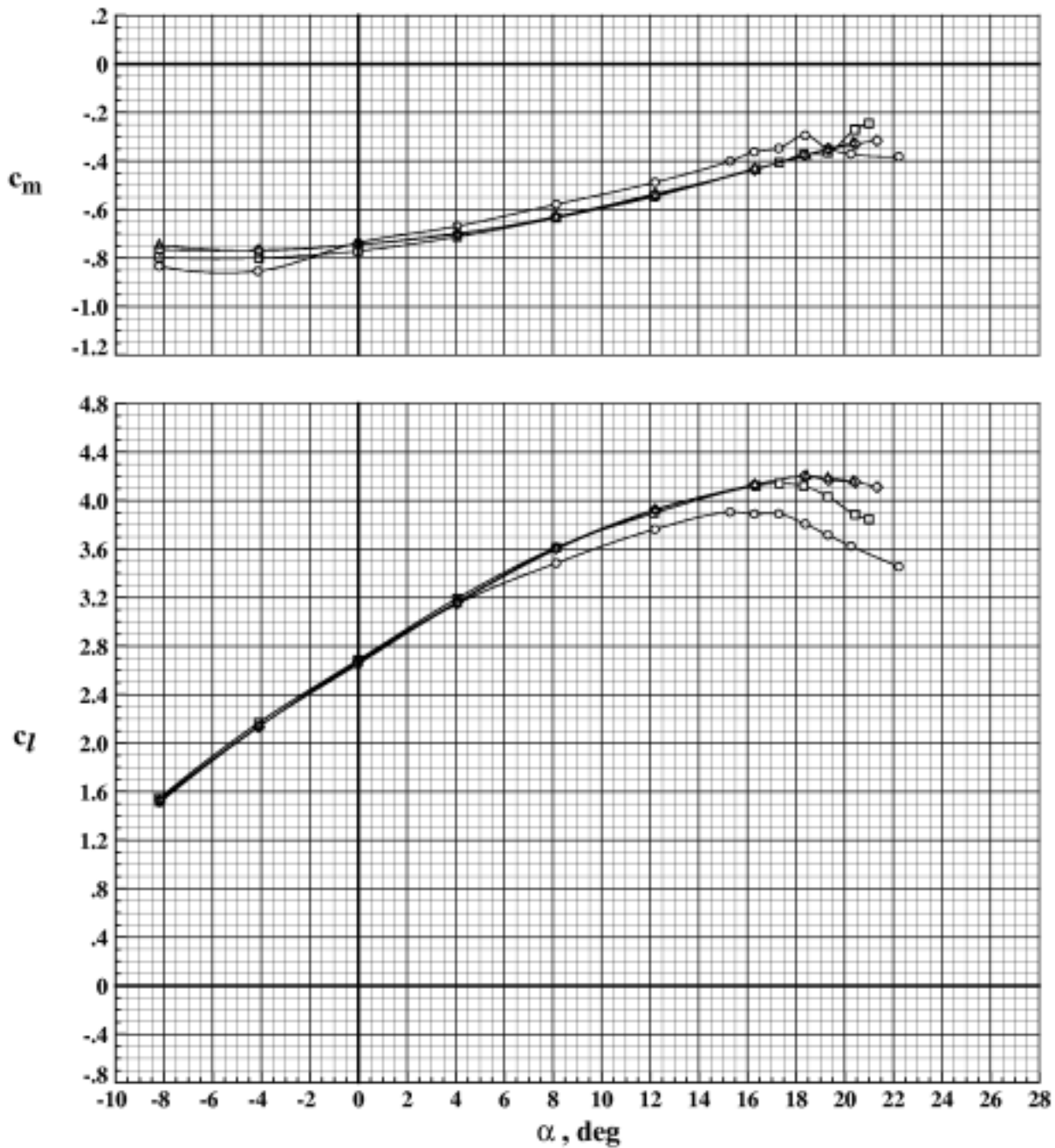


Figure 38. Effect of Reynolds number on aerodynamic performance of EET High-Lift Airfoil with $\delta_s = -40.0^\circ$, $\delta_v = 22.5^\circ$, and $\delta_f = 22.5^\circ$ at $M_\infty = 0.203$.

	Run	$R_n / 10^6$
○	114	2.47
□	115	6.09
◇	116	12.15
△	117	18.15

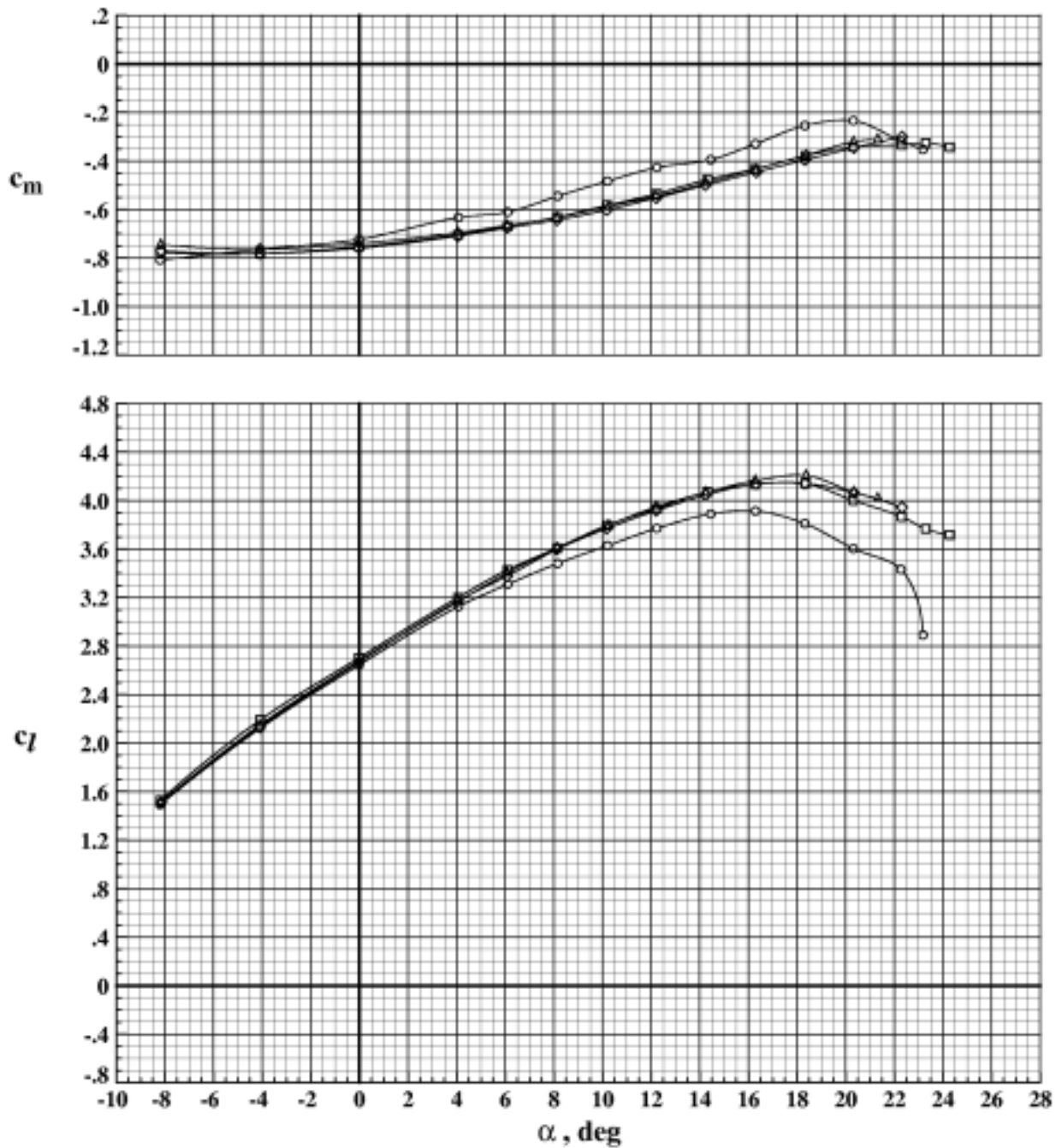


Figure 39. Effect of Reynolds number on aerodynamic performance of EET High-Lift Airfoil with $\delta_s = -40.0^\circ$, $\delta_v = 22.5^\circ$, and $\delta_f = 22.5^\circ$ at $M_\infty = 0.203$.

	Run	$R_n / 10^6$
○	4	2.62
□	6	6.10
◇	9	12.10
△	11	18.10

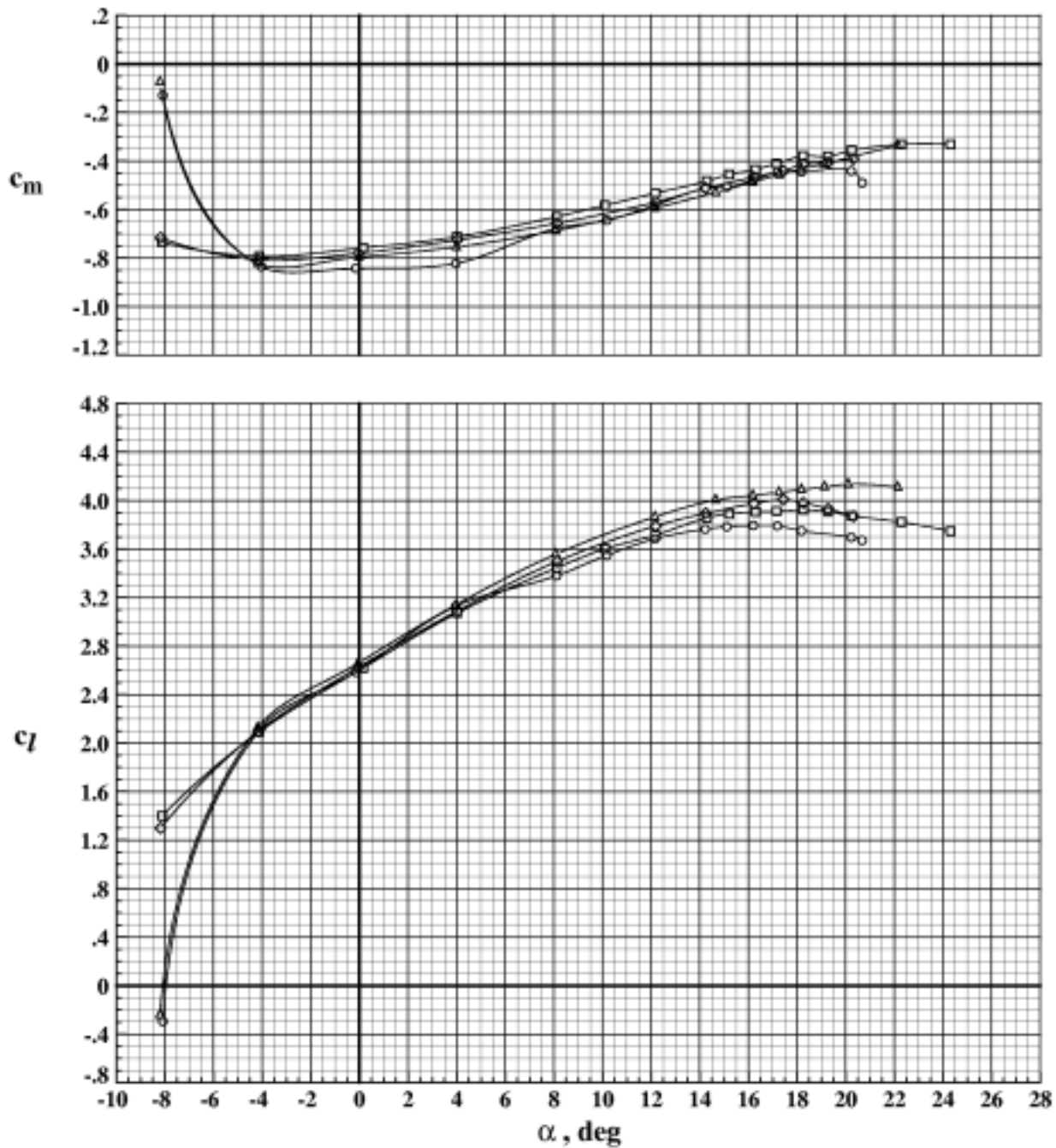


Figure 40. Effect of Reynolds number on aerodynamic performance of EET High-Lift Airfoil with $\delta_s = -50.0^\circ$, $\delta_v = 22.5^\circ$, and $\delta_f = 22.5^\circ$ at $M_\infty = 0.203$.

	Run	$R_n / 10^6$
○	112	2.47
□	106	6.11
◇	107	12.15
△	109	18.21

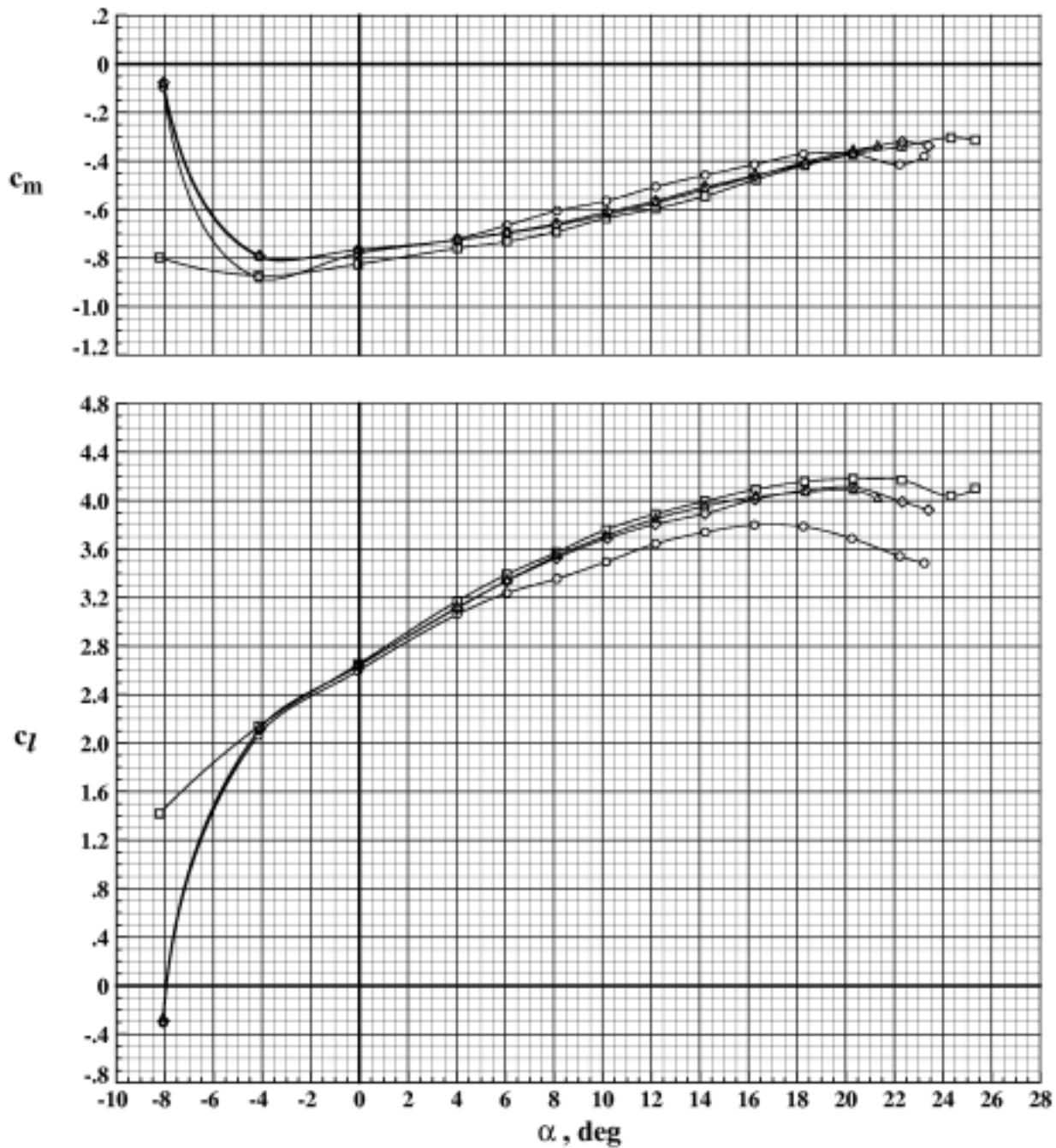


Figure 41. Effect of Reynolds number on aerodynamic performance of EET High-Lift Airfoil with $\delta_s = -50.0^\circ$, $\delta_v = 22.5^\circ$, and $\delta_f = 22.5^\circ$ at $M_\infty = 0.203$.

	Run	$R_n / 10^6$
○	13	2.52
□	15	6.14
◇	17	12.15
△	18	18.18

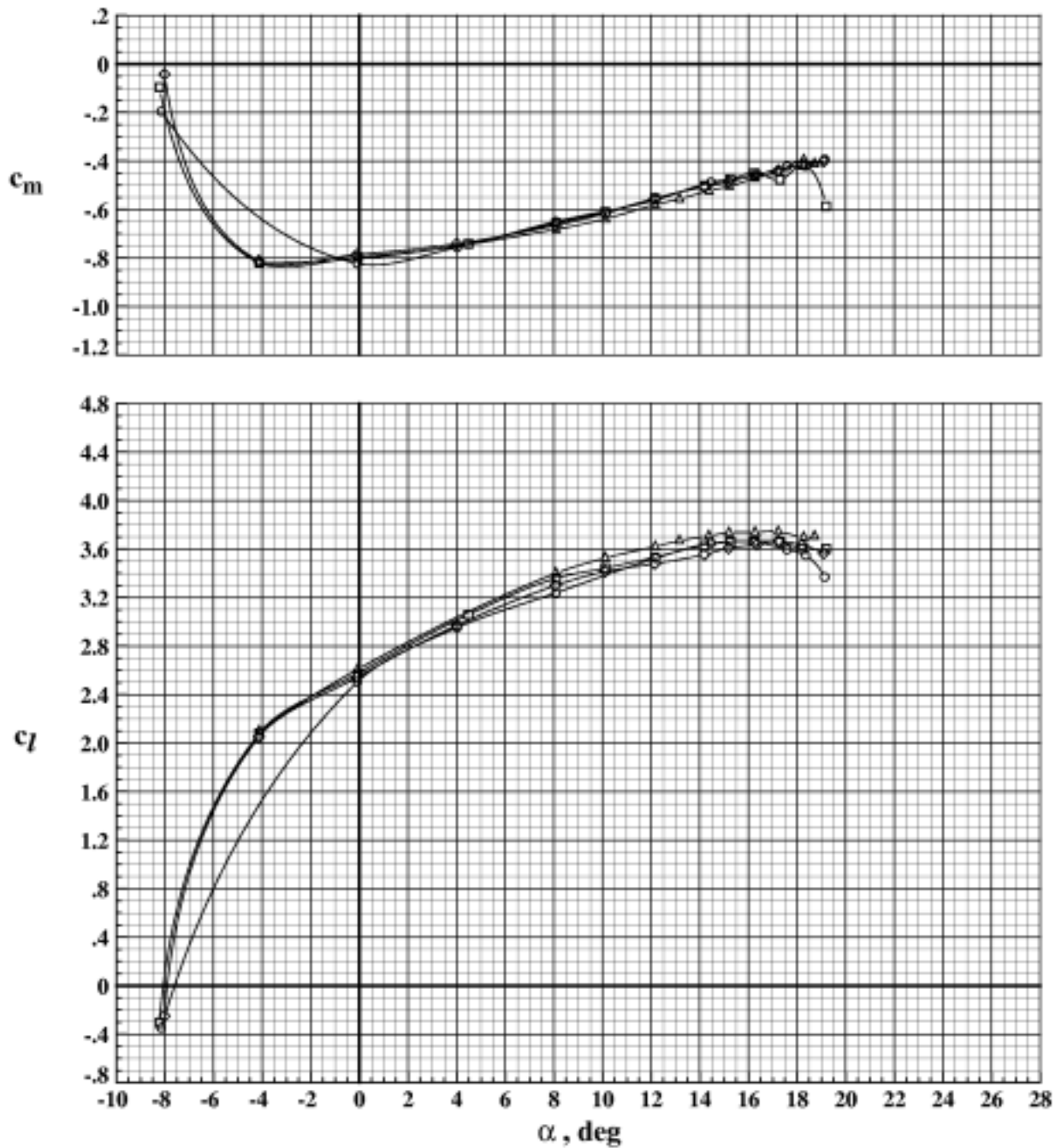


Figure 42. Effect of Reynolds number on aerodynamic performance of EET High-Lift Airfoil with $\delta_s = -60.0^\circ$, $\delta_v = 22.5^\circ$, and $\delta_f = 22.5^\circ$ at $M_\infty = 0.203$.

	Run	$R_n / 10^6$
○	118	2.56
□	119	6.10
◇	120	12.20
△	121	18.19

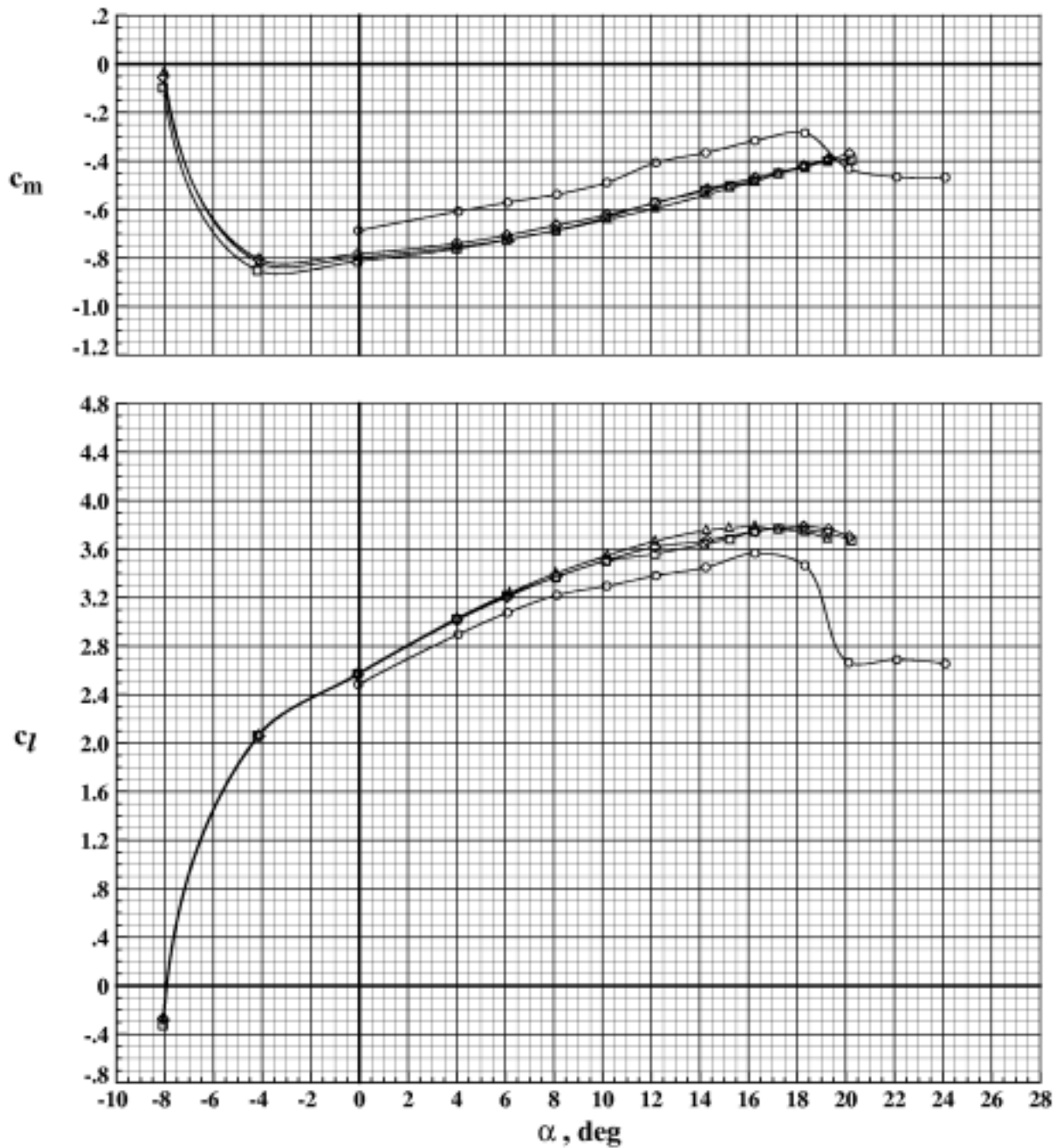


Figure 43. Effect of Reynolds number on aerodynamic performance of EET High-Lift Airfoil with $\delta_s = -60.0^\circ$, $\delta_v = 22.5^\circ$, and $\delta_f = 22.5^\circ$ at $M_\infty = 0.204$.

	Run	$R_n / 10^6$
○	37	2.52
□	39	6.08
◇	41	12.15
△	42	18.20

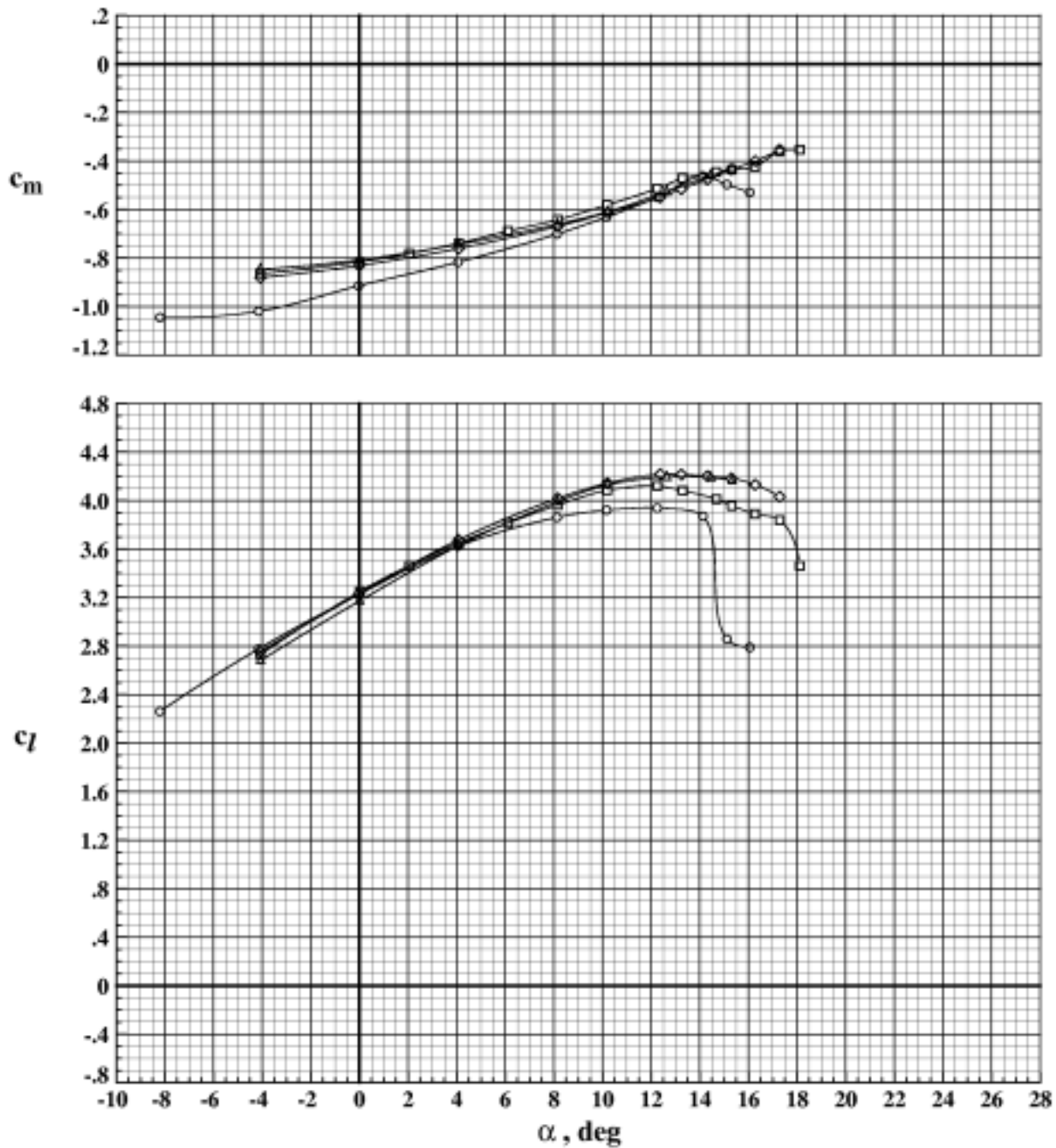


Figure 44. Effect of Reynolds number on aerodynamic performance of EET High-Lift Airfoil with $\delta_s = -30.0^\circ$, $\delta_v = 30.0^\circ$, and $\delta_f = 30.0^\circ$ at $M_\infty = 0.204$.

	Run	$R_n / 10^6$
○	43	2.49
□	44	4.25
◇	45	6.09
△	46	12.16
▴	47	18.22

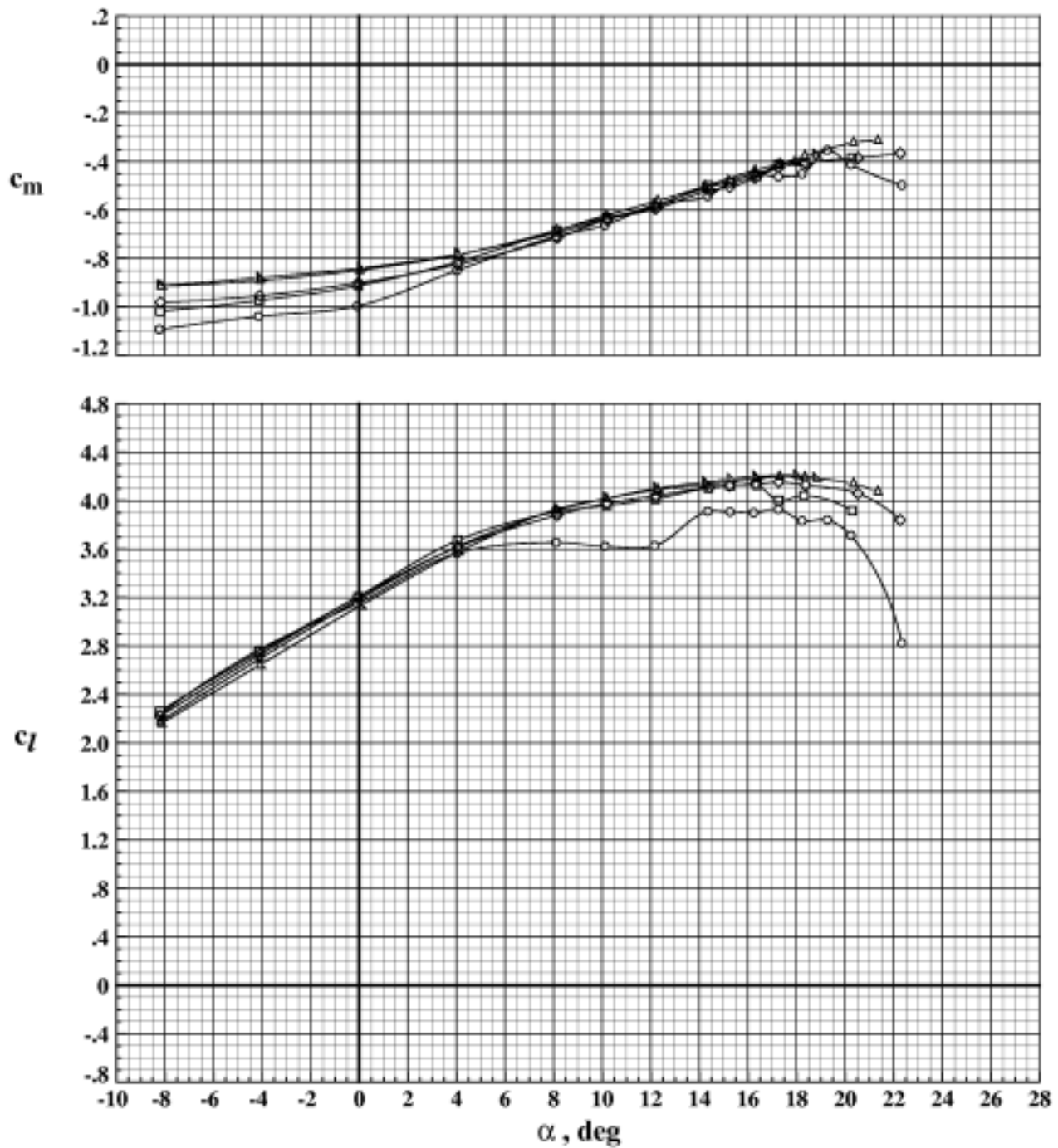


Figure 45. Effect of Reynolds number on aerodynamic performance of EET High-Lift Airfoil with $\delta_s = -40.0^\circ$, $\delta_v = 30.0^\circ$, and $\delta_f = 30.0^\circ$ at $M_\infty = 0.203$.

	Run	$R_n / 10^6$
○	49	2.50
□	50	4.31
◇	51	6.14
△	52	12.15
▽	53	18.26

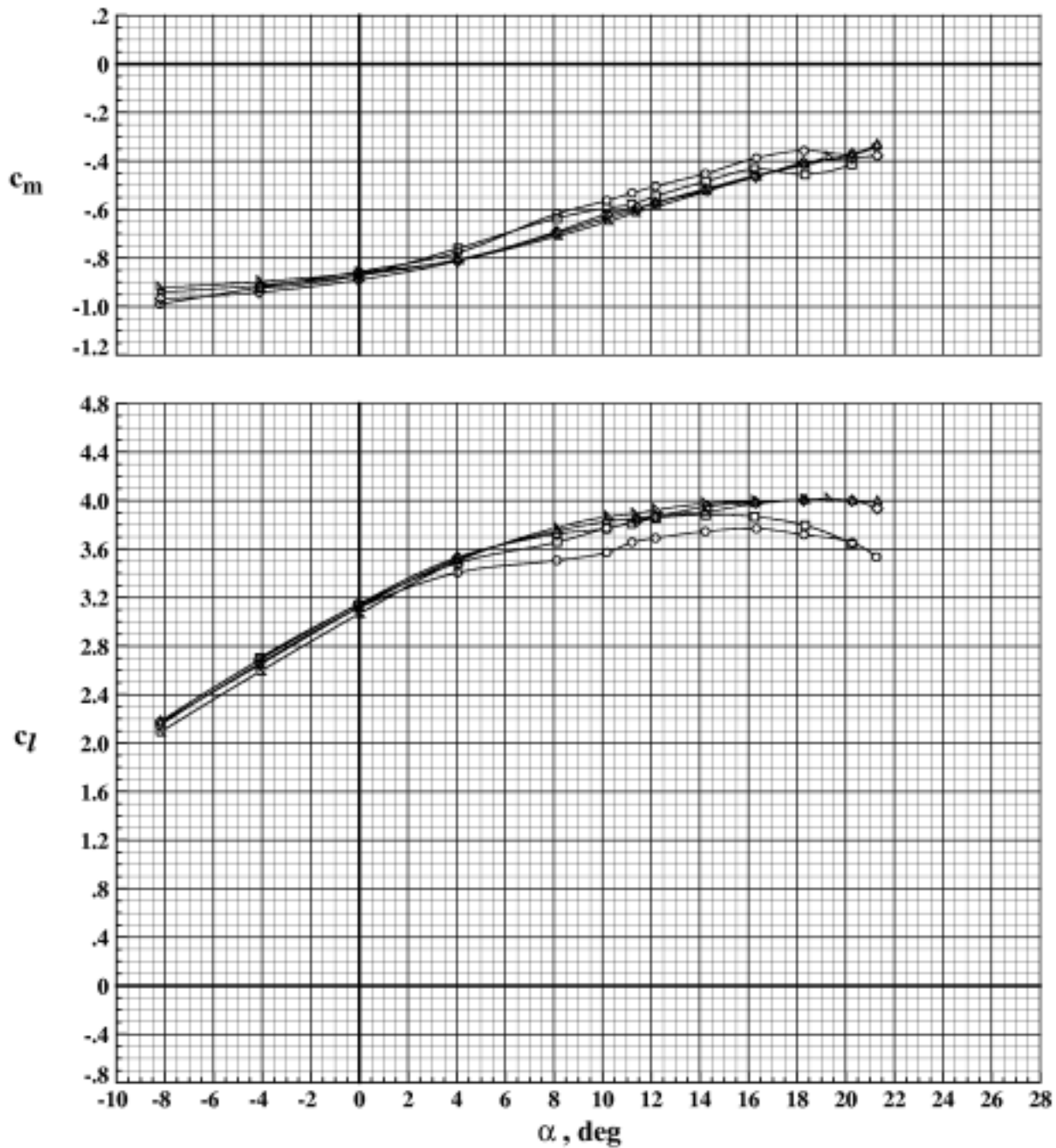


Figure 46. Effect of Reynolds number on aerodynamic performance of EET High-Lift Airfoil with $\delta_s = -50.0^\circ$, $\delta_v = 30.0^\circ$, and $\delta_T = 30.0^\circ$ at $M_\infty = 0.203$.

Run	$R_n / 10^6$	
○	54	2.52
□	55	6.12
◇	56	12.20
△	57	18.44

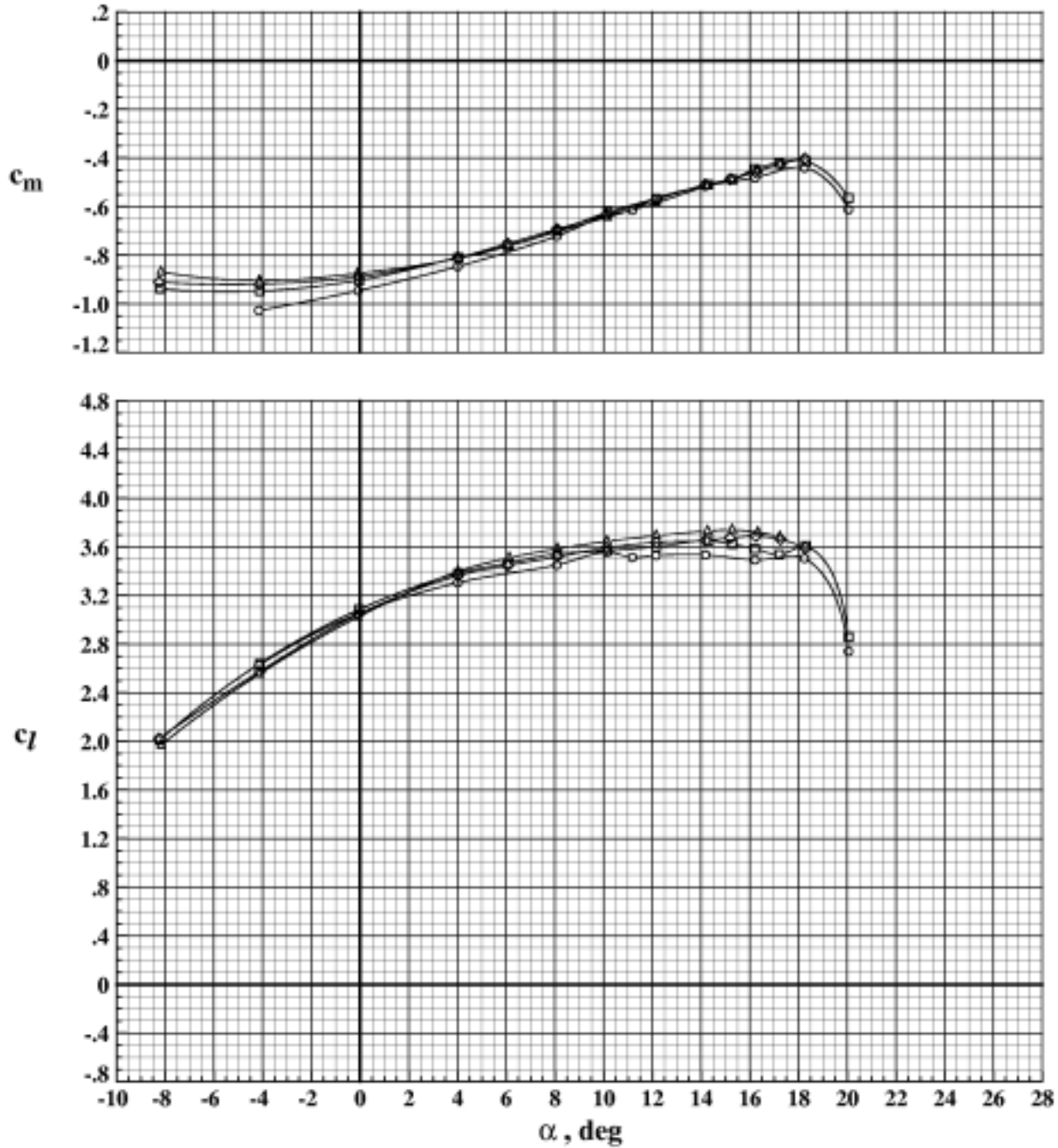


Figure 47. Effect of Reynolds number on aerodynamic performance of EET High-Lift Airfoil with $\delta_s = -60.0^\circ$, $\delta_v = 30.0^\circ$, and $\delta_f = 30.0^\circ$ at $M_\infty = 0.203$.

	Run	M_∞	$R_n / 10^6$
○	82	0.103	1.261
□	83	0.205	2.506
◇	84	0.254	3.121
△	85	0.303	3.706
▽	86	0.355	4.298

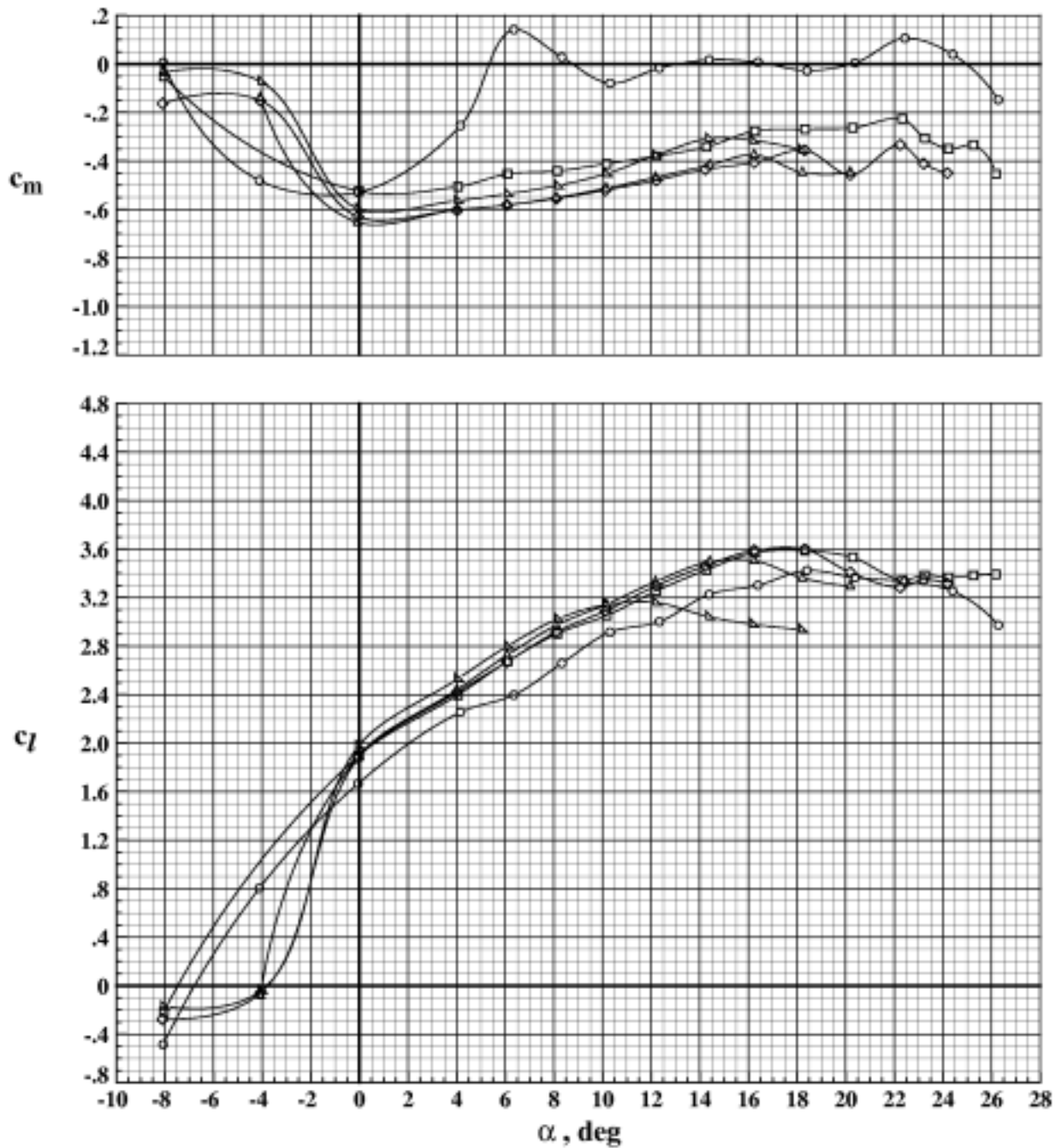


Figure 48. Effect of Mach number on aerodynamic performance of EET High-Lift Airfoil with $\delta_s = -50.0^\circ$, $\delta_v = 15.0^\circ$, and $\delta_f = 15.0^\circ$.

	Run	M_∞	$R_\infty / 10^6$
○	95	0.101	6.000
□	92	0.151	6.094
◇	91	0.202	6.078
△	90	0.253	6.032
▽	88	0.303	6.068
▷	87	0.352	6.027

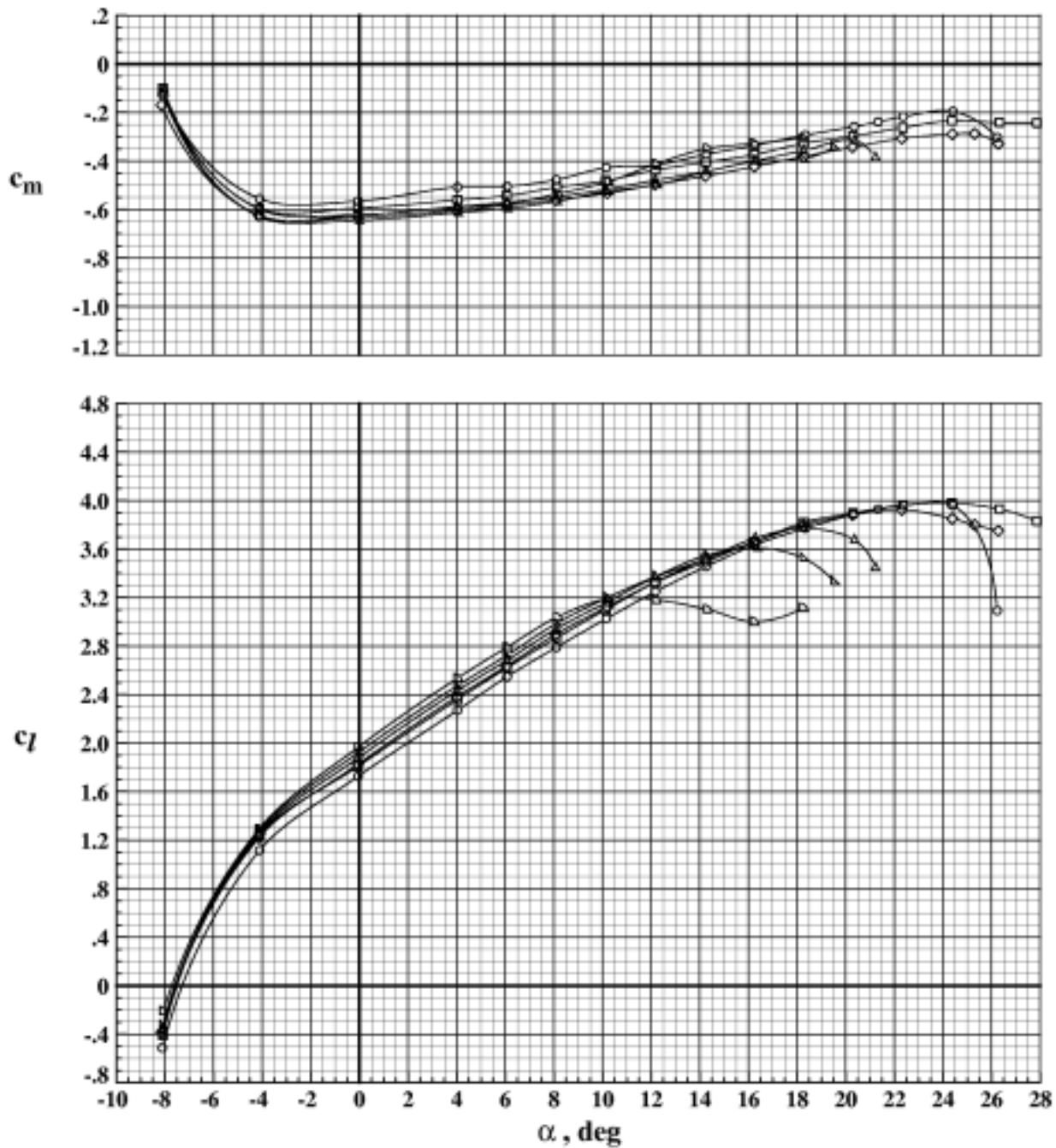


Figure 49. Effect of Mach number on aerodynamic performance of EET High-Lift Airfoil with $\delta_s = -50.0^\circ$, $\delta_v = 15.0^\circ$, and $\delta_T = 15.0^\circ$.

	Run	M_∞	$R_n / 10^6$
○	97	0.152	12.197
□	96	0.203	12.180
◇	94	0.252	12.096
△	93	0.287	12.045

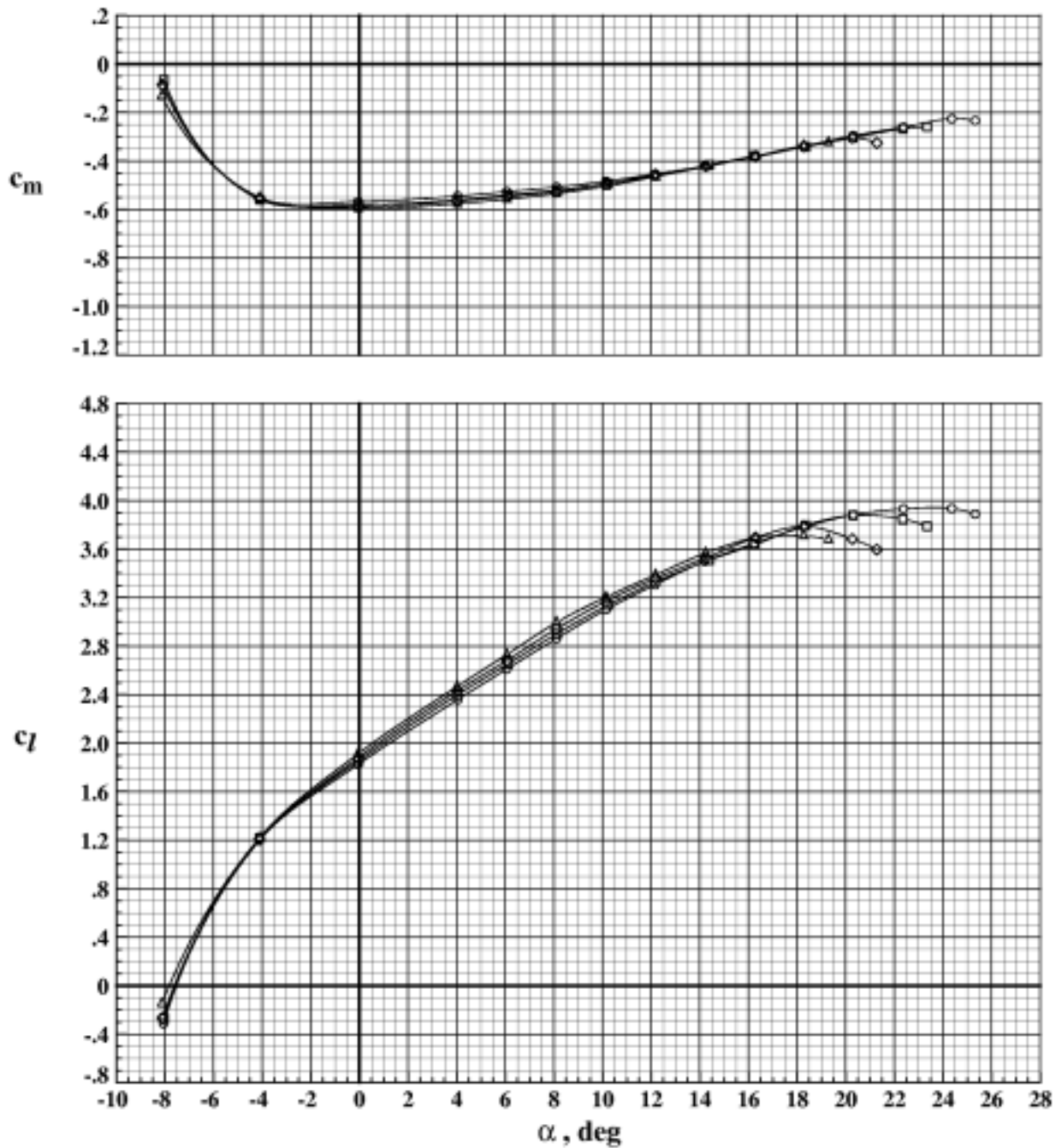


Figure 50. Effect of Mach number on aerodynamic performance of EET High-Lift Airfoil with $\delta_s = -50.0^\circ$, $\delta_v = 15.0^\circ$, and $\delta_T = 15.0^\circ$.

	Run	M_∞	$R_\infty / 10^6$
○	33	0.151	12.126
□	32	0.202	12.117
◇	31	0.252	12.156
△	30	0.283	12.040

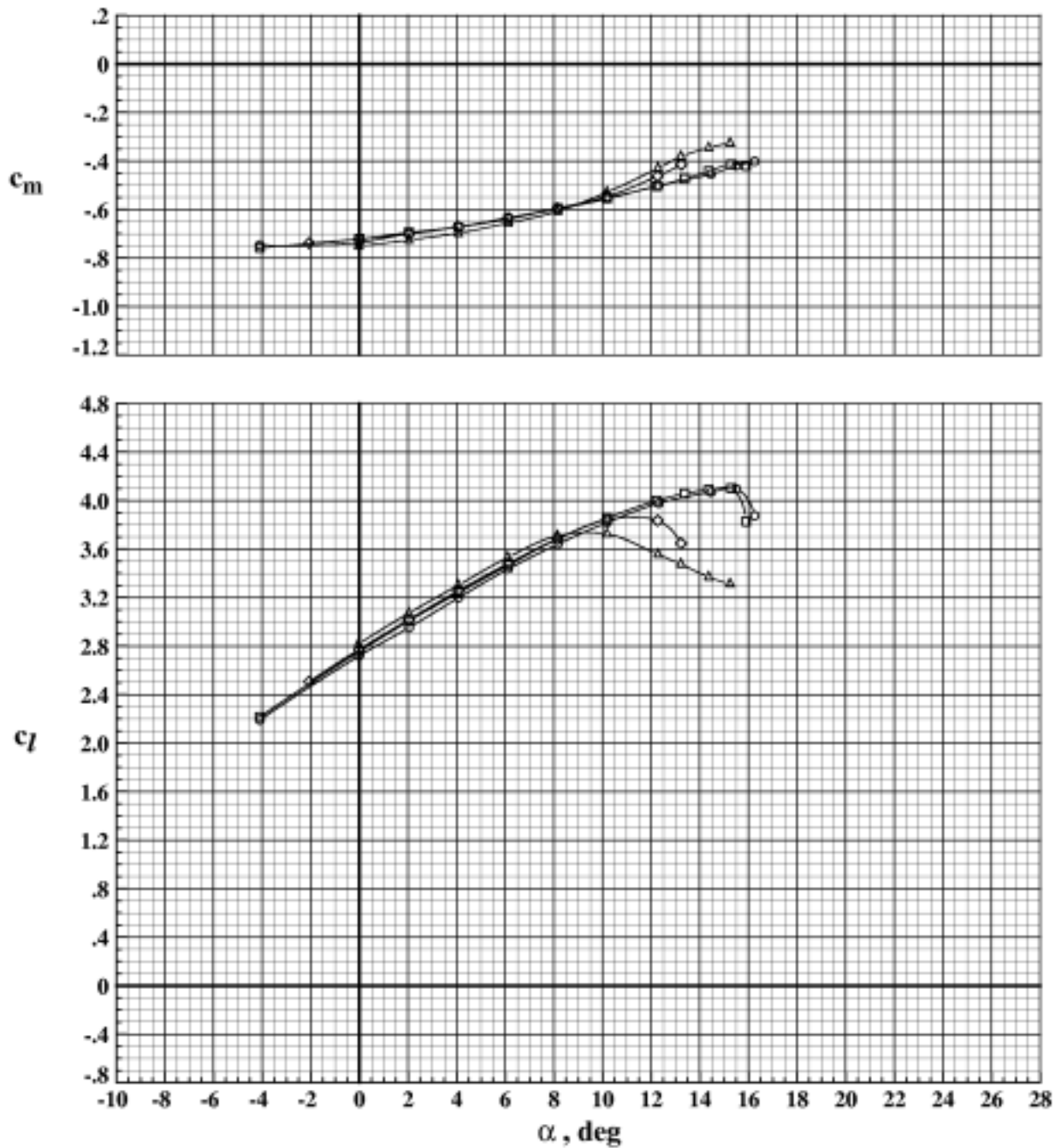


Figure 51. Effect of Mach number on aerodynamic performance of EET High-Lift Airfoil with $\delta_s = -30.0^\circ$, $\delta_v = 22.5^\circ$, and $\delta_f = 22.5^\circ$.

Run	Sidewall Blowing
○	100 On
□	101 Off

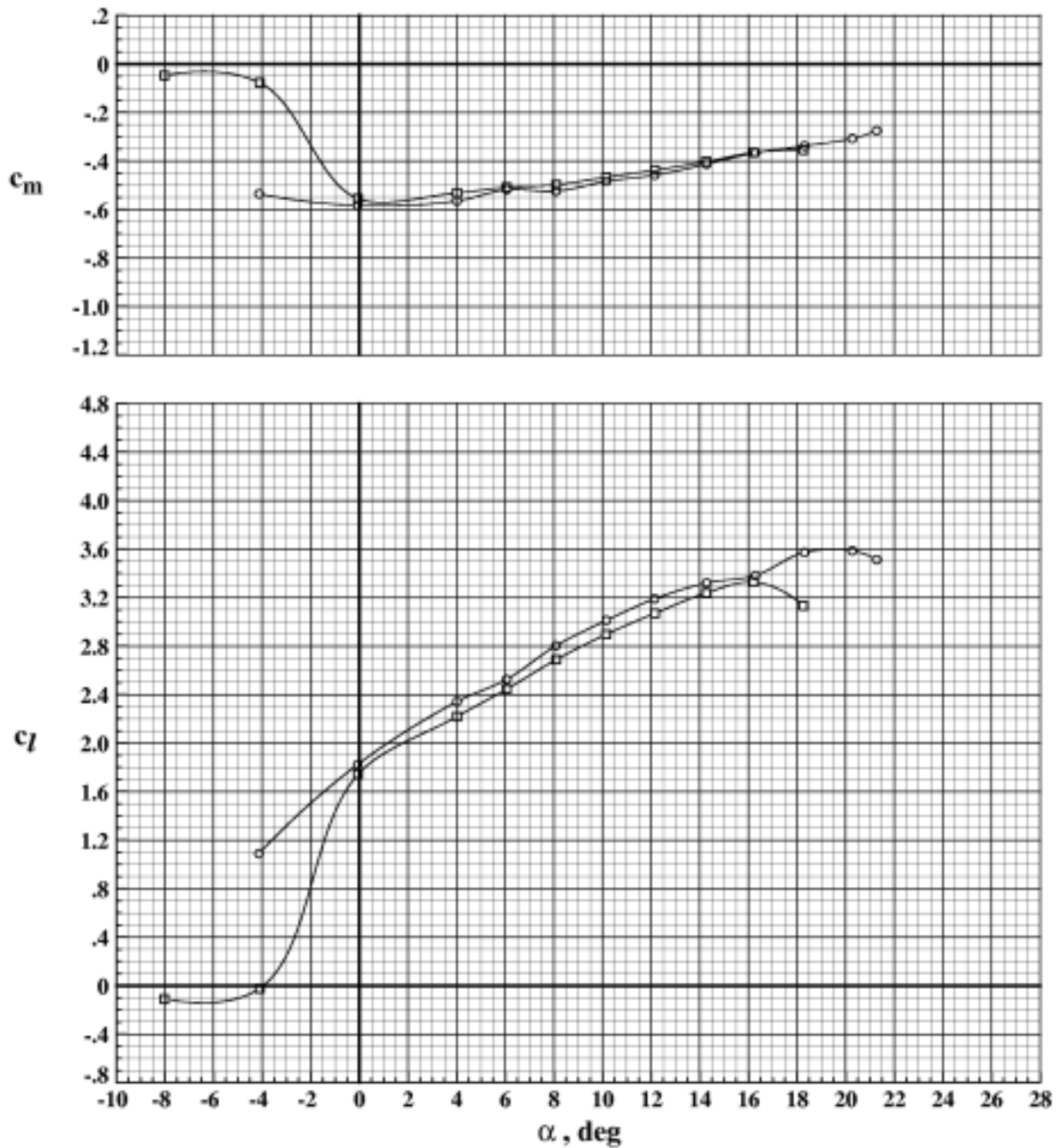


Figure 52. Effect of sidewall blowing on aerodynamic performance of EET High-Lift Airfoil with $\delta_s = -60.0^\circ$, $\delta_v = 15.0^\circ$, and $\delta_f = 15.0^\circ$ at $R_n = 6.117 \times 10^6$ and at $M_\infty = 0.203$.

Run	Sidewall Blowing
○	4 On
□	2 Off

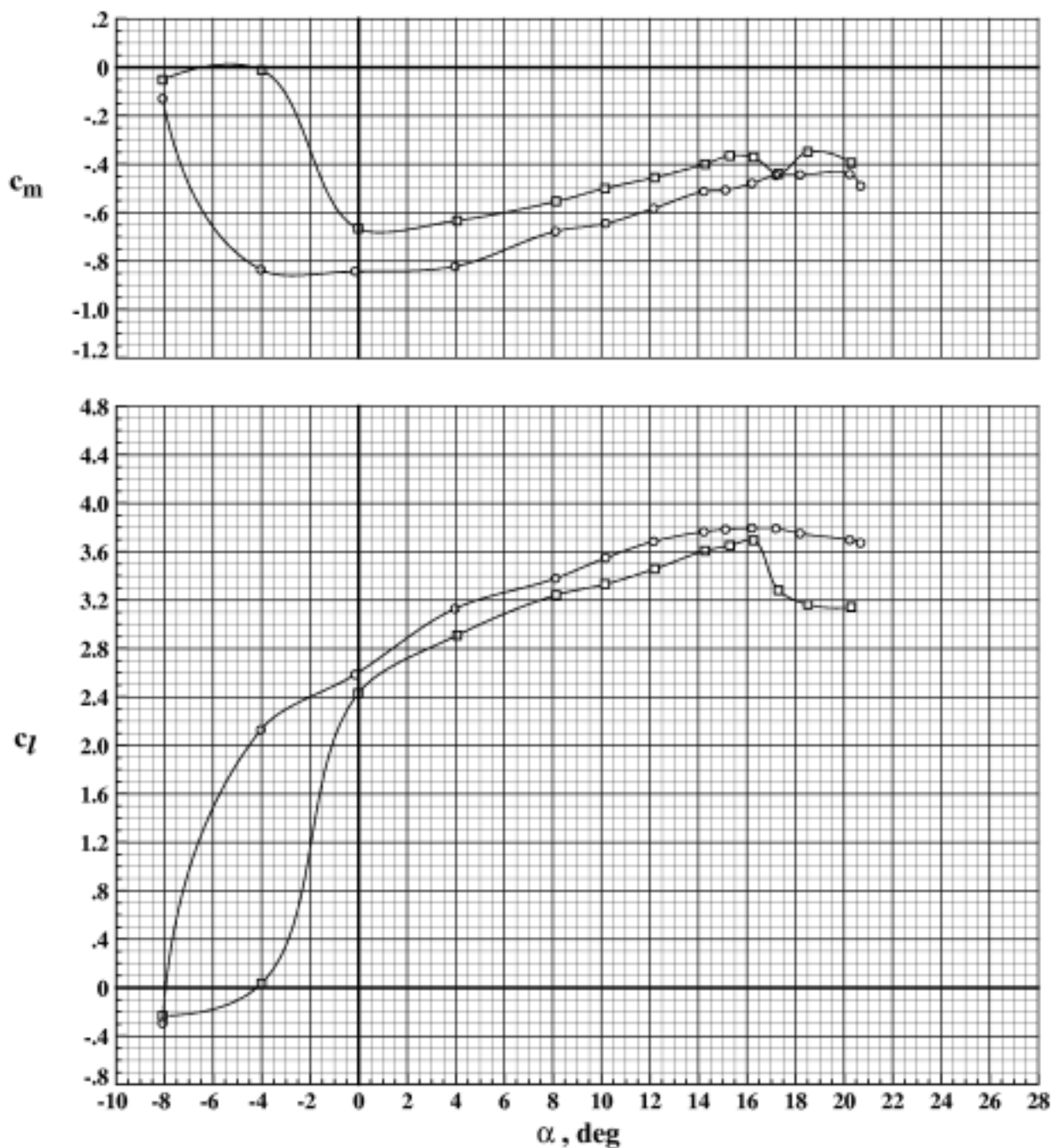


Figure 53. Effect of sidewall blowing on aerodynamic performance of EET High-Lift Airfoil with $\delta_x = -50.0^\circ$, $\delta_y = 22.5^\circ$, and $\delta_z = 22.5^\circ$ at $R_n = 2.613 \times 10^6$ and at $M_\infty = 0.203$.

	Run	Sidewall Blowing
○	112	On
□	104	Off

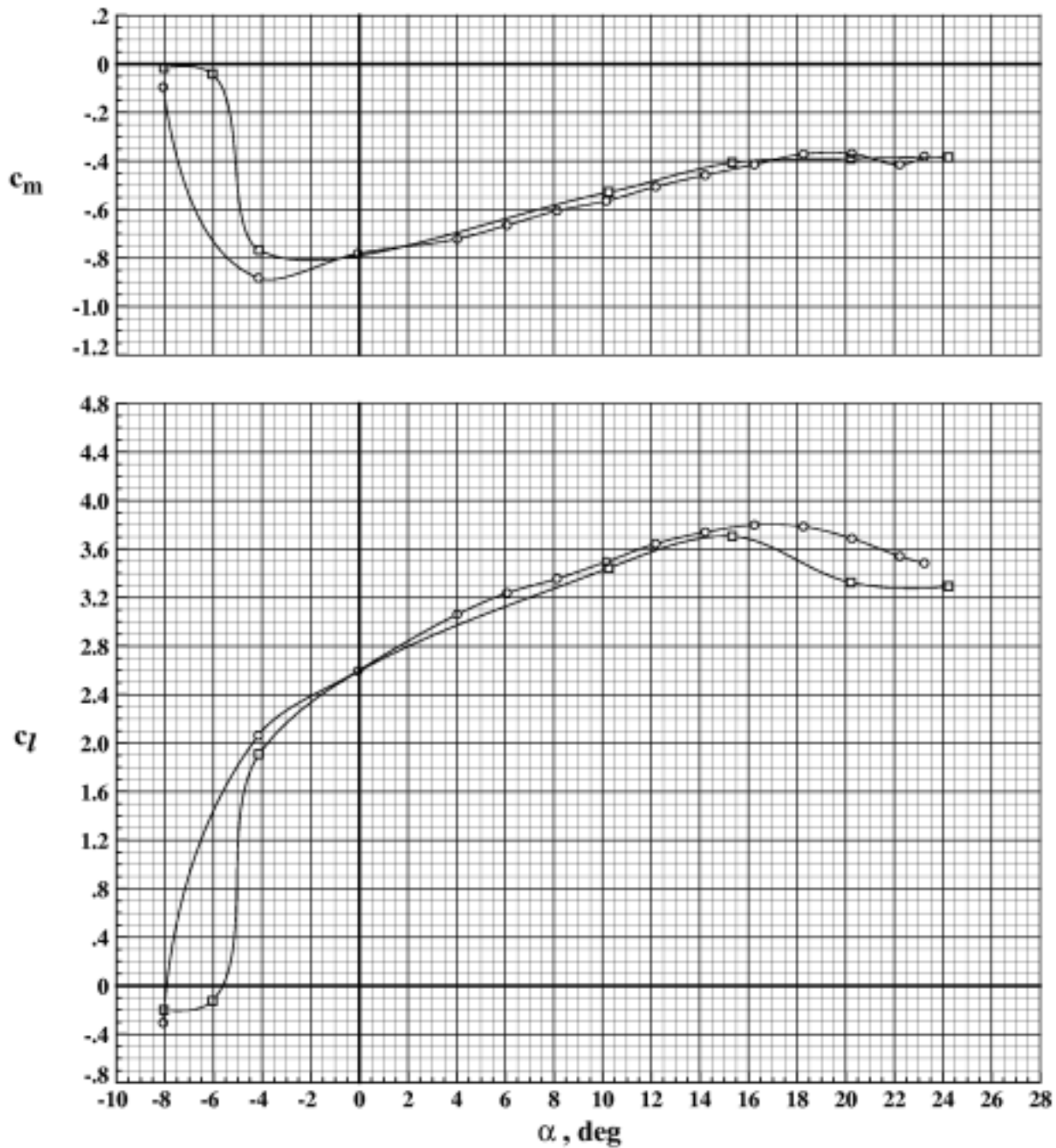


Figure 54. Effect of sidewall blowing on aerodynamic performance of EET High-Lift Airfoil with $\delta_s = -50.0^\circ$, $\delta_v = 22.5^\circ$, and $\delta_f = 22.5^\circ$ at $R_n = 2.489 \times 10^6$ and at $M_\infty = 0.204$.

	Run	Sidewall Blowing
○	109	On
□	111	Off

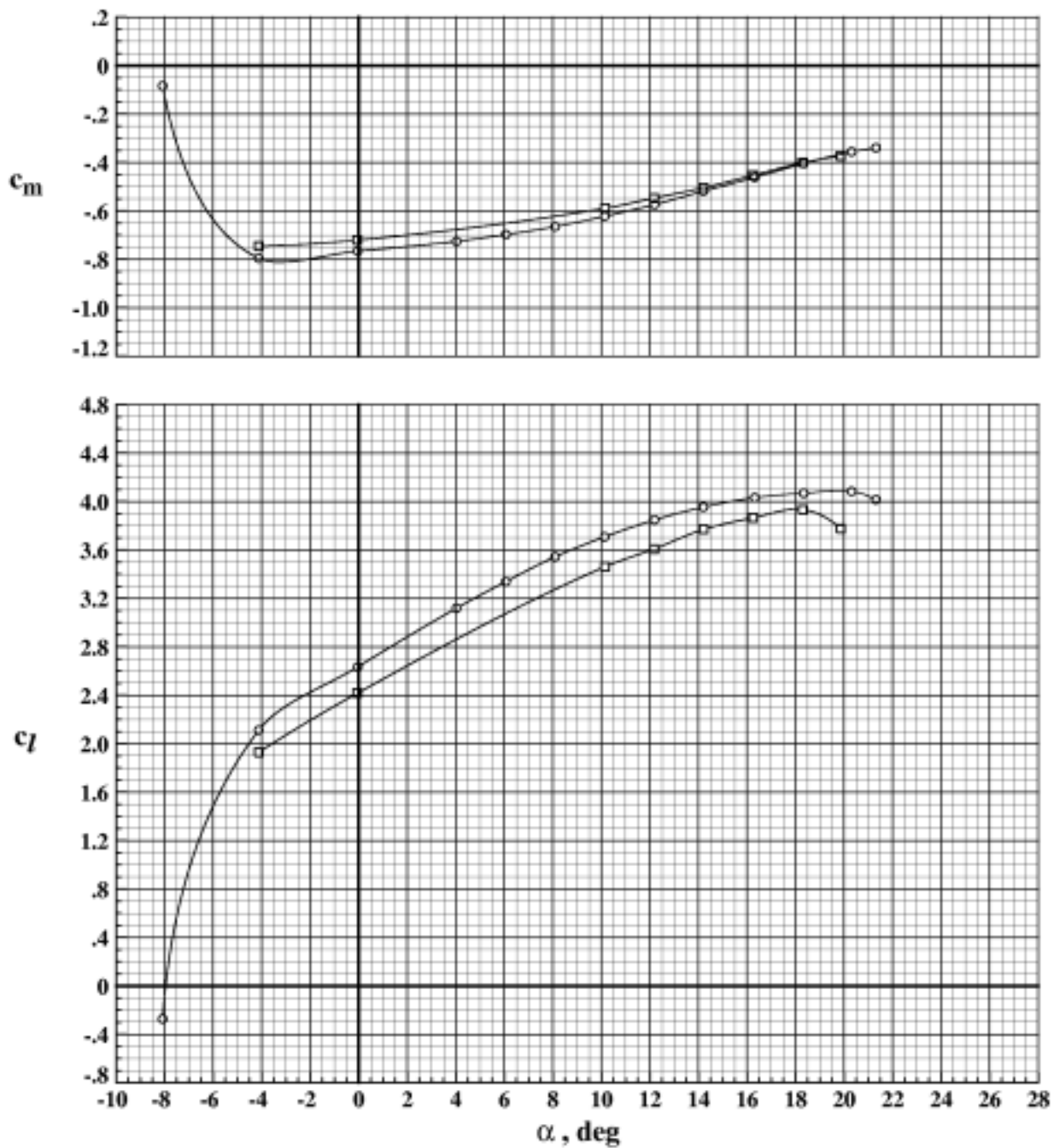


Figure 55. Effect of sidewall blowing on aerodynamic performance of EET High-Lift Airfoil with $\delta_s = -50.0^\circ$, $\delta_v = 22.5^\circ$, and $\delta_f = 22.5^\circ$ at $R_n = 18.180 \times 10^6$ and at $M_\infty = 0.203$.

	Run	Sidewall Blowing
○	13	On
□	14	Off

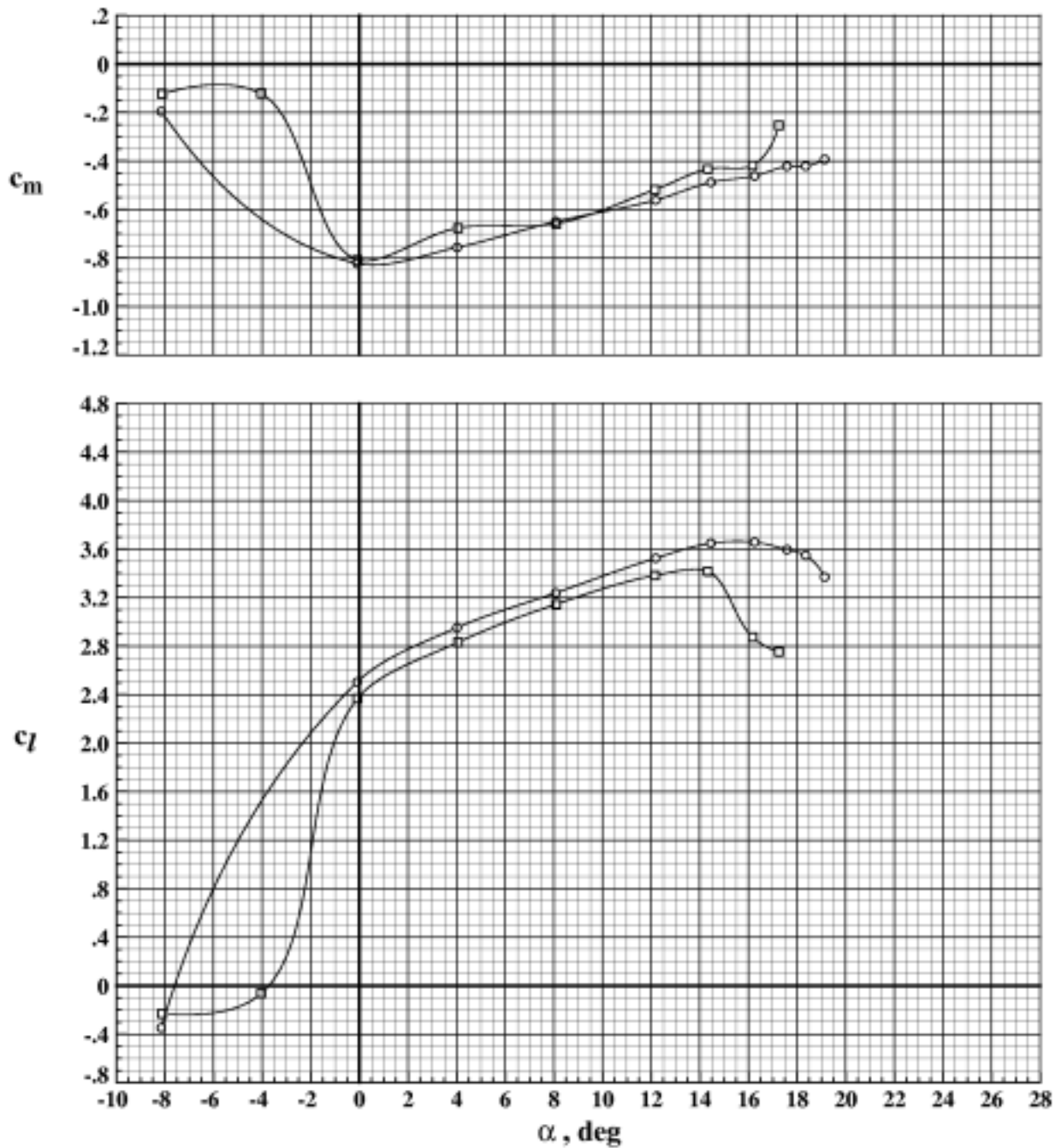


Figure 56. Effect of sidewall blowing on aerodynamic performance of EET High-Lift Airfoil with $\delta_s = -60.0^\circ$, $\delta_v = 22.5^\circ$, and $\delta_f = 22.5^\circ$ at $R_n = 2.518 \times 10^6$ and at $M_\infty = 0.203$.

Run	Sidewall Blowing
○	119 On
□	122 Box 1 Off
◇	125 Box 1,2,3 Off
△	126 Off

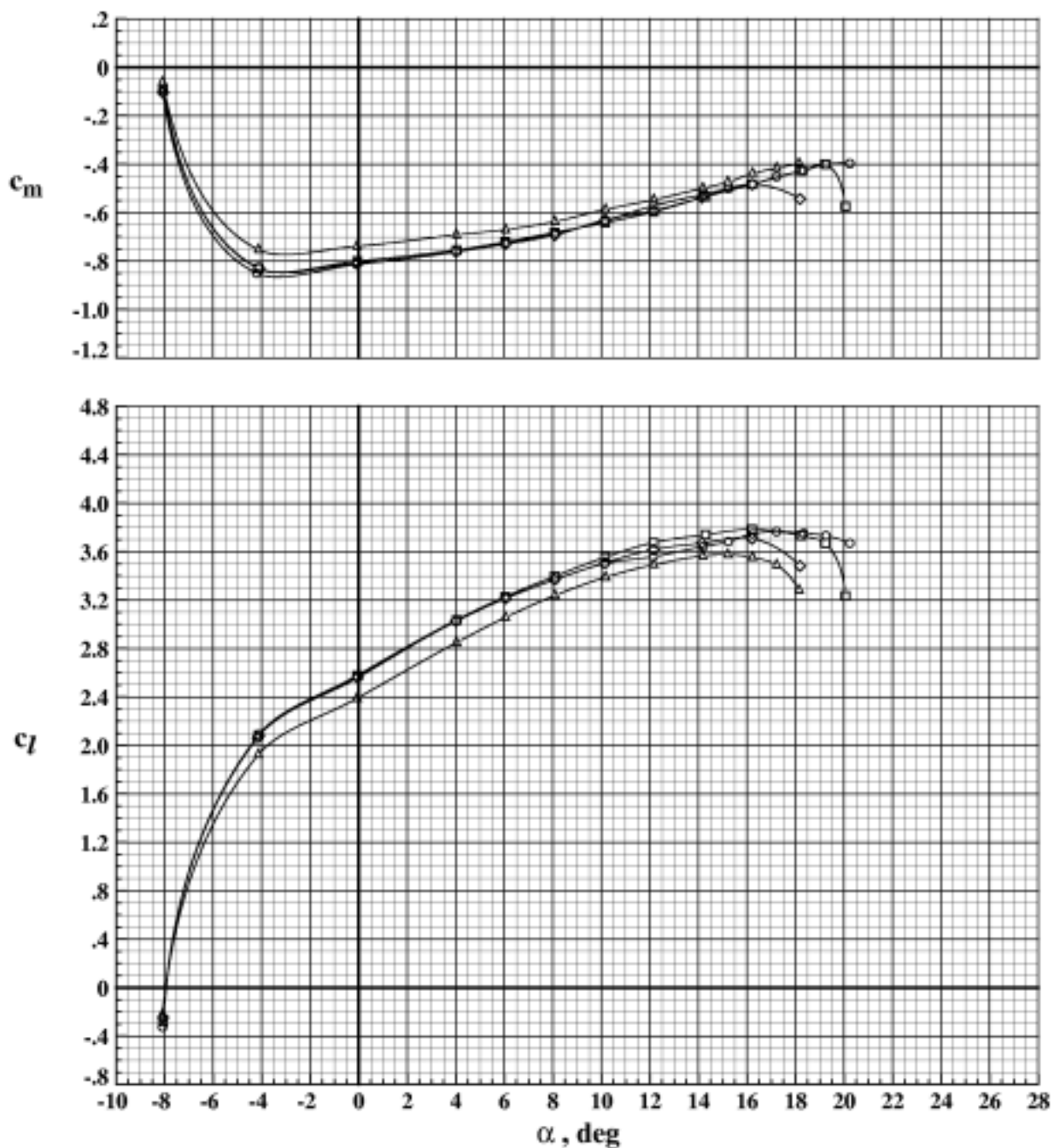


Figure 57. Effect of sidewall blowing on aerodynamic performance of EET High-Lift Airfoil with $\delta_x = -60.0^\circ$, $\delta_y = 22.5^\circ$, and $\delta_z = 22.5^\circ$ at $R_n = 6.093 \times 10^6$ and at $M_\infty = 0.202$.

	Run	Sidewall Blowing
○	37	On
□	36	Off

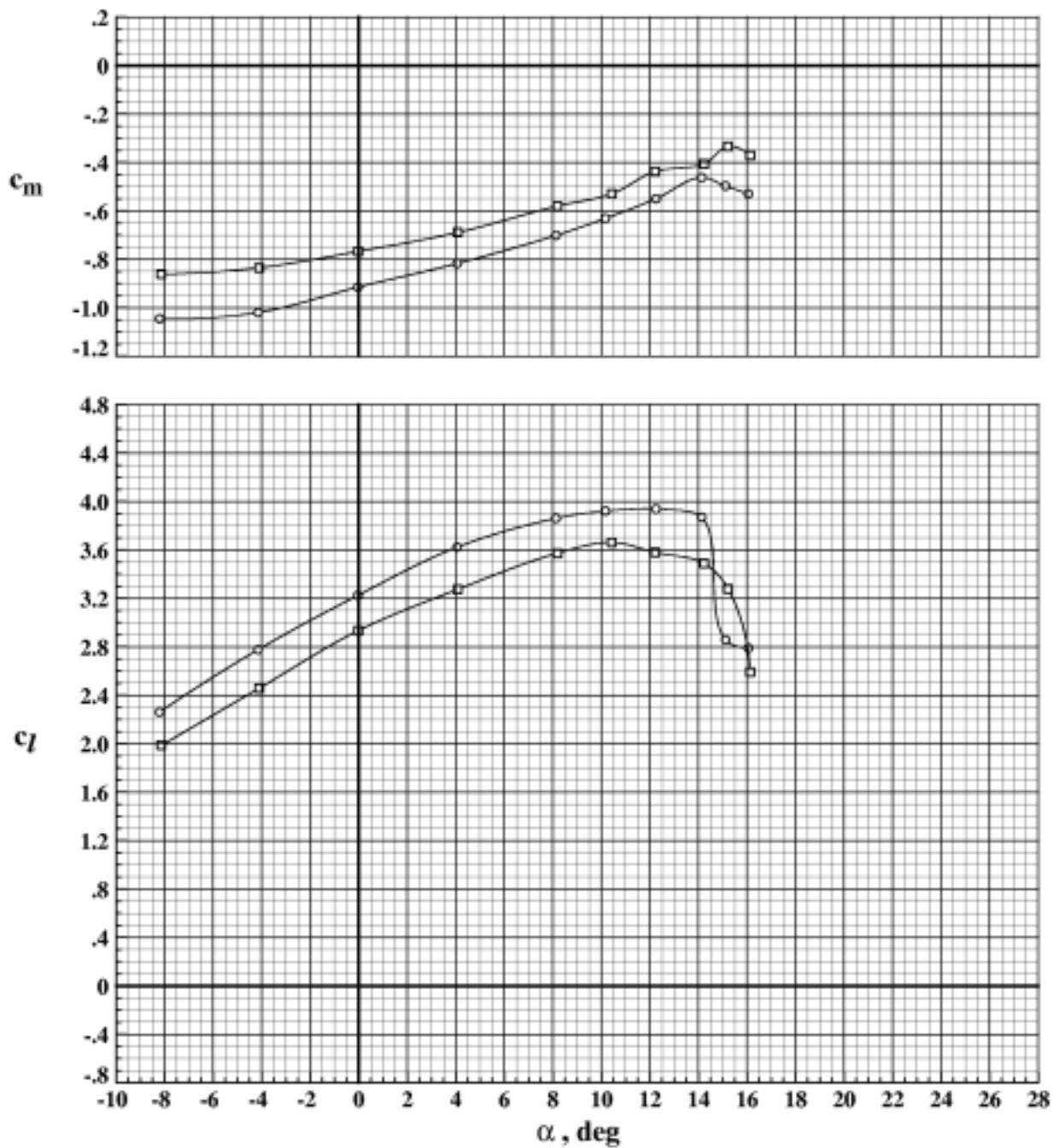


Figure 58. Effect of sidewall blowing on aerodynamic performance of EET High-Lift Airfoil with $\delta_s = -30.0^\circ$, $\delta_v = 30.0^\circ$, and $\delta_f = 30.0^\circ$ at $R_n = 2.493 \times 10^6$ and at $M_\infty = 0.204$.

	Run	Sidewall Blowing
○	39	On
□	40	Off

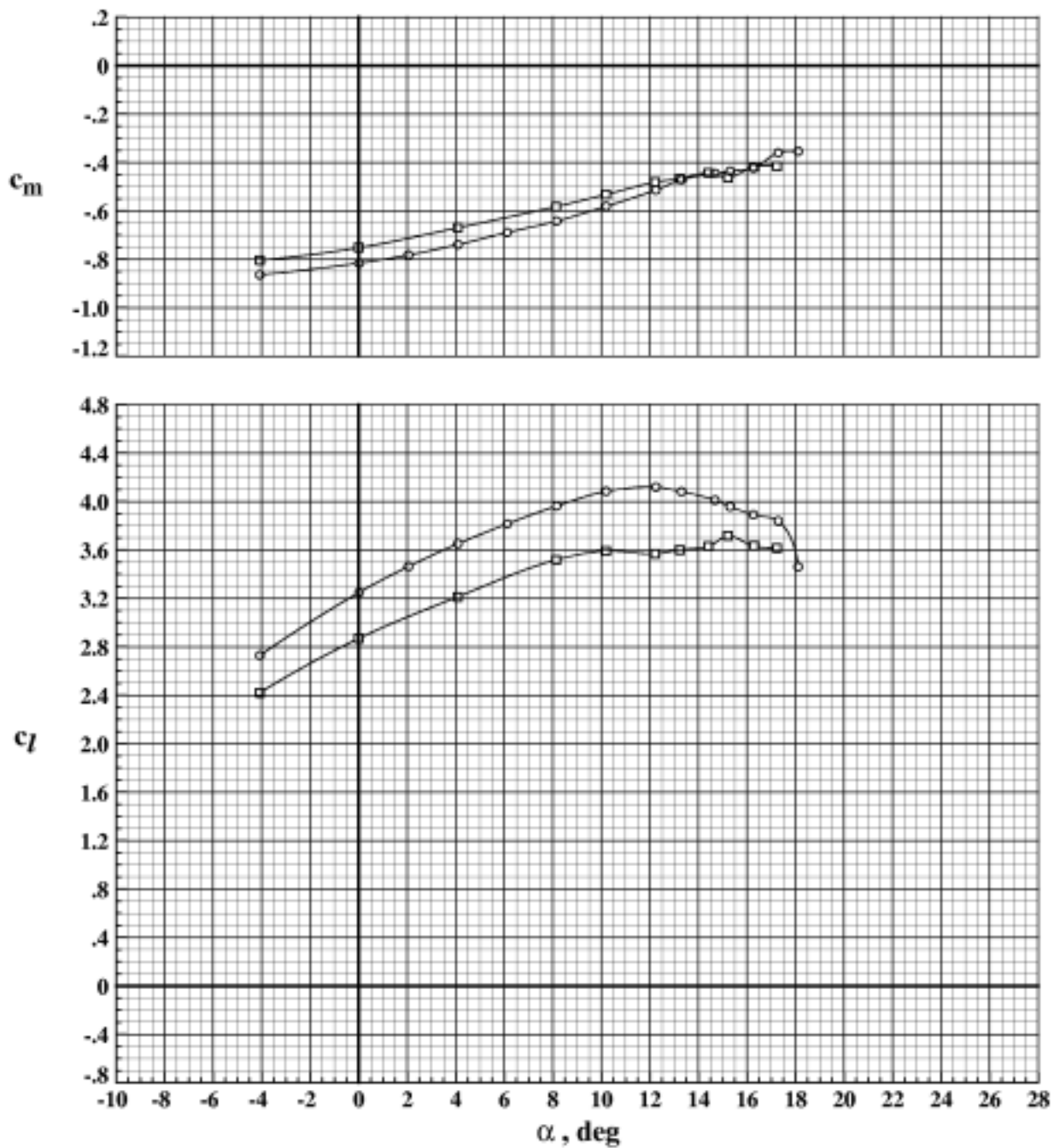


Figure 59. Effect of sidewall blowing on aerodynamic performance of EET High-Lift Airfoil with $\delta_s = -30.0^\circ$, $\delta_v = 30.0^\circ$, and $\delta_f = 30.0^\circ$ at $R_n = 6.089 \times 10^6$ and at $M_\infty = 0.205$.

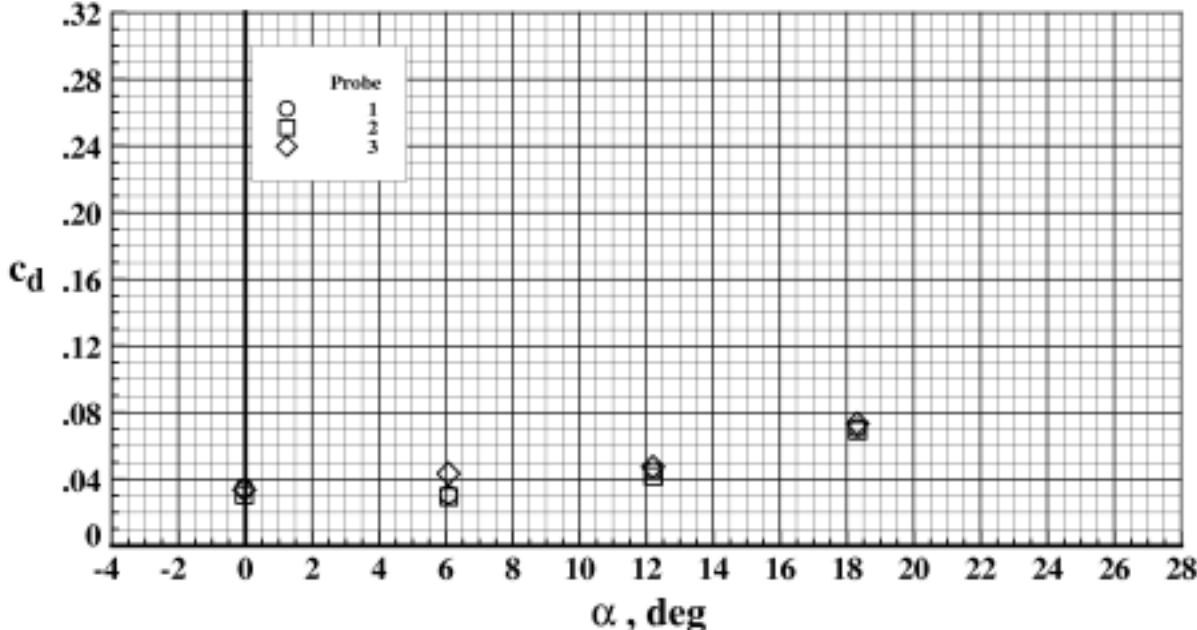


Figure 60. Drag performance for EET High-Lift Airfoil with $\delta_s = -30.0^\circ$, $\delta_v = 7.5^\circ$, and $\delta_f = 7.5^\circ$ at $M_\infty = 0.201$ and $R_n = 6.039 \times 10^6$.

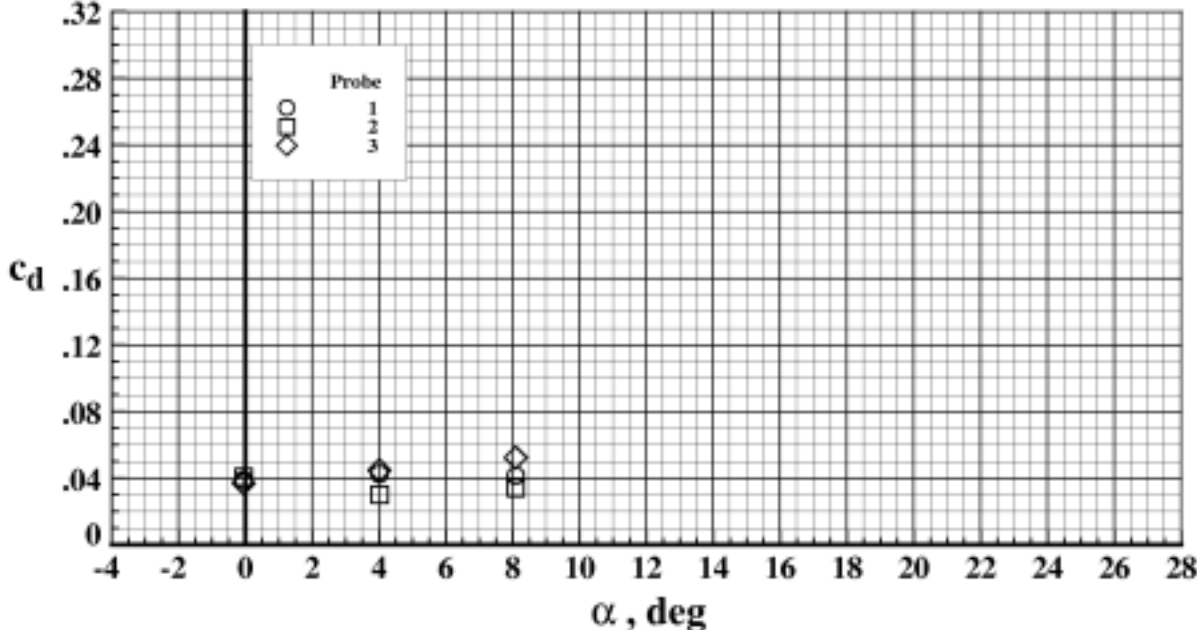


Figure 61. Drag performance for EET High-Lift Airfoil with $\delta_s = -50.0^\circ$, $\delta_v = 7.5^\circ$, and $\delta_f = 7.5^\circ$ at $M_\infty = 0.202$ and $R_n = 12.115 \times 10^6$.

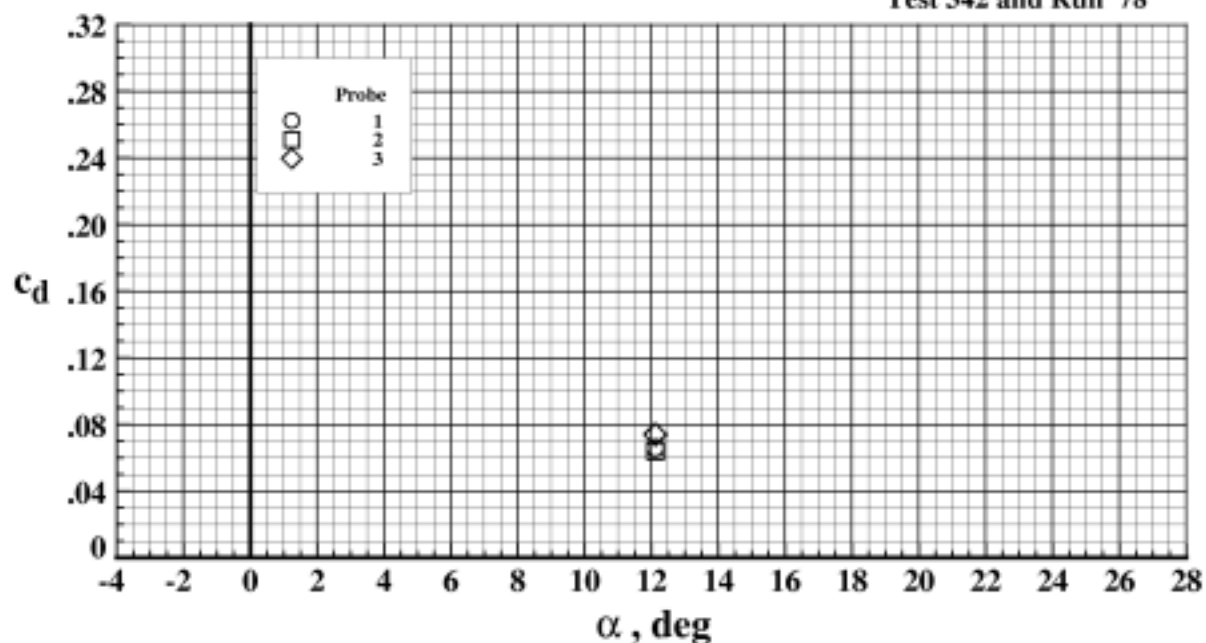


Figure 62. Drag performance for EET High-Lift Airfoil with $\delta_s = -40.0^\circ$, $\delta_v = 15.0^\circ$, and $\delta_T = 15.0^\circ$ at $M_\infty = 0.201$ and $R_n = 2.518 \times 10^6$.

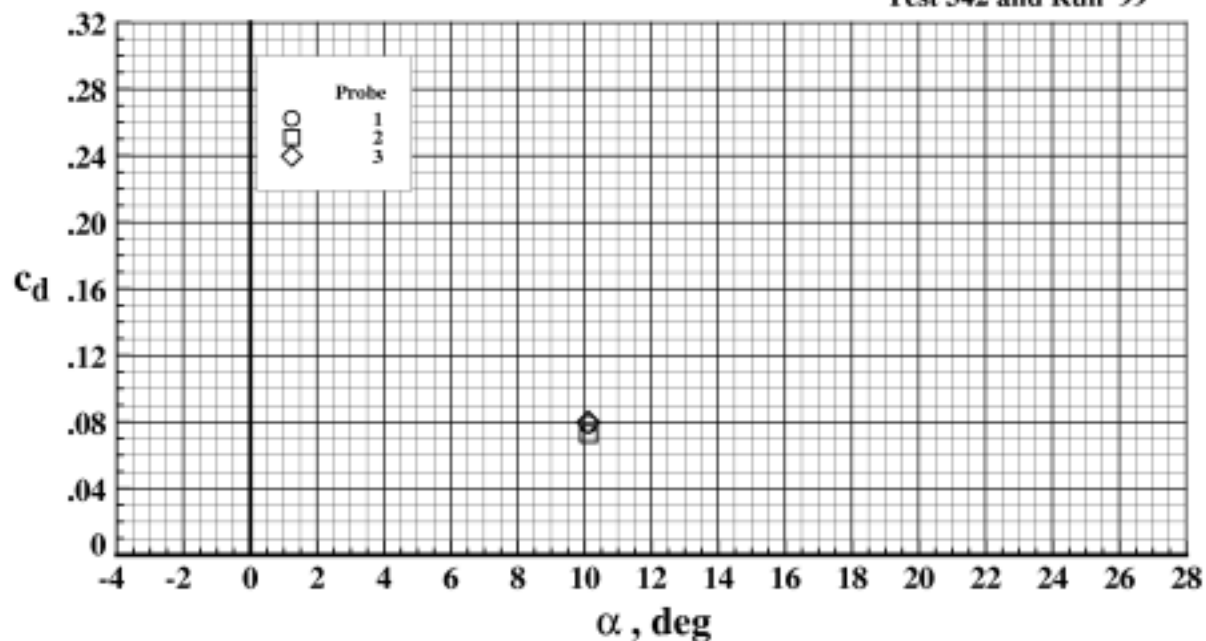


Figure 63. Drag performance for EET High-Lift Airfoil with $\delta_s = -60.0^\circ$, $\delta_v = 15.0^\circ$, and $\delta_T = 15.0^\circ$ at $M_\infty = 0.201$ and $R_n = 2.504 \times 10^6$.

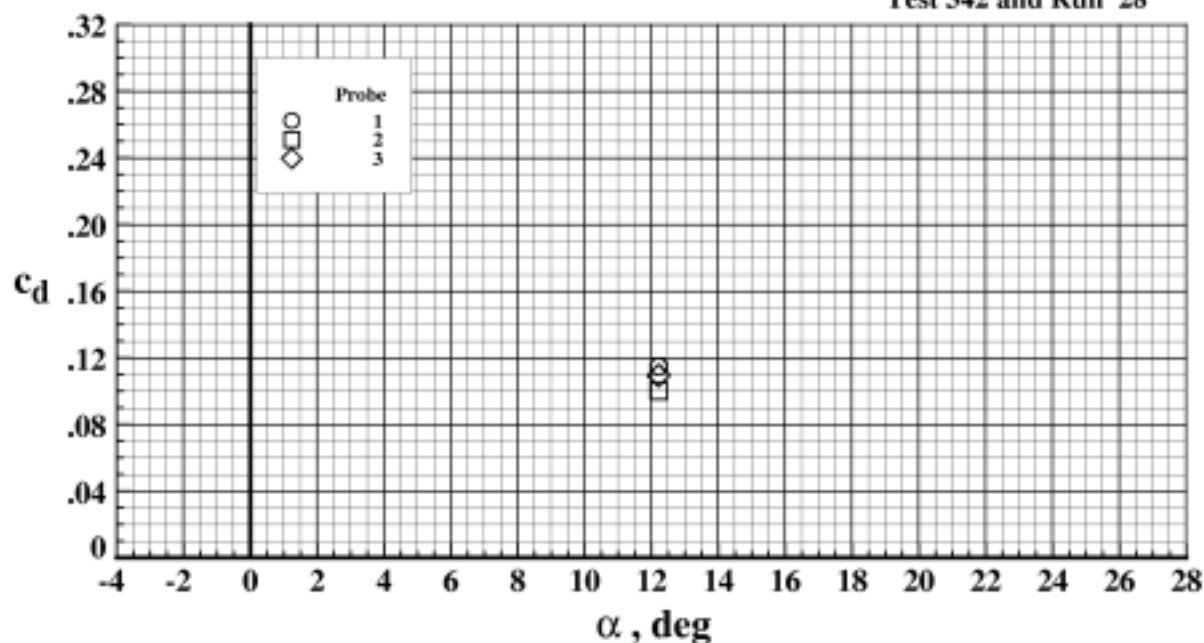


Figure 64. Drag performance for EET High-Lift Airfoil with $\delta_s = -30.0^\circ$, $\delta_v = 22.5^\circ$, and $\delta_f = 22.5^\circ$ at $M_\infty = 0.203$ and $R_n = 2.481 \times 10^6$.

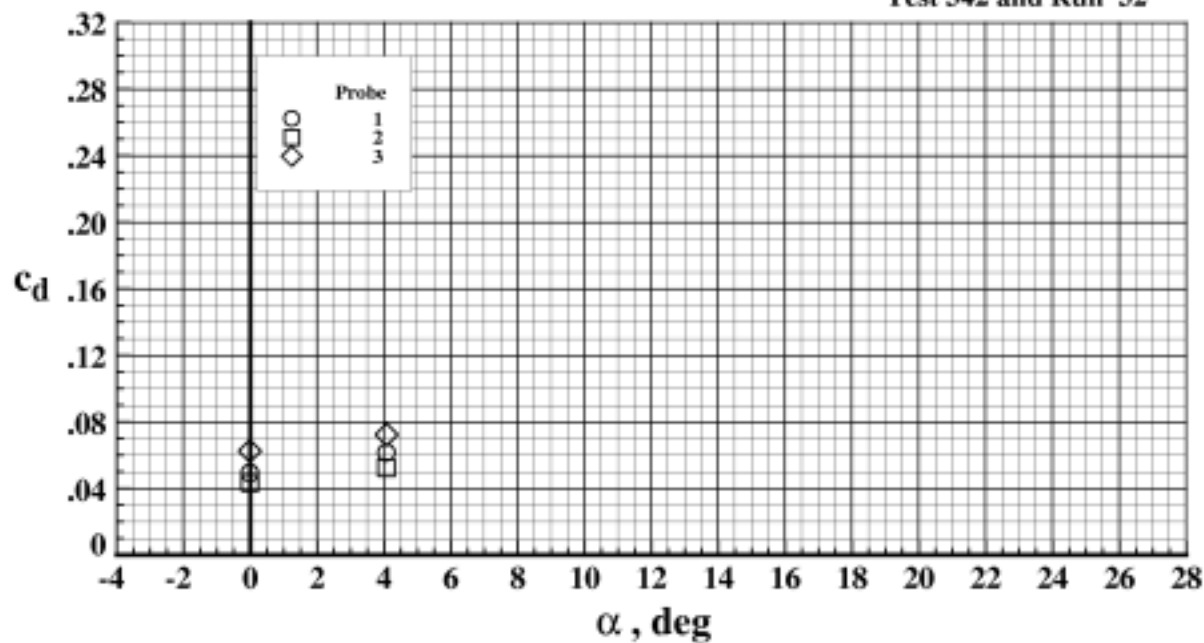


Figure 65. Drag performance for EET High-Lift Airfoil with $\delta_s = -30.0^\circ$, $\delta_v = 22.5^\circ$, and $\delta_f = 22.5^\circ$ at $M_\infty = 0.201$ and $R_n = 12.104 \times 10^6$.

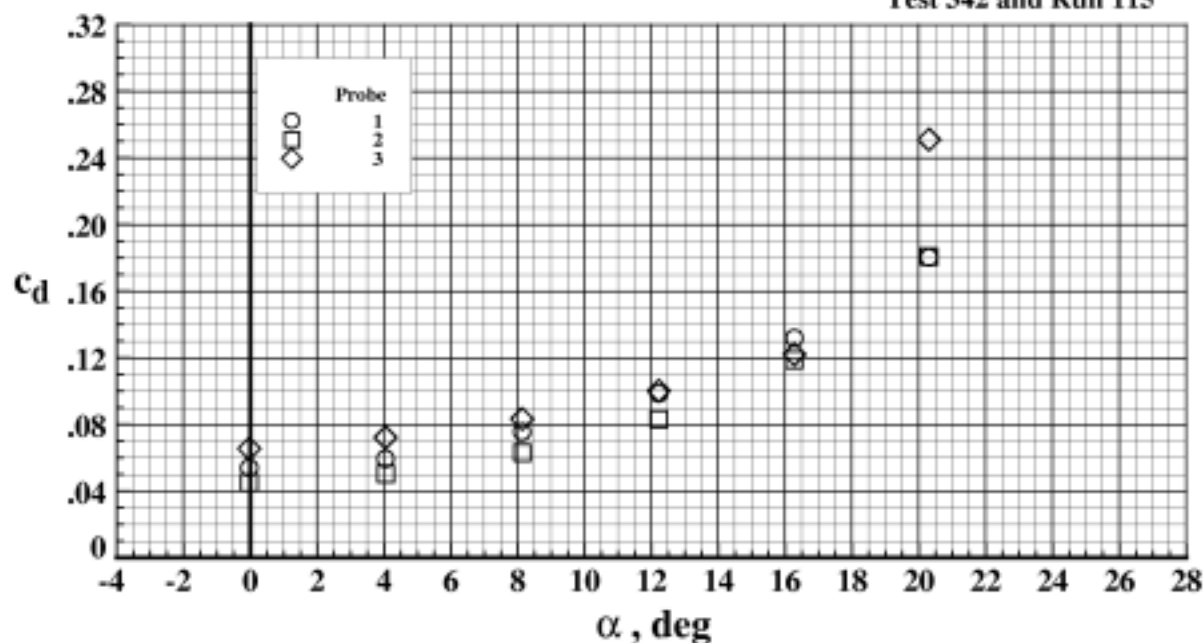


Figure 66. Drag performance for EET High-Lift Airfoil with $\delta_s = -40.0^\circ$, $\delta_v = 22.5^\circ$, and $\delta_T = 22.5^\circ$ at $M_\infty = 0.202$ and $R_n = 6.086 \times 10^6$.

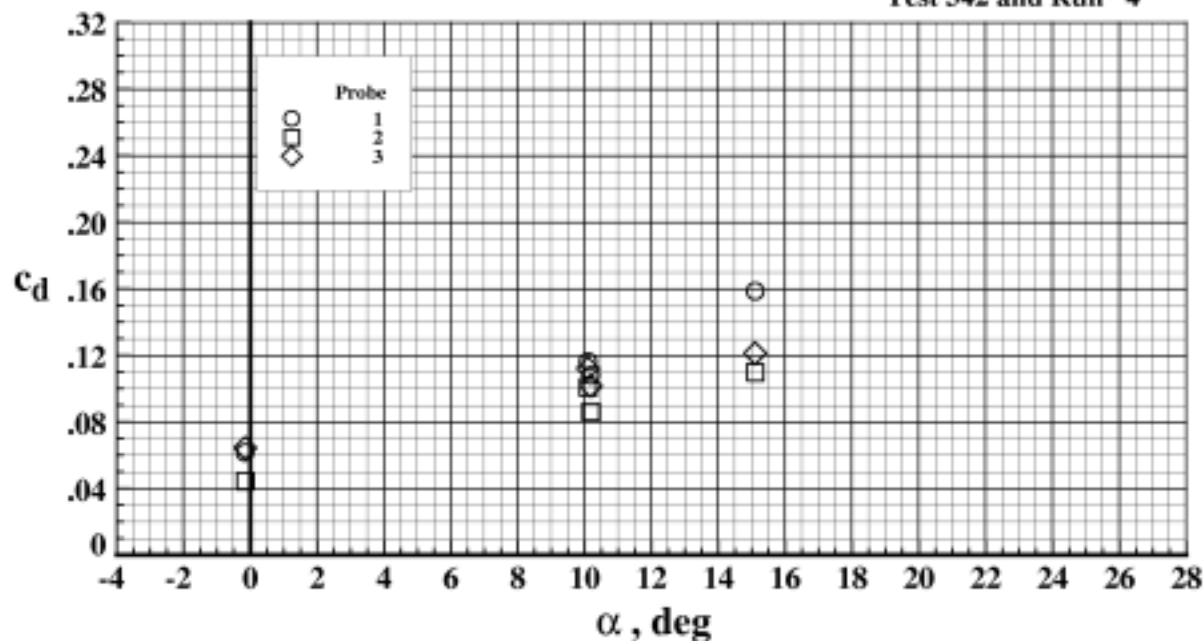


Figure 67. Drag performance for EET High-Lift Airfoil with $\delta_s = -50.0^\circ$, $\delta_v = 22.5^\circ$, and $\delta_T = 22.5^\circ$ at $M_\infty = 0.202$ and $R_n = 2.606 \times 10^6$.

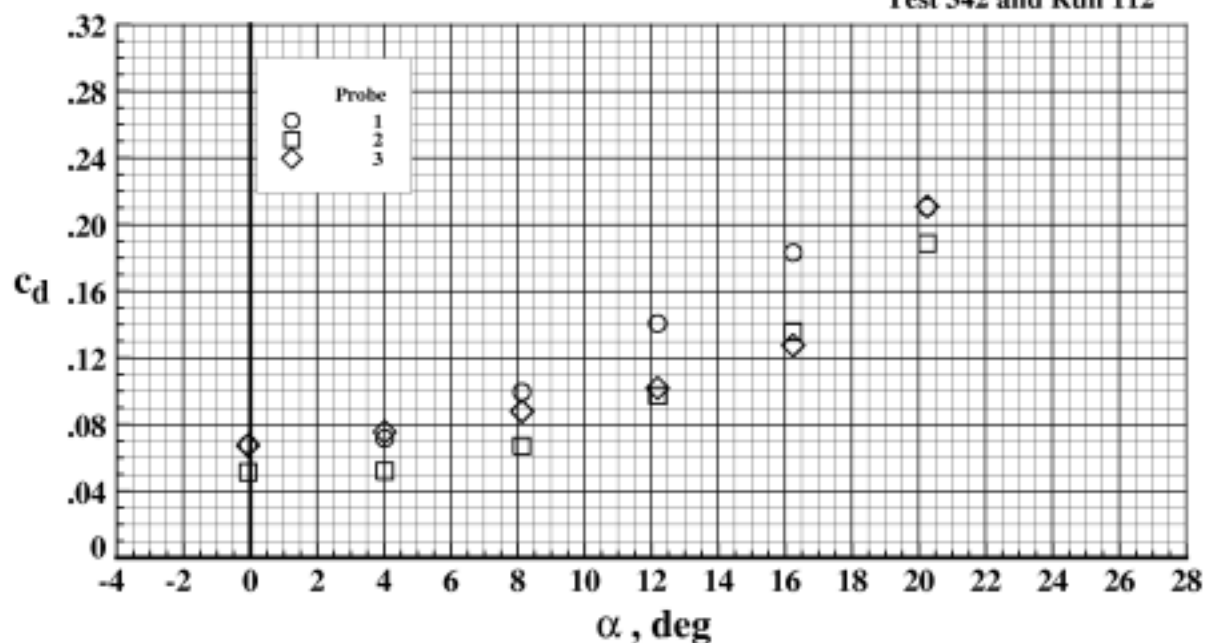


Figure 68. Drag performance for EET High-Lift Airfoil with $\delta_s = -50.0^\circ$, $\delta_v = 22.5^\circ$, and $\delta_T = 22.5^\circ$ at $M_\infty = 0.203$ and $R_n = 2.466 \times 10^6$.

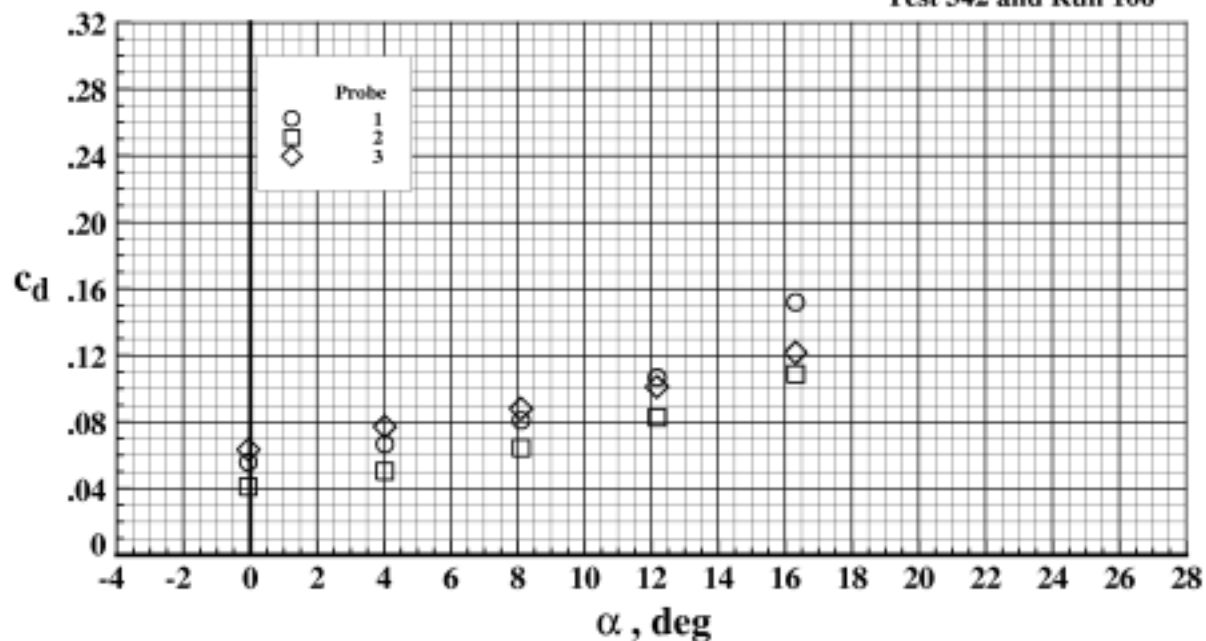


Figure 69. Drag performance for EET High-Lift Airfoil with $\delta_s = -50.0^\circ$, $\delta_v = 22.5^\circ$, and $\delta_T = 22.5^\circ$ at $M_\infty = 0.202$ and $R_n = 6.094 \times 10^6$.

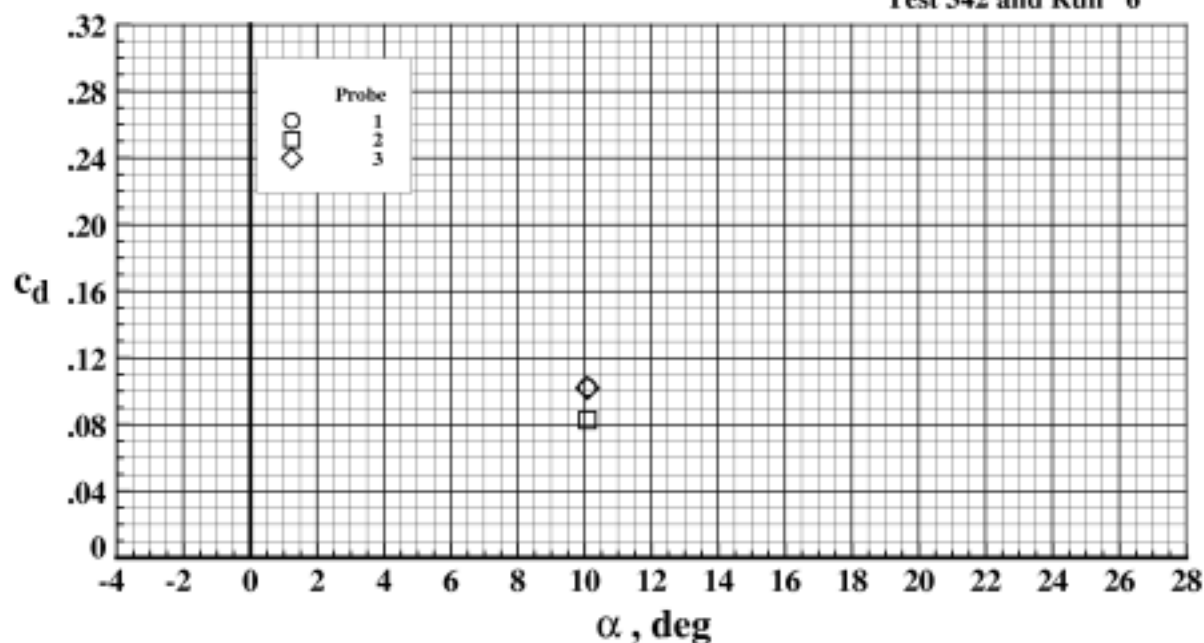


Figure 70. Drag performance for EET High-Lift Airfoil with $\delta_s = -50.0^\circ$, $\delta_v = 22.5^\circ$, and $\delta_f = 22.5^\circ$ at $M_\infty = 0.204$ and $R_n = 6.082 \times 10^6$.

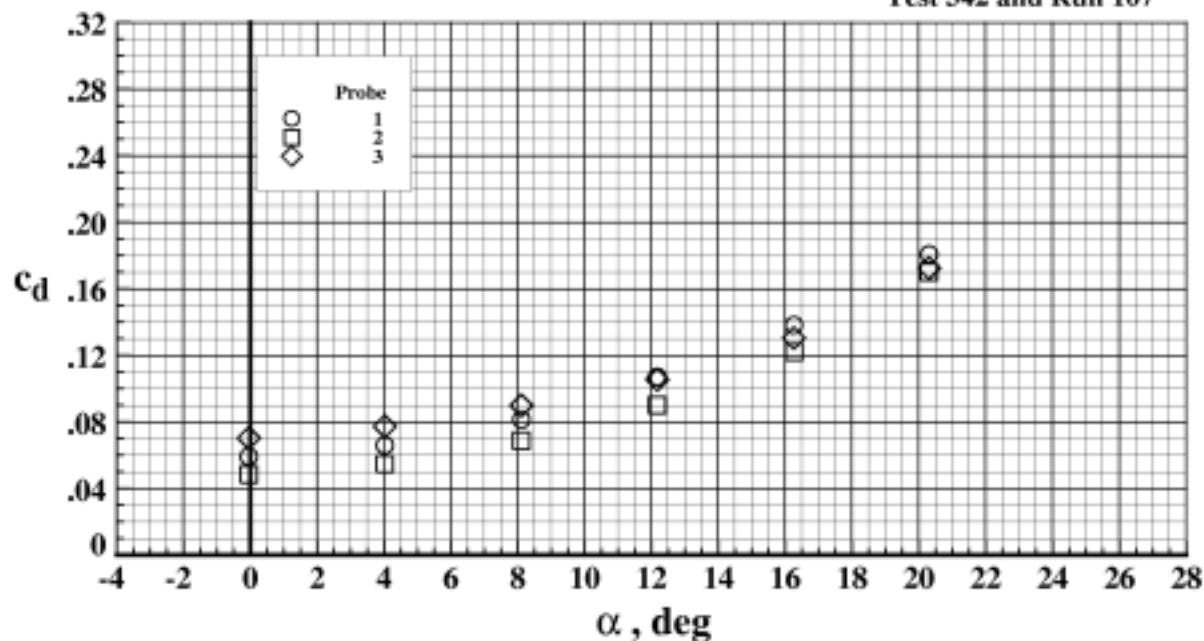


Figure 71. Drag performance for EET High-Lift Airfoil with $\delta_s = -50.0^\circ$, $\delta_v = 22.5^\circ$, and $\delta_f = 22.5^\circ$ at $M_\infty = 0.202$ and $R_n = 12.129 \times 10^6$.

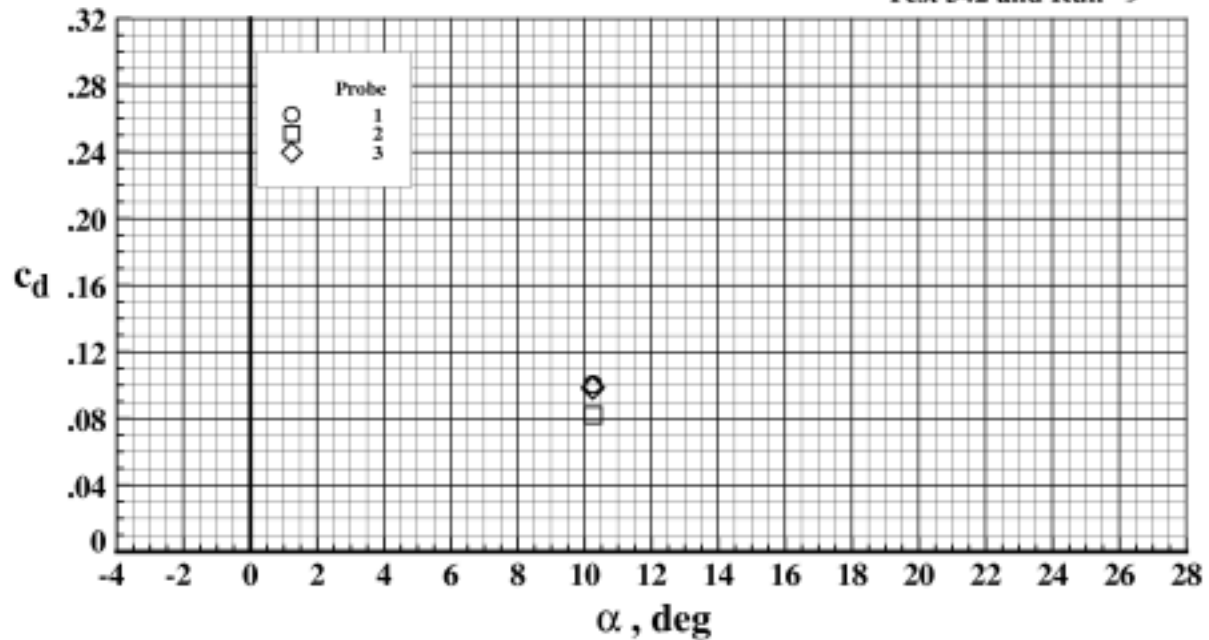


Figure 72. Drag performance for EET High-Lift Airfoil with $\delta_s = -50.0^\circ$, $\delta_v = 22.5^\circ$, and $\delta_f = 22.5^\circ$ at $M_\infty = 0.201$ and $R_n = 11.973 \times 10^6$.

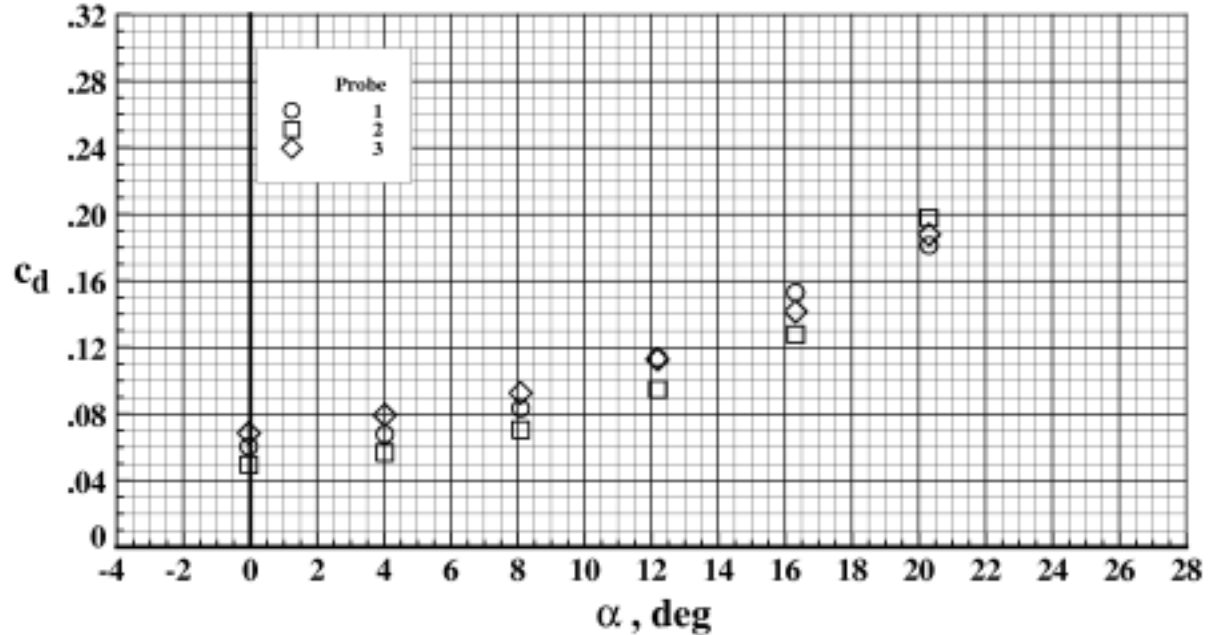


Figure 73. Drag performance for EET High-Lift Airfoil with $\delta_s = -50.0^\circ$, $\delta_v = 22.5^\circ$, and $\delta_f = 22.5^\circ$ at $M_\infty = 0.203$ and $R_n = 18.221 \times 10^6$.

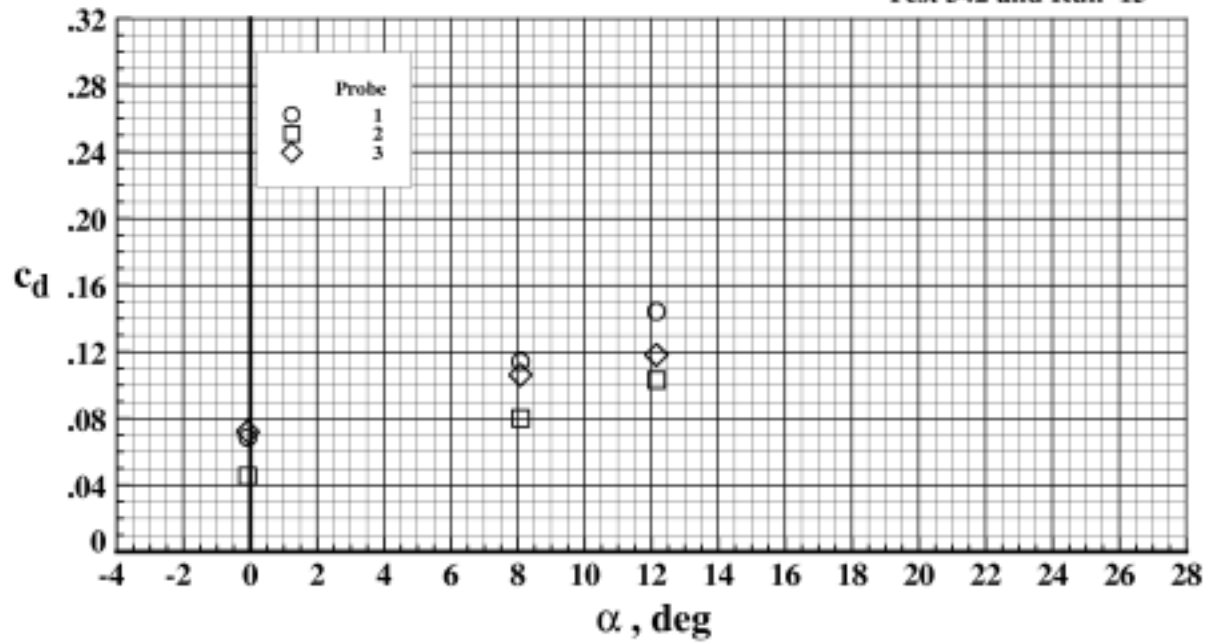


Figure 74. Drag performance for EET High-Lift Airfoil with $\delta_s = -60.0^\circ$, $\delta_v = 22.5^\circ$, and $\delta_f = 22.5^\circ$ at $M_\infty = 0.204$ and $R_n = 6.134 \times 10^6$.

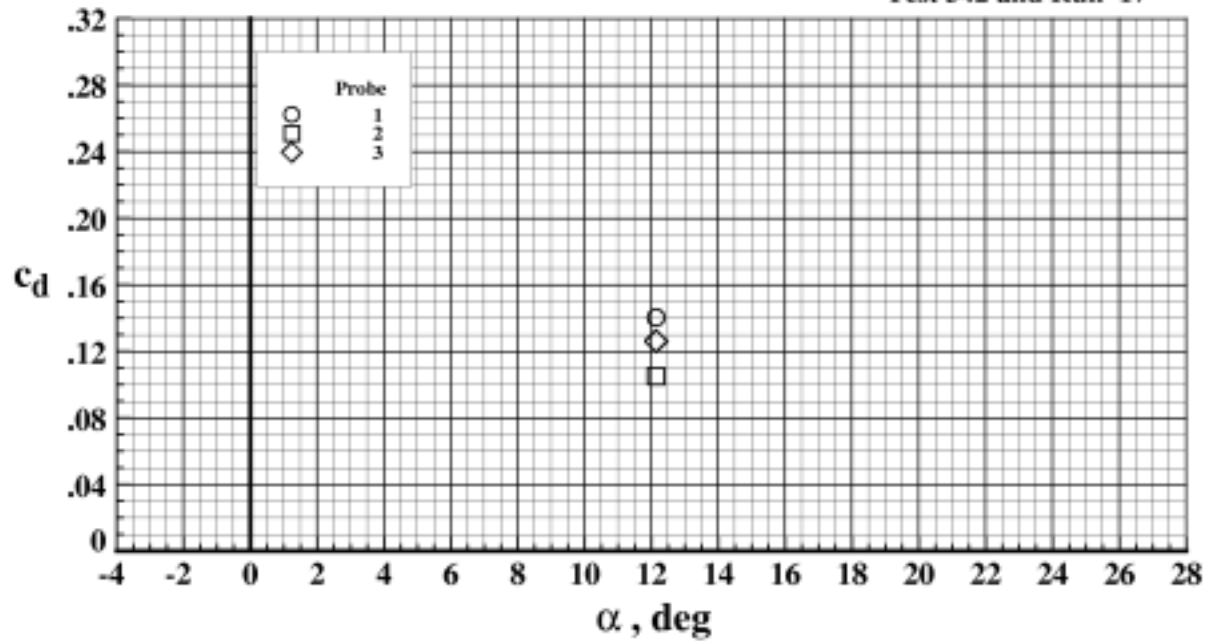


Figure 75. Drag performance for EET High-Lift Airfoil with $\delta_s = -60.0^\circ$, $\delta_v = 22.5^\circ$, and $\delta_f = 22.5^\circ$ at $M_\infty = 0.203$ and $R_n = 12.101 \times 10^6$.

Test 342 and Run 18

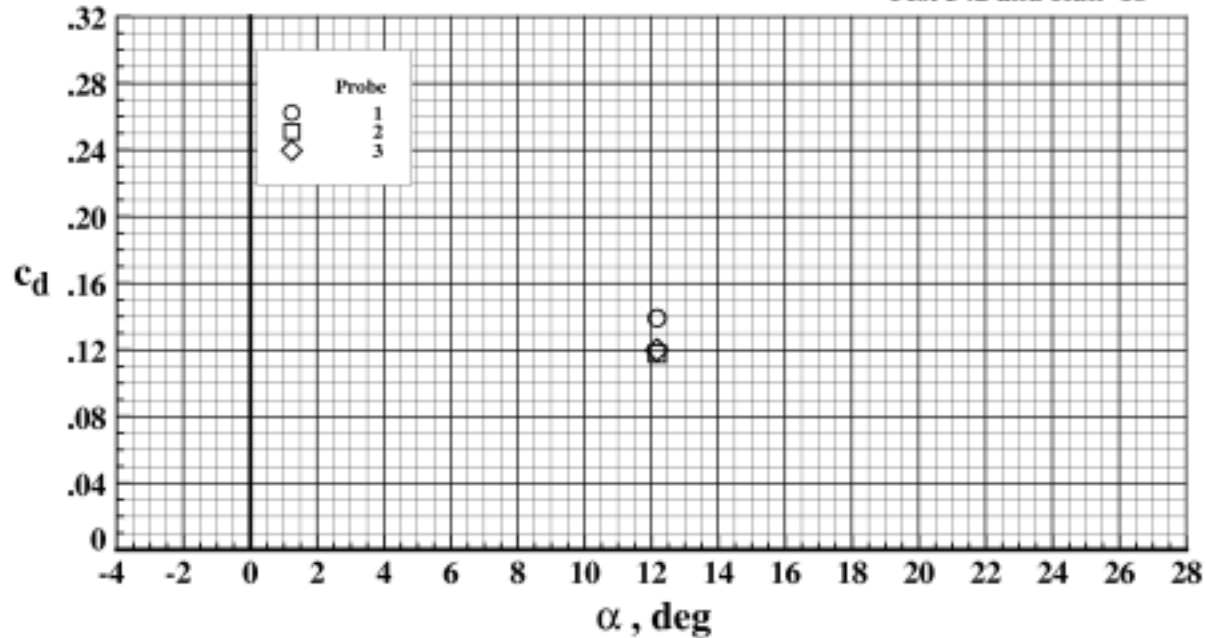


Figure 76. Drag performance for EET High-Lift Airfoil with $\delta_s = -60.0^\circ$, $\delta_v = 22.5^\circ$, and $\delta_f = 22.5^\circ$ at $M_\infty = 0.203$ and $R_n = 18.129 \times 10^6$.

Test 342 and Run 49

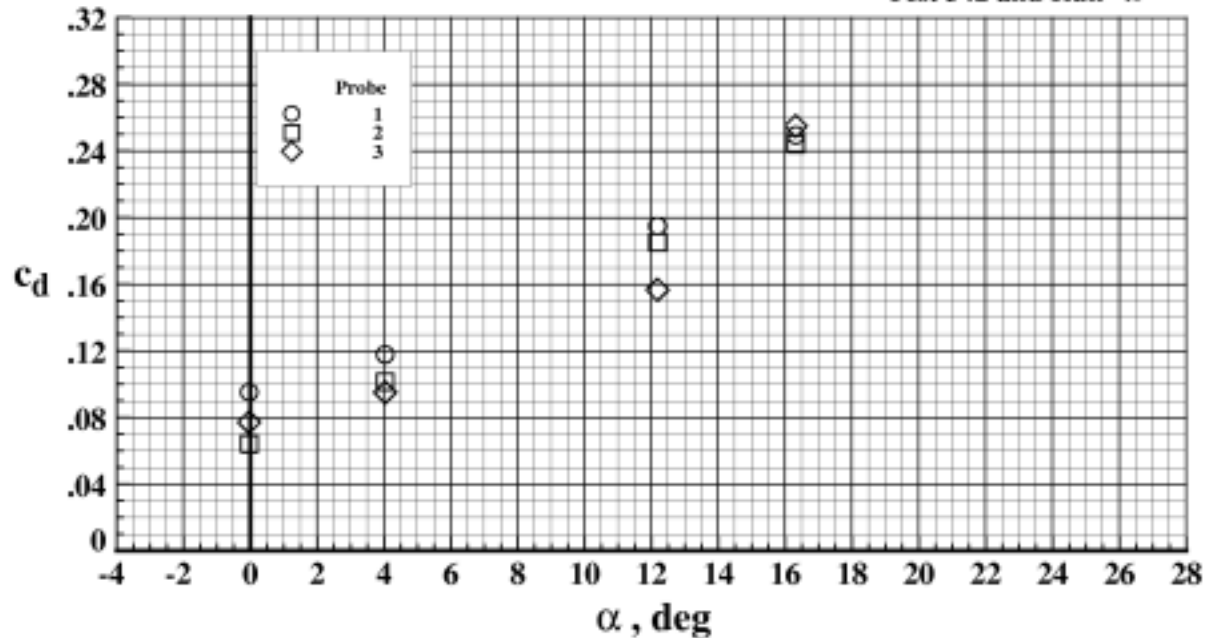


Figure 77. Drag performance for EET High-Lift Airfoil with $\delta_s = -50.0^\circ$, $\delta_v = 30.0^\circ$, and $\delta_f = 30.0^\circ$ at $M_\infty = 0.204$ and $R_n = 2.488 \times 10^6$.

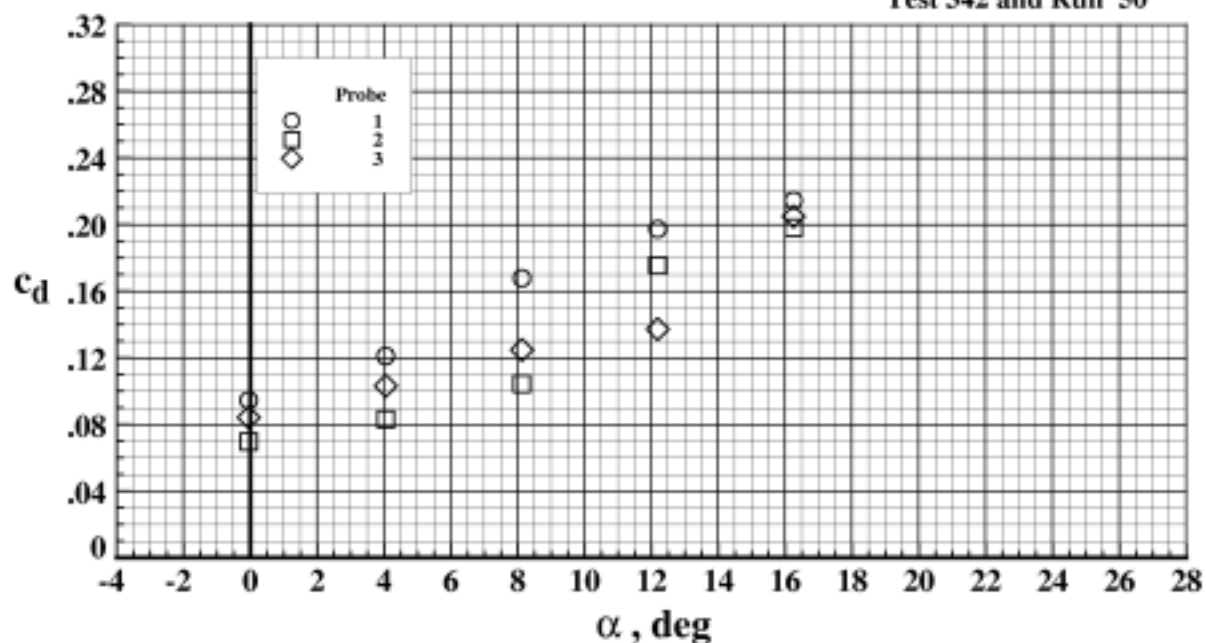


Figure 78. Drag performance for EET High-Lift Airfoil with $\delta_s = -50.0^\circ$, $\delta_v = 30.0^\circ$, and $\delta_f = 30.0^\circ$ at $M_\infty = 0.203$ and $R_n = 4.295 \times 10^6$.

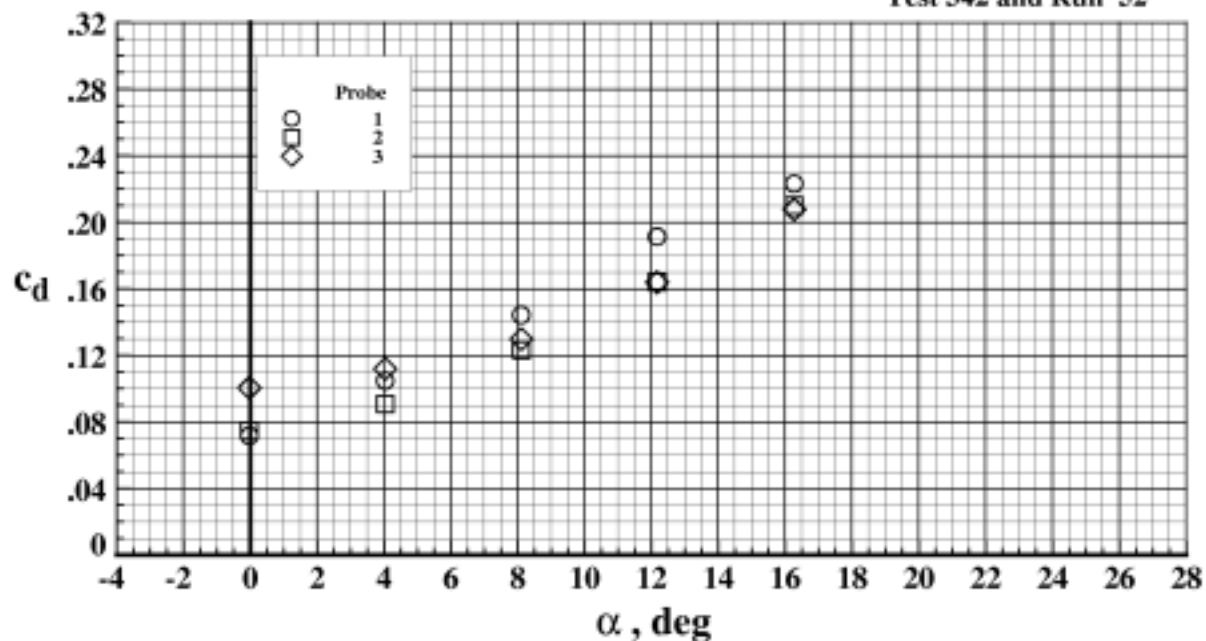


Figure 79. Drag performance for EET High-Lift Airfoil with $\delta_s = -50.0^\circ$, $\delta_v = 30.0^\circ$, and $\delta_f = 30.0^\circ$ at $M_\infty = 0.203$ and $R_n = 12.145 \times 10^6$.

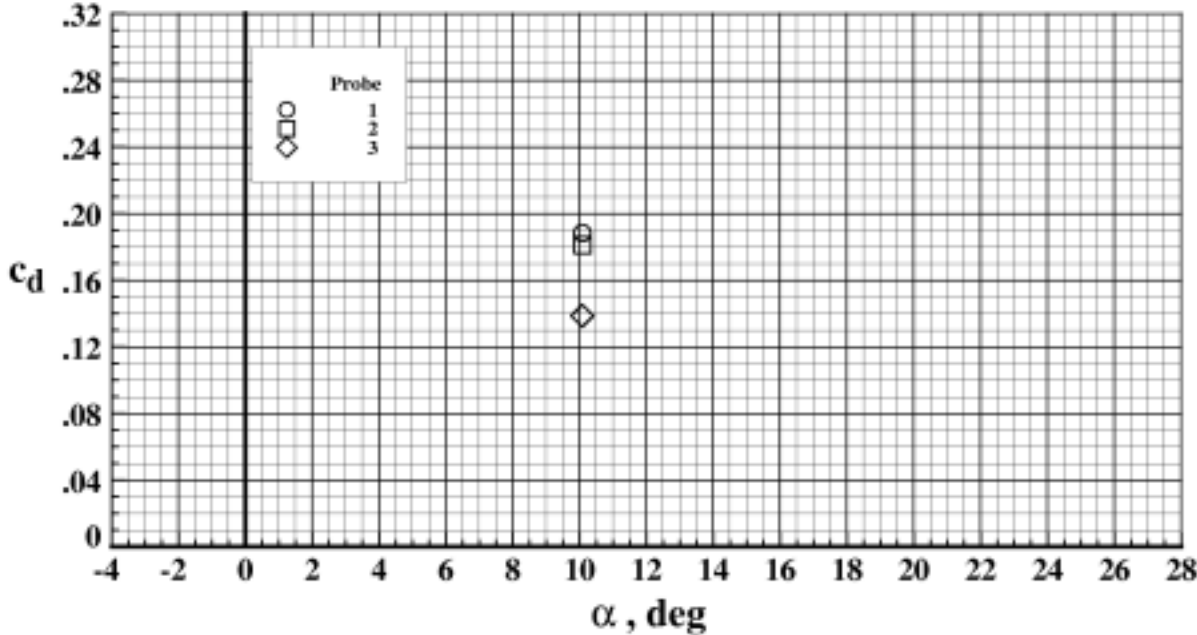
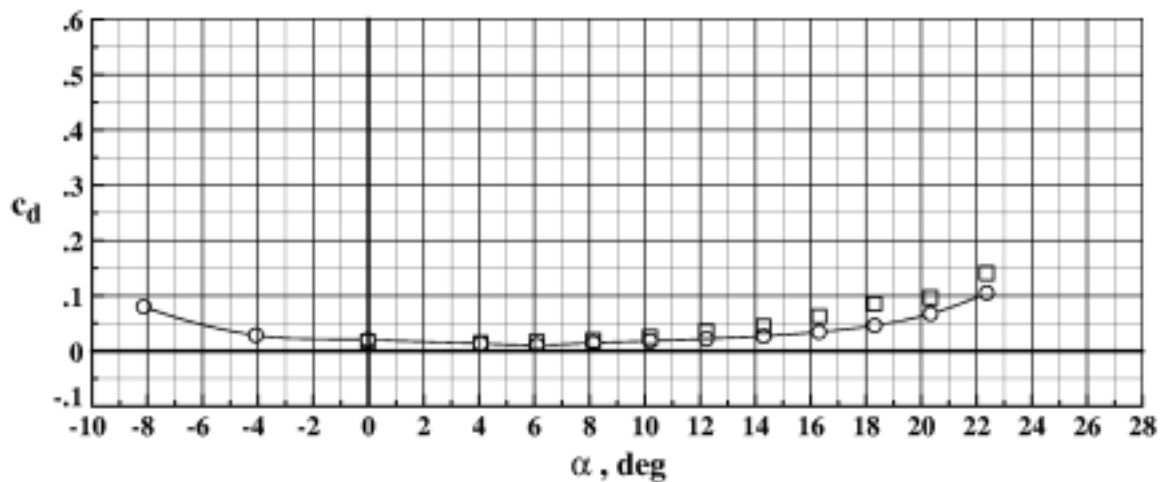
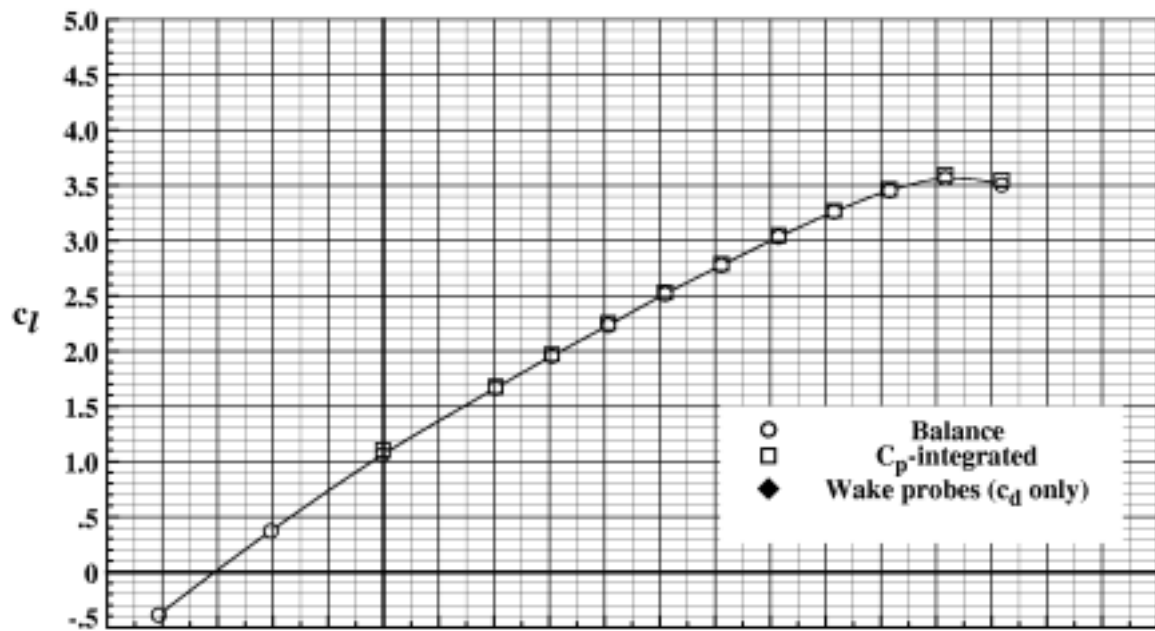
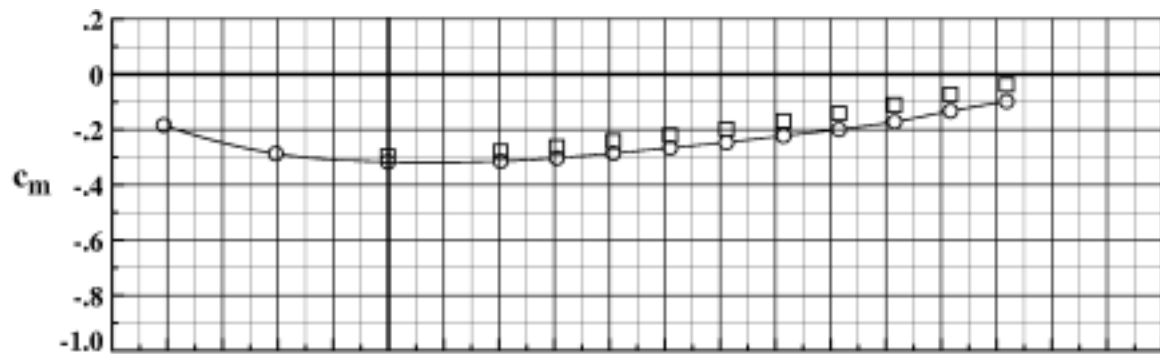
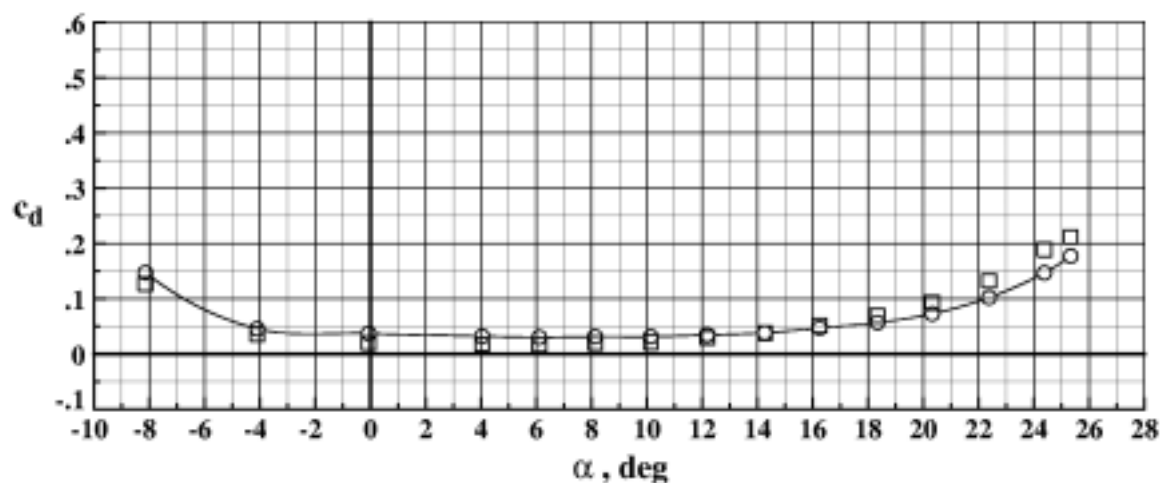
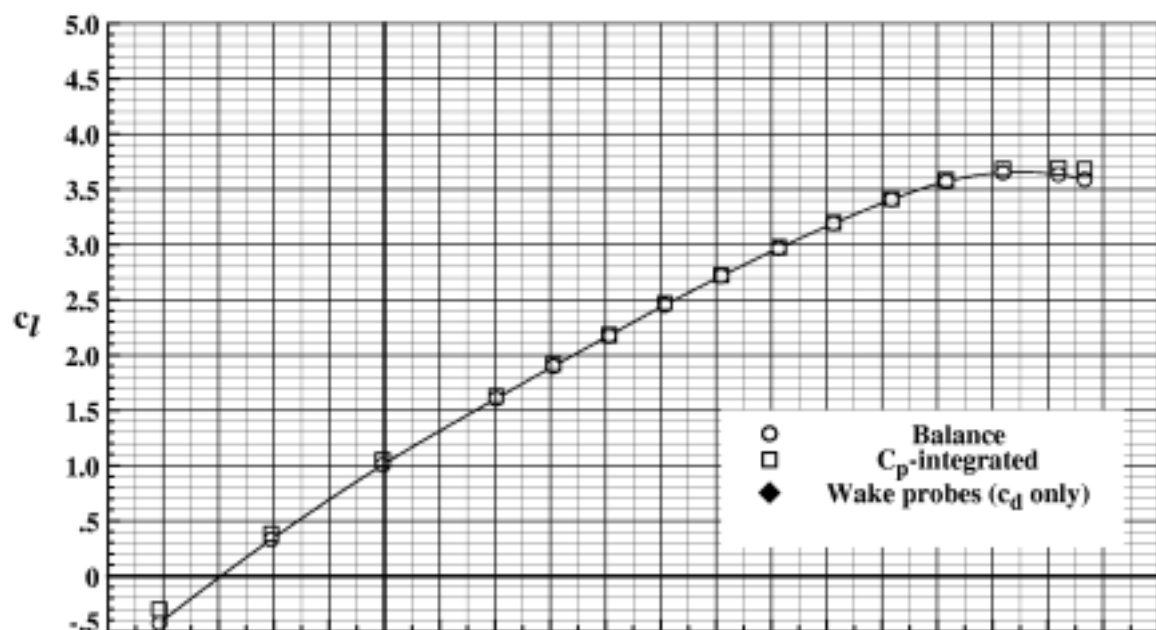
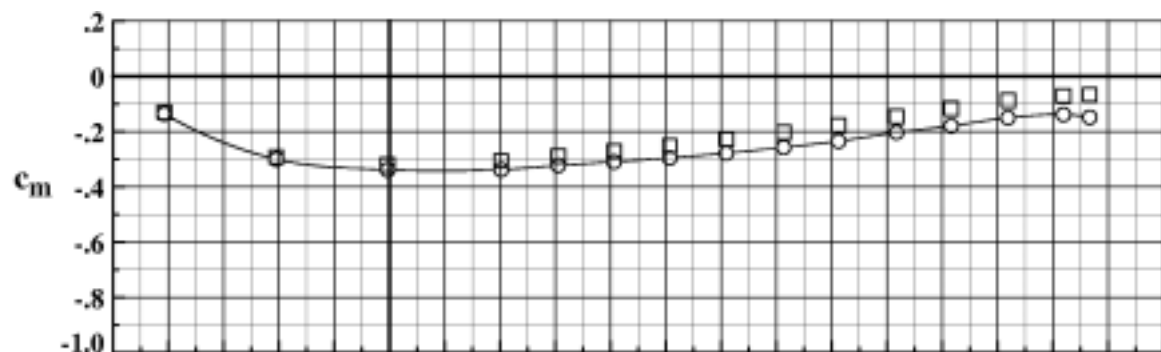


Figure 80. Drag performance for EET High-Lift Airfoil with $\delta_s = -60.0^\circ$, $\delta_v = 30.0^\circ$, and $\delta_T = 30.0^\circ$ at $M_\infty = 0.203$ and $R_n = 2.526 \times 10^6$.



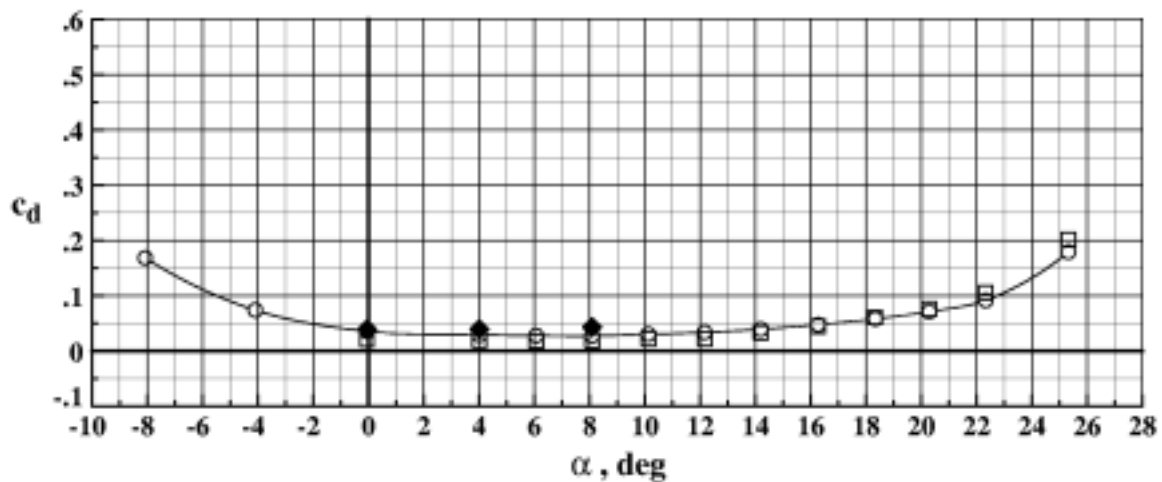
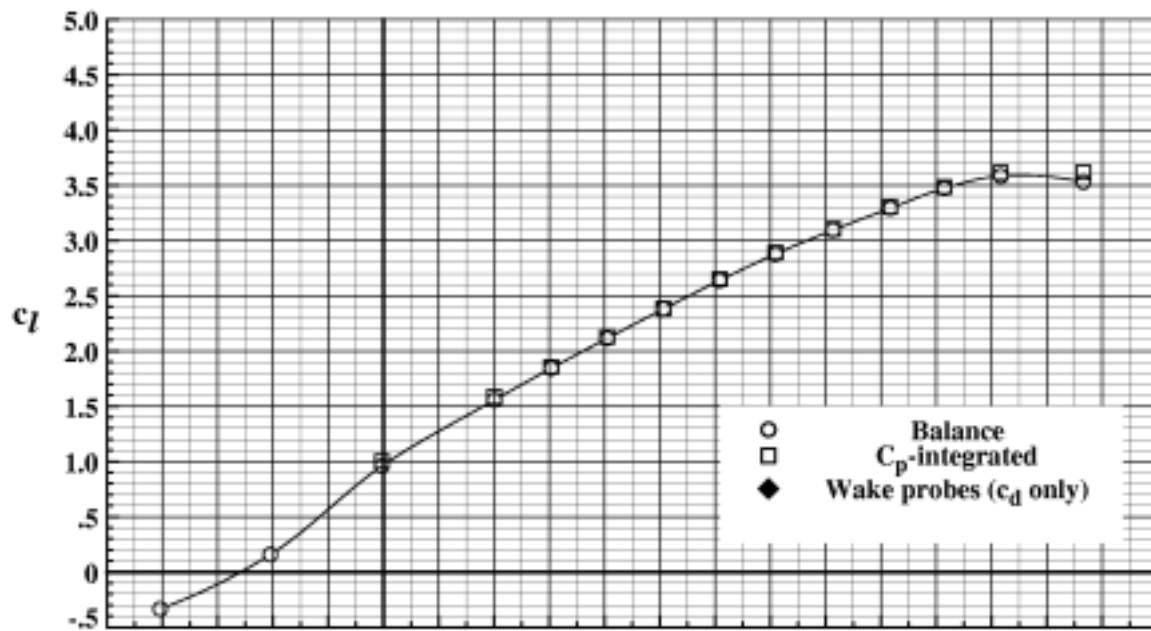
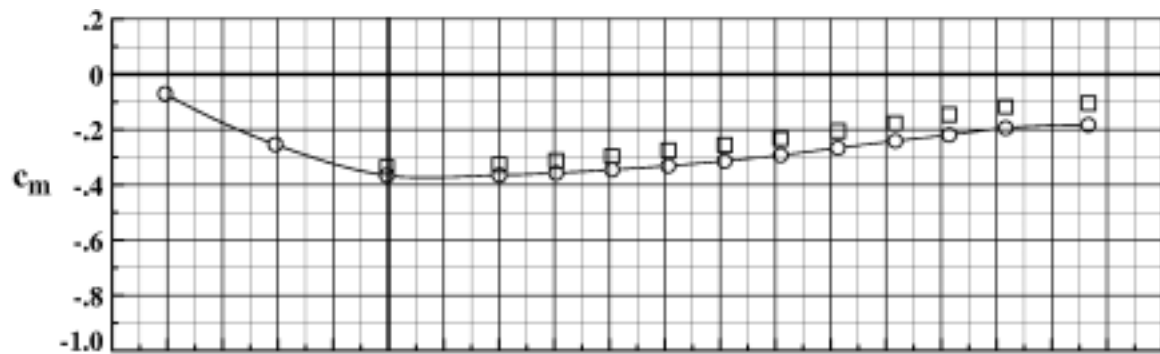
(a) $\delta_s = -30.0^\circ$, $M_\infty = 0.202$, $R_x = 12.036 \times 10^6$, Run 72.

Figure 81. Balance and C_p -integrated data for EET High-Lift Airfoil with $\delta_v = 7.5^\circ$ and $\delta_f = 7.5^\circ$.



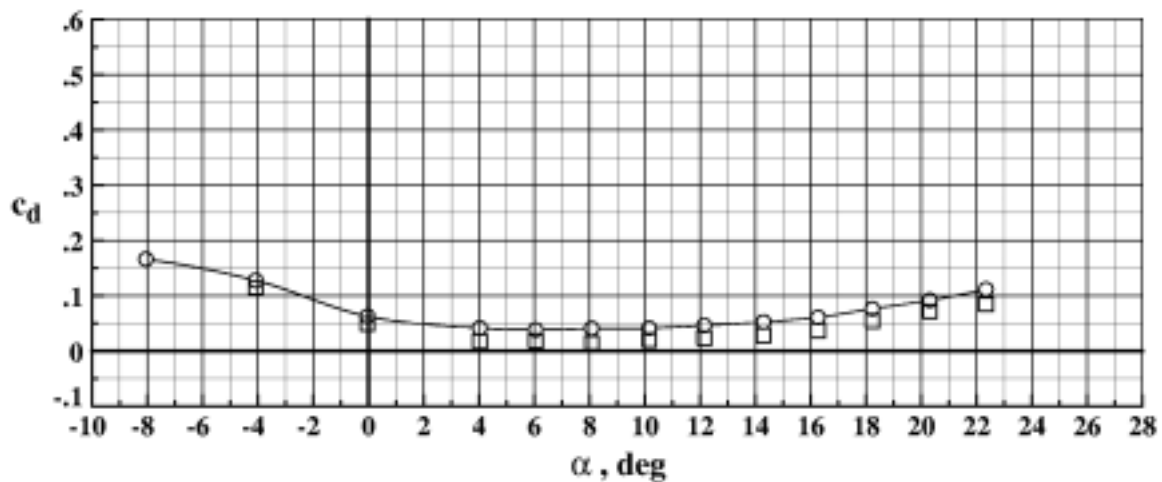
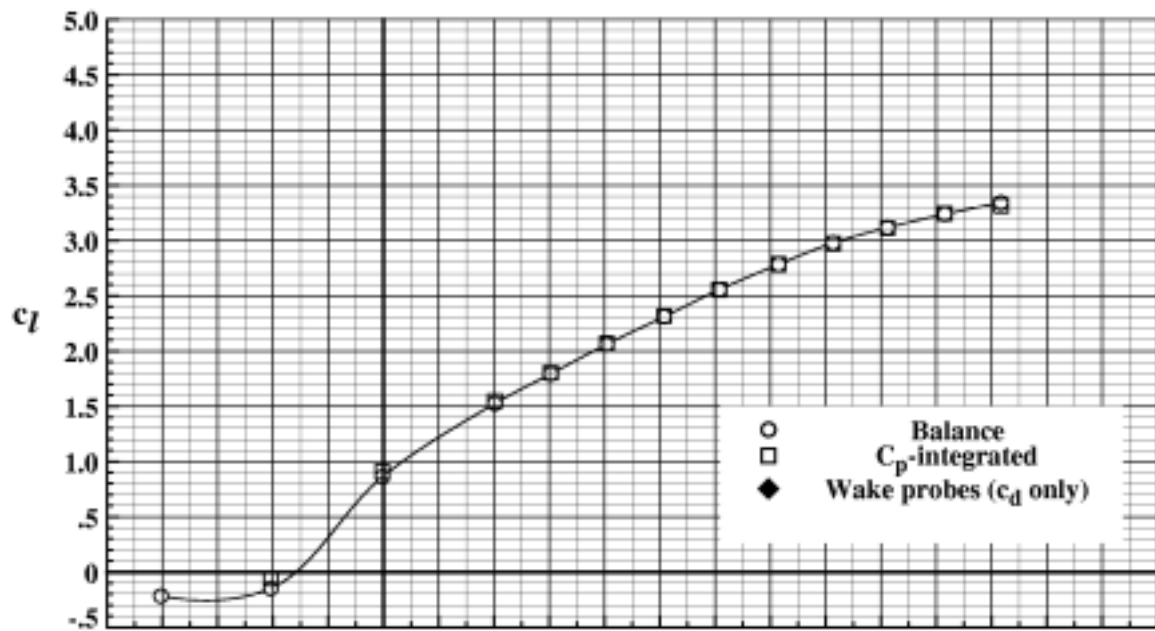
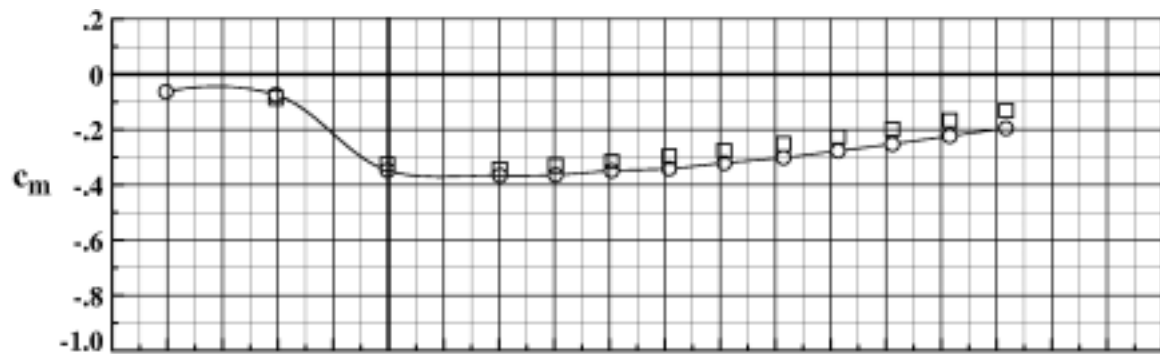
(b) $\delta_s = -40.0^\circ$, $M_\infty = 0.202$, $R_n = 12.098 \times 10^6$, Run 68.

Figure 81. Continued.



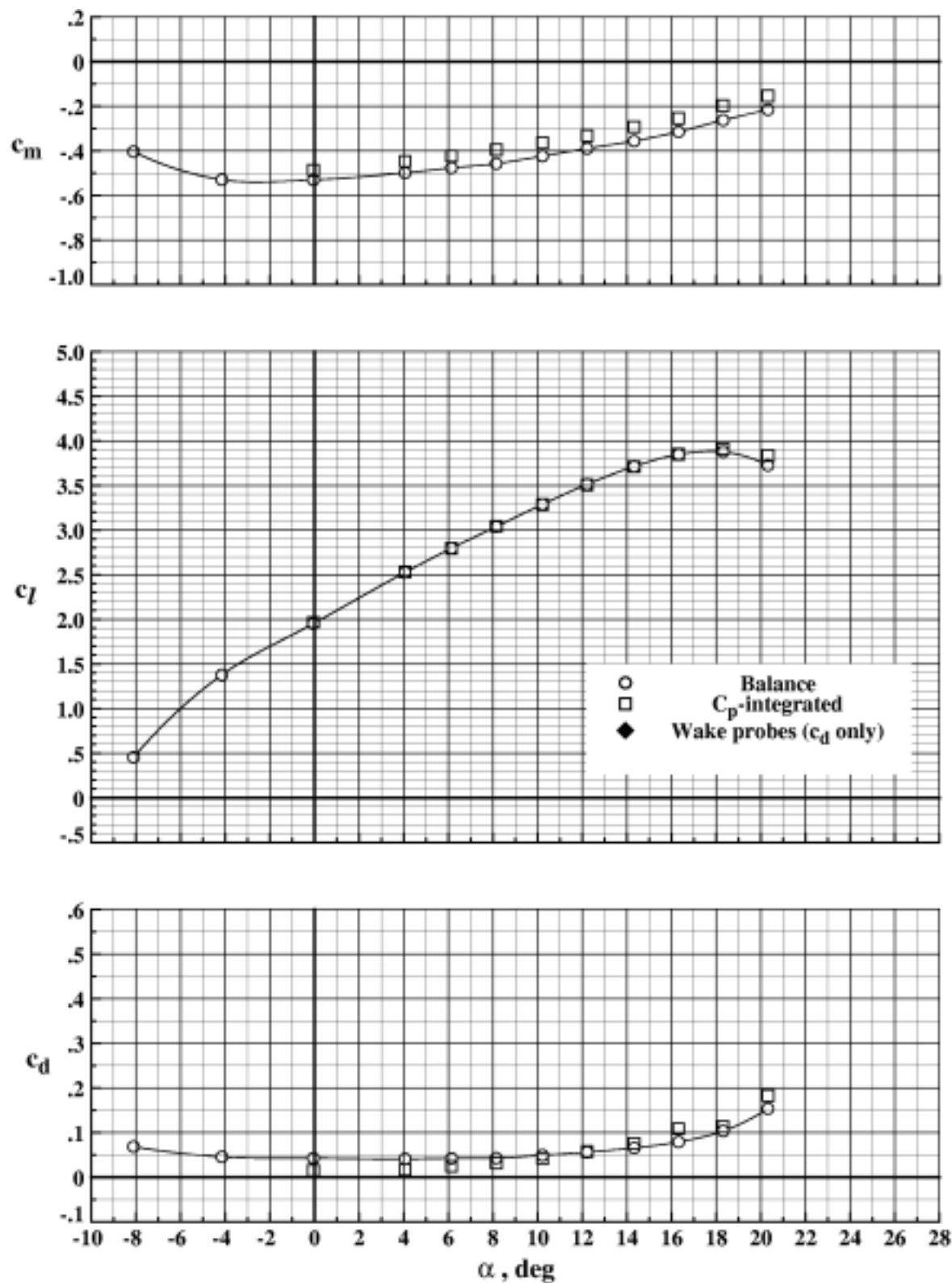
(c) $\delta_s = -50.0^\circ$, $M_\infty = 0.203$, $R_n = 12.127 \times 10^6$, Run 64.

Figure 81. Continued.



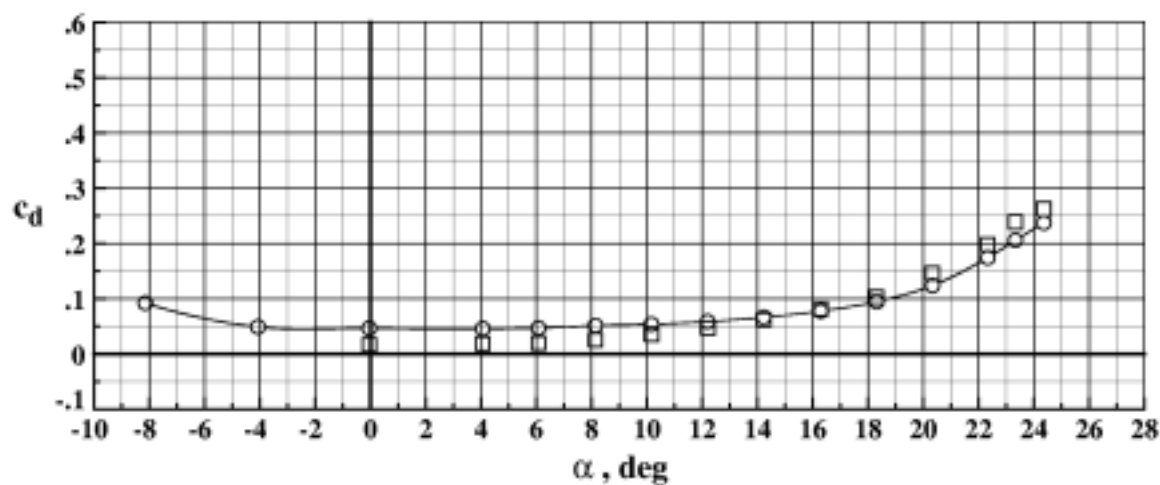
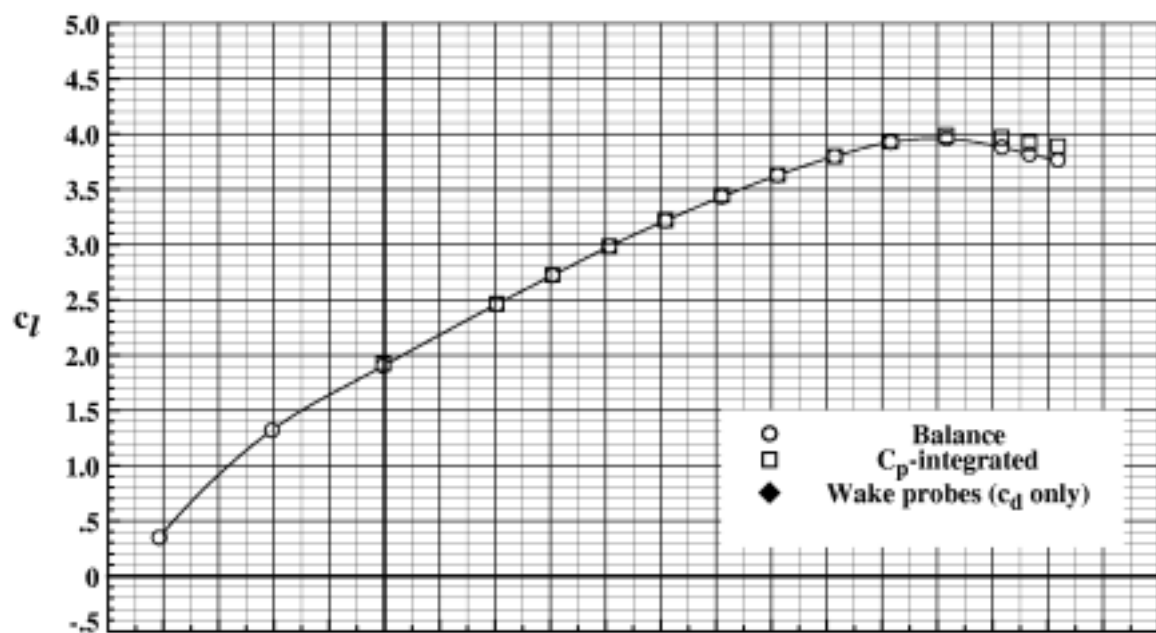
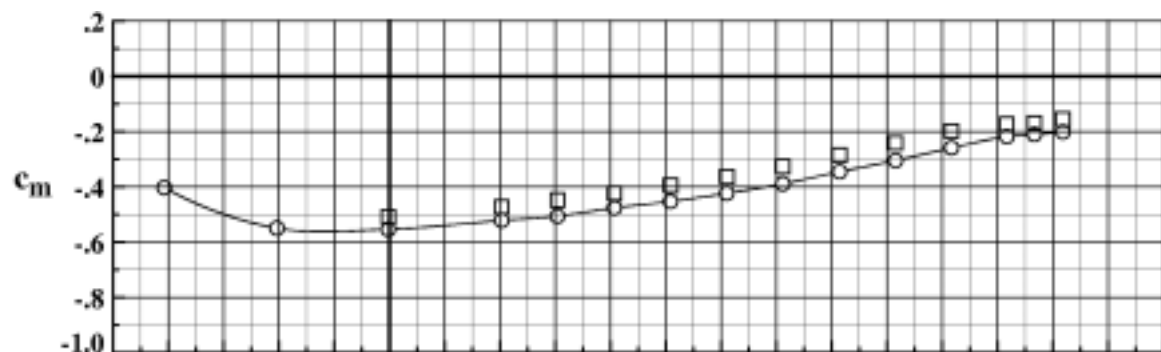
(d) $\delta_s = -60.0^\circ$, $M_\infty = 0.202$, $R_n = 12.163 \times 10^6$, Run 60.

Figure 81. Concluded.



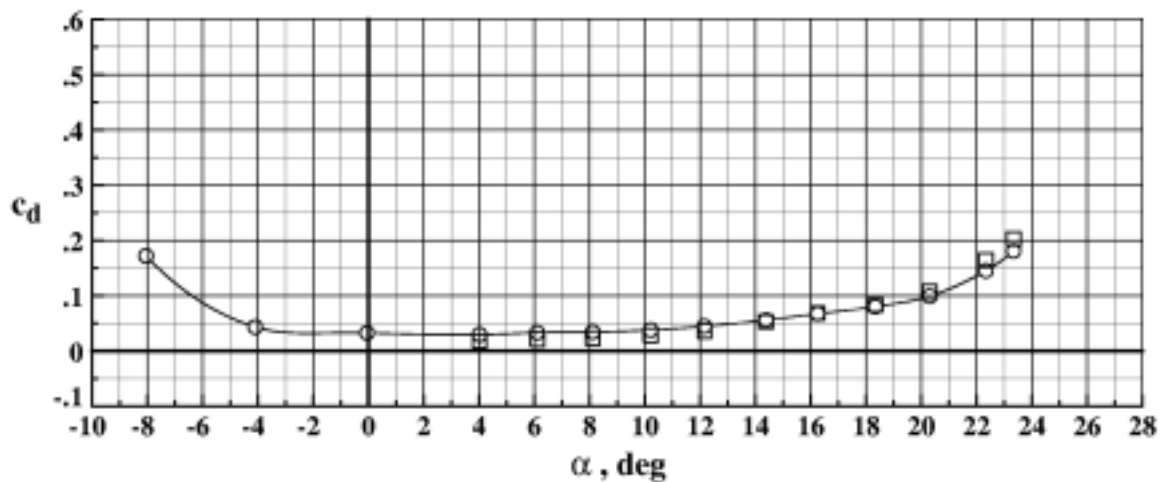
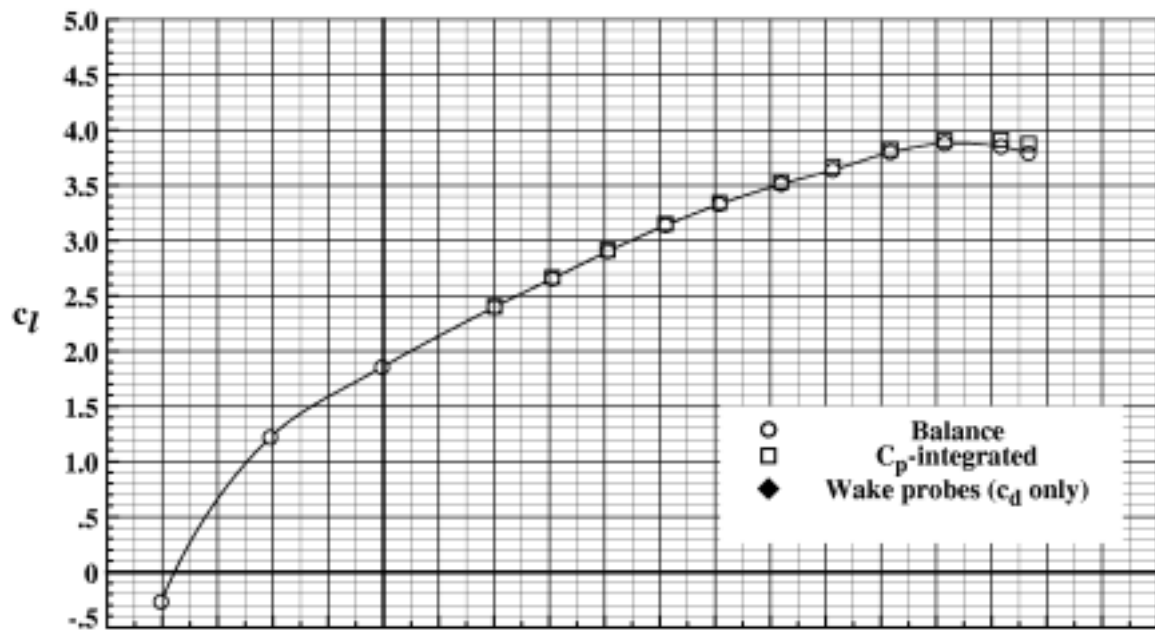
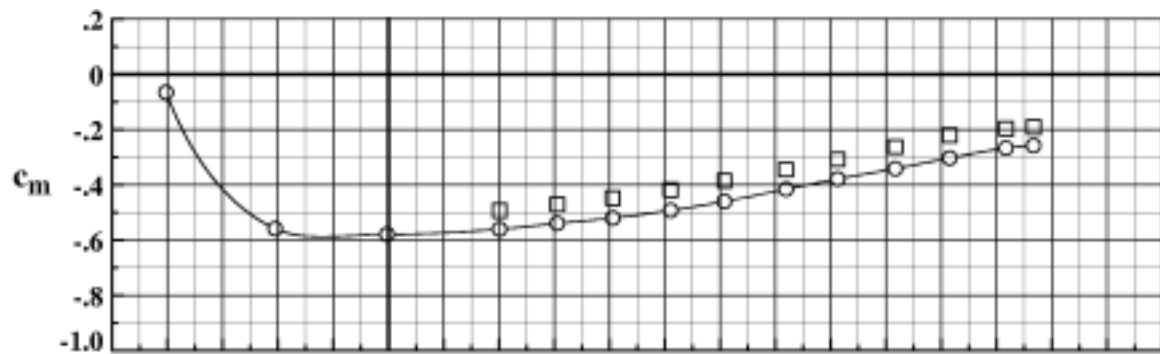
(a) $\delta_s = -30.0^\circ$, $M_\infty = 0.202$, $R_n = 12.096 \times 10^6$, Run 76.

Figure 82. Balance and C_p -integrated data for EET High-Lift Airfoil with $\delta_v = 15.0^\circ$ and $\delta_f = 15.0^\circ$.



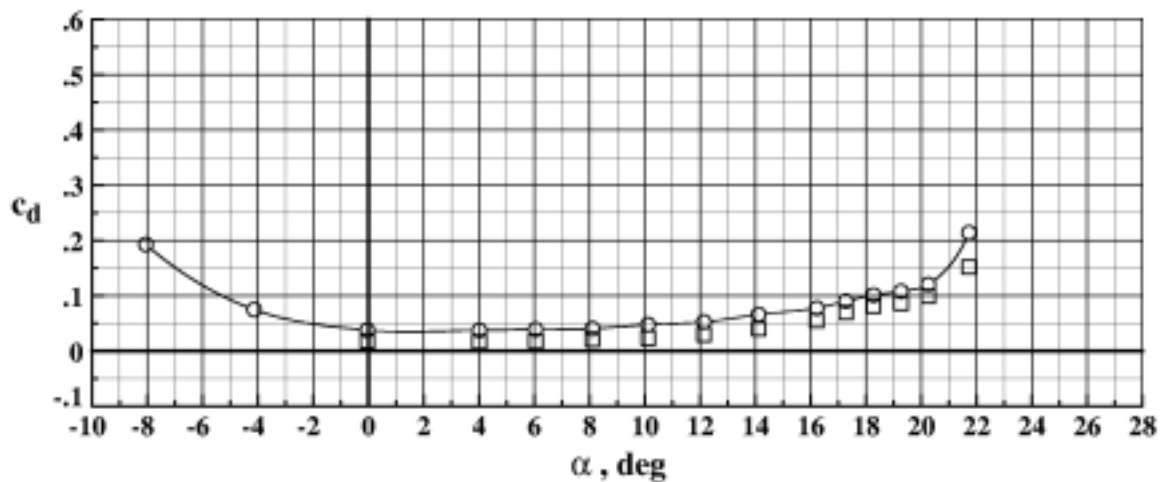
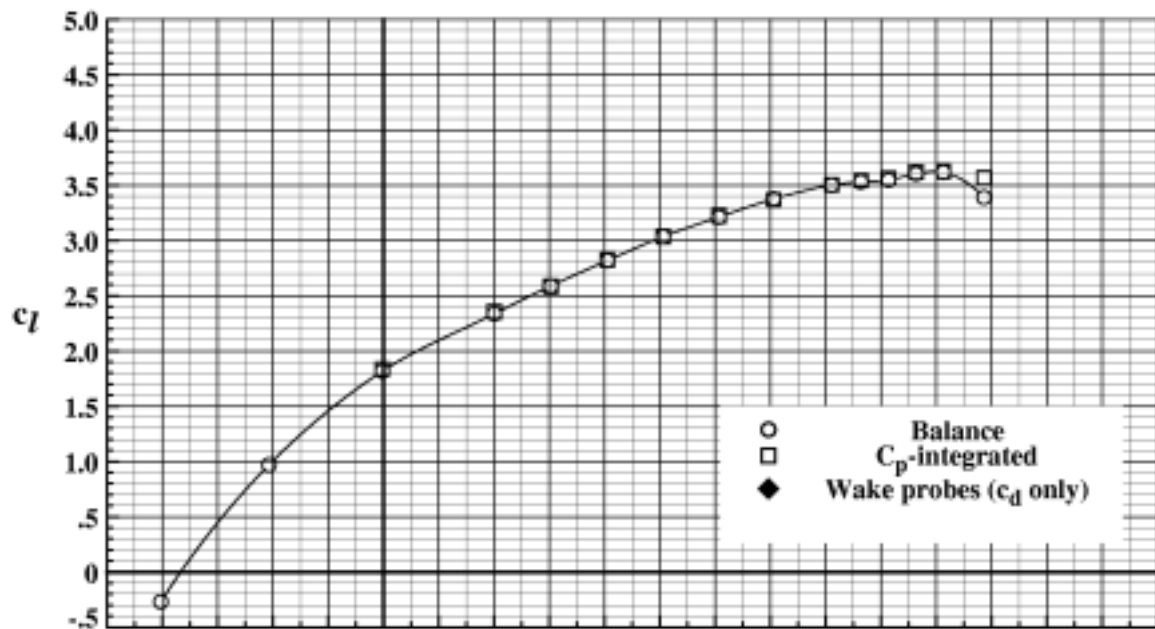
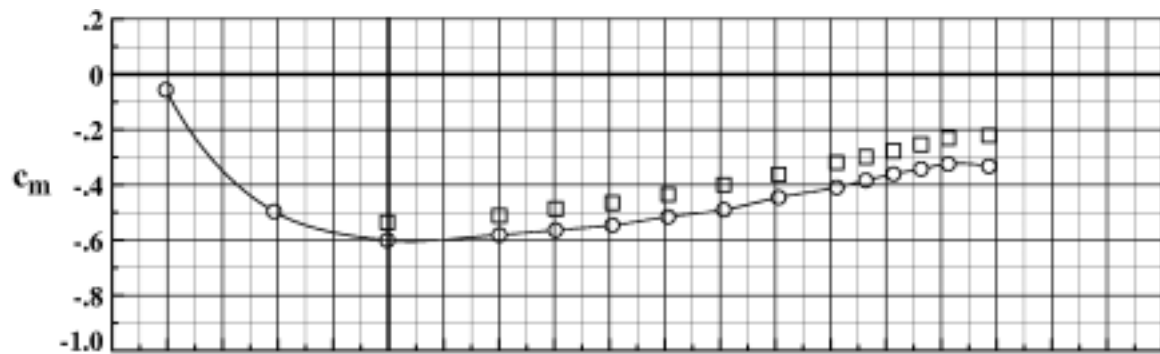
(b) $\delta_s = -40.0^\circ$, $M_\infty = 0.202$, $R_n = 12.149 \times 10^6$, Run 80.

Figure 82. Continued.



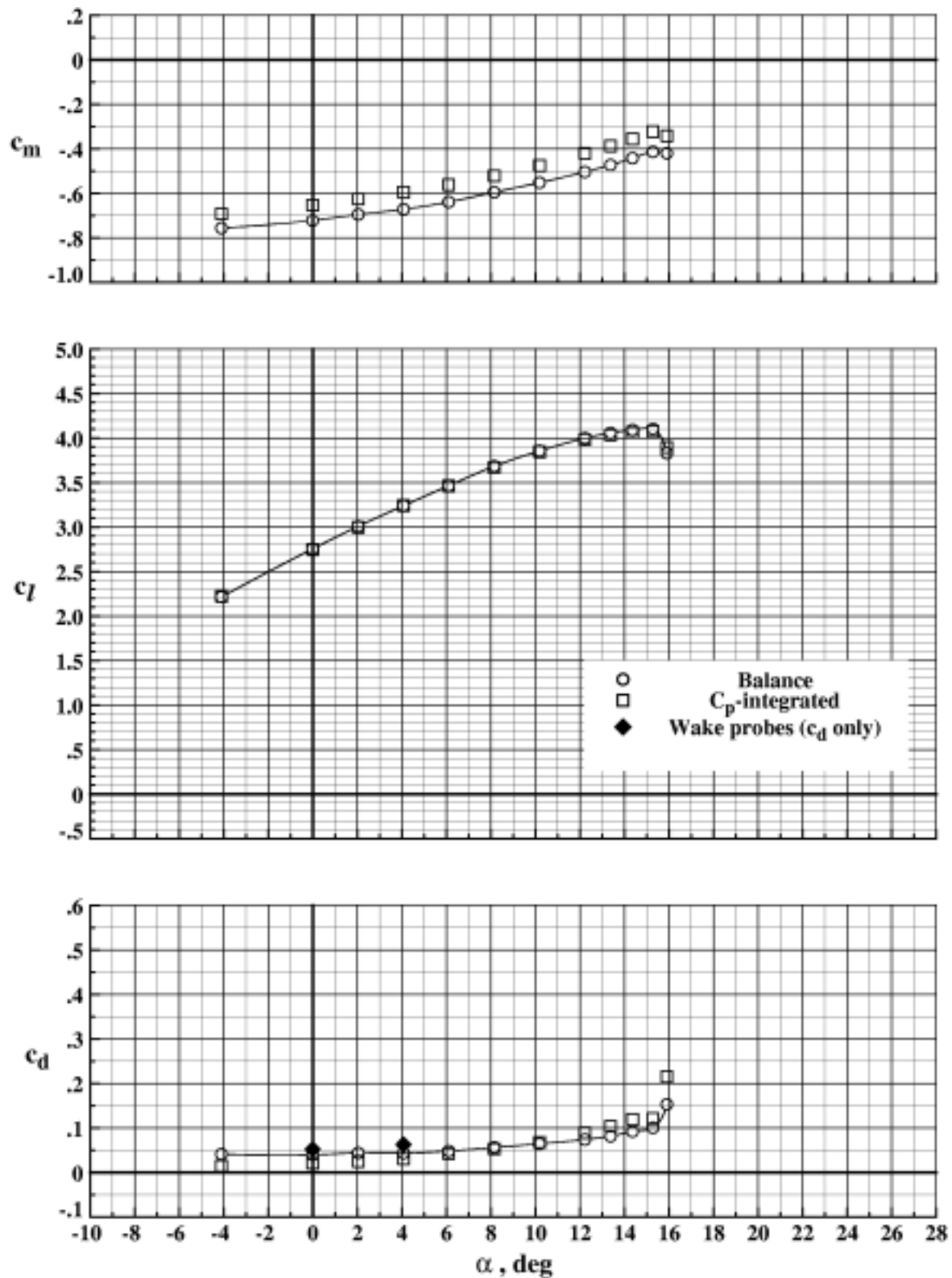
(c) $\delta_s = -50.0^\circ$, $M_\infty = 0.203$, $R_n = 12.180 \times 10^6$, Run 96.

Figure 82. Continued.



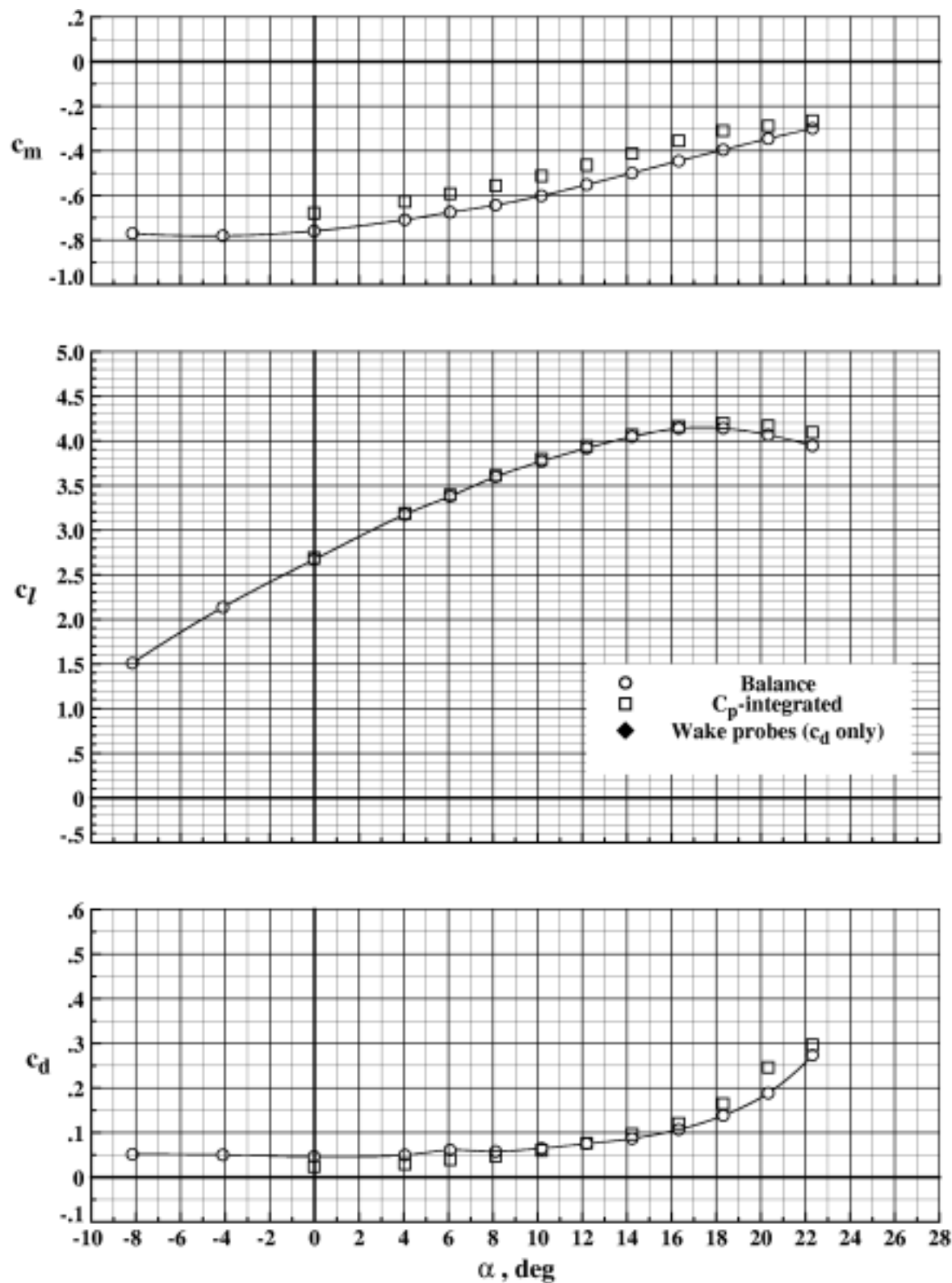
(d) $\delta_s = -60.0^\circ$, $M_\infty = 0.202$, $R_n = 12.139 \times 10^6$, Run 102.

Figure 82. Concluded.



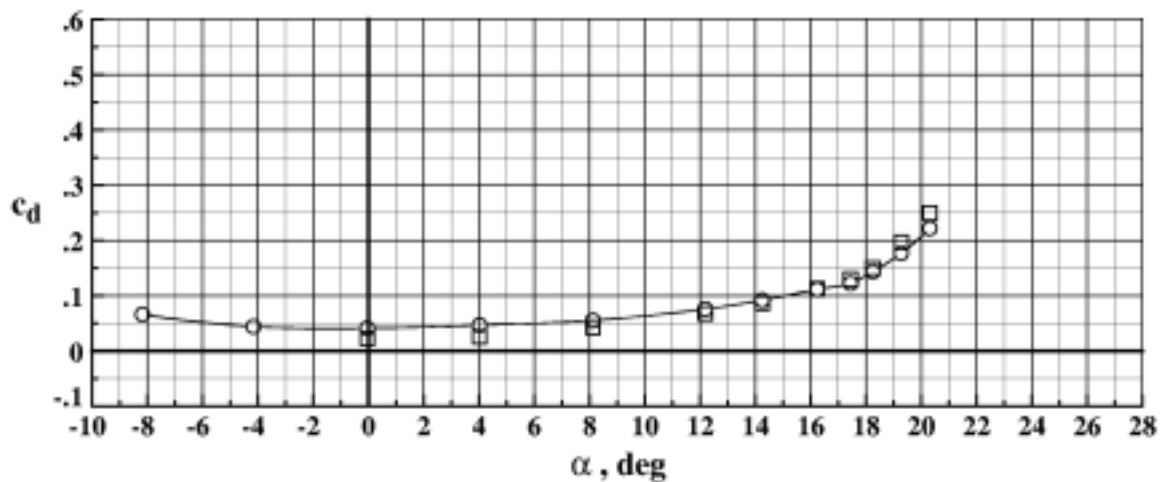
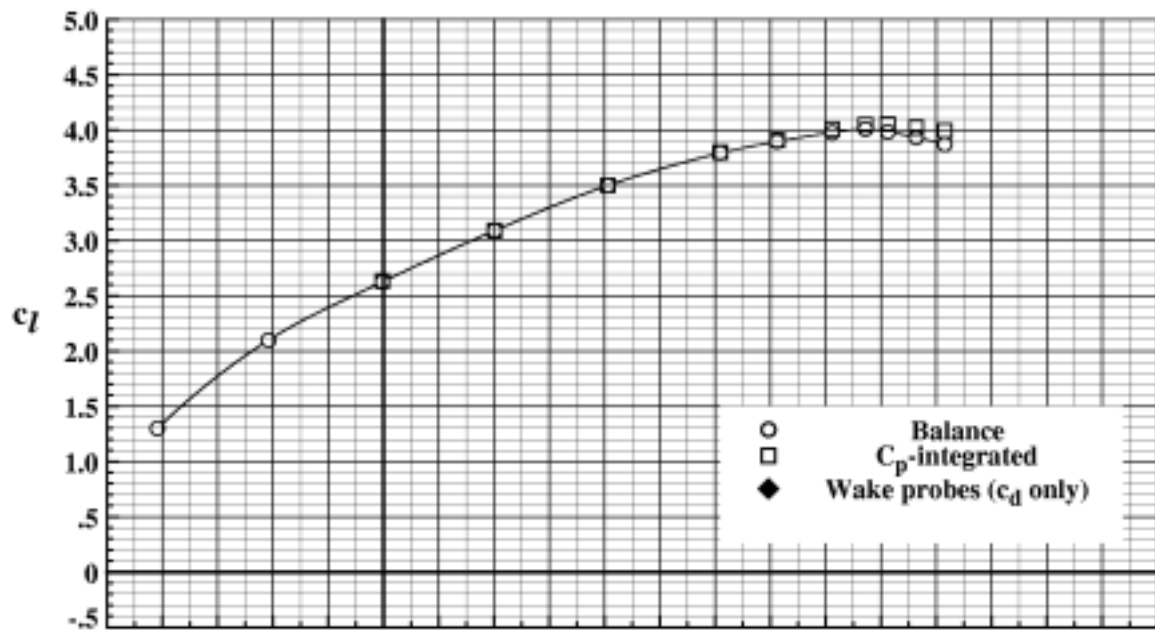
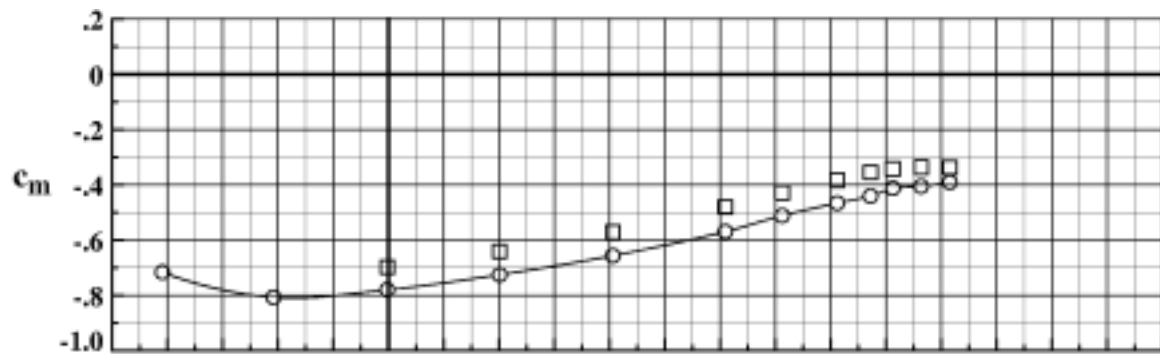
(a) $\delta_s = -30.0^\circ$, $M_\infty = 0.202$, $R_n = 12.117 \times 10^6$, Run 32.

Figure 83. Balance and C_p -integrated data for EET High-Lift Airfoil with $\delta_v = 22.5^\circ$ and $\delta_f = 22.5^\circ$.



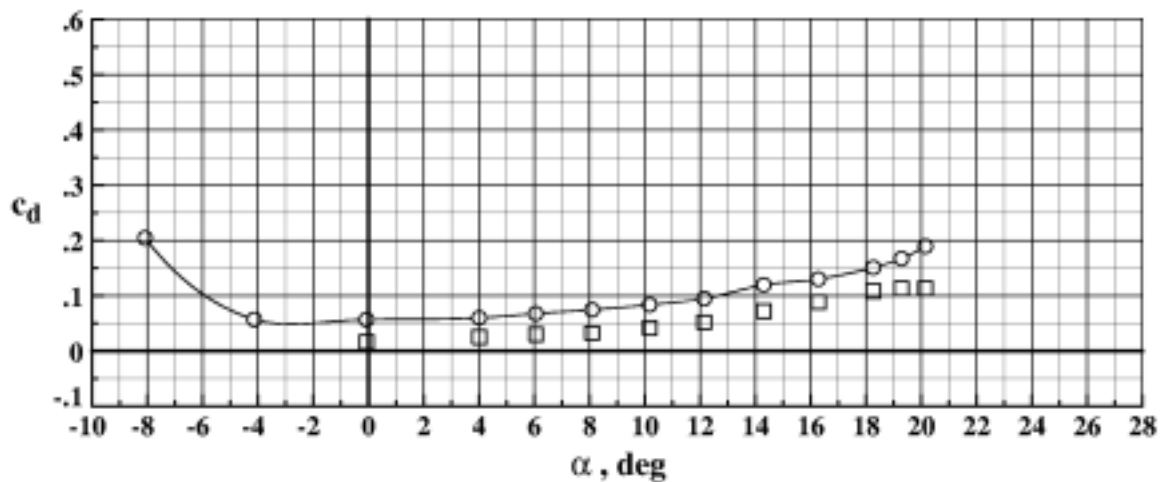
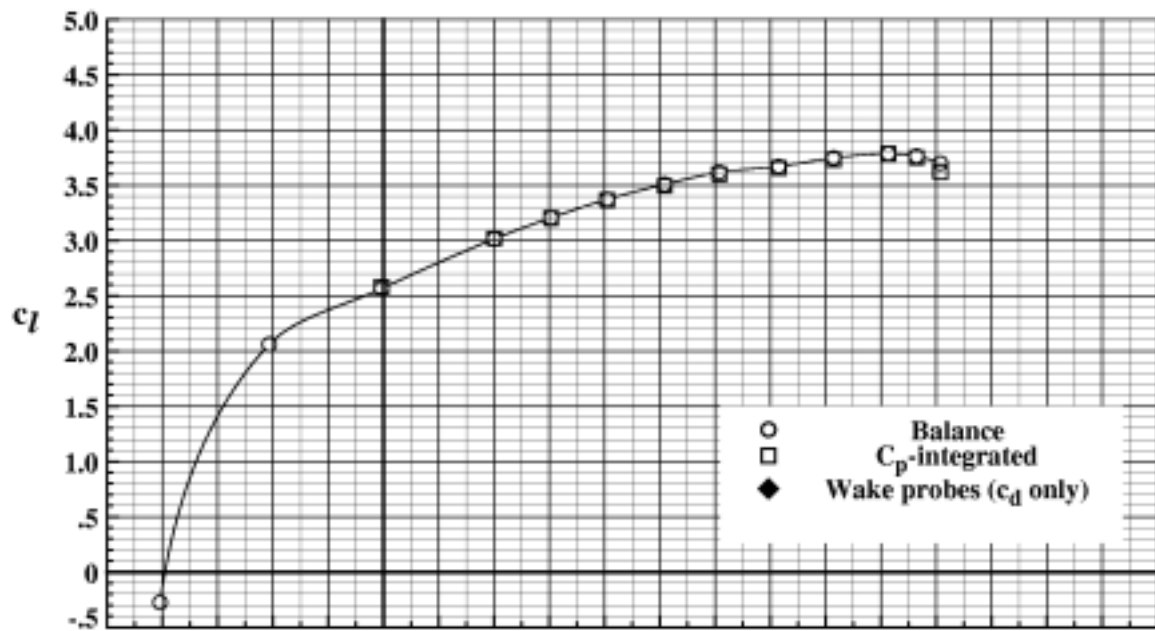
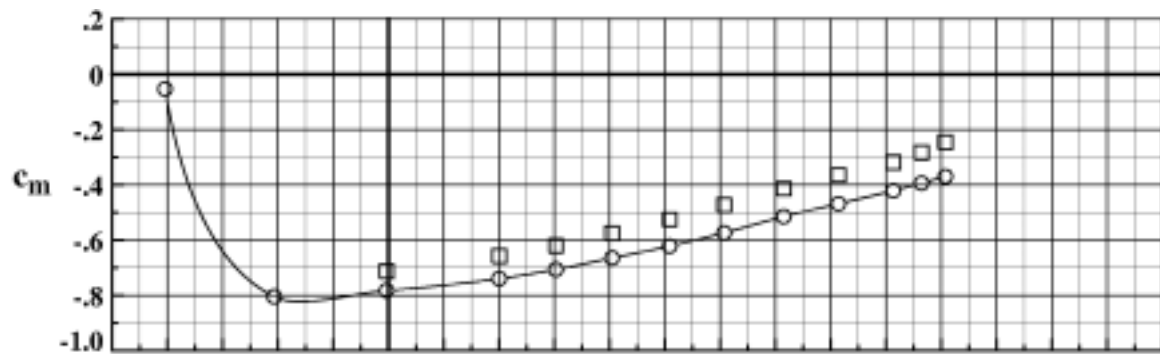
(b) $\delta_s = -40.0^\circ$, $M_\infty = 0.202$, $R_n = 12.154 \times 10^6$, Run 116.

Figure 83. Continued.



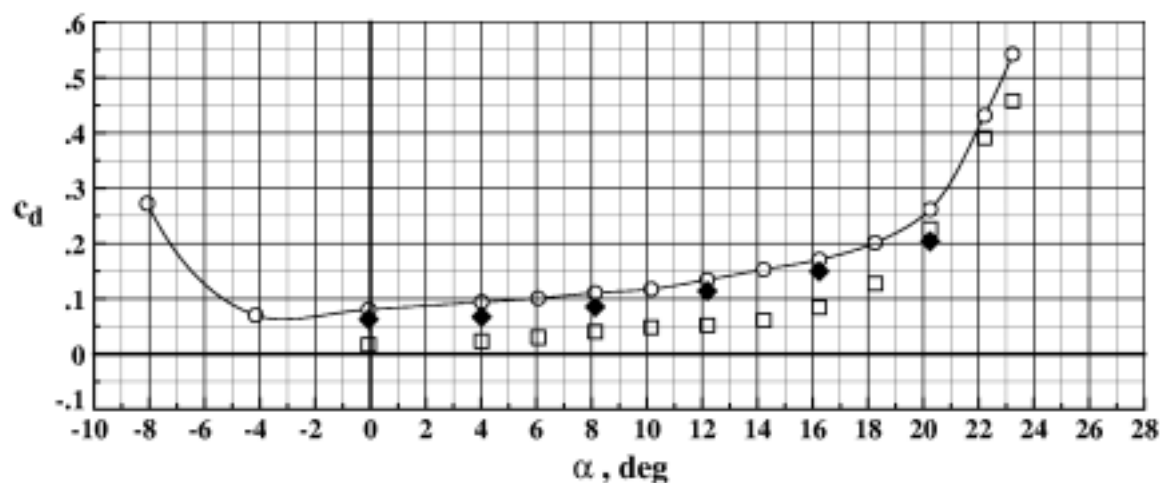
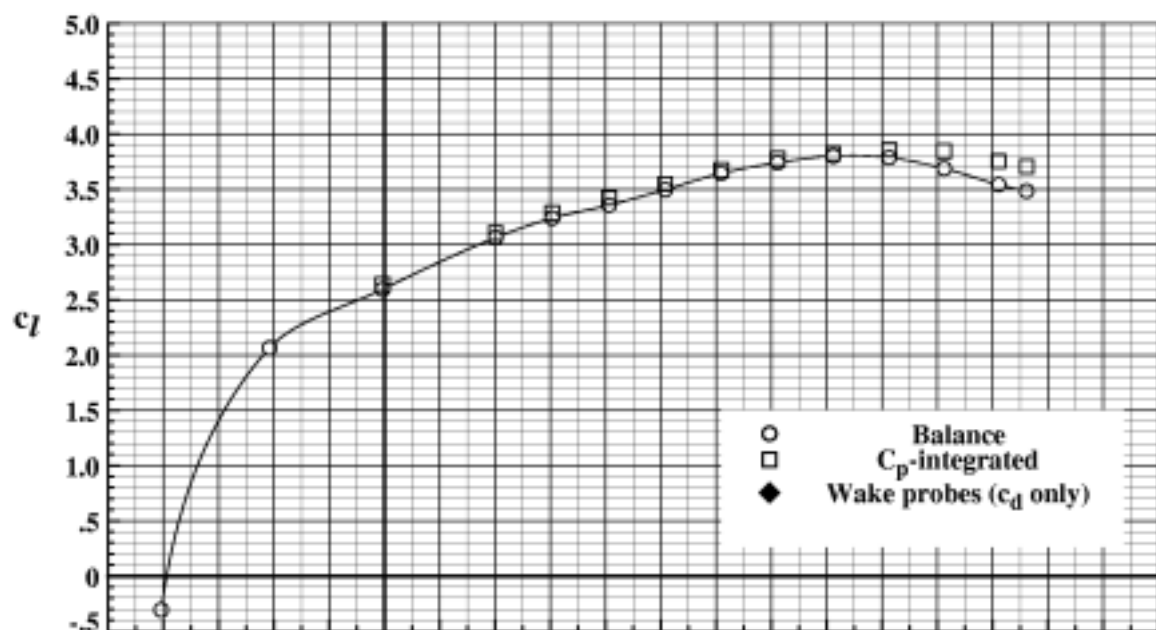
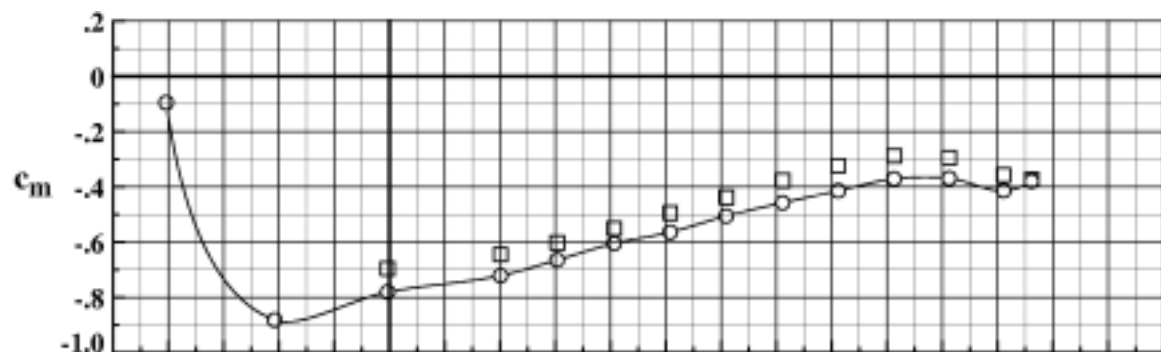
(c) $\delta_s = -50.0^\circ$, $M_\infty = 0.202$, $R_n = 12.104 \times 10^6$, Run 9.

Figure 83. Continued.



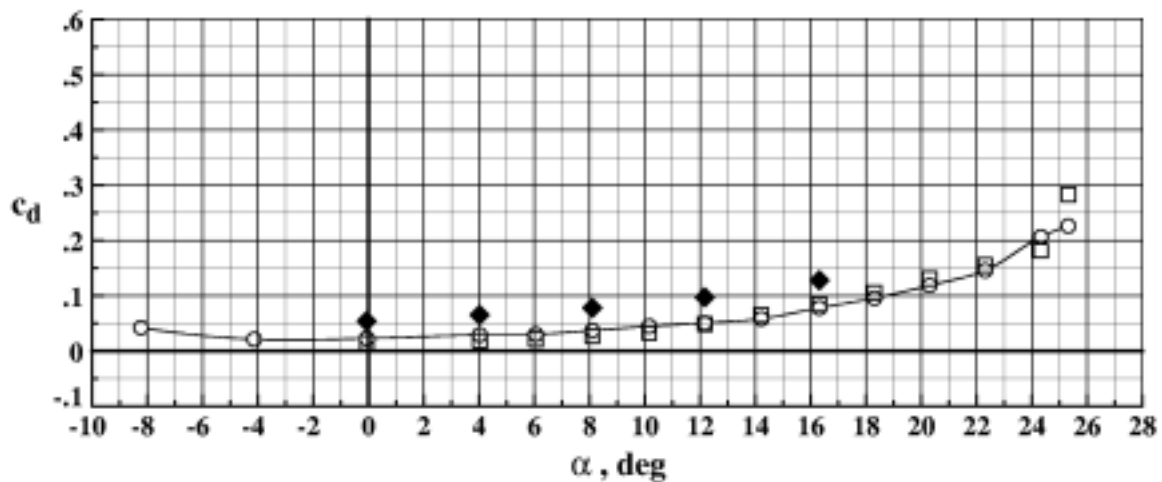
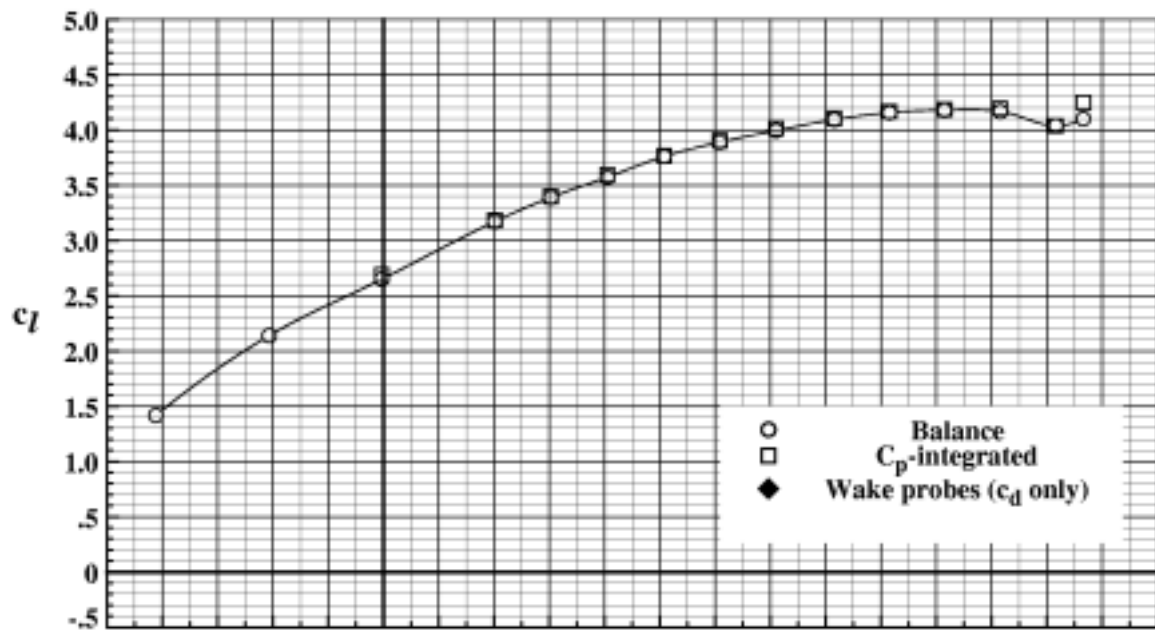
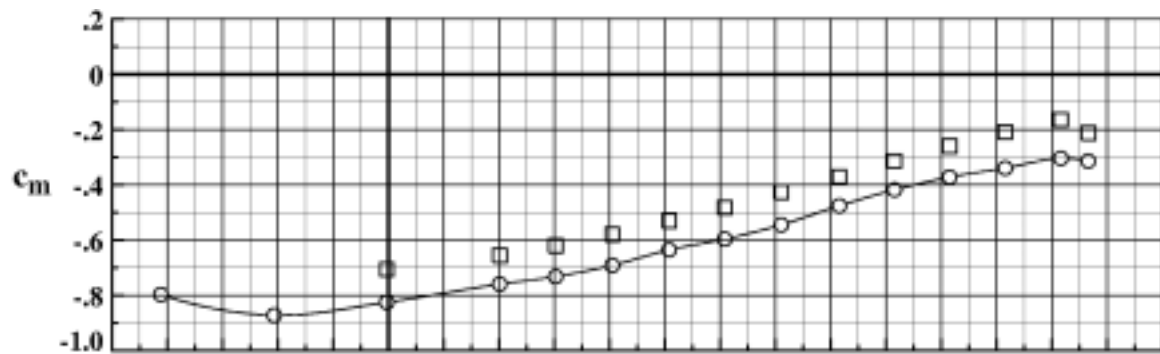
(d) $\delta_s = -60.0^\circ$, $M_\infty = 0.203$, $R_x = 12.204 \times 10^6$, Run 120.

Figure 83. Concluded.



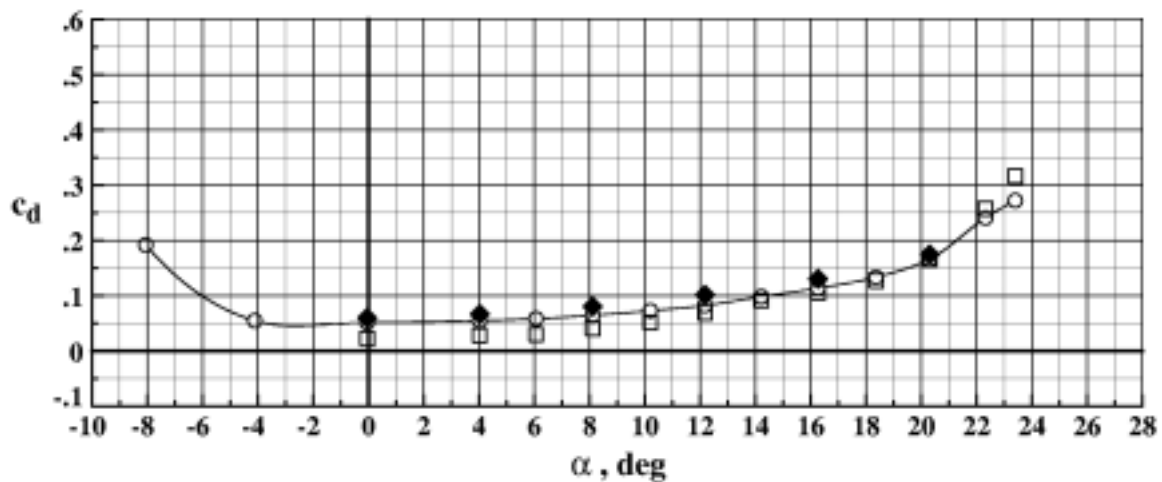
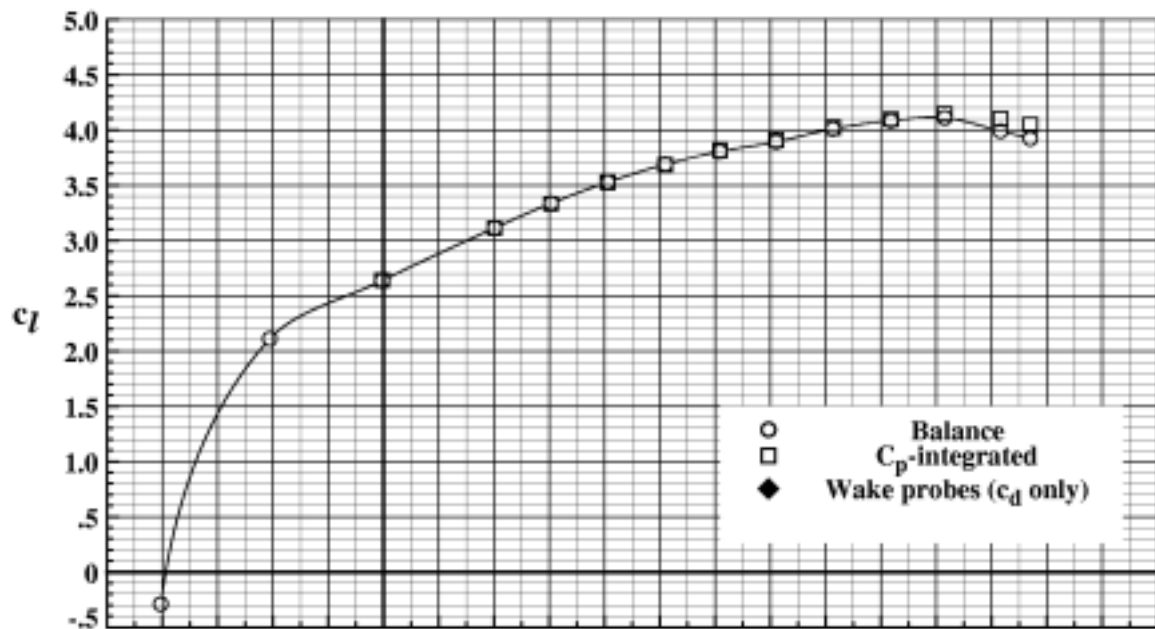
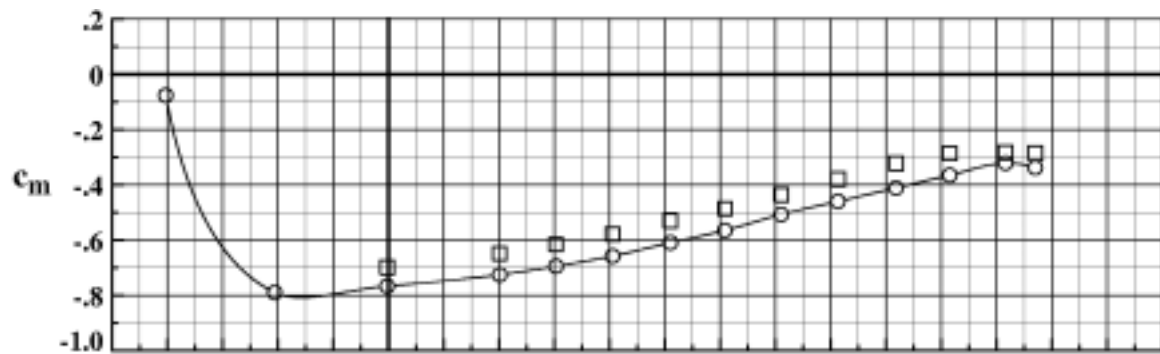
(a) $\delta_s = -50.0^\circ$, $M_\infty = 0.203$, $R_n = 2.470 \times 10^6$, Run 112.

Figure 84. Balance and C_p -integrated data for EET High-Lift Airfoil with $\delta_v = 22.5^\circ$ and $\delta_f = 22.5^\circ$.



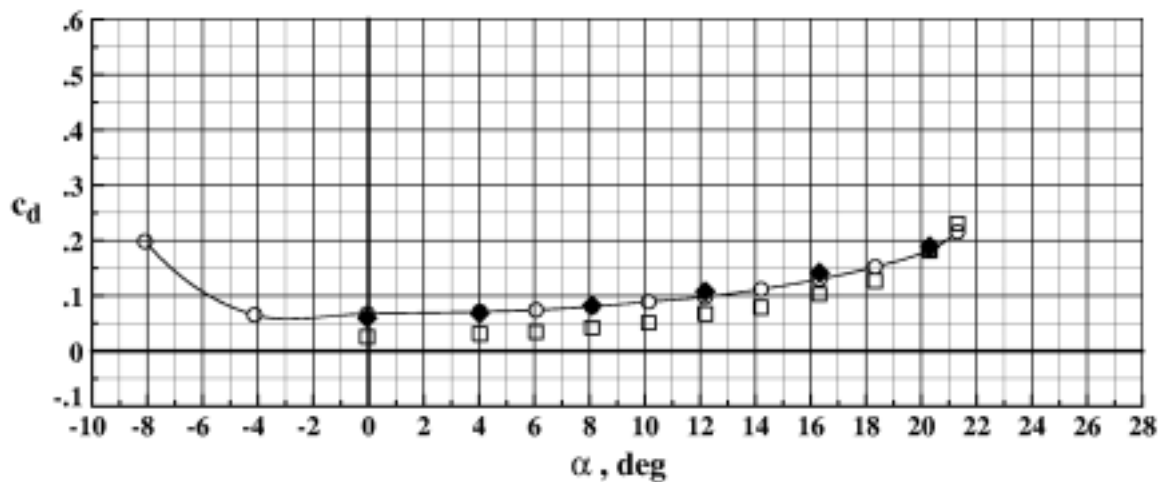
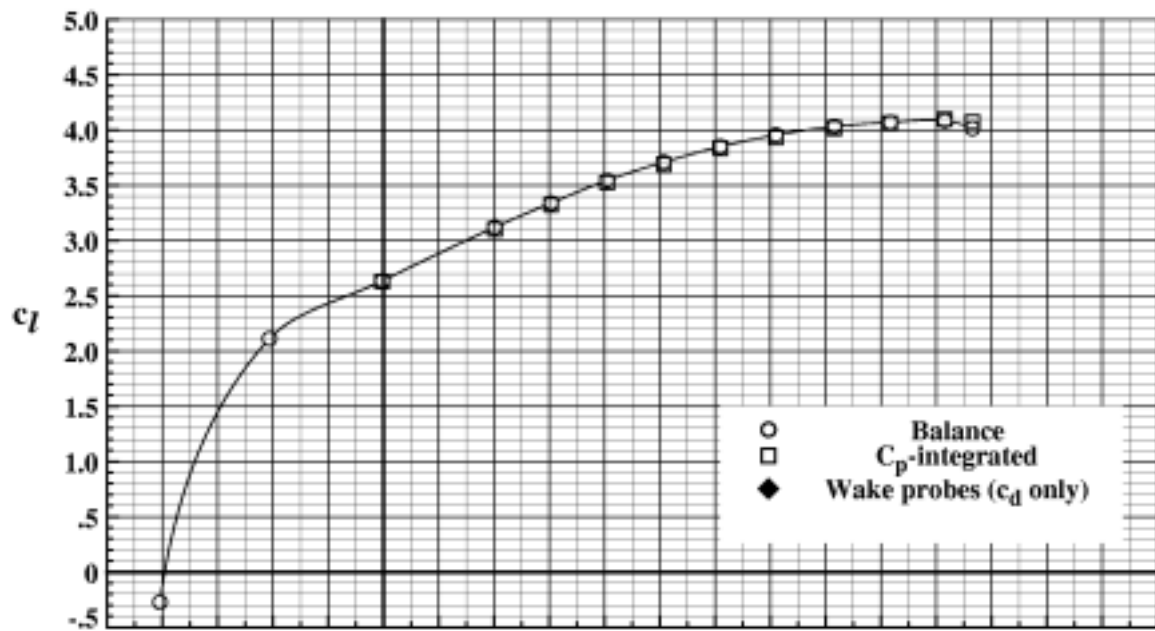
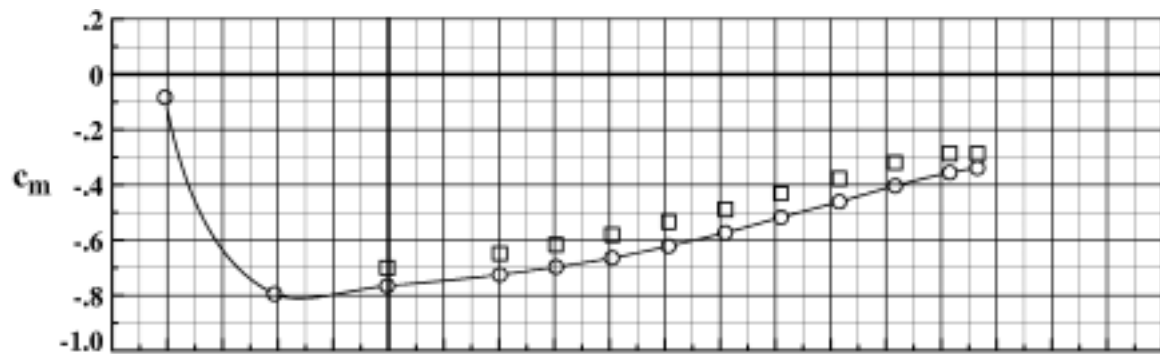
(b) $\delta_s = -50.0^\circ$, $M_\infty = 0.202$, $R_n = 6.113 \times 10^6$, Run 106.

Figure 84. Continued.



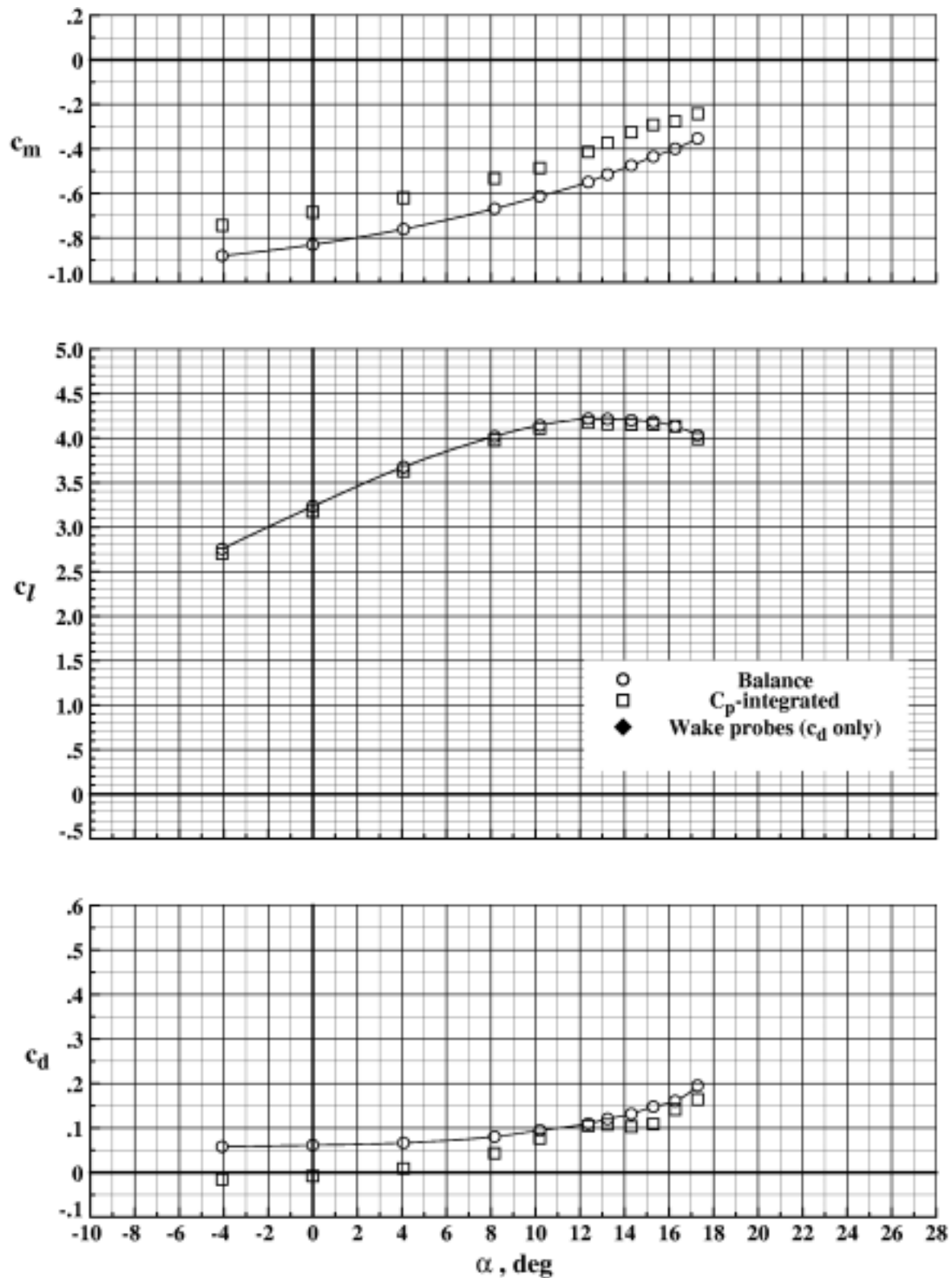
(c) $\delta_s = -50.0^\circ$, $M_\infty = 0.203$, $R_n = 12.148 \times 10^6$, Run 107.

Figure 84. Continued.



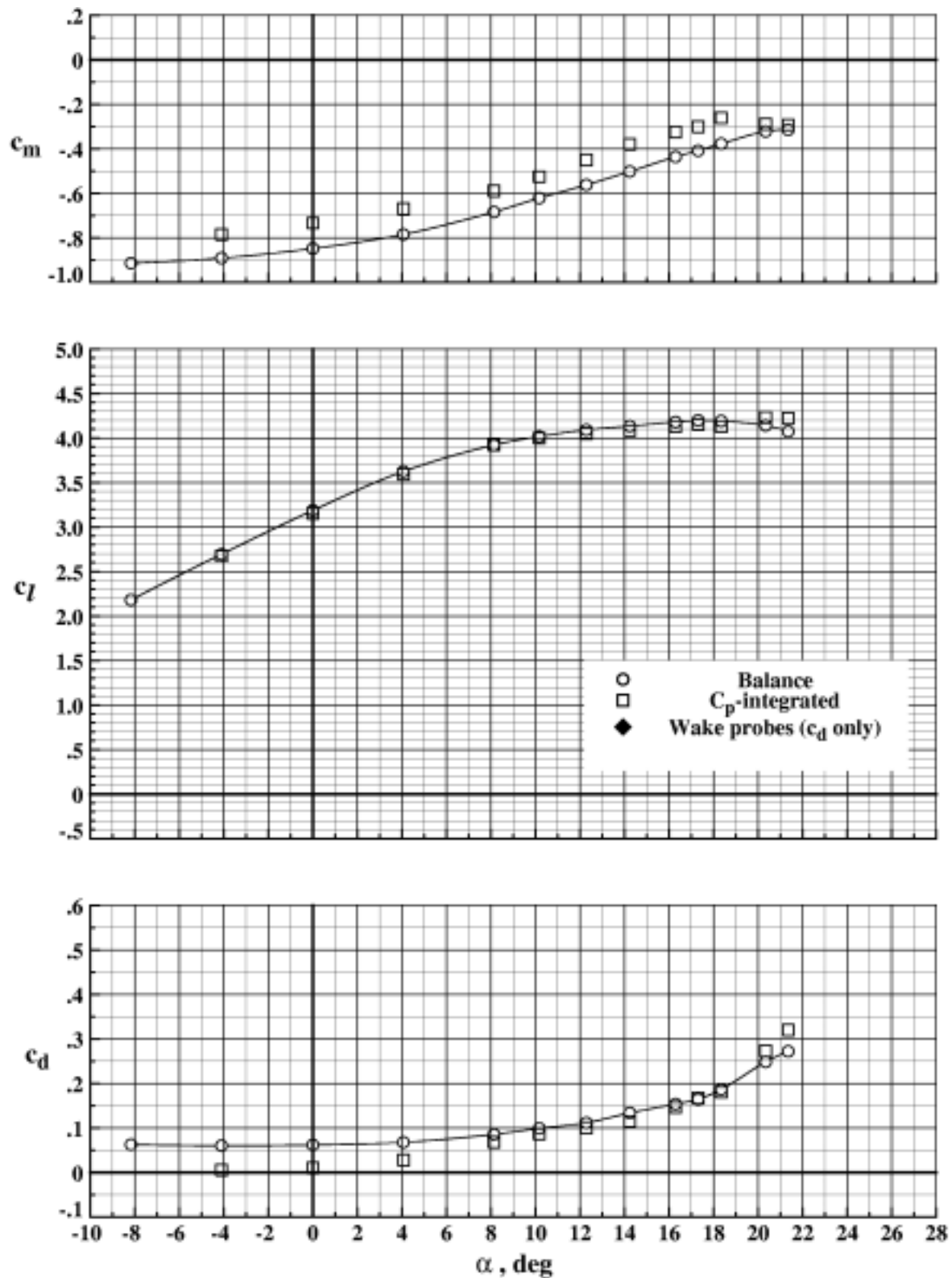
(d) $\delta_3 = -50.0^\circ$, $M_\infty = 0.203$, $R_n = 18.211 \times 10^6$, Run 109.

Figure 84. Concluded.



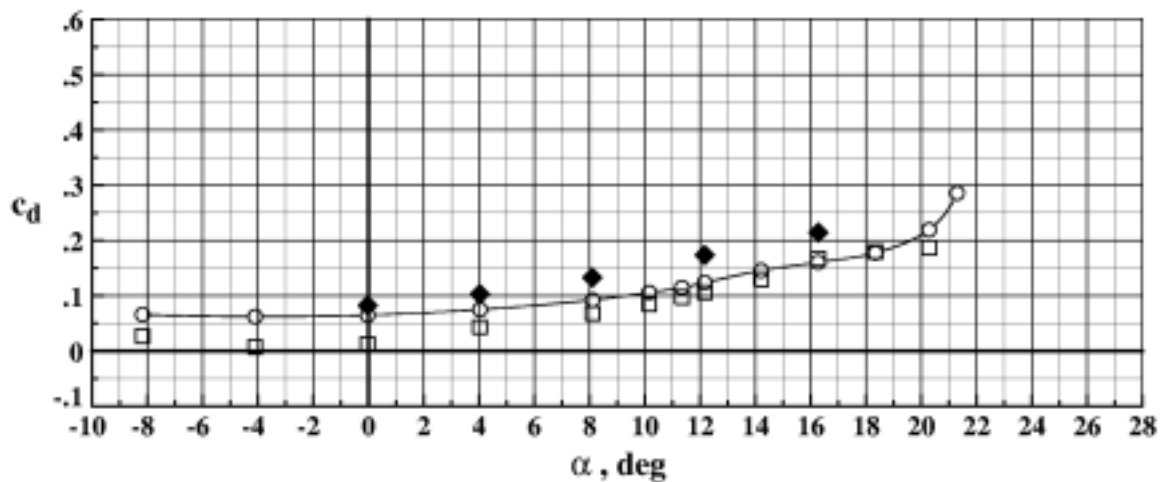
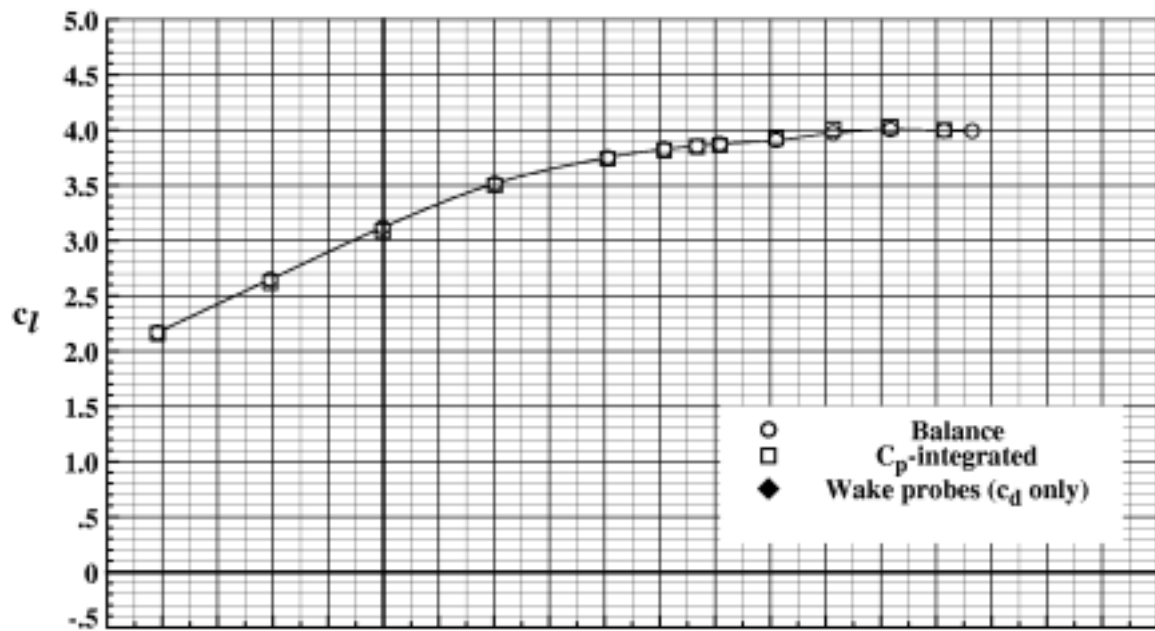
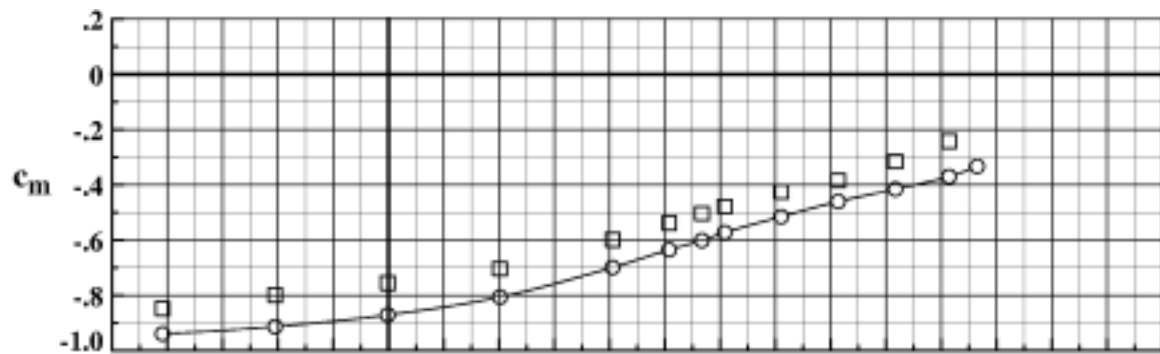
(a) $\delta_s = -30.0^\circ$, $M_\infty = 0.202$, $R_n = 12.147 \times 10^6$, Run 41.

Figure 85. Balance and C_p -integrated data for EET High-Lift Airfoil with $\delta_v = 30.0^\circ$ and $\delta_f = 30.0^\circ$.



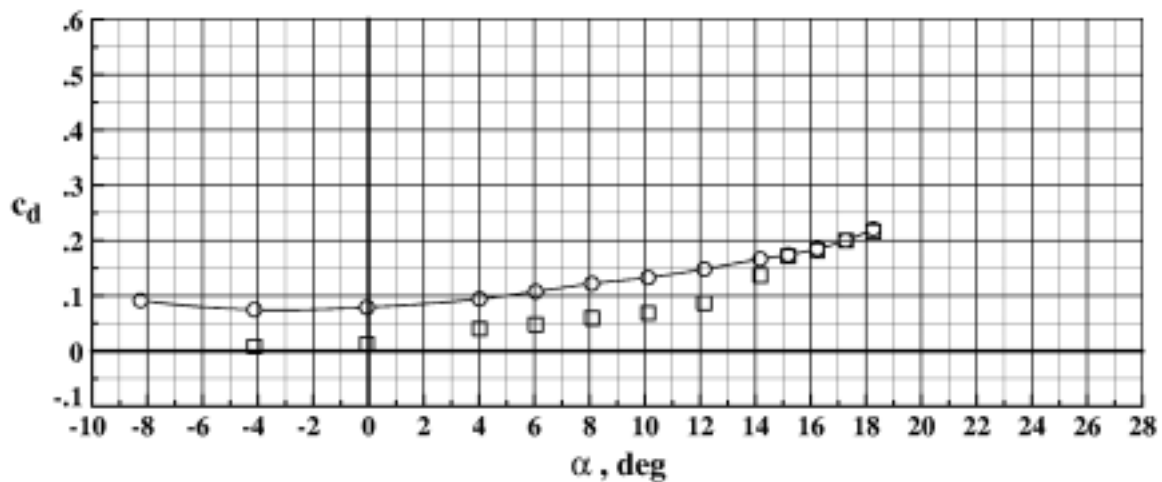
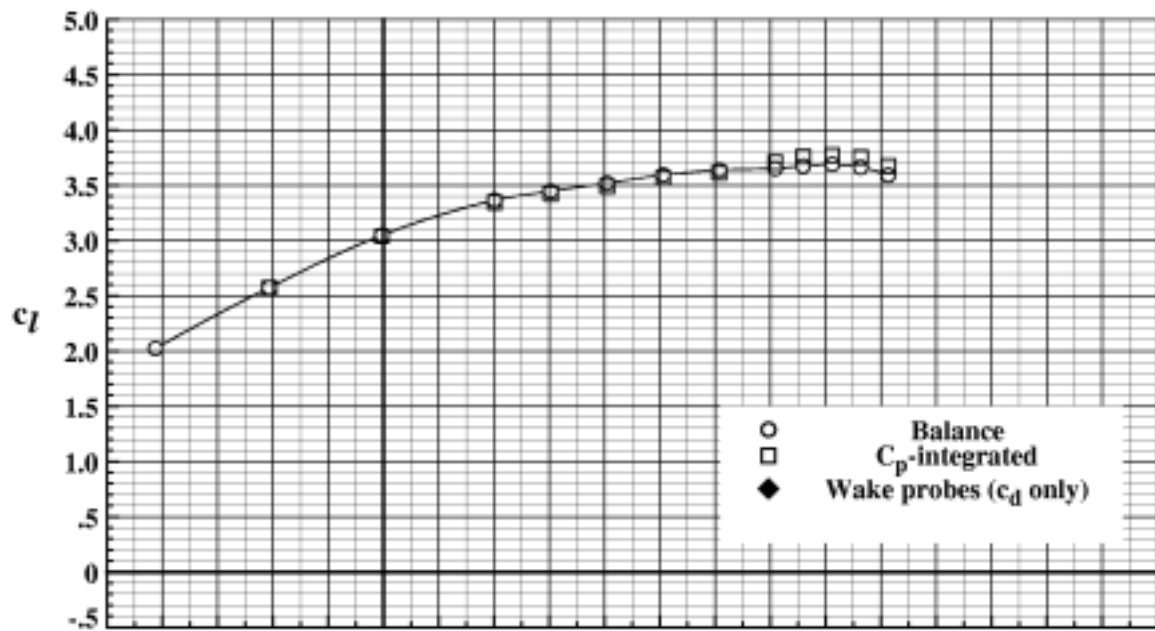
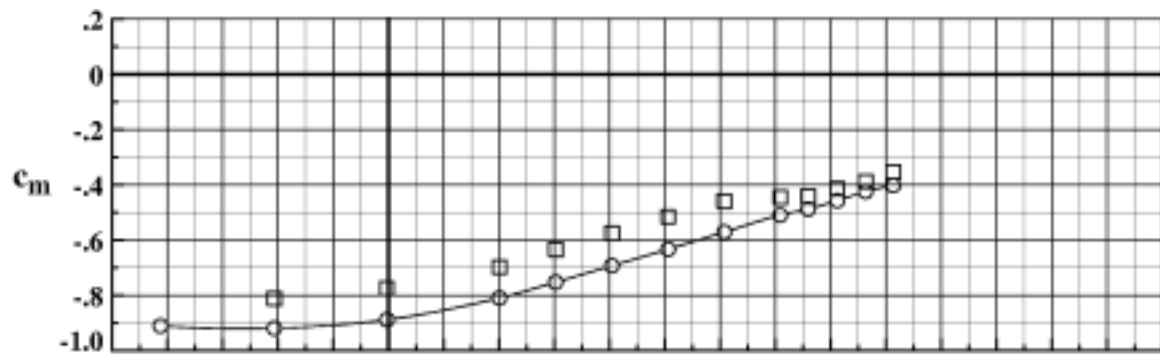
(b) $\delta_s = -40.0^\circ$, $M_\infty = 0.203$, $R_n = 12.157 \times 10^6$, Run 46.

Figure 85. Continued.



(c) $\delta_s = -50.0^\circ$, $M_\infty = 0.203$, $R_n = 12.146 \times 10^6$, Run 52.

Figure 85. Continued.



(d) $\delta_s = -60.0^\circ$, $M_\infty = 0.203$, $R_n = 12.205 \times 10^6$, Run 56.

Figure 85. Concluded.

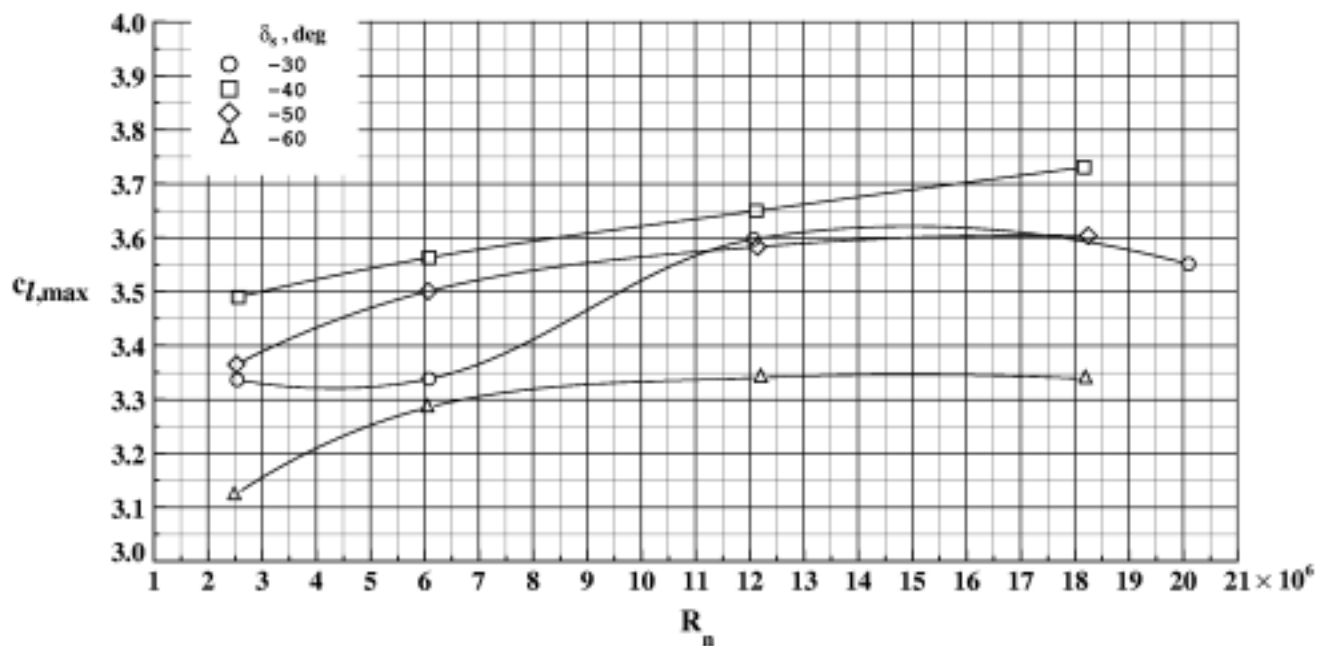


Figure 86. Effect of Reynolds number on maximum lift performance of EET High-Lift Airfoil with $\delta_v = 7.5^\circ$ and $\delta_f = 7.5^\circ$.

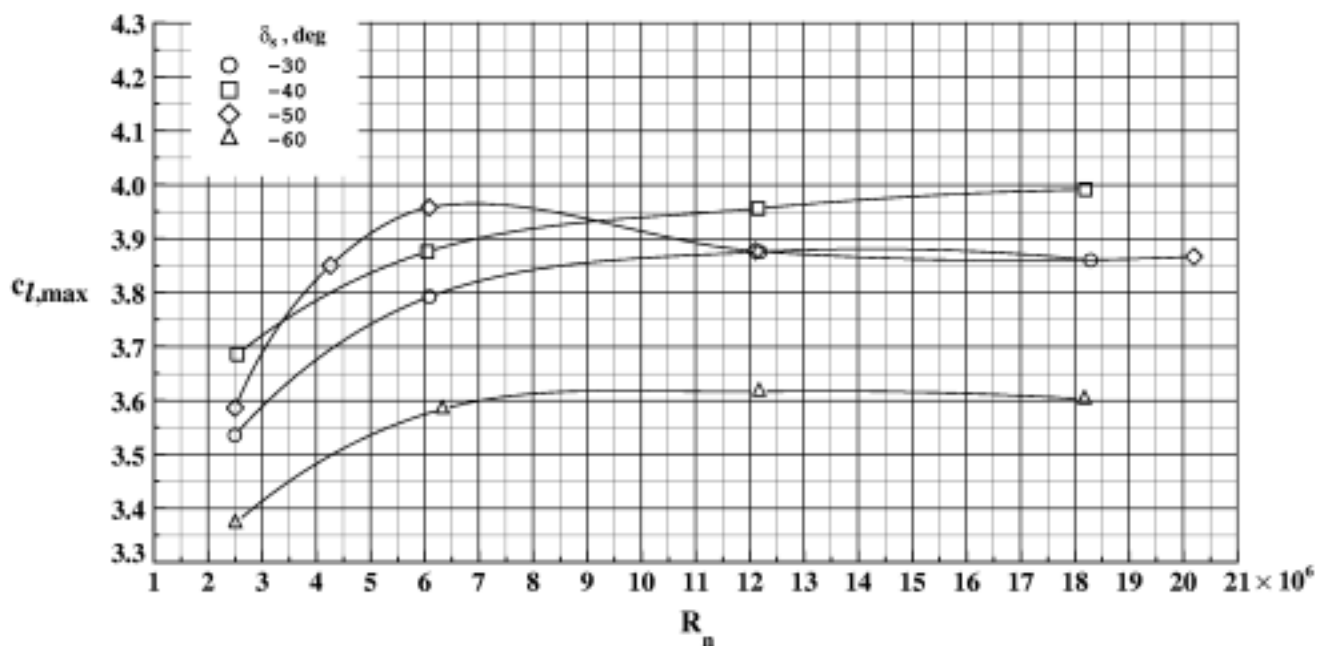


Figure 87. Effect of Reynolds number on maximum lift performance of EET High-Lift Airfoil with $\delta_v = 15.0^\circ$ and $\delta_f = 15.0^\circ$.

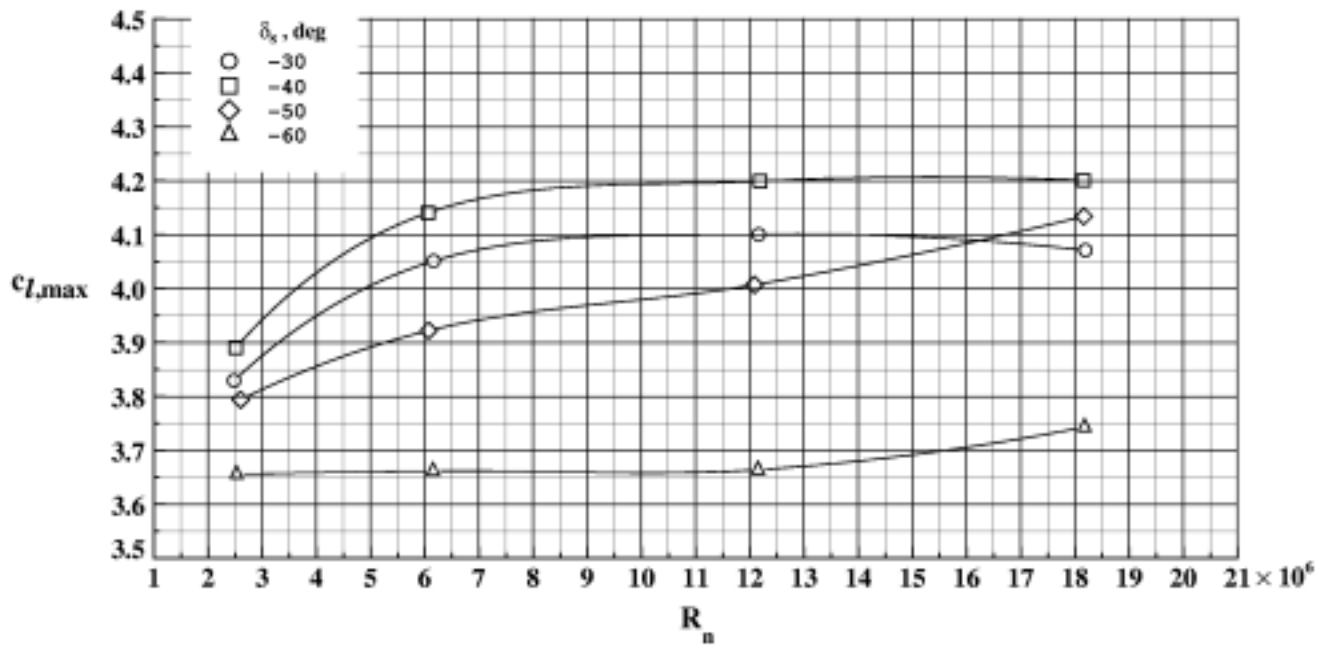


Figure 88. Effect of Reynolds number on maximum lift performance of EET High-Lift Airfoil with $\delta_v = 22.5^\circ$ and $\delta_\Gamma = 22.5^\circ$.

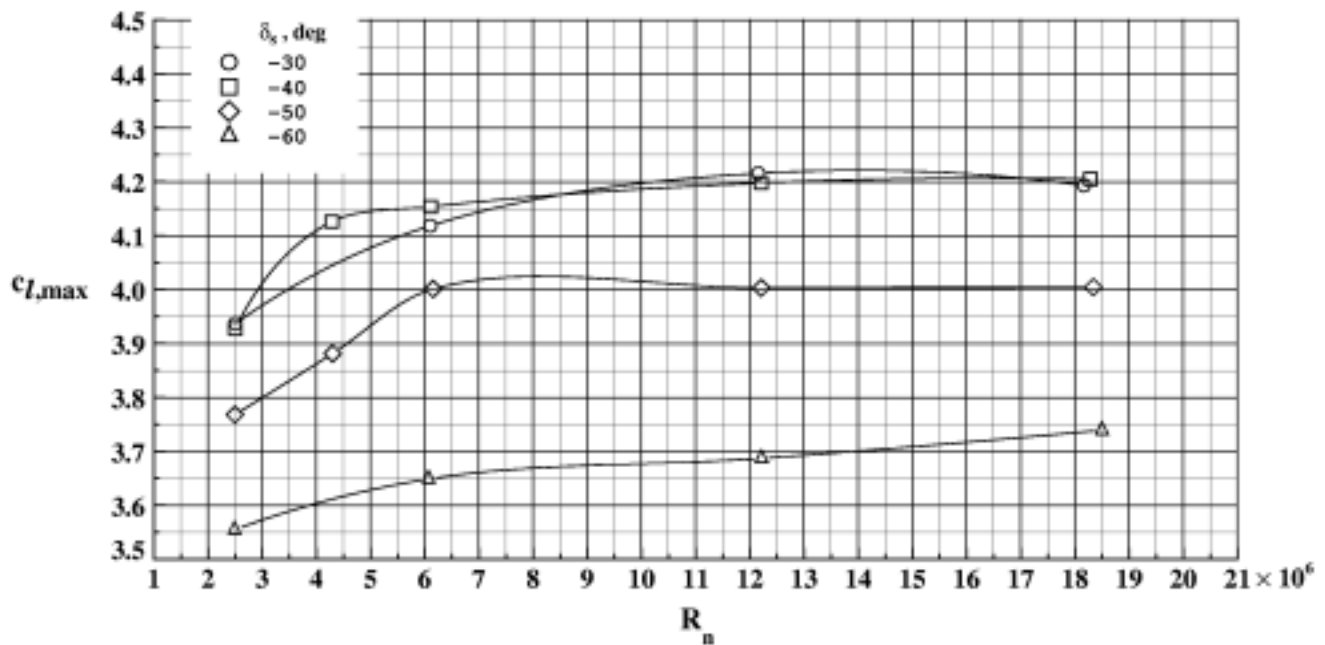
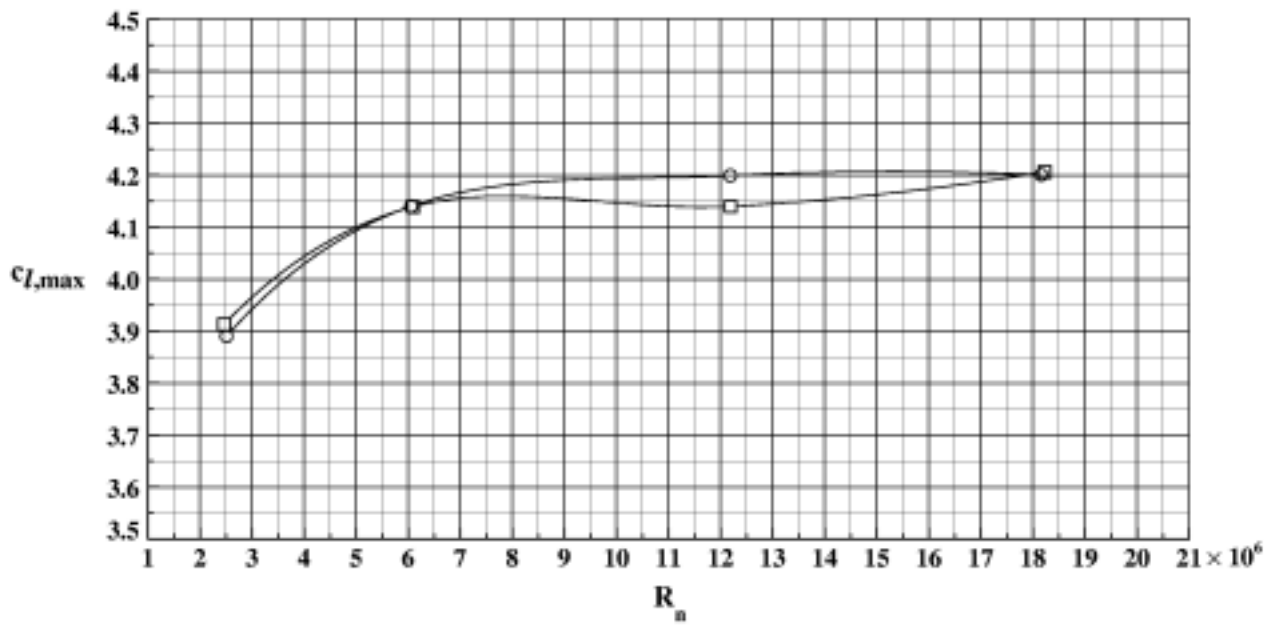
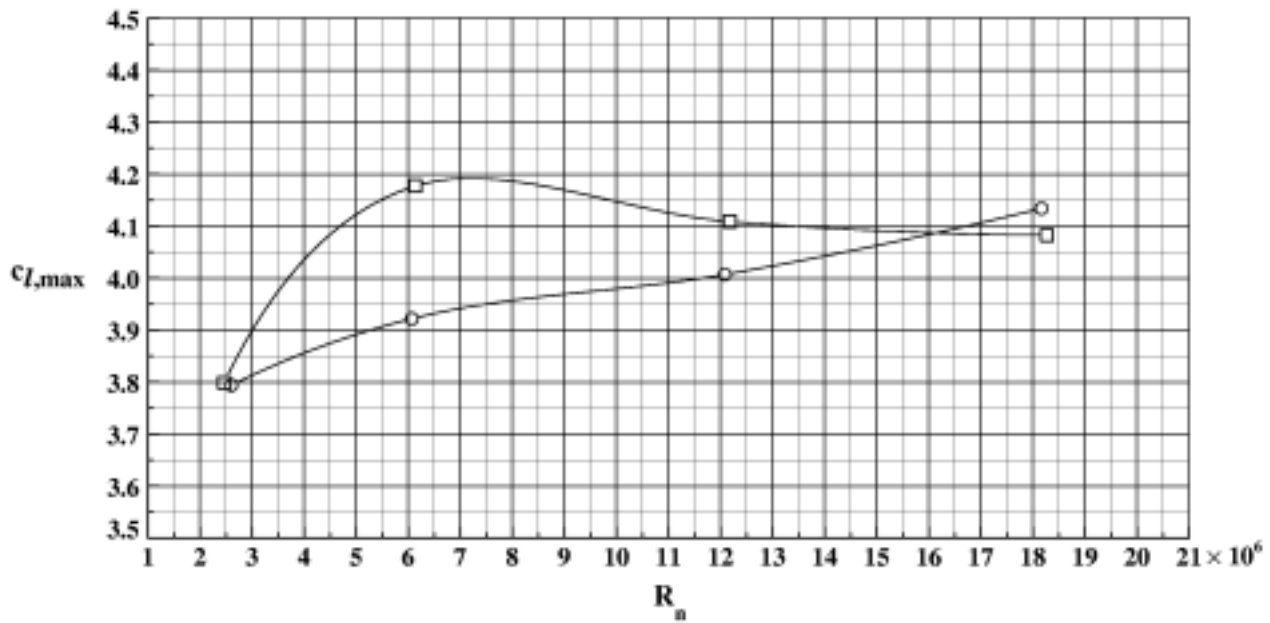


Figure 89. Effect of Reynolds number on maximum lift performance of EET High-Lift Airfoil with $\delta_v = 30.0^\circ$ and $\delta_\Gamma = 30.0^\circ$.



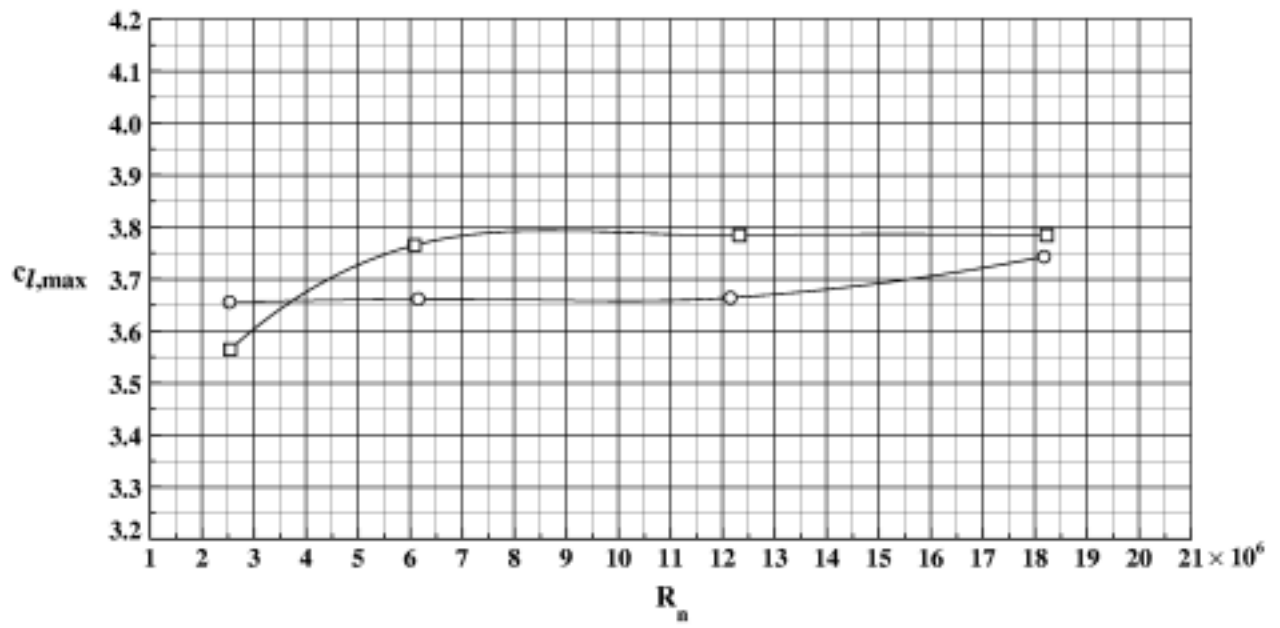
(a) $\delta_s = -40^\circ$.

Figure 90. Effect of Reynolds number on maximum lift performance of EET High-Lift Airfoil with $\delta_v = 22.5^\circ$ and $\delta_f = 22.5^\circ$. Each curve represents repeat runs for the same configuration.



(b) $\delta_s = -50^\circ$.

Figure 90. Continued.



(c) $\delta_s = -60^\circ$.

Figure 90. Concluded.

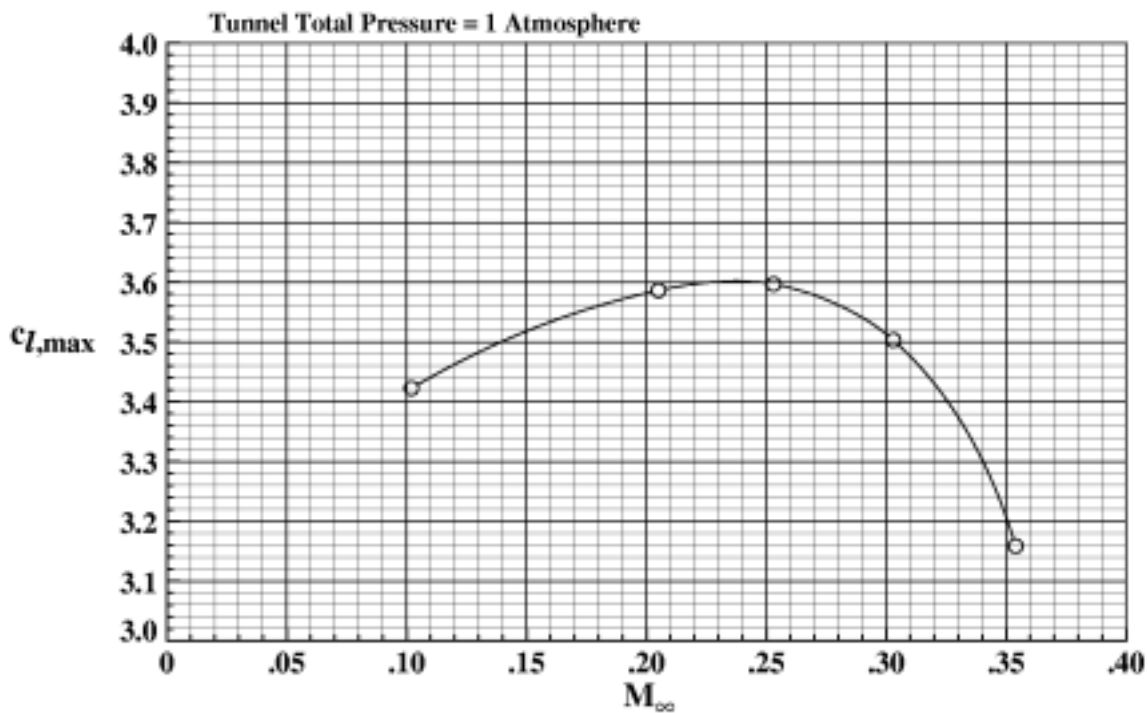


Figure 91. Effect of Mach number on maximum lift performance of EET High-Lift Airfoil with $\delta_s = -50.0^\circ$, $\delta_v = 15.0^\circ$, and $\delta_f = 15.0^\circ$.

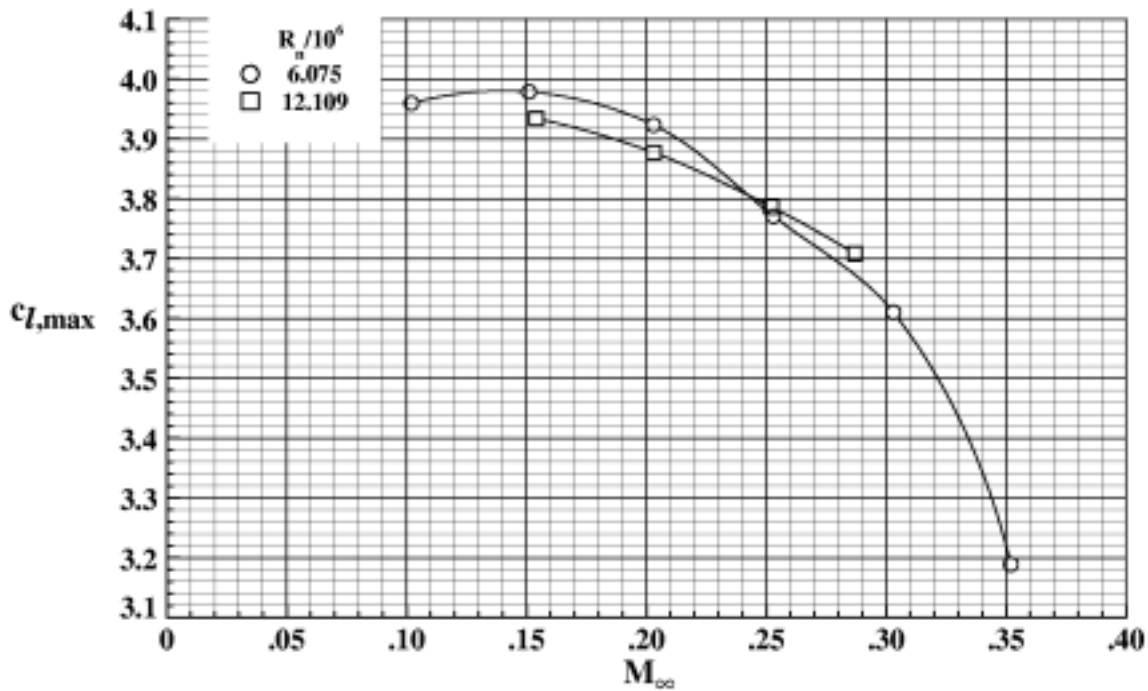


Figure 92. Effect of Mach number on maximum lift performance of EET High-Lift Airfoil with $\delta_s = -50.0^\circ$, $\delta_v = 15.0^\circ$, and $\delta_f = 15.0^\circ$.

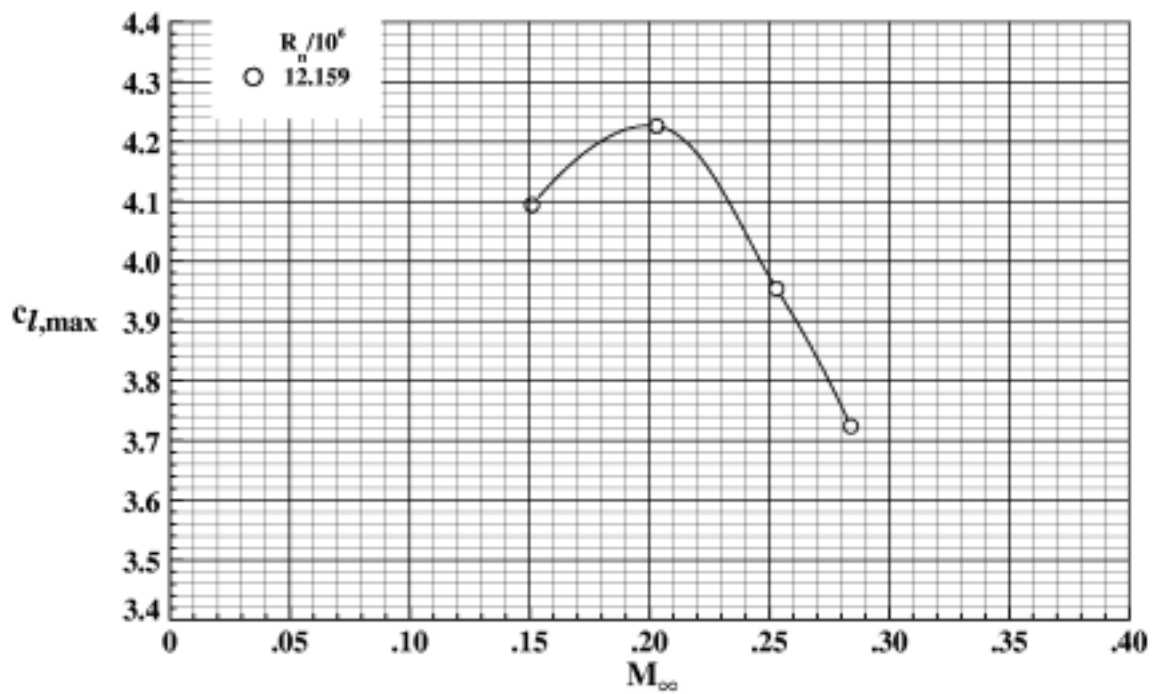


Figure 93. Effect of Mach number on maximum lift performance of EET High-Lift Airfoil with $\delta_s = -30.0^\circ$, $\delta_v = 22.5^\circ$, and $\delta_f = 22.5^\circ$.

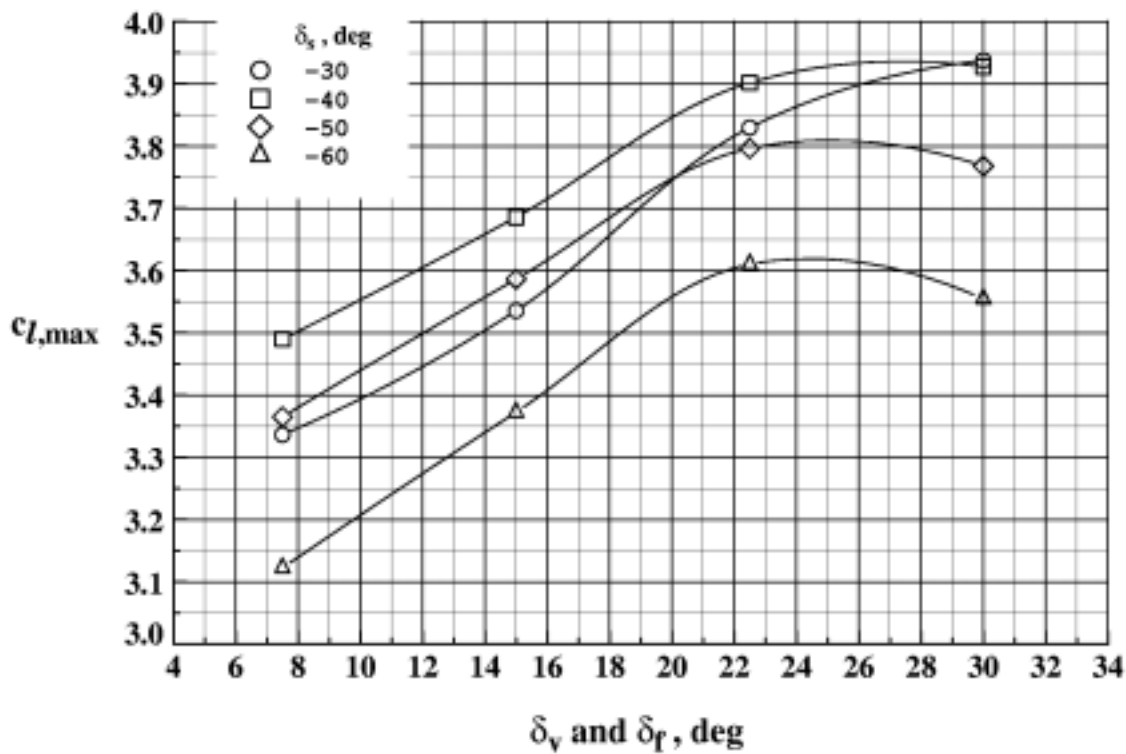


Figure 94. Effect of vane-flap deflection on maximum lift performance of EET High-Lift Airfoil at a Reynolds number of 2.51×10^6 .

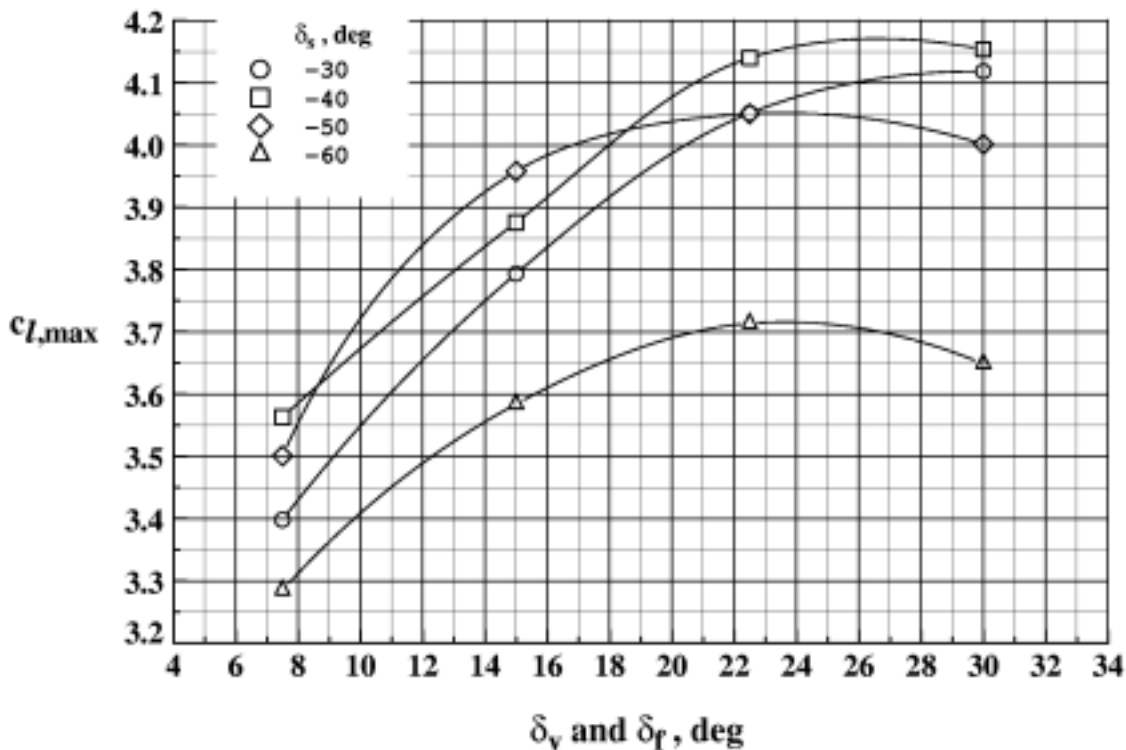


Figure 95. Effect of vane-flap deflection on maximum lift performance of EET High-Lift Airfoil at a Reynolds number of 6.11×10^6 .

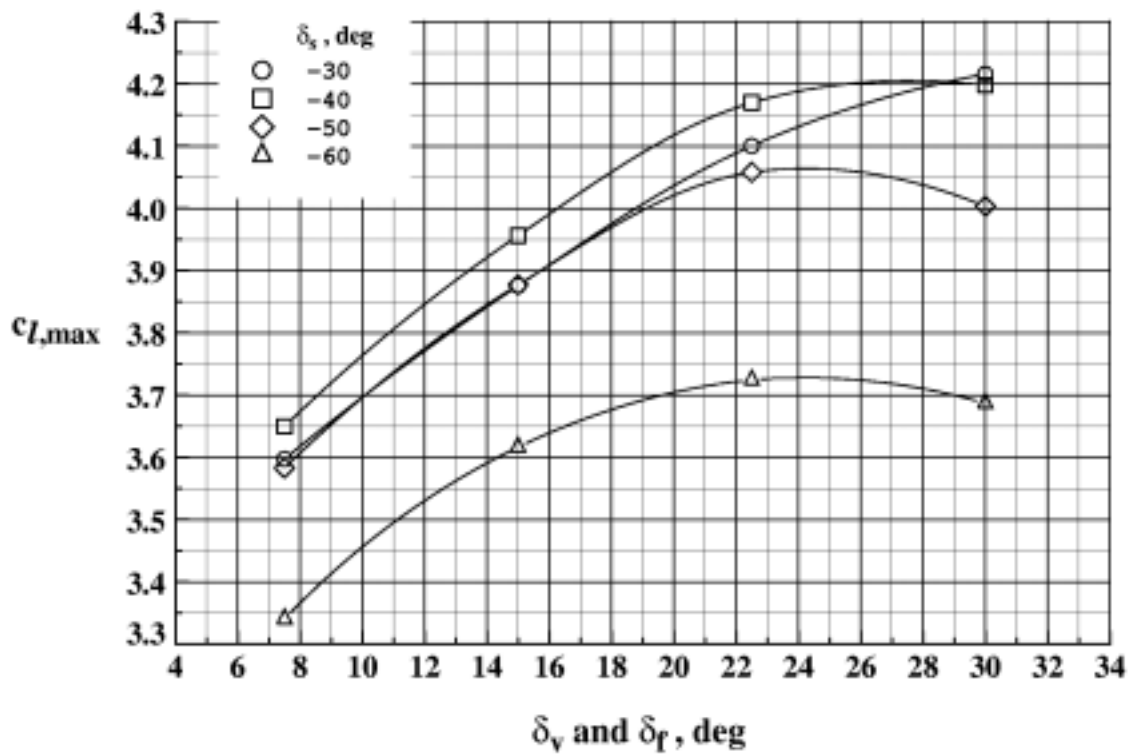


Figure 96. Effect of vane-flap deflection on maximum lift performance of EET High-Lift Airfoil at a Reynolds number of 12.17×10^6 .

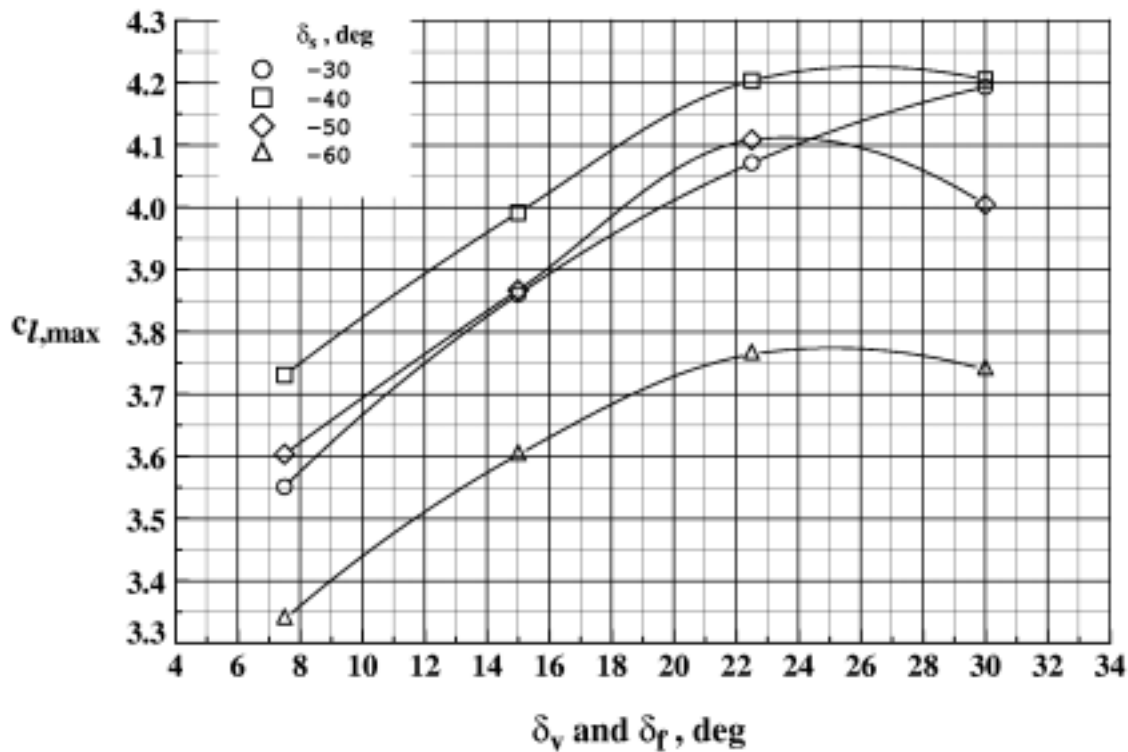


Figure 97. Effect of vane-flap deflection on maximum lift performance of EET High-Lift Airfoil at a Reynolds number of 18.48×10^6 .

REPORT DOCUMENTATION PAGE				Form Approved OMB No. 0704-0188	
<p>The public reporting burden for this collection of information is estimated to average 1 hour per response, including the time for reviewing instructions, searching existing data sources, gathering and maintaining the data needed, and completing and reviewing the collection of information. Send comments regarding this burden estimate or any other aspect of this collection of information, including suggestions for reducing this burden, to Department of Defense, Washington Headquarters Services, Directorate for Information Operations and Reports (0704-0188), 1215 Jefferson Davis Highway, Suite 1204, Arlington, VA 22202-4302. Respondents should be aware that notwithstanding any other provision of law, no person shall be subject to any penalty for failing to comply with a collection of information if it does not display a currently valid OMB control number.</p> <p>PLEASE DO NOT RETURN YOUR FORM TO THE ABOVE ADDRESS.</p>					
1. REPORT DATE (DD-MM-YYYY)		2. REPORT TYPE		3. DATES COVERED (From - To)	
12-2002		Technical Memorandum			
4. TITLE AND SUBTITLE Experimental Test Results of Energy Efficient Transport (EET) High-Lift Airfoil in Langley Low-Turbulence Pressure Tunnel				5a. CONTRACT NUMBER	
				5b. GRANT NUMBER	
				5c. PROGRAM ELEMENT NUMBER	
6. AUTHOR(S) Morgan, Harry L., Jr.				5d. PROJECT NUMBER	
				5e. TASK NUMBER	
				5f. WORK UNIT NUMBER 706-17-31-02	
7. PERFORMING ORGANIZATION NAME(S) AND ADDRESS(ES) NASA Langley Research Center Hampton, VA 23681-2199				8. PERFORMING ORGANIZATION REPORT NUMBER L-18221	
9. SPONSORING/MONITORING AGENCY NAME(S) AND ADDRESS(ES) National Aeronautics and Space Administration Washington, DC 20546-0001				10. SPONSOR/MONITOR'S ACRONYM(S) NASA	
				11. SPONSOR/MONITOR'S REPORT NUMBER(S) NASA/TM-2002-211780	
12. DISTRIBUTION/AVAILABILITY STATEMENT Unclassified - Unlimited Subject Category 2 Availability: NASA CASI (301) 621-0390 Distribution: Standard					
13. SUPPLEMENTARY NOTES Morgan, Langley Research Center. An electronic version can be found at http://techreports.larc.nasa.gov/ltrs/ or http://techreports.larc.nasa.gov/cgi-bin/NTRS CD-ROM supplement available from NASA CASI on request.					
14. ABSTRACT This report describes the results of an experimental study conducted in the Langley Low-Turbulence Pressure Tunnel to determine the effects of Reynolds number and Mach number on the two-dimensional aerodynamic performance of the Langley Energy Efficient Transport (EET) High-Lift Airfoil. The high-lift airfoil was a supercritical-type airfoil with a thickness-to-chord ratio of 0.12 and was equipped with a leading-edge slat and a double-slotted trailing-edge flap. The leading-edge slat could be deflected -30°, -40°, -50°, and -60°, and the trailing-edge flaps could be deflected to 15°, 30°, 45°, and 60°. The gaps and overlaps for the slat and flaps were fixed at each deflection resulting in 16 different configurations. All 16 configurations were tested through a Reynolds number range of 2.5 to 18 million at a Mach number of 0.20. Selected configurations were also tested through a Mach number range of 0.10 to 0.35. The plotted and tabulated force, moment, and pressure data are available on the CD-ROM supplement L-18221.					
15. SUBJECT TERMS High-lift airfoil; Pressure data; Energy efficient transport					
16. SECURITY CLASSIFICATION OF:			17. LIMITATION OF ABSTRACT	18. NUMBER OF PAGES	19a. NAME OF RESPONSIBLE PERSON
a. REPORT	b. ABSTRACT	c. THIS PAGE			STI Help Desk (email: help@sti.nasa.gov)
U	U	U	UU	158	19b. TELEPHONE NUMBER (Include area code) (301) 621-0390